

UNCLASSIFIED

AD **408 778**

DEFENSE DOCUMENTATION CENTER

FOR

SCIENTIFIC AND TECHNICAL INFORMATION

CAMERON STATION, ALEXANDRIA, VIRGINIA



UNCLASSIFIED

NOTICE: When government or other drawings, specifications or other data are used for any purpose other than in connection with a definitely related government procurement operation, the U. S. Government thereby incurs no responsibility, nor any obligation whatsoever; and the fact that the Government may have formulated, furnished, or in any way supplied the said drawings, specifications, or other data is not to be regarded by implication or otherwise as in any manner licensing the holder or any other person or corporation, or conveying any rights or permission to manufacture, use or sell any patented invention that may in any way be related thereto.

NOTICES

When Government drawings, specifications, or other data are used for any purpose other than in connection with a definitely related Government procurement operation, the United States Government thereby incurs no responsibility nor any obligation whatsoever; and the fact that the Government may have formulated, furnished, or in any way supplied the said drawings, specifications, or other data, is not to be regarded by implication or otherwise as in any manner licensing the holder or any other person or corporation, or conveying any rights or permission to manufacture, use, or sell any patented invention that may in any way be related thereto.

Qualified requesters may obtain copies of this report from the Armed Services Technical Information Agency, (ASTIA), Arlington Hall Station, Arlington 12, Virginia.

This report has been released to the Office of Technical Services, U.S. Department of Commerce, Washington 25, D.C., in stock quantities for sale to the general public.

Copies of this report should not be returned to the Aeronautical Systems Division unless return is required by security considerations, contractual obligations, or notice on a specific document.

B

FOREWORD

This report was prepared by the Westinghouse Research Laboratory, Pittsburgh, Pennsylvania, under Task No. 415604 of Project No. 4156, "Heat Diode Converter". The work was administered under the direction of Electronic Technology Laboratory, Aeronautical Systems Division. Mr. Lawrence E. Porter was project engineer for the Laboratory.

The studies presented began in May 1961 and were concluded in December 1962. Milton Gottlieb, of the Westinghouse Electric Corporation was responsible for the research activity.

The authors wish to express their gratitude to Messrs. C. R. Taylor and D. F. Ennulat of the Westinghouse Research Laboratory for their able technical assistance in performing the experimental work reported herein.

This report is the final report and it concludes the work on contract AF 33(616)-8262. The contractor's report number is 62-918-274-R4.

ABSTRACT

The work presented in this report represents an eighteen month program in which experimental and theoretical investigations were made on several aspects of the cesium plasma thermionic converter. Data were taken on the electron emission properties of tungsten, tantalum, molybdenum, niobium, rhenium, iridium and tantalum carbide. Two methods were used in this study; one was the measurement of the I-V characteristics of diodes using emitters of these materials and the other was the direct measurement of the saturation emission current density by the plasma-anode technique. It is possible to make some separation between emission effects and transport effects by combining results of those two measurements. Studies were made on several important loss mechanisms in the thermionic converter. Among these were the thermal conduction loss in the cesium vapor, losses associated with electron scattering in the plasma, and losses due to reflection of electrons by the collector. A study was also made of the evaporative loss of the emitter in the presence of cesium. The experimental data collected has been used for an extensive theoretical analysis of the efficiency and lifetime of a thermionic converter. Theoretical treatments are also given for energy and mass transfer in the cesium plasma and of electron emission in the presence of a plasma.

PUBLICATION REVIEW

This report presents the scientific findings of an Air Force sponsored program. It does not direct any specific application thereof. The report is approved for publication to achieve an exchange and stimulation of ideas.



KENNETH R. HUTCHINSON
CHIEF, Low Power Tube Section
Electronic Technology Laboratory

TABLE OF CONTENTS

	Page
Chap. 1 Current-Voltage Characteristics of Variable Spacing Diode with Refractory Material Emitters	1.1
Chap. 2 Saturation Emission Current Measurements on Refractory Materials Using "Plasma-Anode" Technique	2.1
References	2.15
Chap. 3 Evaporation of Molybdenum in the Presence of Cesium Vapor	3.1
References	3.11
Chap. 4 Reflection of Electrons from Cesium Coated Surfaces	4.1
References	4.19
Chap. 5 Thermionic Diode Currents in Transverse Magnetic Fields and Scattering of Electrons by Cesium Atoms	5.1
References	5.8
Chap. 6 Thermal Conductivity of Cesium and Rubidium Vapor	6.1
References	6.12
Chap. 7 Theoretical Efficiency of Thermionic Energy Converter	7.1
References	7.22
Chap. 8 Lifetime of Thermionic Energy Converter	8.1
References	8.14
Chap. 9 Anomalous Richardson Emission Constants	9.1
References	9.6
Chap. 10 Electron and Ion Emission from Cesium Coated Refractory Metals in Electric Fields	10.1
References	10.5
Chap. 11 Potential Distributions in High Pressure Cesium Thermionic Diodes	11.1
Chap. 12 Space Charge Limited Currents in High Pressure Cesium Thermionic Diodes	12.1
Distribution List	13.1

List of Illustrations

		page
1-1	Variable Spacing Cell	1.8
1-2	Telescopic View of Emitter-Collector Assembly	1.9
1-3	Test Circuit	1.10
1-4 to 1-9	Current-Voltage Characteristics with Tantalum Emitter	1.11 to 1.16
1-10 to 1-21	Current-Voltage Characteristics with Molybdenum Emitter	1.17 to 1.28
1-22 to 1-29	Current-Voltage Characteristics with Niobium Emitter	1.29 to 1.36
1-30 to 1-37	Current-Voltage Characteristics with Rhenium Emitter	1.37 to 1.44
1-38 to 1-45	Current-Voltage Characteristics with Tantalum Carbide Emitter	1.45 to 1.52
1-46 to 1-55	Current-Voltage Characteristics with Iridium Emitter	1.53 to 1.62
2-1	Plasma-Anode Discharge Tube	2.16
2-2	Measuring Circuit	2.17
2-3	Mounting Detail of Test Emitter	2.18
2-4	S-Curve Characteristics of Tungsten and Tantalum for $T_{Cs} = 373^{\circ}K$ ($P_{Cs} = 5 \times 10^{-4}$ torr)	2.19
2-5	S-Curve Characteristics of Rhenium for $T_{Cs} = 398^{\circ}K$ ($P_{Cs} = 2.3 \times 10^{-3}$ torr).	2.20
2-6	Thermionic Emission Switched from Low Current to High Current Mode with Rhenium at $1750^{\circ}K$ and $T_{Cs} = 462^{\circ}K$ ($P_{Cs} = 5 \times 10^{-2}$ torr)	2.21
2-7	Extrapolation of Double-Mode Behavior to Zero Net Positive Ion Current Arrival at Test Emitter for Rhenium at $2160^{\circ}K$ and $T_{Cs} = 398^{\circ}K$ ($P_{Cs} = 2.3 \times 10^{-3}$ torr)	2.22
2-8	S-Curve Characteristics for $T_{Cs} = 373^{\circ}K$ ($P_{Cs} = 5 \times 10^{-4}$ torr)	2.23
2-9	S-Curve Characteristics for $T_{Cs} = 398^{\circ}K$ ($P_{Cs} = 2.3 \times 10^{-3}$ torr)	2.24
2-10	S-Curve Characteristics for $T_{Cs} = 423^{\circ}K$ ($P_{Cs} = 9 \times 10^{-3}$ torr)	2.25

List of Illustrations (Cont'd)

		page
3-1	Evaporation of Molybdenum as a Function of Temperature	3.12
3-2	Diagram of Experimental Cell	3.13
3-3	Transport Ratio as a Function of Pressure x Spacing	3.14
4-1	Tube and Circuit for Electron Reflection Measurements	4.20
4-2	Photograph of Electron Reflection Tube	4.21
4-3	Relative Currents to the Target and the Two Collector Electrodes vs. Deflecting Grid Voltage	4.22
4-4	Measured Reflection Coefficient and Target Current vs. Primary Electron Energy and Potential for Advance-Cesium $\phi = 3.14$ eV	4.23
4-5	Semilog Plot of Target Current vs. Potential Used to Obtain Zero of Primary Electron Energy and Estimate the Target Work Function for Advance-Cesium	4.24
4-6 to 4-10	Reflection Coefficient for Advance-Cesium Target	4.25 to 4.29
4-11 to 4-16	Reflection Coefficient for Molybdenum-Cesium Target	4.30 to 4.35
4-17 to 4-20	Reflection Coefficient for Tungsten-Cesium Target	4.36 to 4.39
4-21 to 4-22	Reflection Coefficient for Tantalum-Cesium Target	4.40 to 4.41
4-23 to 4-26	Reflection Coefficient for Copper-Cesium Target	4.42 to 4.45
4-27 to 4-28	Reflection Coefficient for Platinum-Cesium Target	4.46 to 4.47
4-29 to 4-32	Reflection Coefficient for Silver-Cesium Target	4.48 to 4.51
4-33 to 4-34	Reflection Coefficient for 301 Stainless Steel-Cesium Target	4.52 to 4.53
4-35 to 4-36	Reflection Coefficient for Monel-Cesium Target	4.54 to 4.55
4-37 to 4-38	Reflection Coefficient for Inconel-Cesium Target	4.56 to 4.57
4-39 to 4-40	Reflection Coefficient for Platinum Black-Cesium Target	4.58 to 4.59
4-41 to 4-46	Retarding Potential Plots with Copper-Cesium Target	4.60 to 4.65

List of Illustrations (Cont'd)

		page
5-1	Photograph of Cells Used for Measurements	5.9
5-2	Measuring Circuit	5.10
5-3	I_0/I vs. (Magnetic Field) ² for 0.225" Spacing	5.11
5-4	I_0/I vs. (Magnetic Field) ² for 0.020" Spacing	5.12
5-5	Dependence of Current Ratio on Cell Potential	5.13
5-6	Available Data on Electron Scattering	5.14
6-1	Thermal Conductivity Measurement Cell	6.13
6-2	Measuring Circuit	6.14
6-3	Filament Power vs. Temperature	6.15
6-4	Thermal Conductance vs. Pressure for Cesium	6.16
6-5	λ_e^2 vs. Temperature from Theory	6.17
6-6	Experimental and Theoretical Thermal Conductivity vs. Temperature	6.18
6-7	Vapor Pressure of Cesium and Rubidium	6.19
6-8	Filament Power vs. Temperature for Long Filament	6.20
6-9	Filament Power vs. Temperature for Short Filament	6.21
6-10	Thermal Conductance vs. Pressure for Rubidium	6.22
6-11	Thermal Conductivity vs. Temperature	6.23
7-1	Basic Thermionic Diode	7.23
7-2	Modes of Operation	7.23
7-3	β as a Function of $\bar{\gamma}$ and the Ideal Efficiency, $\bar{\eta}_0$	7.24
7-4	Optimum Values of $\bar{\eta}$, $\bar{\gamma}$ and β as Functions of the Ideal Efficiency, η_0	7.25
7-5	Work Function of Tungsten as a Function of Fractional Coverage by Cesium	7.26
7-6	Fractional Coverage as a Function of Cesium Temperature and Surface Temperature	7.27
7-7	Work Function as a Function of Cesium Bath Temperature and Surface Temperature	7.28
7-8	Thermal Conductivity of Cesium Plasma as a Function of Spacing and Pressure	7.29

List of Illustrations (Cont'd)

		page
7-9	Efficiency as a Function of Cathode and Anode Temperatures	7.30
7-10	Efficiency as a Function of Cathode and Anode Temperatures	7.31
7-11	Efficiency as a Function of Spacing and Cathode Temperature	7.32
7-12	Efficiency as a Function of Spacing and Anode, Cathode and Cesium Temperatures	7.33
7-13	Optimum Anode and Cesium Temperatures as a Function of Cathode Temperature	7.34
7-14	Optimum Anode and Cesium Temperatures as a Function of Cathode Temperature	7.35
8-1	Time to Lose 2.5 Microns by Evaporation from Molybdenum, Columbium, Tantalum and Tungsten as a Function of Temperature	8.15
8-2	Relative Lifetime of a Cathode as a Function of Cesium Bath Temperature and Spacing	8.16
8-3	The Relationship between Evaporative Lifetime and Efficiency for Tungsten and Molybdenum	8.17
8-4	Power-to-Weight Ratio, Optimum Anode Temperature and Efficiency at Minimum Weight as a Function of Cathode Temperature	8.18
9-1	Basic Thermionic Diode	9.7
9-2	Modes of Operation	9.7
10-1	Atom and Ion Evaporation Rates vs. Fractional Monolayer Coverage of Cesium on Tungsten, after Taylor and Langmuir	10.6
11-1	Current-Voltage Characteristics at Two Spacings	11.12
11-2	Electron Temperature Plot	11.13
11-3	Sheath Voltages vs. Current	11.14
11-4	Potential Distributions at Four Different Cell Currents	11.15
12-1	Graphical Solution for Electron Density	12.7

CHAPTER ONE

CURRENT VOLTAGE CHARACTERISTICS OF VARIABLE SPACING DIODE
WITH REFRACTORY MATERIAL EMITTERS

A program was carried out to study the current-voltage characteristics of cesium plasma thermionic diodes with a variety of refractory material emitters. These emitters have included tantalum, molybdenum, niobium, rhenium, iridium and tantalum carbide. Measurements were made over wide ranges of emitter temperature, cesium pressure and electrode spacing. The purpose of this program was to find materials best suited for thermionic conversion, and to provide design information for thermionic conversion hardware.

A universal cell was constructed for these studies, in which the emitters are easily interchangeable and in which the interelectrode spacing can be varied continuously. A photograph of this cell is shown in Figure 1-1. The two flanges are sealed with a bakeable, copper shear gasket. The emitters are in the form of ribbons, 0.010 in. thick, 0.080 in. or 0.160 in. wide and about 2 cm. long. They are fastened to the binding posts in the lower flange. The collector plate is fastened at each end to a micrometer drive on the upper flange, so that the electrode surfaces can be kept accurately parallel even at very close spacing. The cell has an optical port which views the emitter-collector assembly, and the emitter temperature is measured with an optical pyrometer. The window material is sapphire, which is resistant

Manuscript released by the author January 30, 1963 for publication as an ASD Technical Documentary Report.

to darkening by cesium even at high temperatures. The interelectrode spacing is also measured through this port by means of a cathetometer. The spacing may be adjusted down to 0.001 in., and a photograph taken through the port with the gap set at 0.0015 in. is shown in Figure 1-2. The emitter is directly heated with half-wave rectified a-c power, and the measurements are made during the off part of the cycle, so that there is no voltage drop along the emitter associated with input power. The voltage across a variable load resistor is measured with an oscilloscope. A mercury wetted switch, which is in phase with the heating power, opens the cell output circuit during the heating part of the cycle so that there is no voltage across the load resistor. The switch is closed with a very low value of resistance (0.01 ohm) during the measuring part of the cycle. Correction is made for voltage drops in the leads, filaments and switch. A diagram of the measuring circuit is shown in Figure 1-3.

A set of emission data for tantalum is shown in Figures 1-4 to 1-9. At a cesium reservoir temperature of 202°C, 0.0148 in. spacing, the emission current is bistable at cathode temperatures of 1549°C and 1661°C. When the spacing is reduced to 0.075 in., an interesting feature occurs in the emission, as shown in Figure 1-5. At cathode temperatures of 1774°C and 1661°C, the cell current is tristable with voltage. A "heel" forms in the current curve at these temperatures which is more prominent at the lower temperature. This phenomenon is not understood at the present time, and must be further studied. At a cesium reservoir temperature of 248°C, the current is no longer bistable over the range

of cathode temperatures measured, as shown in Figures 1-6 and 1-7. At 0.075 in. spacing, it appears that a low voltage arc is struck at negative cell voltages for the two highest emitter temperatures. Figures 1-8 and 1-9 show the behavior at a cesium reservoir temperature of 295°C.

A set of emission data was taken for a 2 mm. wide molybdenum emitter, the results of which appear in Figures 1-10 to 1-18. Data was taken of spacings of 0.004 in. and 0.015 in. for cesium reservoir temperatures between 202°C and 325°C. Bistable behavior occurs only at the 202°C reservoir temperature.

The low voltage arcing phenomenon which occurs at the higher cesium pressures appears to be initiated in these curves at about zero cell voltage. Since this has been reported for larger output cell voltages, the effect of geometry on the current-voltage characteristics was studied by repeating these measurements using an emitter which was twice as wide, 0.160 in. A set of data was taken for cesium reservoir temperatures of 300°C and 325°C, and spacings of 0.065 in. and 0.015 in. The emitter temperature range was from 1479°C to 1840°C. The curves for this data are shown in Figures 1-19 to 1-21. It was found that for lower cesium pressures the change in geometry had no effect on the characteristic, while at these higher pressures there was a great effect. For the wider emitter, the curves are shifted by about one volt to more negative voltages, so that well defined arcing occurs for voltages less than zero. Current densities up to 10 amps/cm² were measured, but these points do not appear to fit well on the curves.

A peculiarity observed in the characteristics is that the currents corresponding to the lowest emitter temperature are not always lower than that corresponding to higher emitter temperatures. The currents for the 1479°C emitter temperature are lowest up to a cell voltage of about 0.2 volts. Then the current rises and exceeds those for higher emitter temperature. The characteristics at the 325°C cesium reservoir temperature appear to be shifted by about one half a volt toward higher output voltages.

A set of current-voltage data was taken for a 4 mm wide niobium emitter. Data was taken for cesium reservoir temperatures of 200°C , 250°C , 300°C and 325°C . Emitter temperatures from 1479°C - 1840°C were measured at emitter-collector spacings of 0.005 in. and 0.015 in. The results are shown on the curves of Figures 1-22 to 1-29. The conclusion may be drawn immediately that niobium is an inferior thermionic converter emitter material as compared to tungsten, tantalum or molybdenum. At the lowest cesium pressures, cell currents remain low well into the region of positive cell voltages. At the 250°C cesium bath temperature arcing occurs at negative cell voltages for the two highest emitter temperatures. An interesting feature here, however, is that the currents are greater for the 0.015 in. spacing than for the 0.005 in., so that apparently the optimum spacing lies between 0.005 in. and 0.015 in. for these conditions. At a cesium reservoir temperature of 300°C there is only a small change in current with spacing, but the same low emitter temperature phenomenon which was observed for molybdenum also occurs here.

That is that the I-V characteristic for the lowest emitter temperature is lowest for negative cell voltages, but crosses the higher temperature characteristic at about +0.25 volts. This phenomenon is clearly shown in the two sets of curves for the 325°C bath temperature; for cell voltages more negative than about 0 at 0.015 in. or -0.2 at 0.005 in. the currents are higher for higher emitter temperatures and at voltages more positive than these, the currents are higher for lower emitter temperatures. A complete cross-over of the I-V curves occurs at 0 volts and -0.2 volts. An understanding of this data will require further analysis.

A set of current-voltage characteristics was measured in the variable spacing cell for a 4 mm wide rhenium emitter. Measurements were done for cesium reservoir temperatures from 200°C to 325°C, emitter temperatures from 1479°C - 1840°C, and emitter-collector spacings of 0.005 in. and 0.015 in. The data is shown on the curves in Figure 1-30 to Figure 1-37. The results indicate that rhenium is a favorable thermionic converter emitter material. Short circuit cell currents of approximately 30 amps/cm² are indicated, and currents around 16 amps/cm² at an output voltage of 0.5 volts. Nowhere within the range of measurement was there observed a decrease of current with decreasing spacing, as was the case with molybdenum and niobium.

At the lowest cesium reservoir temperature, 200°C, the characteristics exhibit the triple mode behavior which has also been observed at low cesium pressures with other refractory metals as emitters. This is shown on Figures 1-30 and 1-31.

The crossover of current for the low temperature characteristics are illustrated well for rhenium on Figures 1-34 and 1-35. It appears that the crossover would also have occurred for the characteristics on Figures 1-36 and 1-37, if the measurements had gone to higher currents.

A tantalum carbide emitter was fabricated for the variable spacing cell by firing a tantalum ribbon at 1200°C in an ethylene atmosphere, and monitoring the change in its resistance as an indicator of its carburization. After this treatment, an x-ray reflection picture was taken, which showed that the carbide formation was complete to the penetration depth of the x-ray beam. A set of current voltage characteristics were measured over the usual range of cesium pressures, but only emitter temperatures of 1479°C and 1598°C were tested. The resulting curves are shown in Figures 1-38 to Figures 1-45. The emitter was again subjected to x-ray examination after the data had been taken. This examination indicated that while TaC was the predominant component before the measurements, Ta_2C was predominant after the measurements. Because of this uncertainty in the composition, the data cannot be accepted with a high degree of reliability. There is no indication that this material would be desirable for thermionic conversion.

An iridium emitter was tested in the cell, although the evaporation rate of iridium is excessively high and the characteristics for the higher temperatures could not be measured. Measurements were done for emitter temperatures of 1497°C and 1598°C at cesium reservoir temperatures of 150°C to 275°C . These measurements are shown in

Figures 1-46 to 1-55. High values of current are obtainable for relatively low emitter temperatures and cesium pressure, so that iridium might be favorable where lower temperature emitter operation is desired.

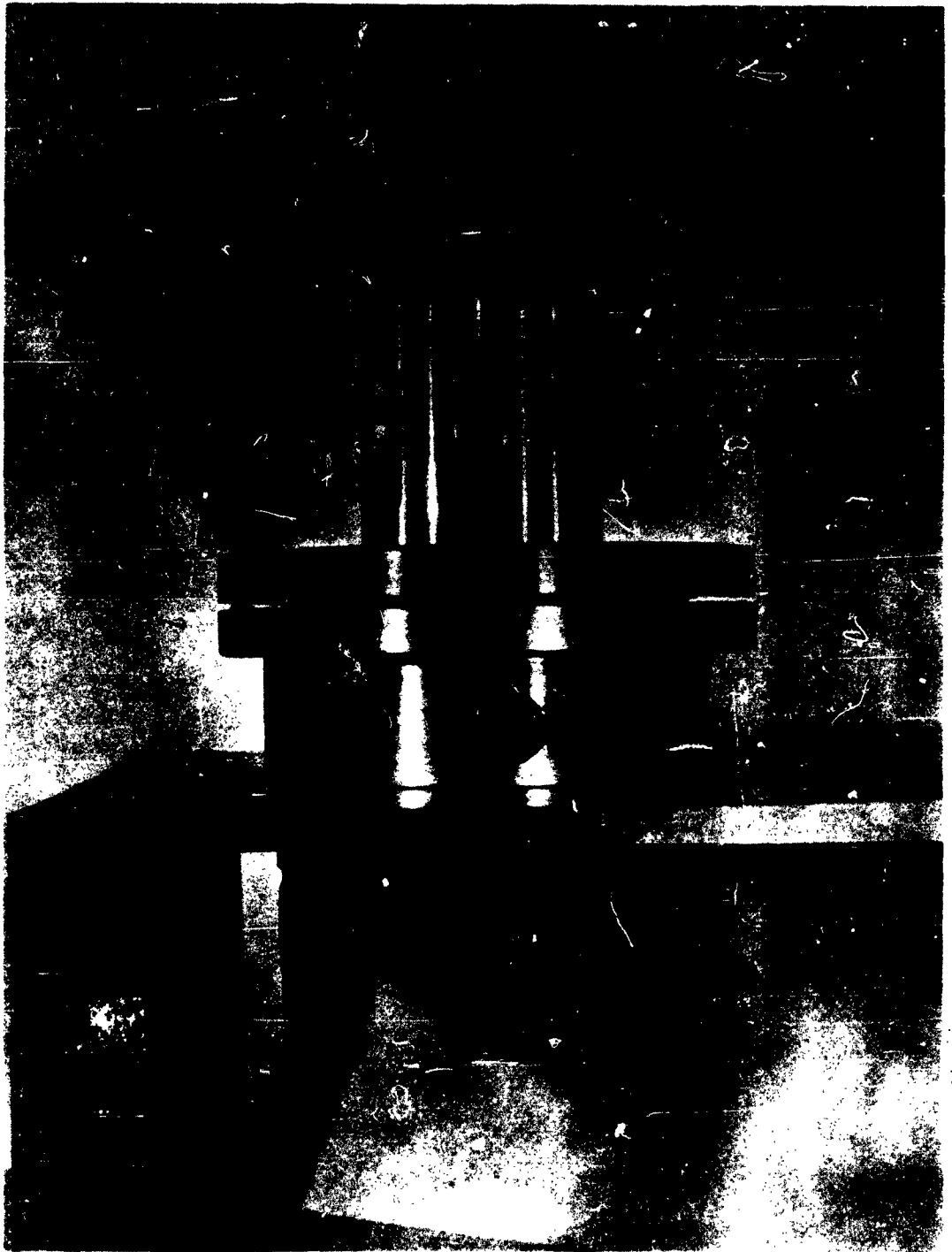


Fig. 1-1 - Variable Spacing Cell

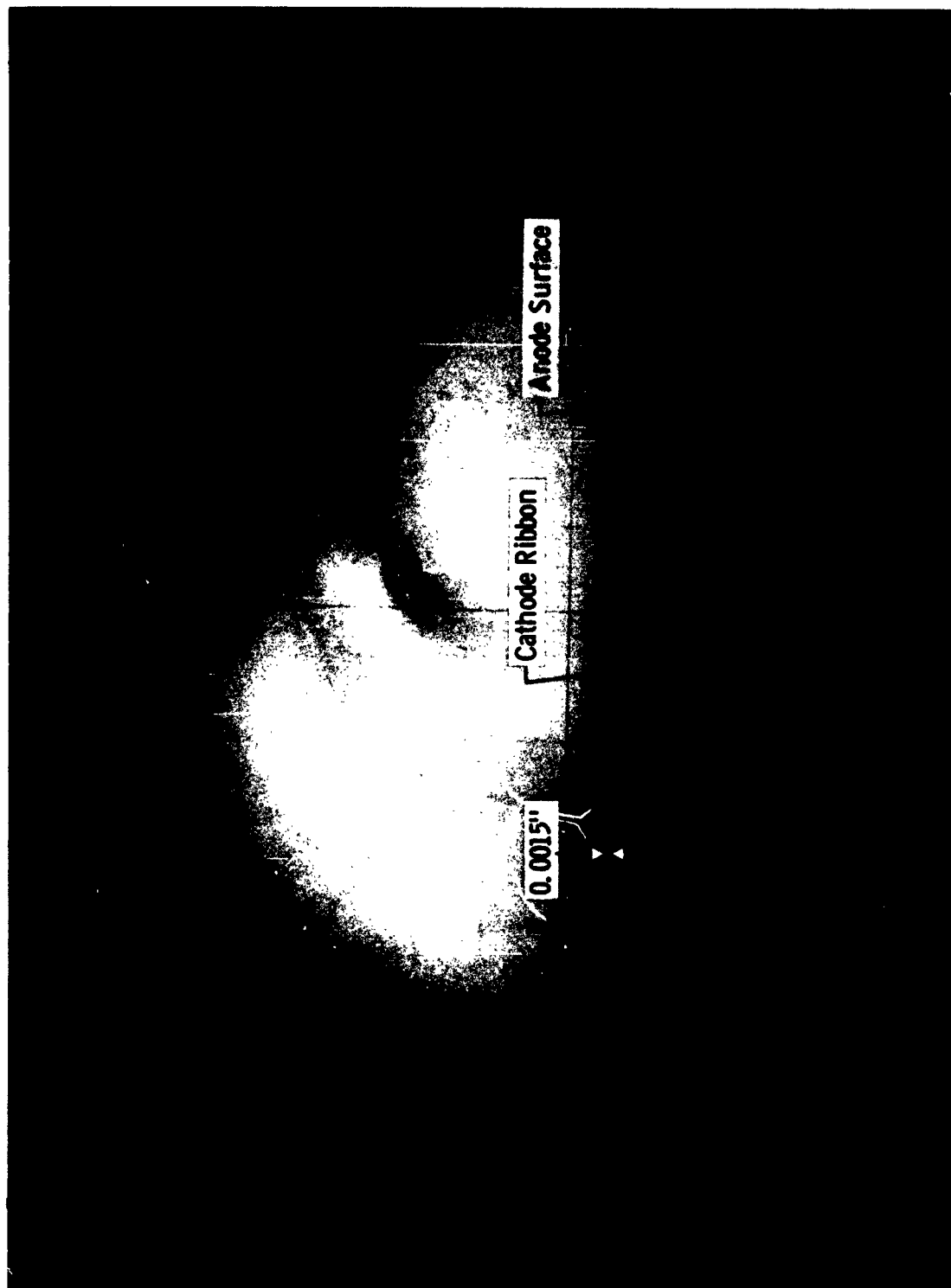


Fig. 1-2 - Telescopic View of Emitter-Collector Assembly

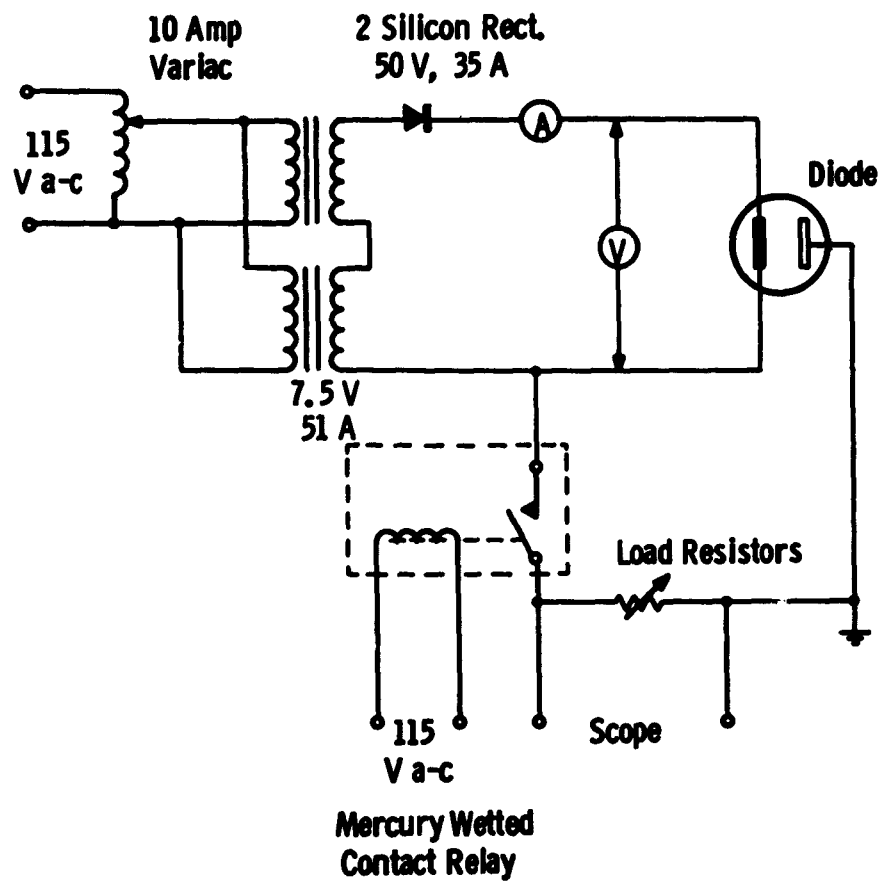


Fig. 1-3. Test Circuit

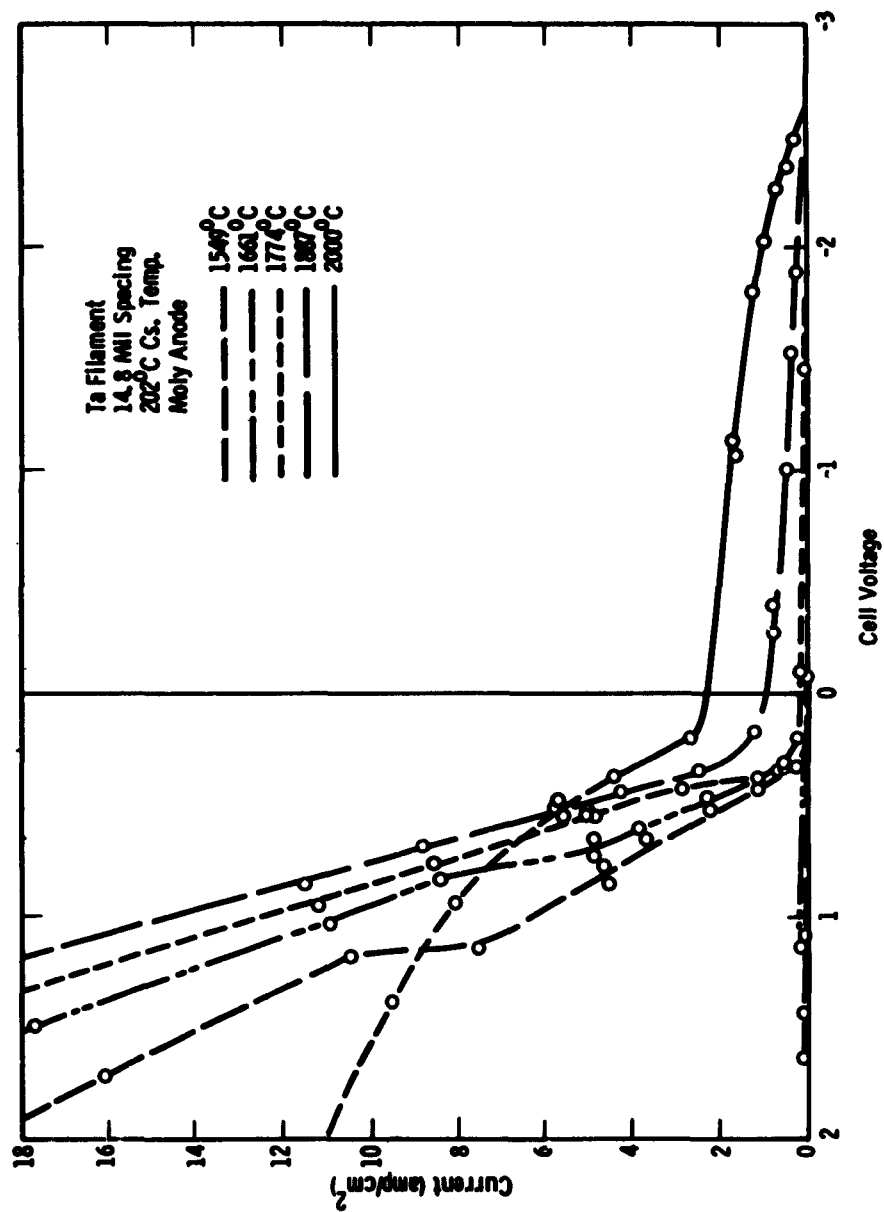


Fig. 1-4. Current Voltage Characteristics with Tantalum Emitter

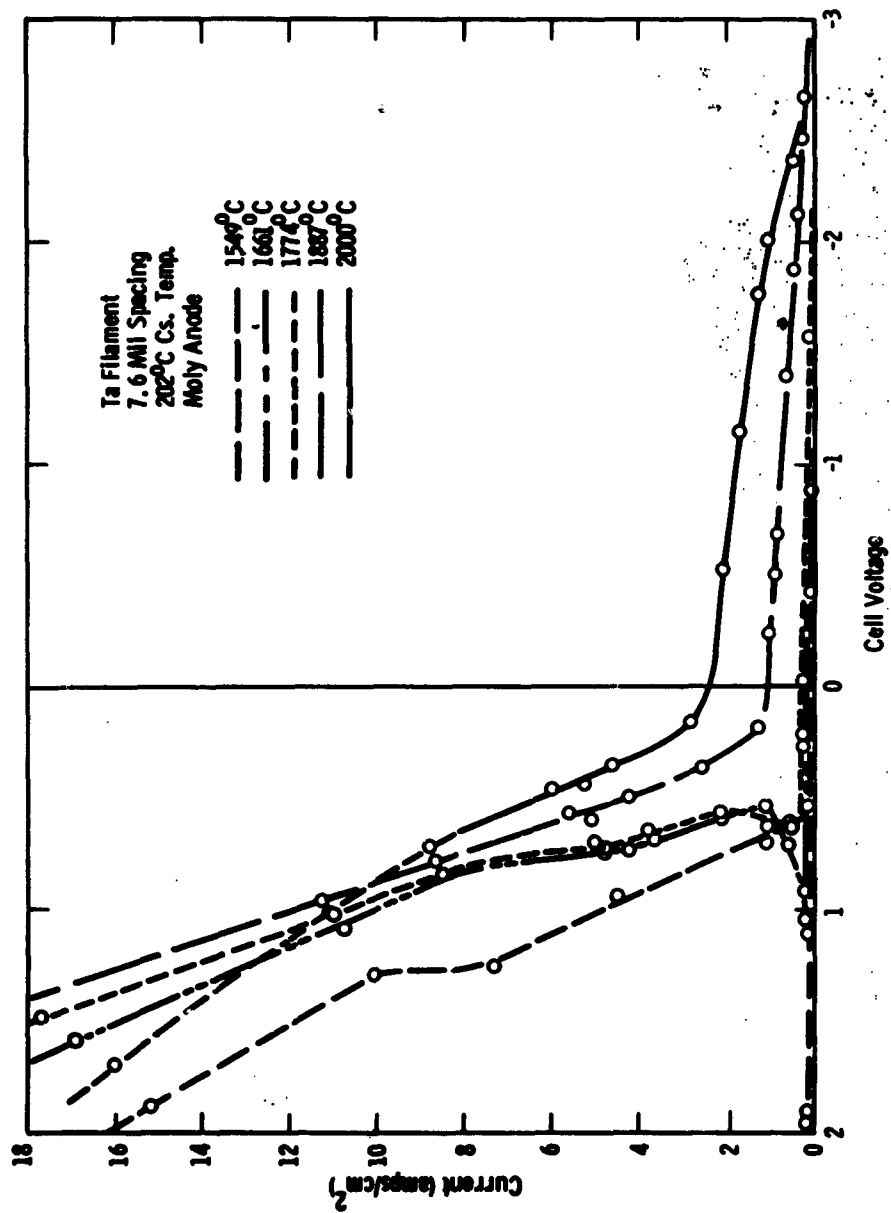


Fig. 1-5. Current Voltage Characteristics with Tantalum Emitter

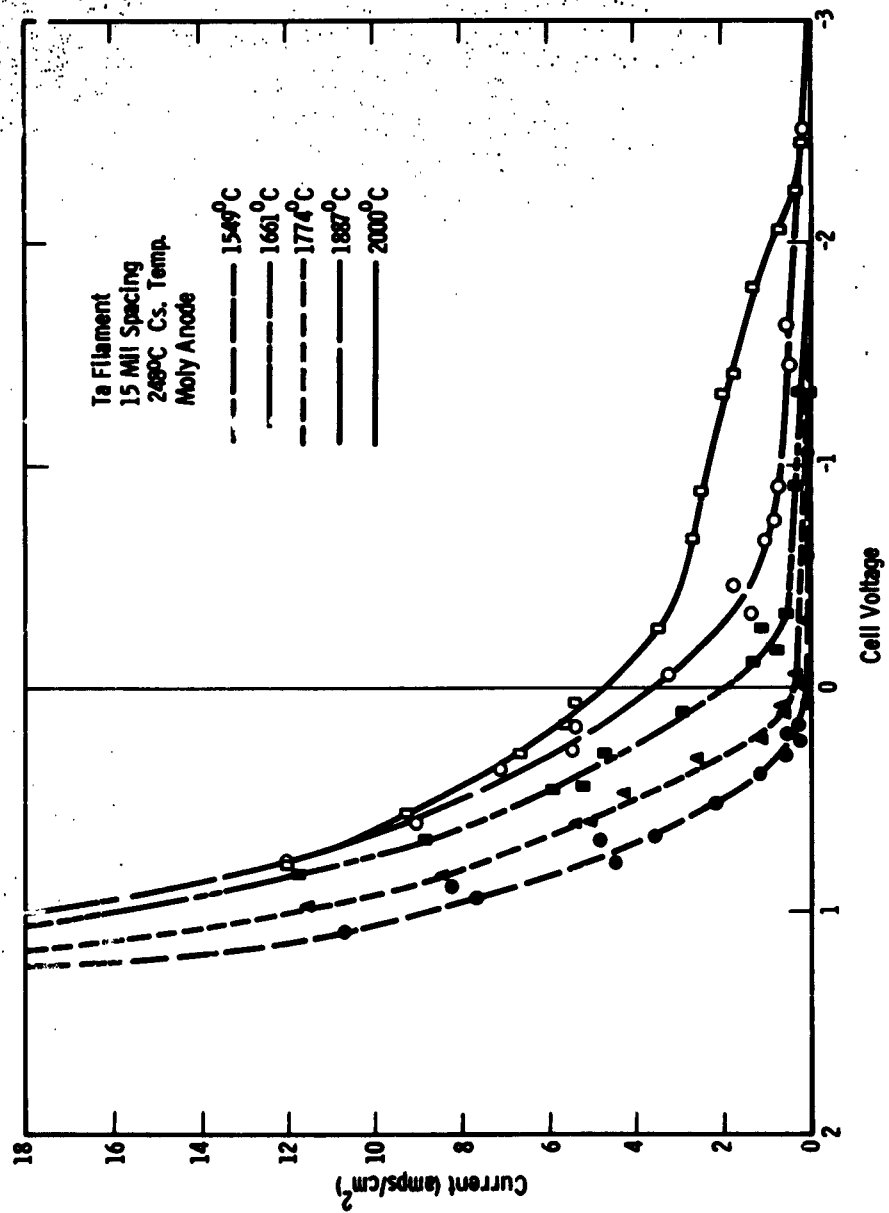


Fig. 1-6. Current Voltage Characteristics with Tantalum Emitter

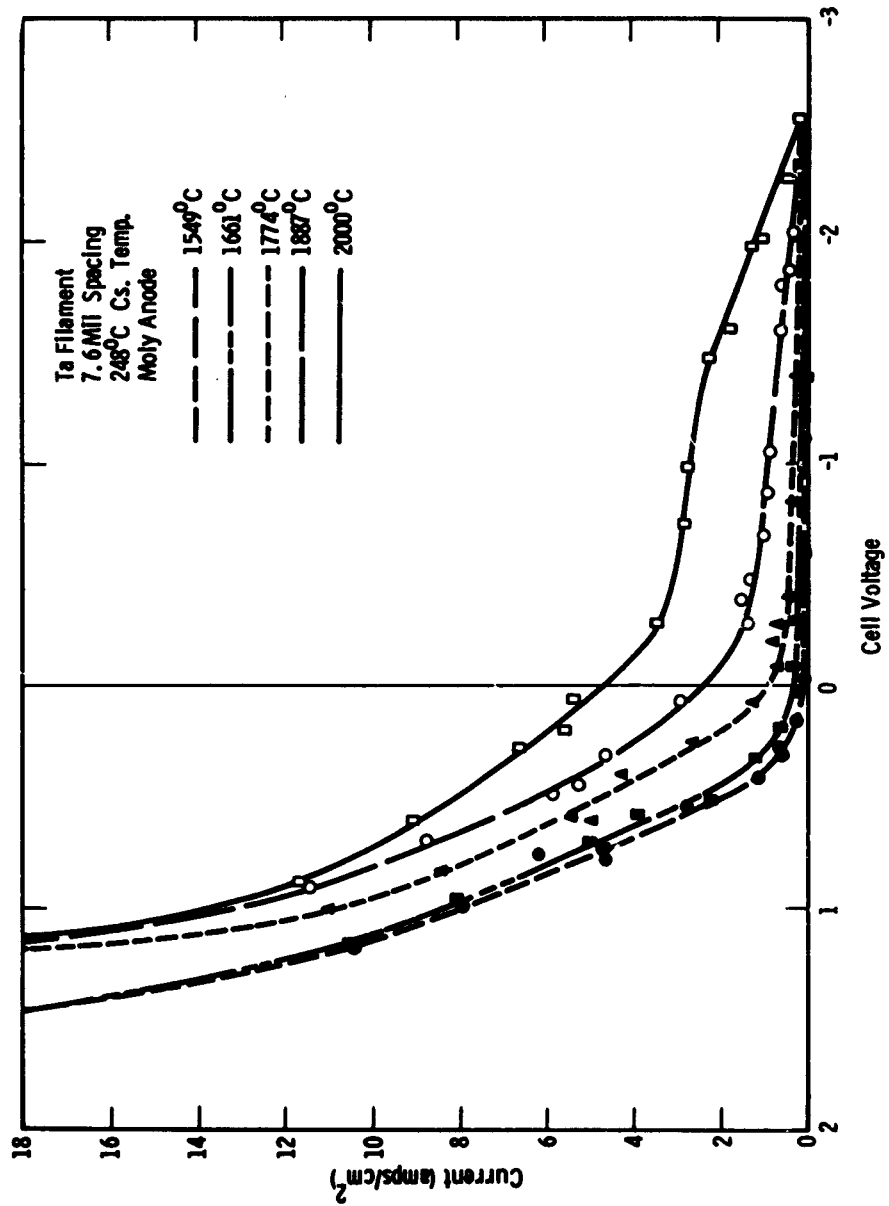


Fig. 1-7. Current Voltage Characteristics with Tantalum Emitter

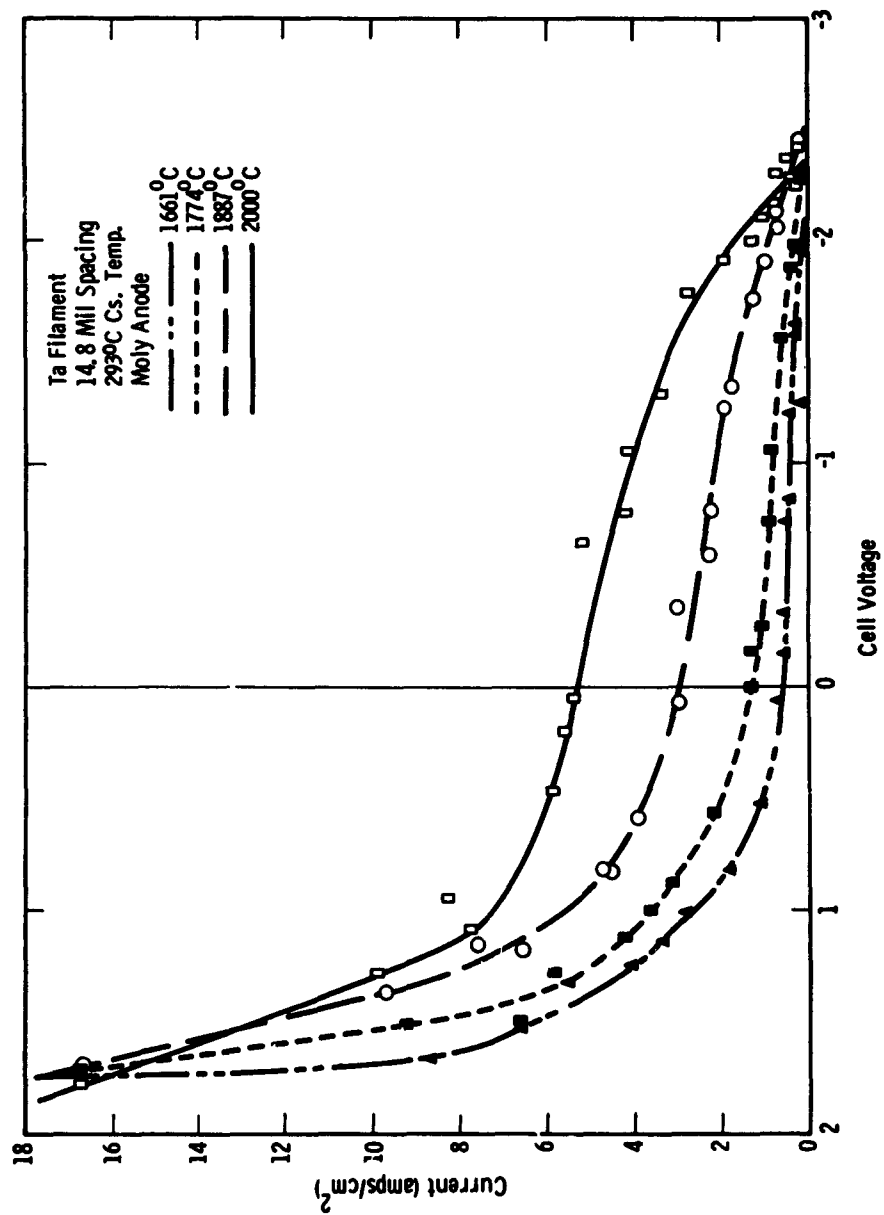


Fig. 1-8. Current Voltage Characteristics with Tantalum Emitter

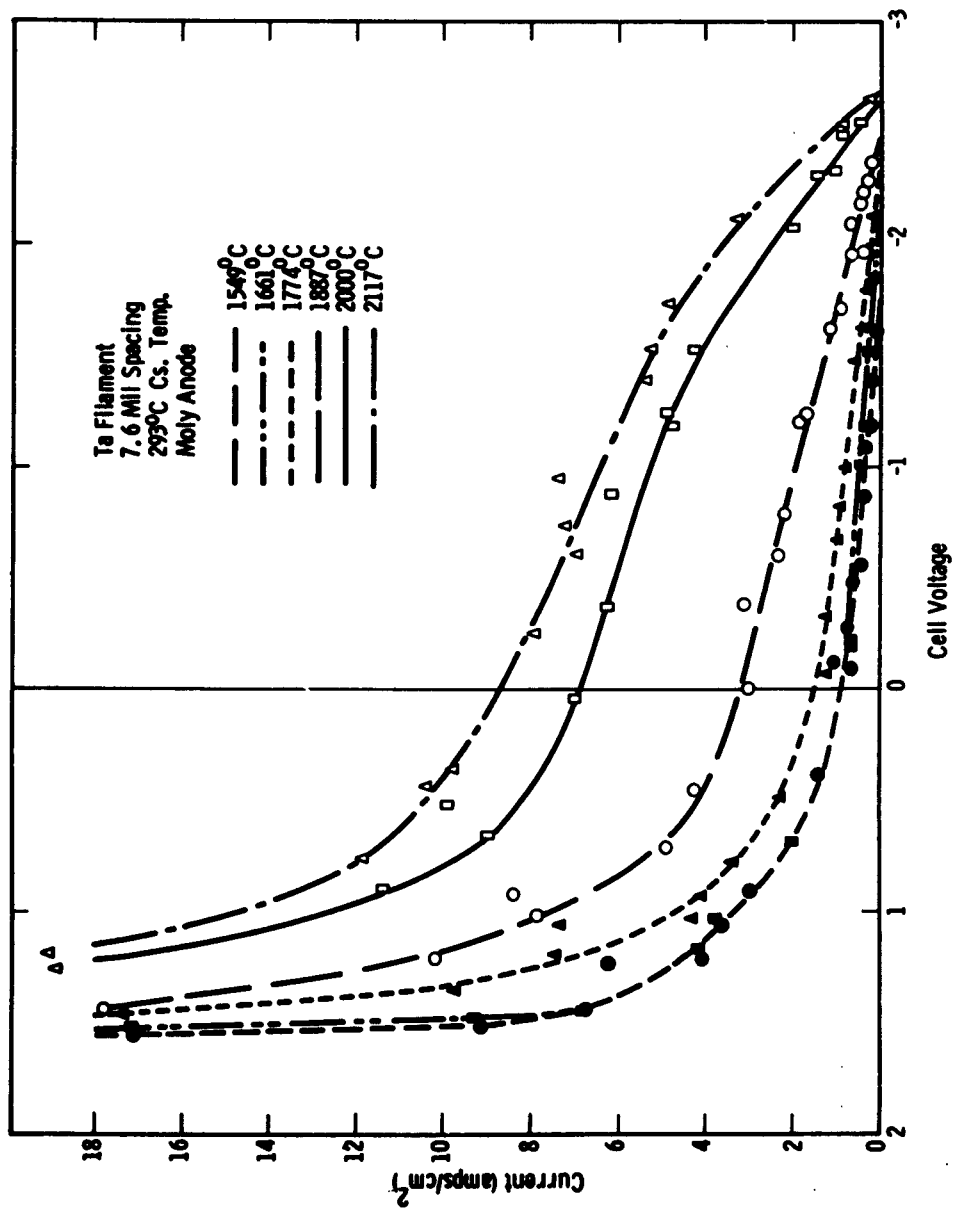


Fig. 1-9. Current Voltage Characteristics with Tantalum Emitter

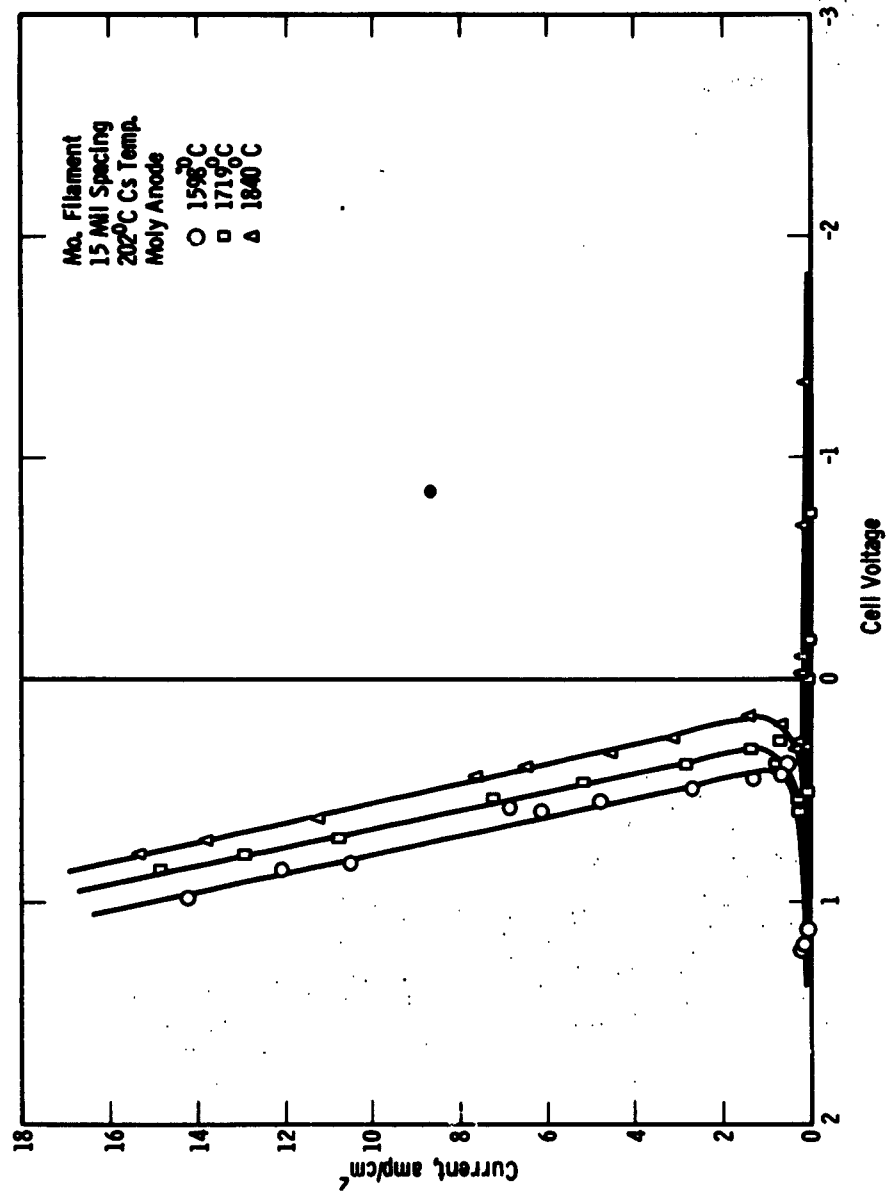


Fig. 1-10. Current Voltage Characteristics with Molybdenum Emitter

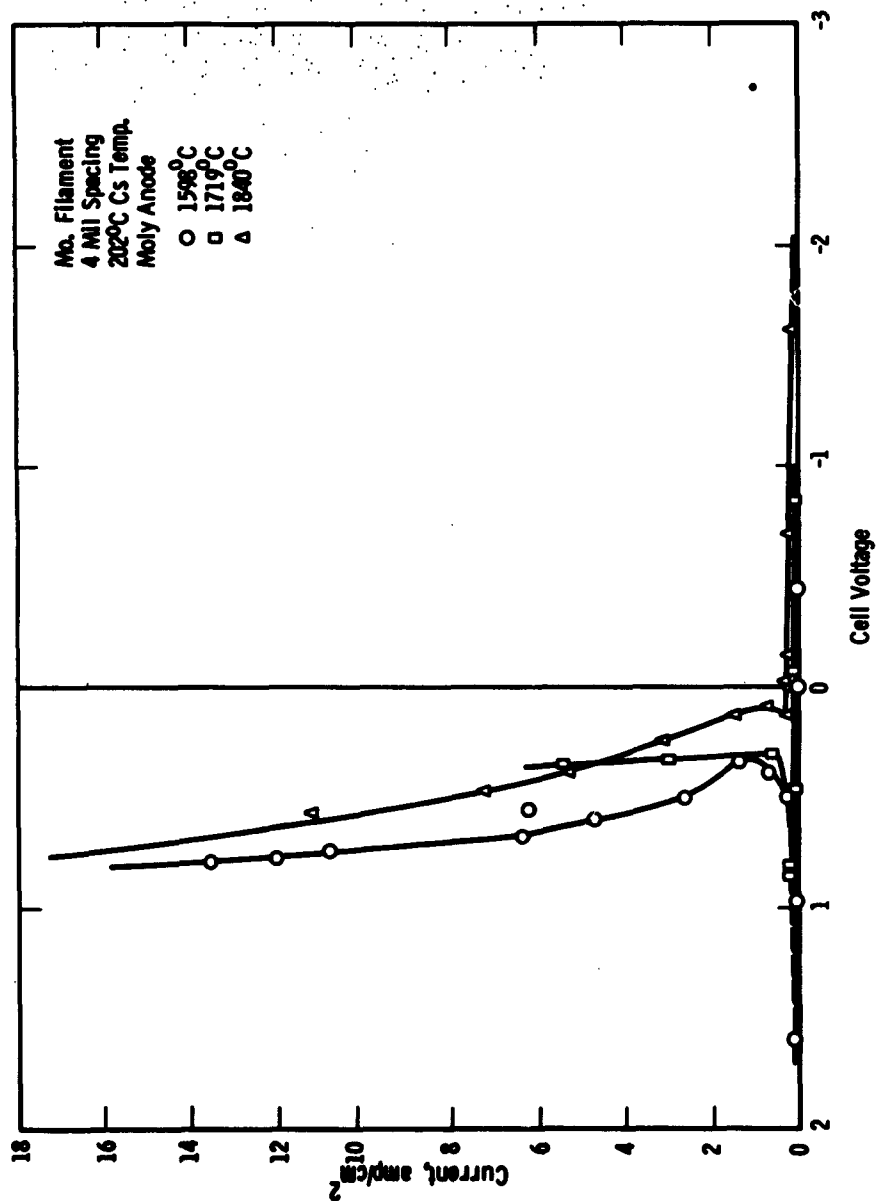


Fig. 1-11. Current Voltage Characteristics with Molybdenum Emitter

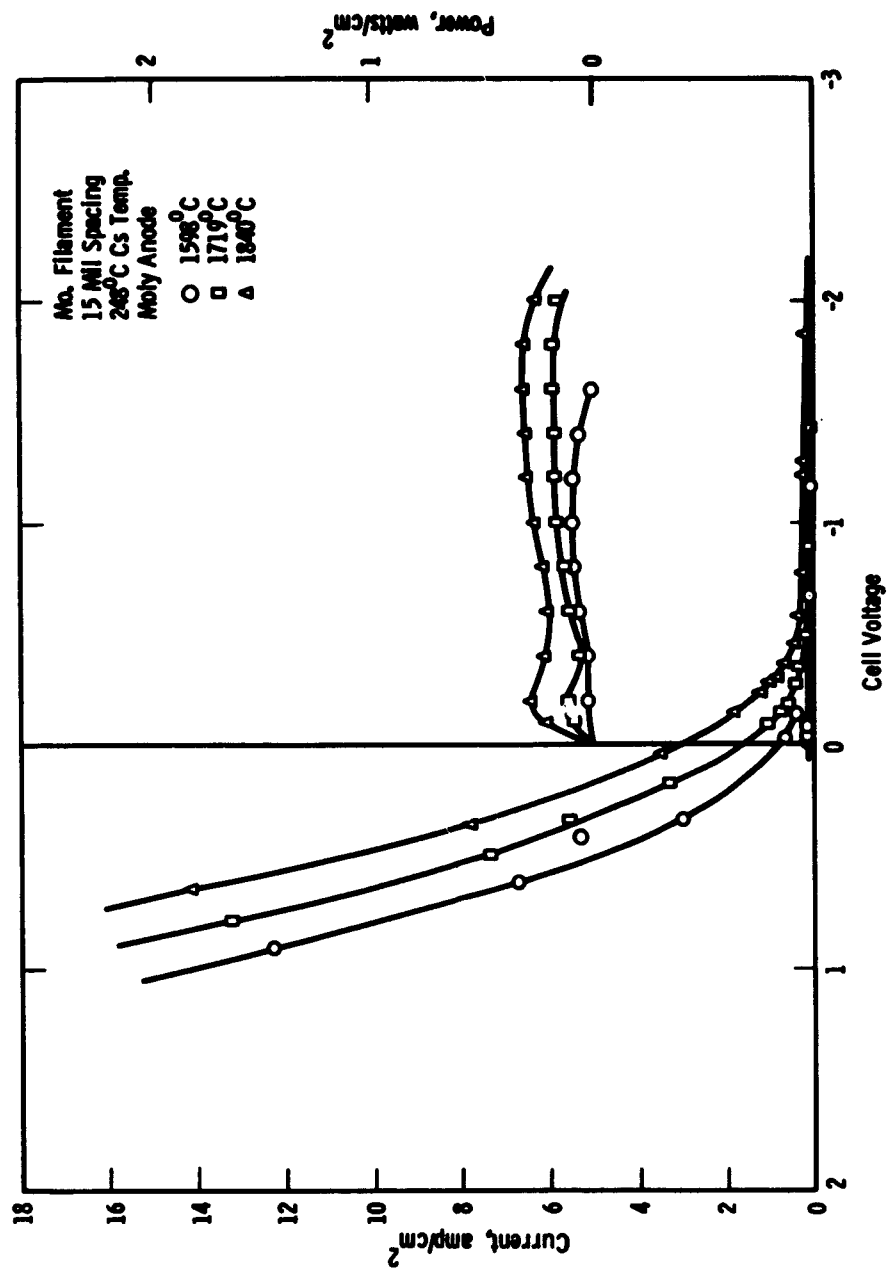


Fig. 1-12. Current Voltage Characteristics with Molybdenum Emitter

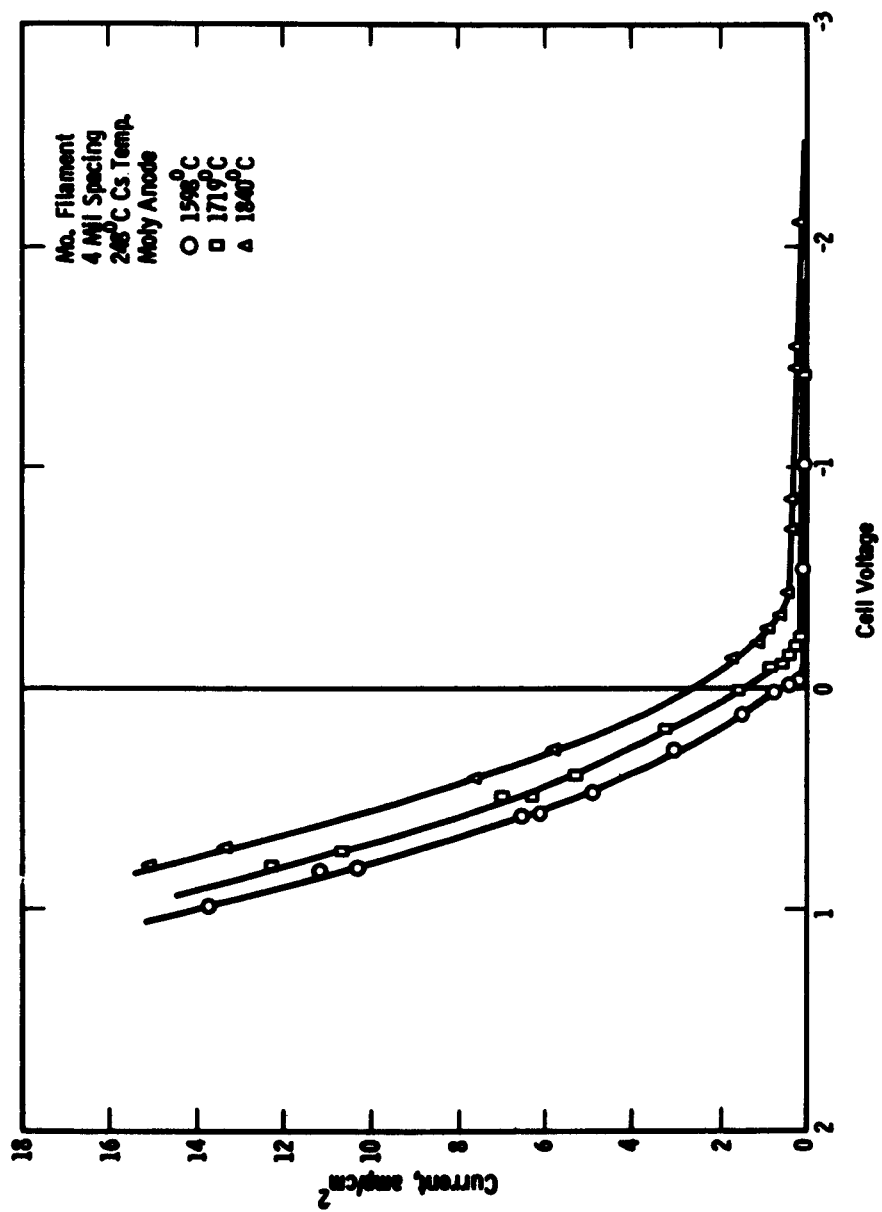


Fig. 1-13. Current Voltage Characteristics with Molybdenum Emitter

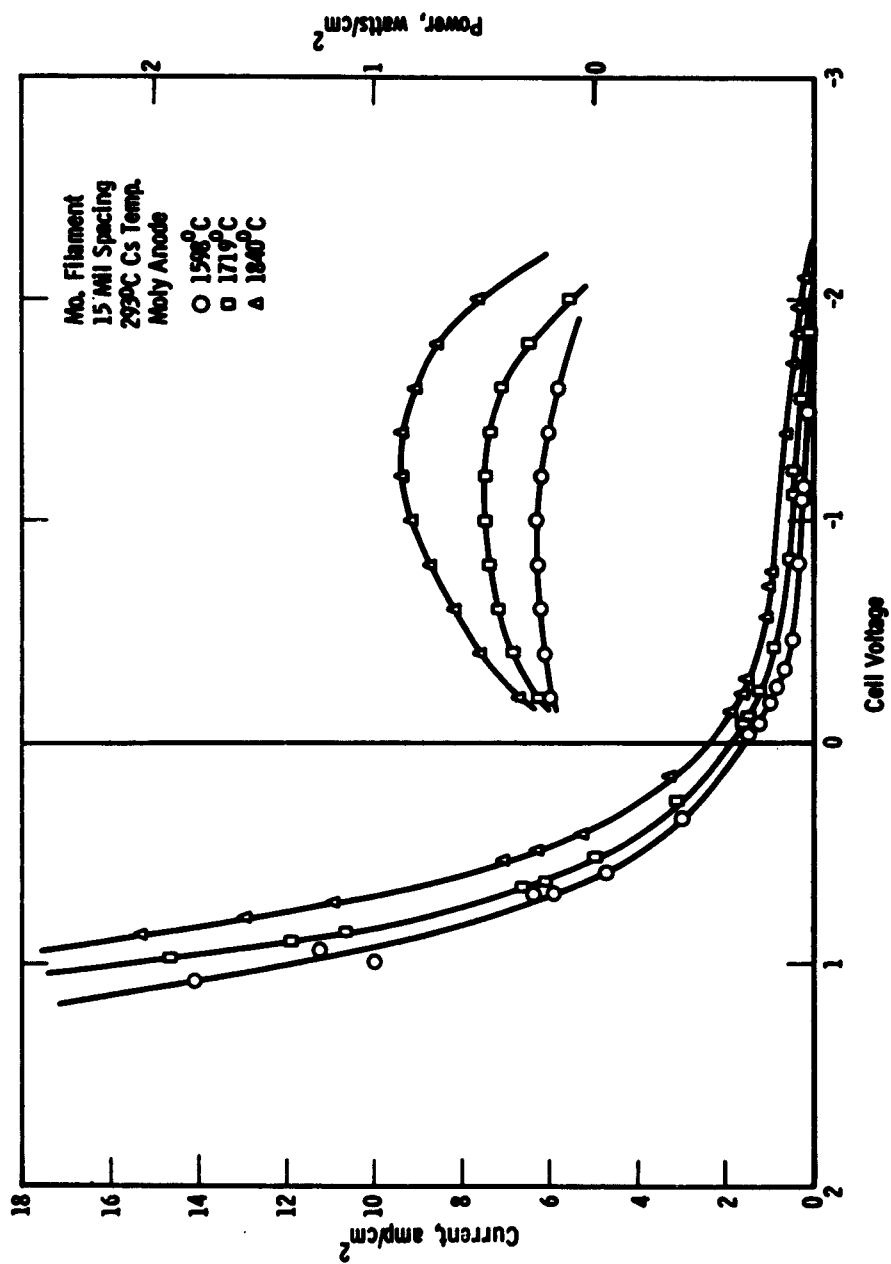


Fig. 1-14. Current Voltage Characteristics with Molybdenum Emitter

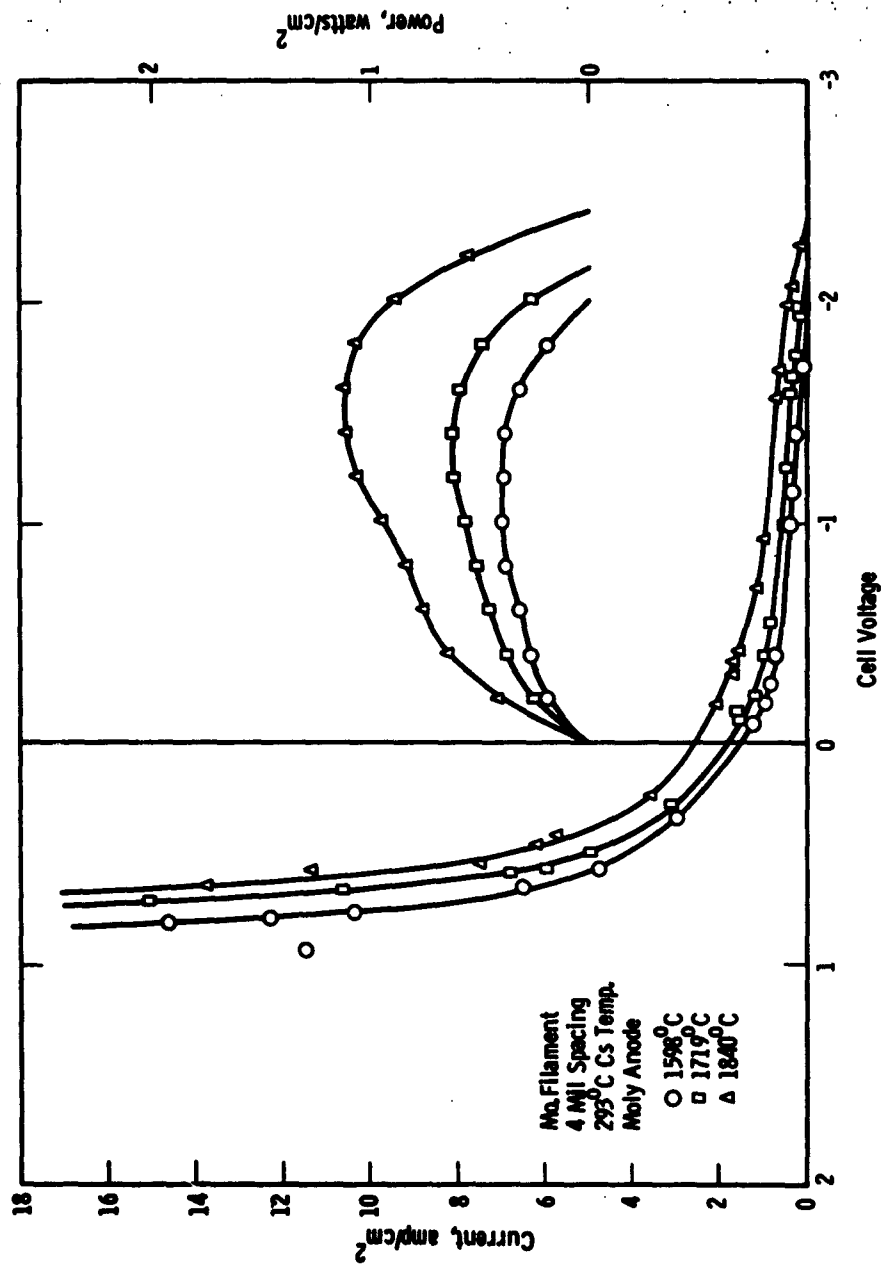


Fig. 1-15. Current Voltage Characteristics with Molybdenum Emitter

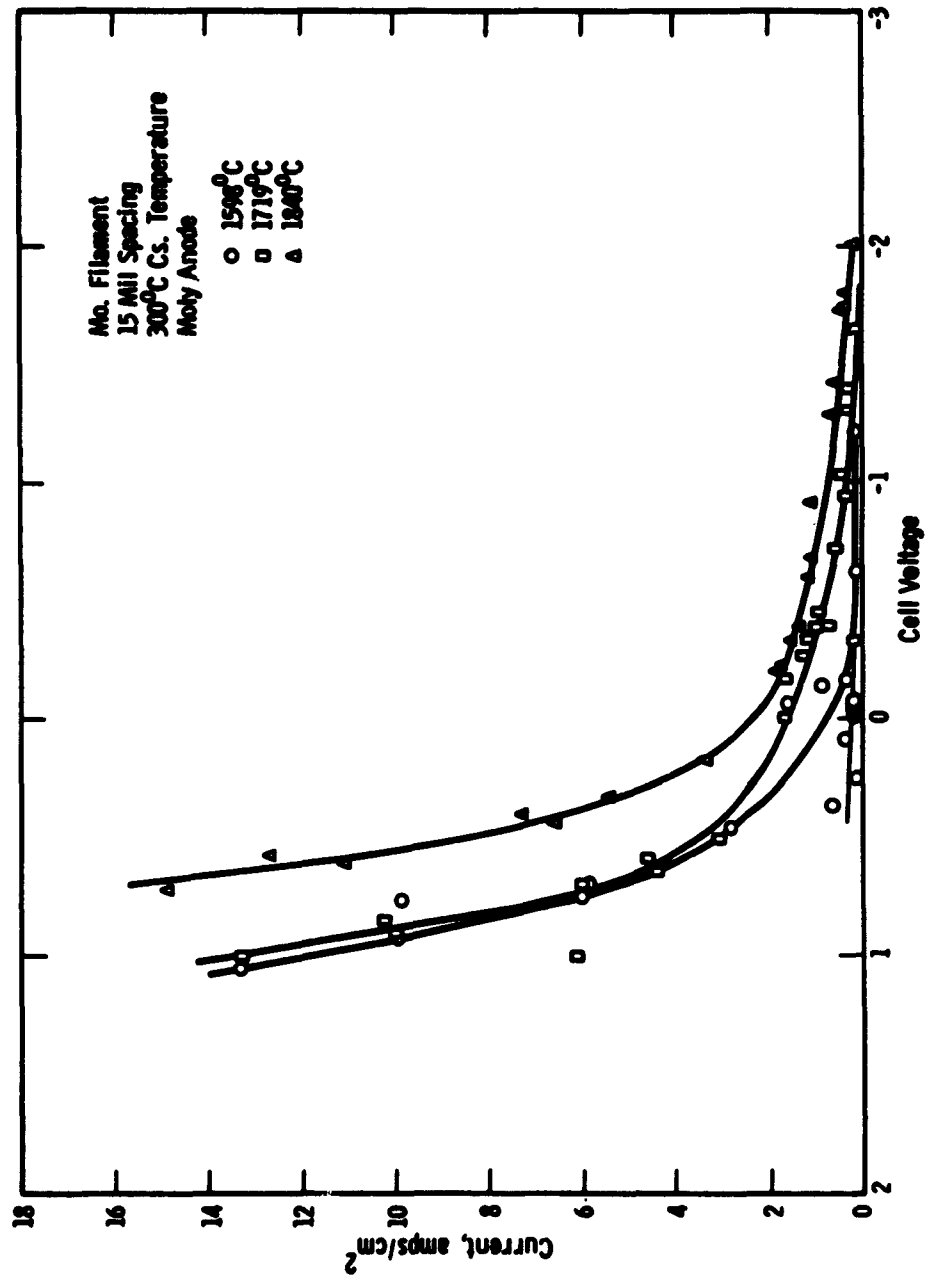


Fig. 1-16. Current Voltage Characteristics with Molybdenum Emitter

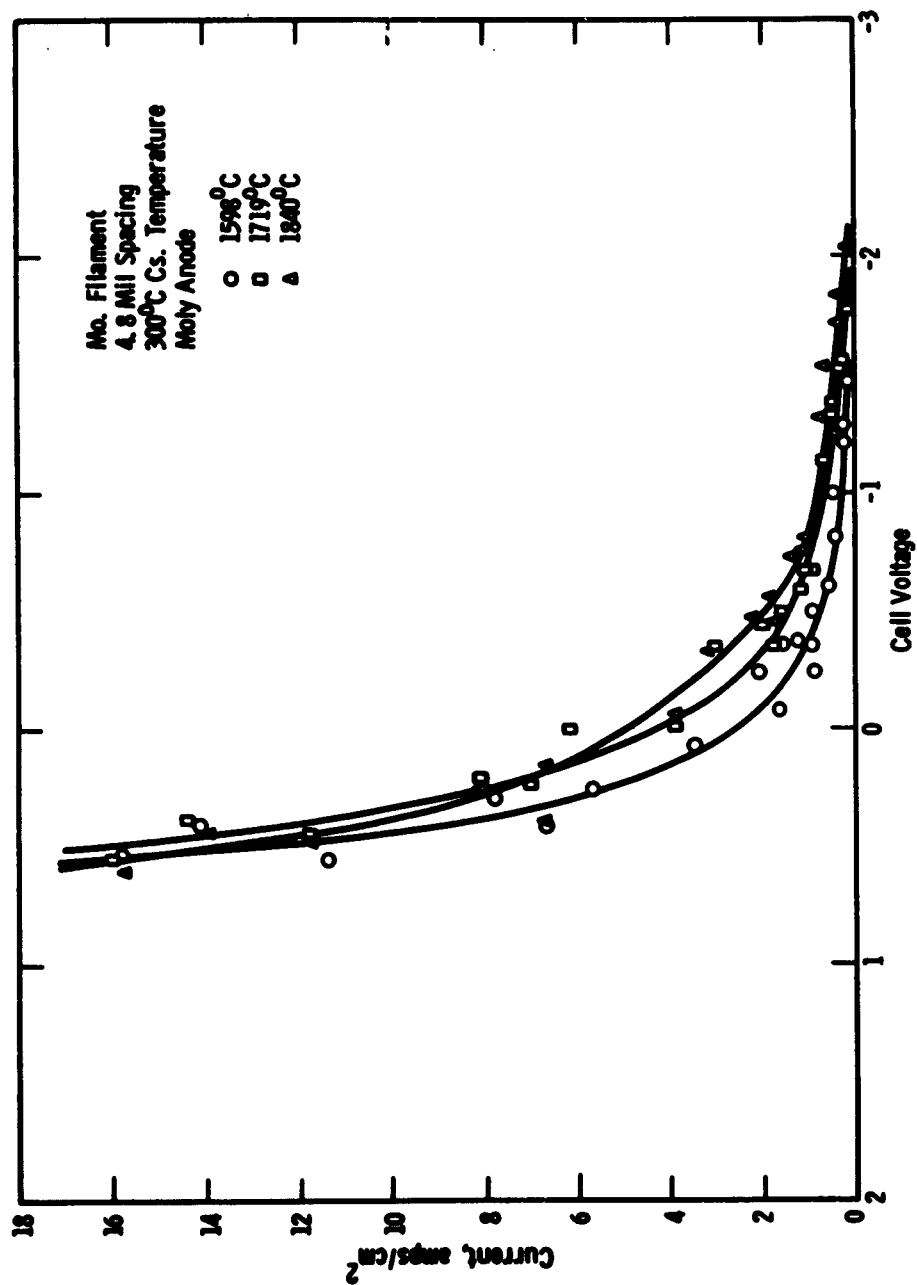


Fig. 1-17. Current Voltage Characteristics with Molybdenum Emitter

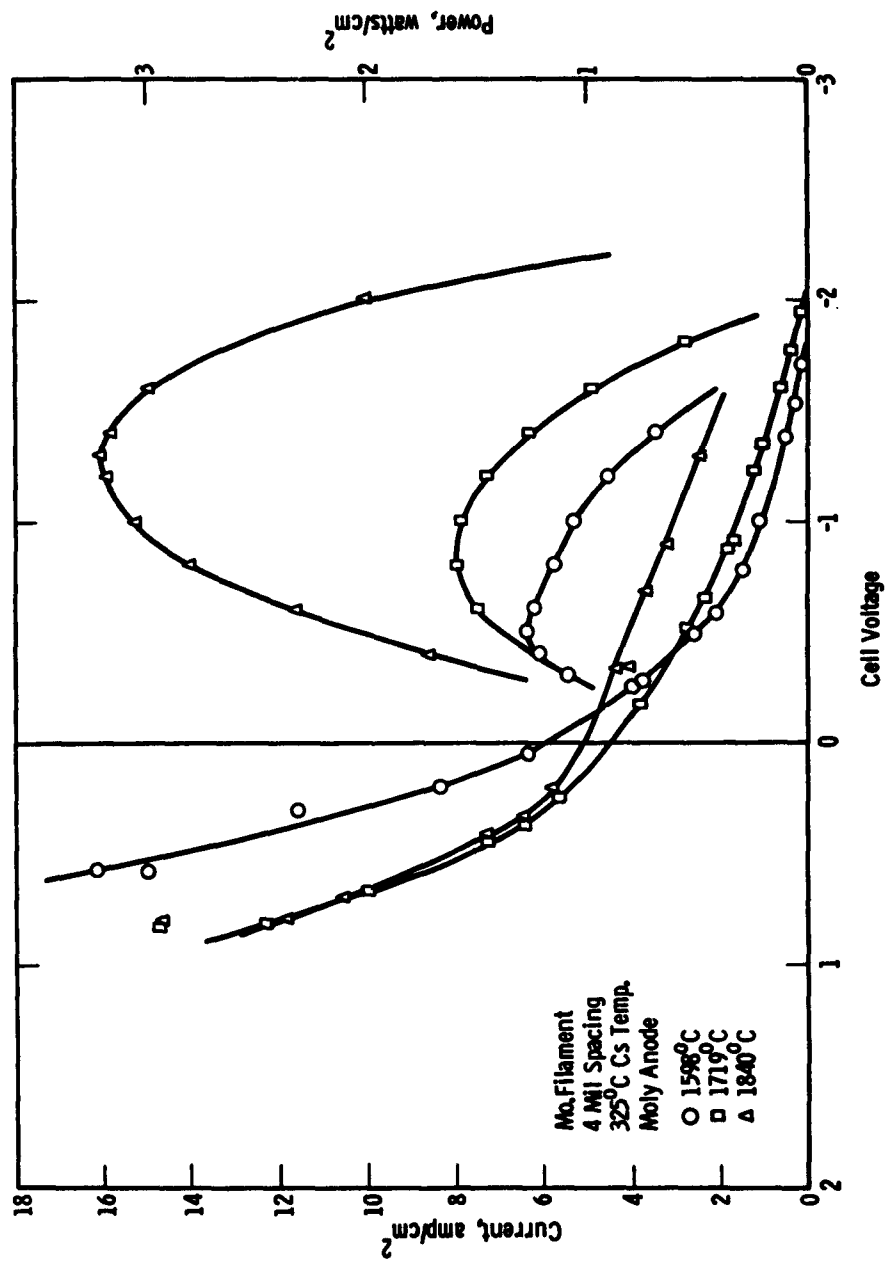


Fig. 1-18. Current Voltage Characteristics with Molybdenum Emitter

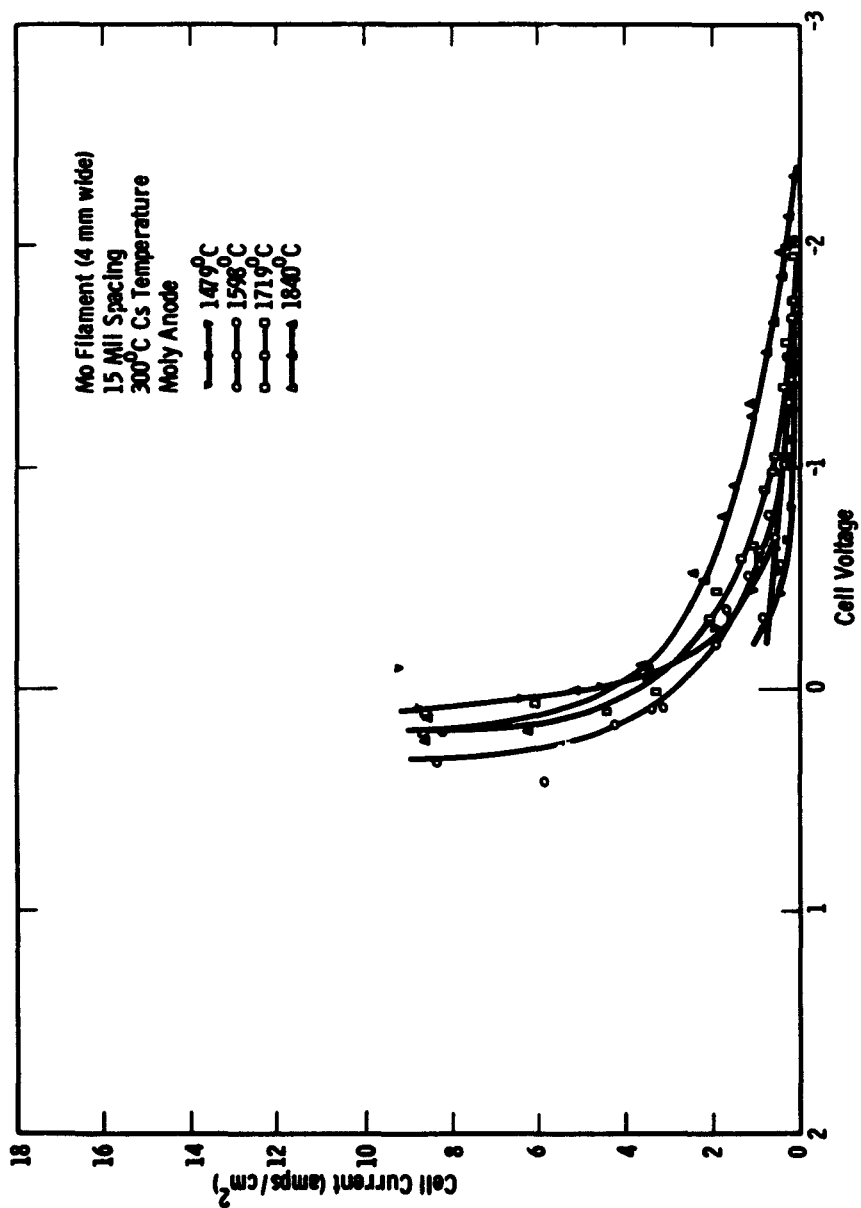


Fig. 1-19. Current Voltage Characteristics with Molybdenum Emitter

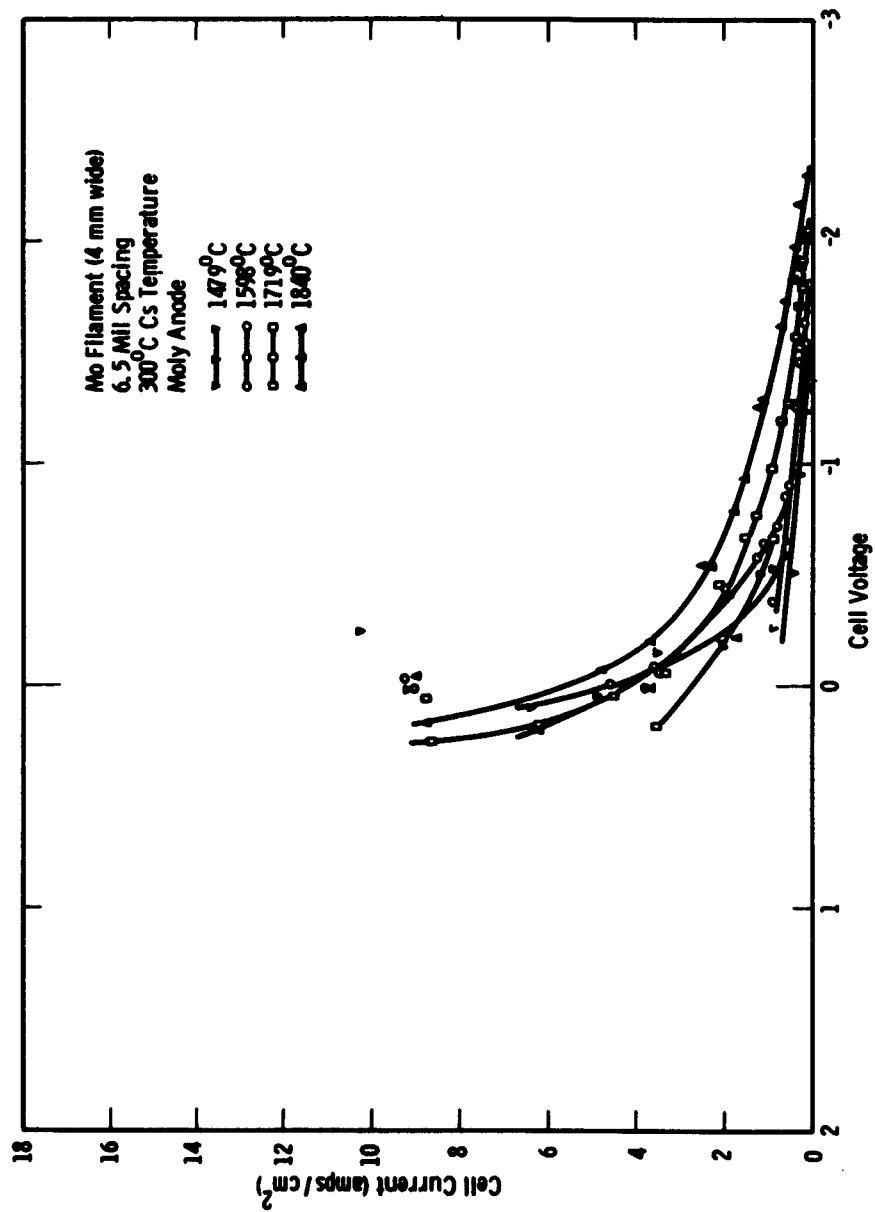


Fig. 1-20. Current Voltage Characteristics with Molybdenum Emitter

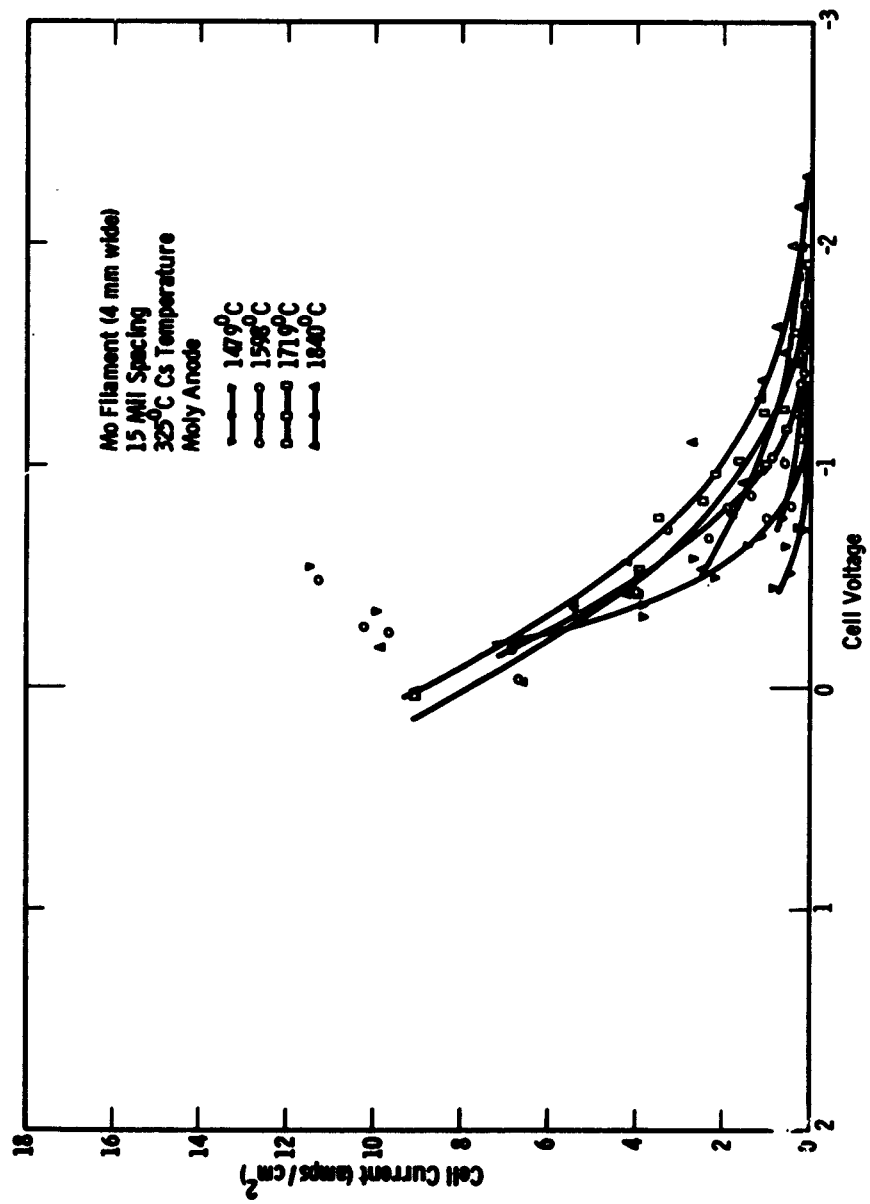


Fig. 1-21. Current Voltage Characteristics with Molybdenum Emitter

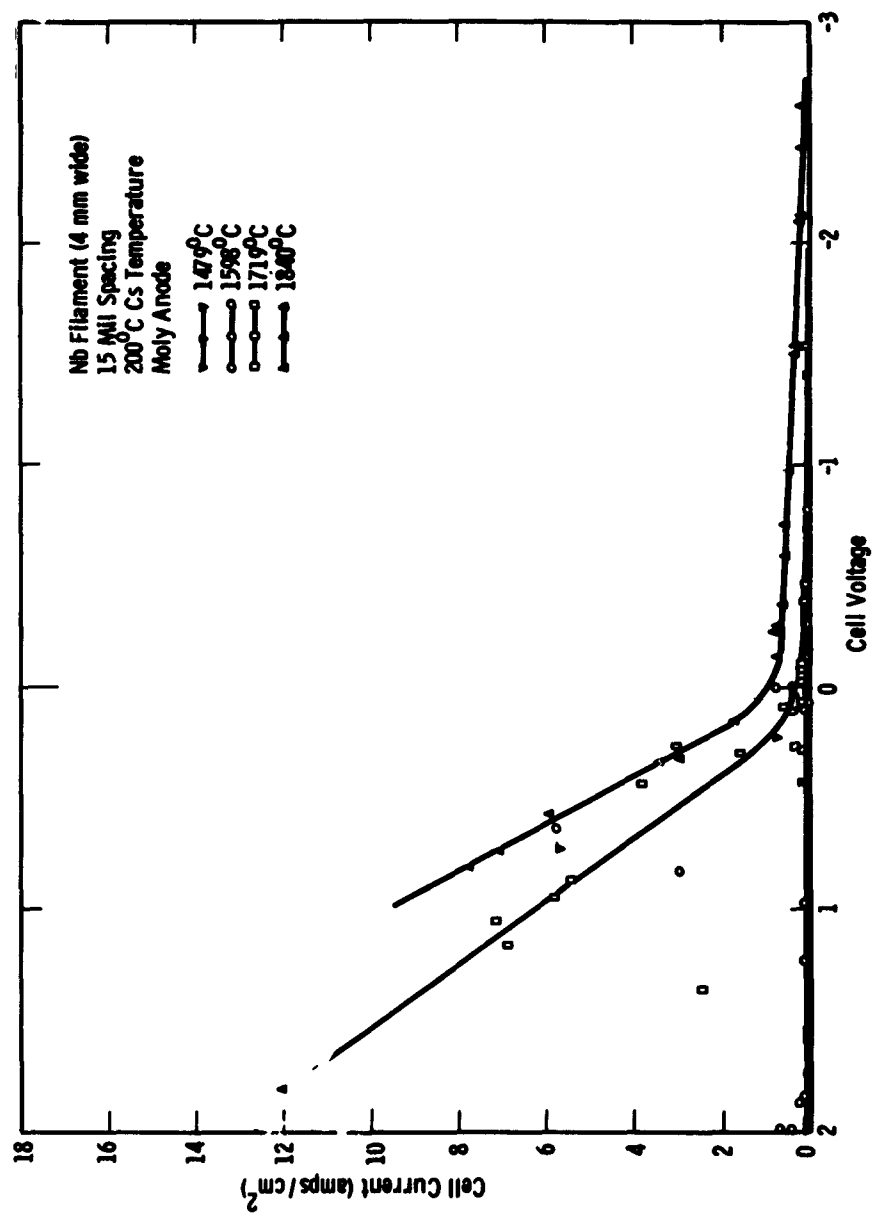


Fig. 1-22. Current Voltage Characteristics with Niobium Emitter

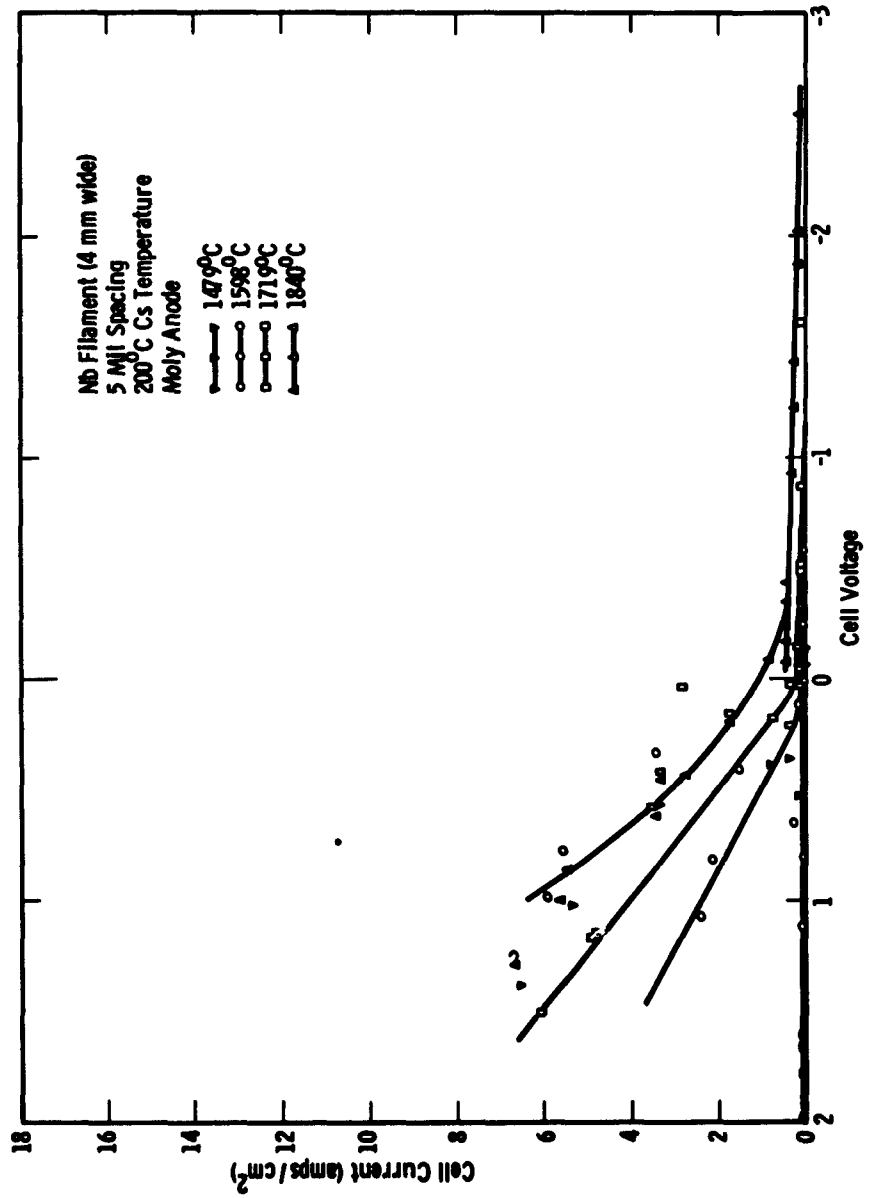


Fig. 1-23. Current Voltage Characteristics with Niobium Emitter

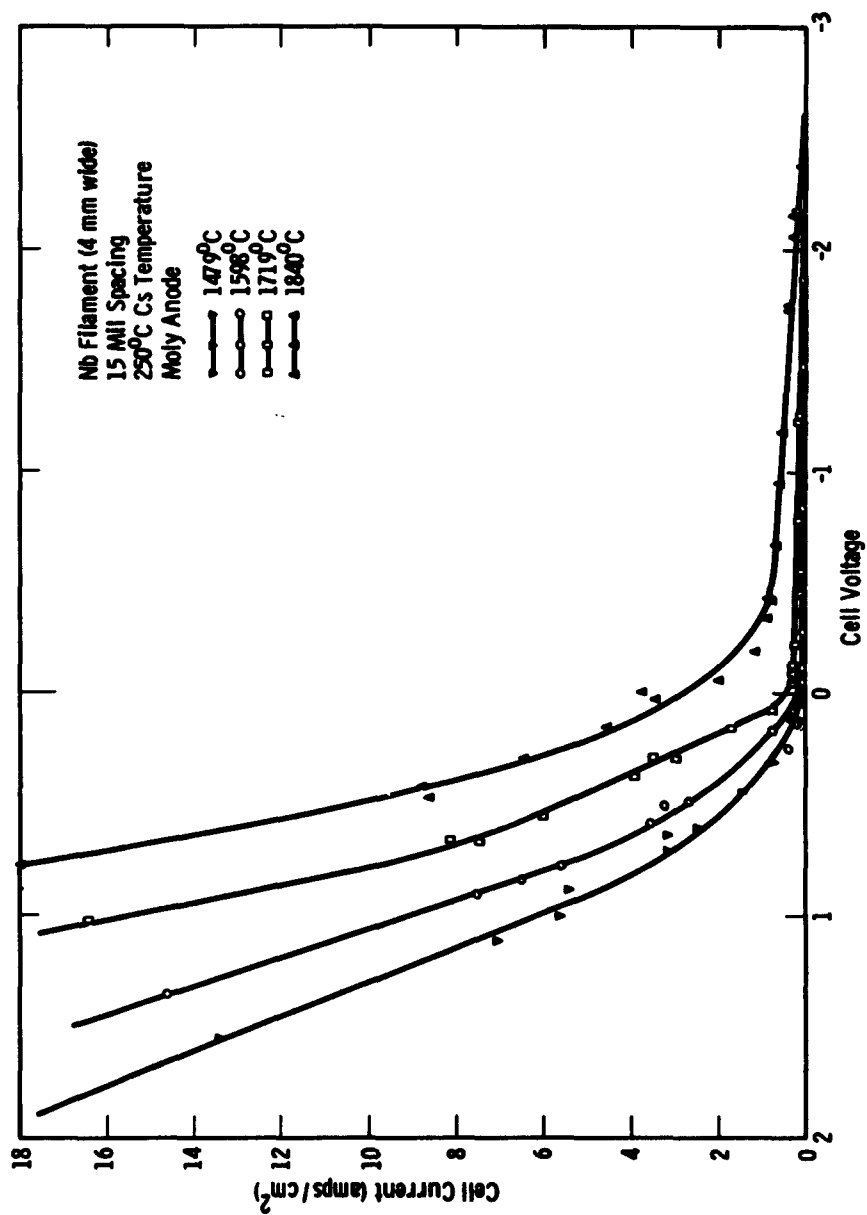


Fig. 1-24. Current Voltage Characteristics with Niobium Emitter

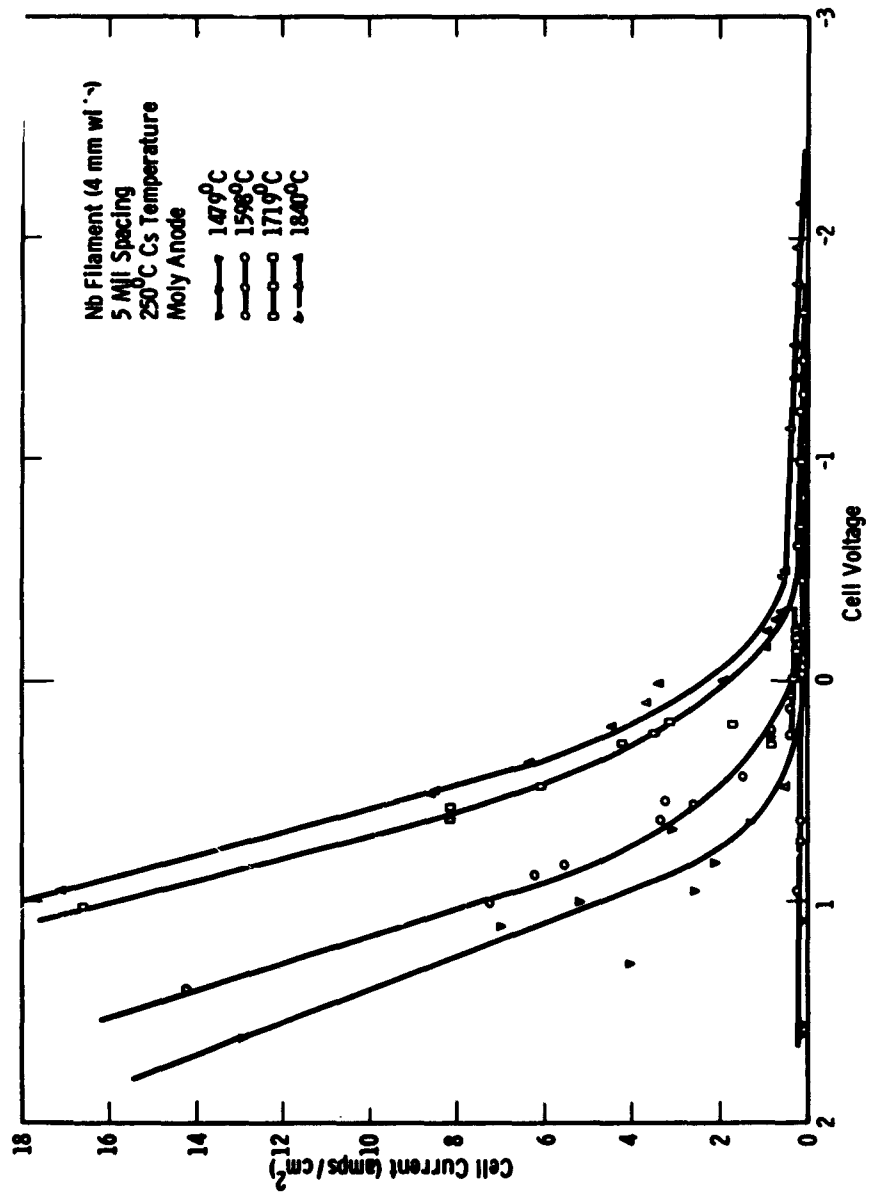


Fig. 1-25. Current Voltage Characteristics with Niobium Emitter

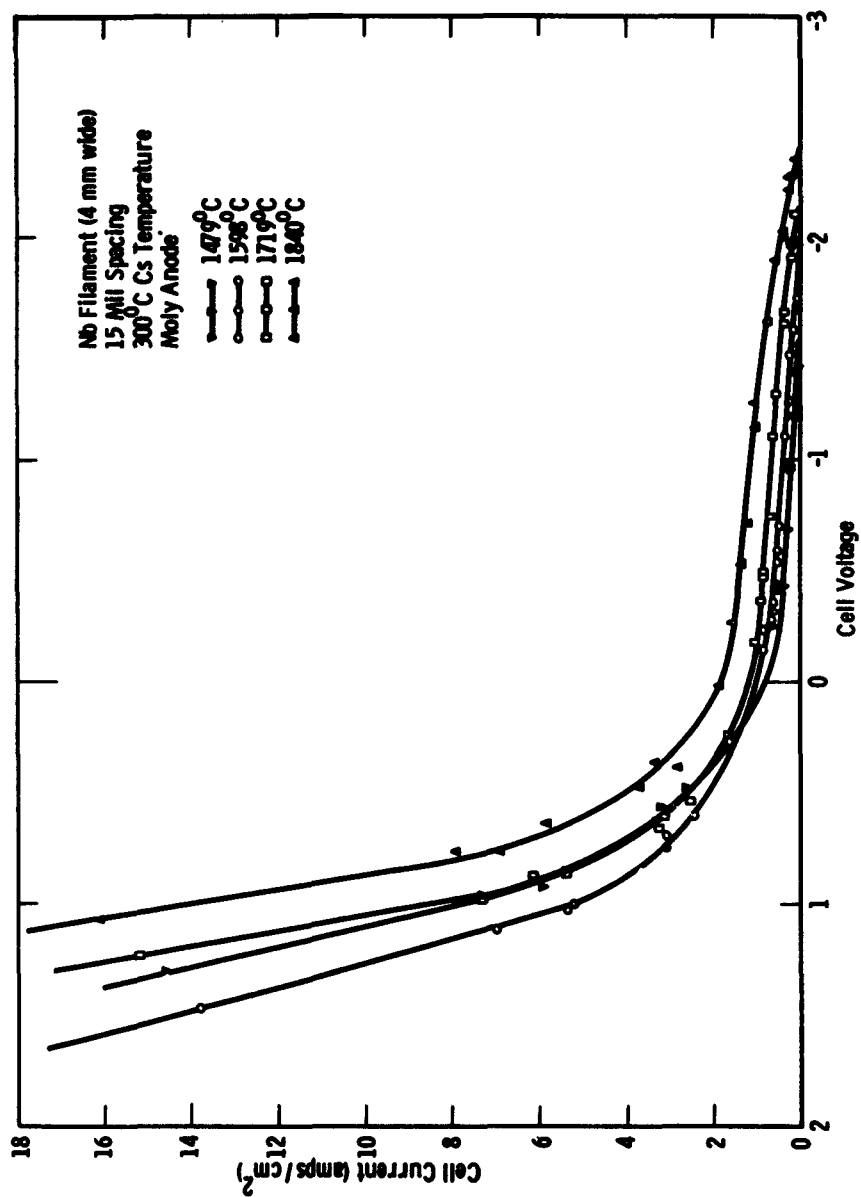


Fig. 1-26. Current Voltage Characteristics with Niobium Emitter

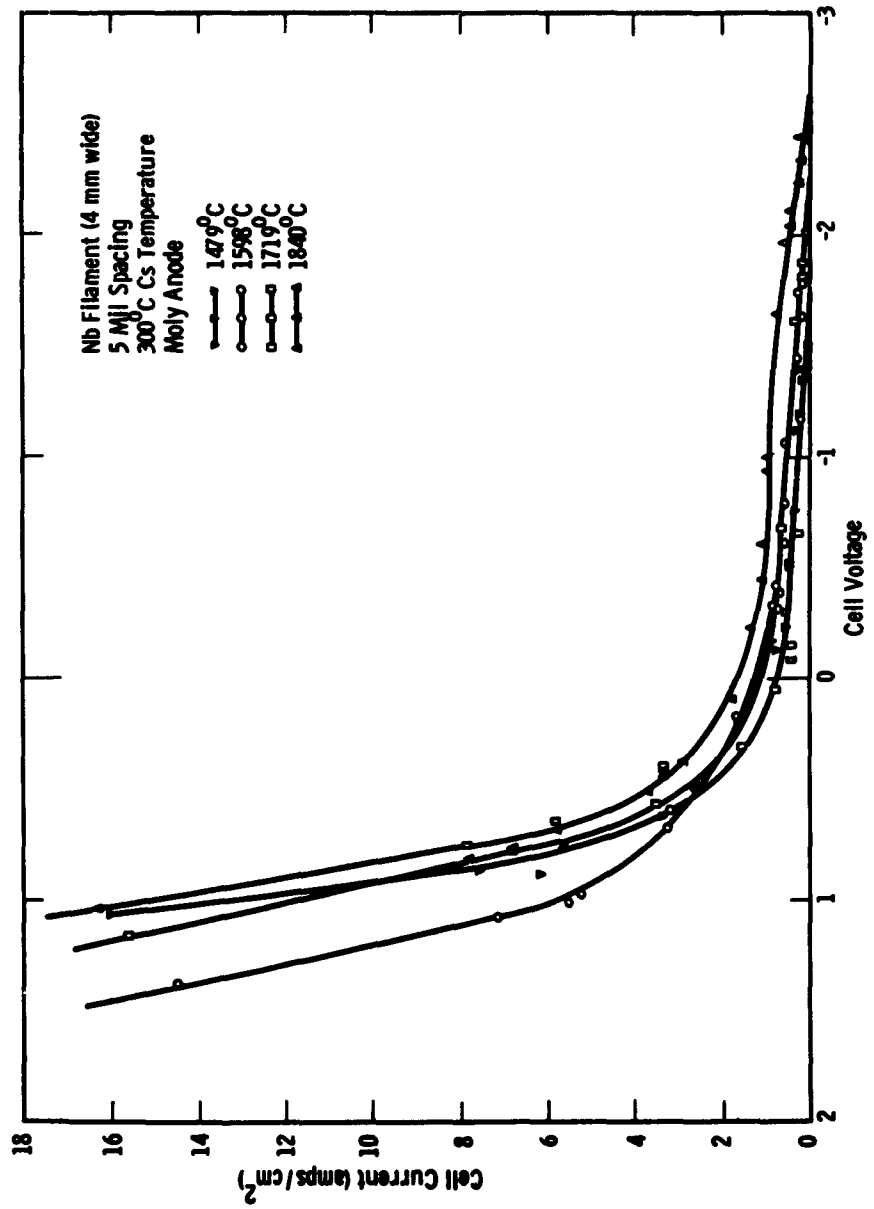


Fig. 1-27. Current Voltage Characteristics with Niobium Emitter

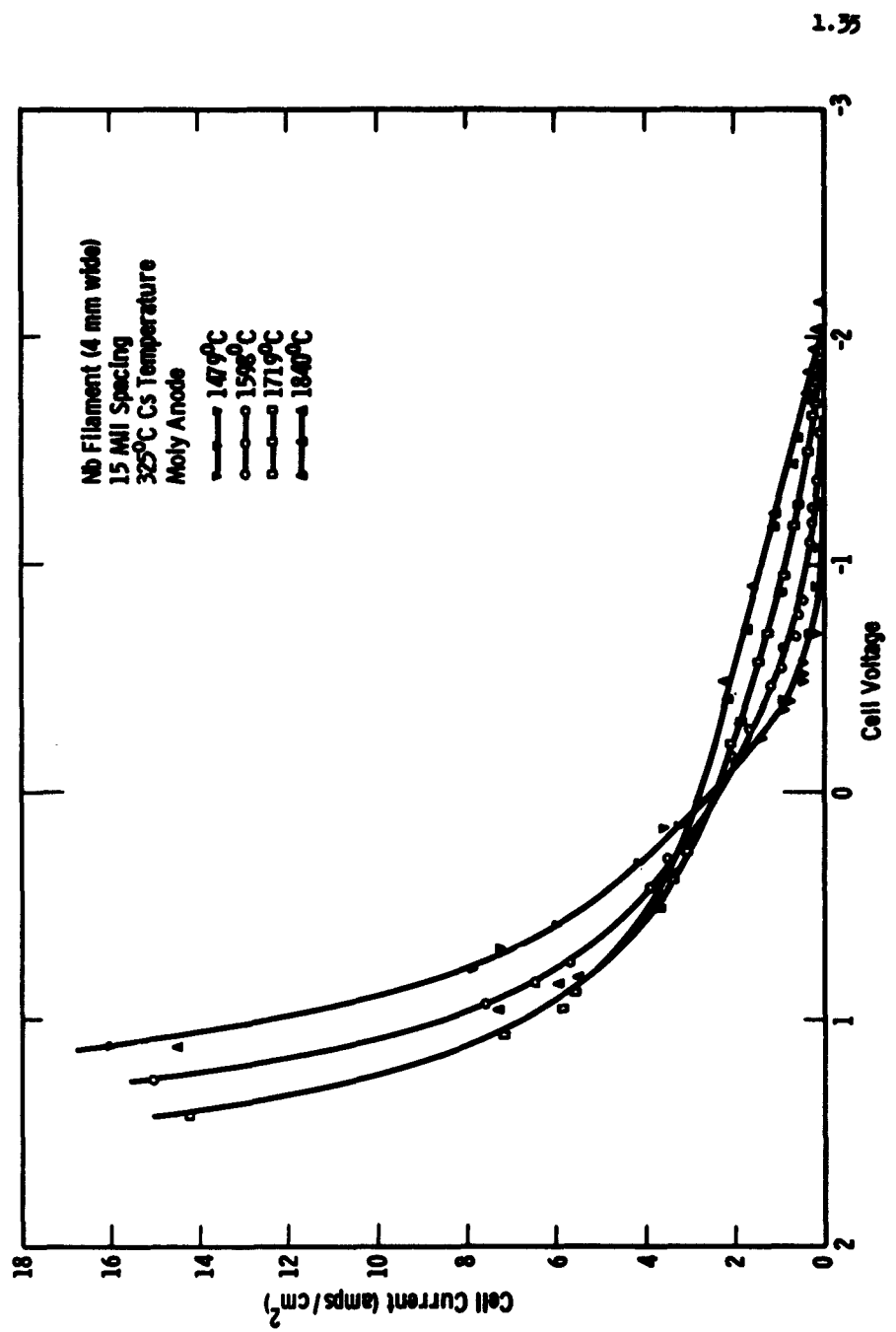


Fig. 1-28. Current Voltage Characteristics with Niobium Emitter

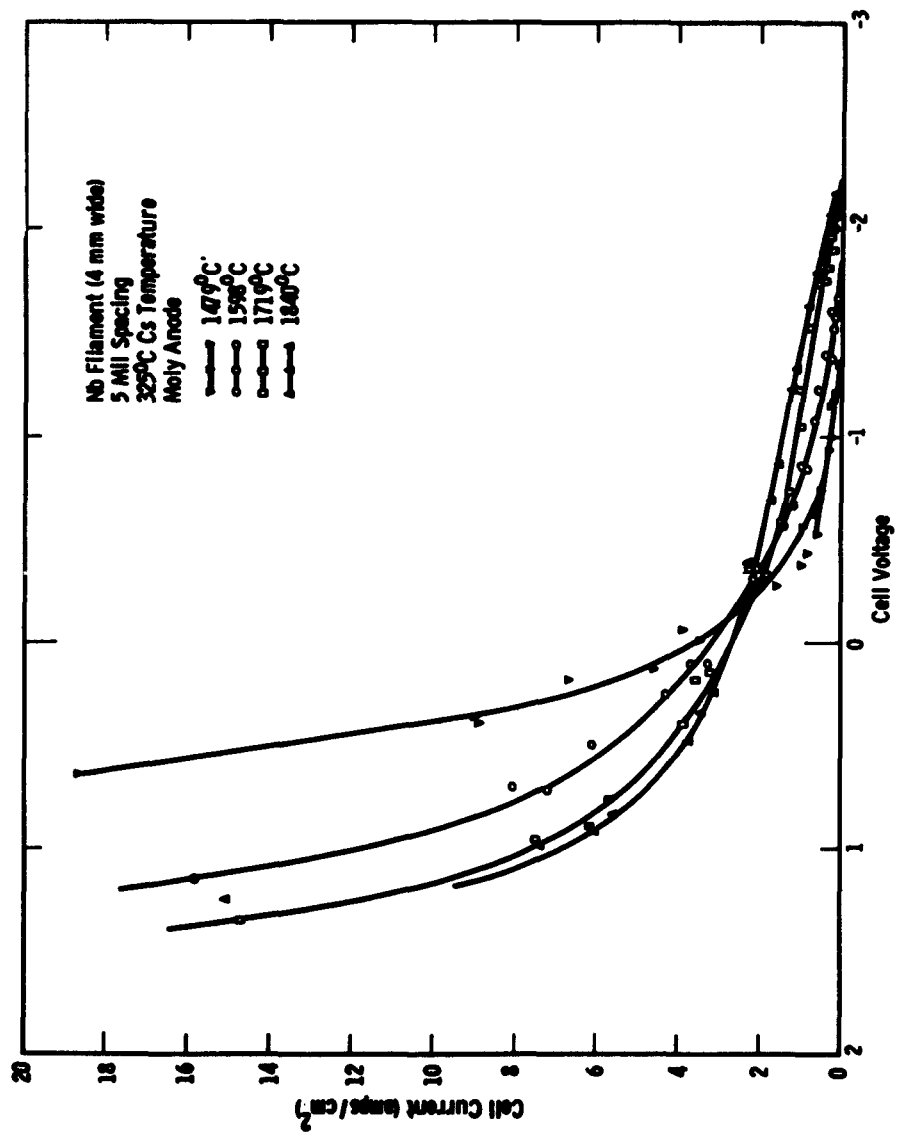


Fig. 1-29. Current Voltage Characteristics with Niobium Emitter

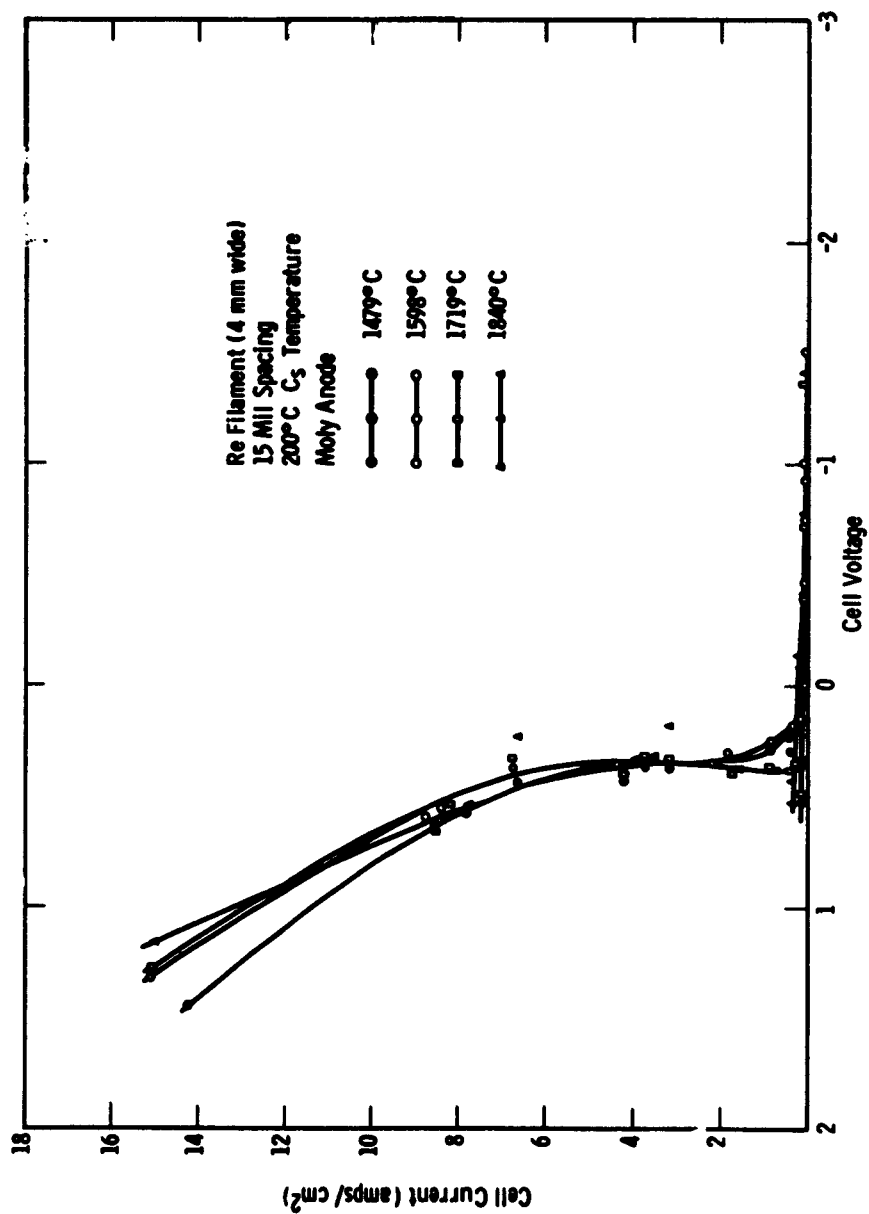


Fig. 1-30. Current Voltage Characteristics with Rhenium Emitter

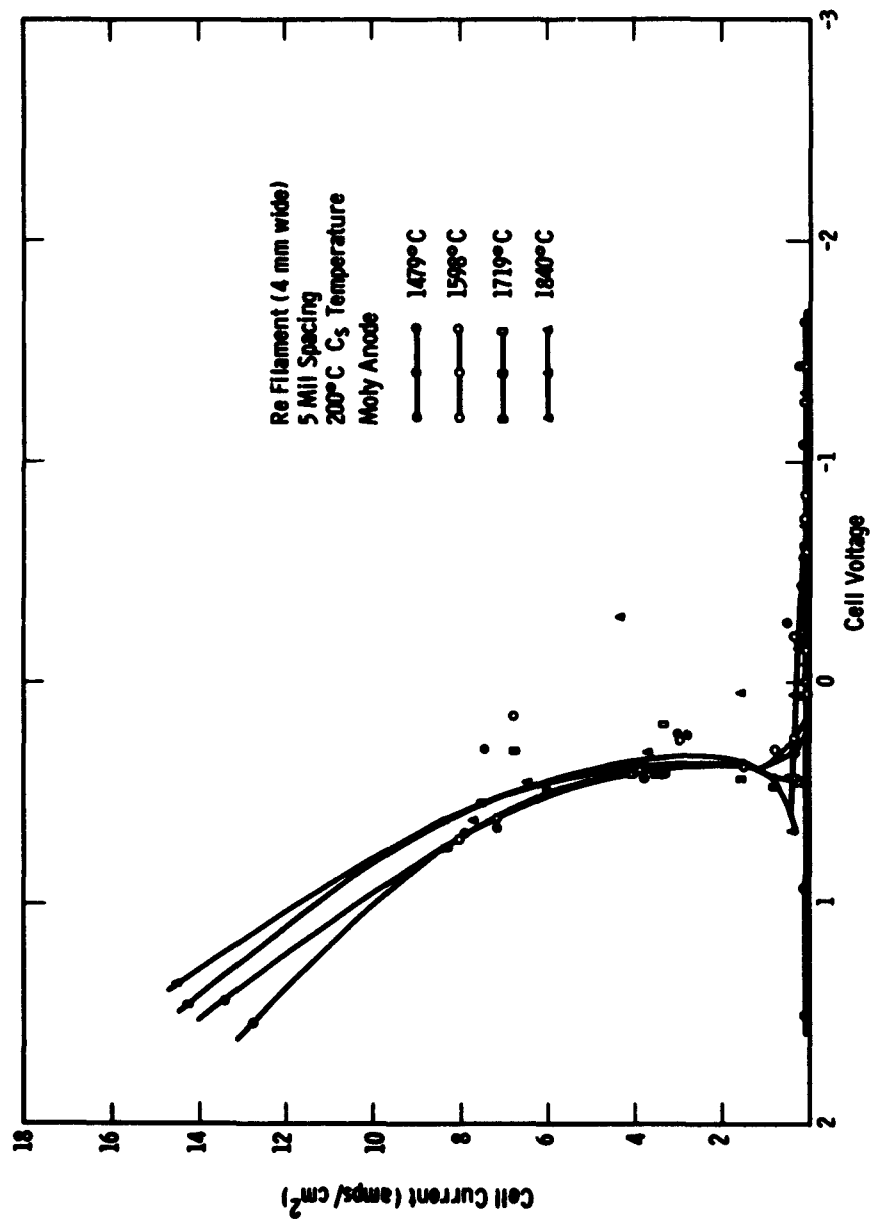


Fig. 1-31. Current Voltage Characteristics with Rhenium Emitter

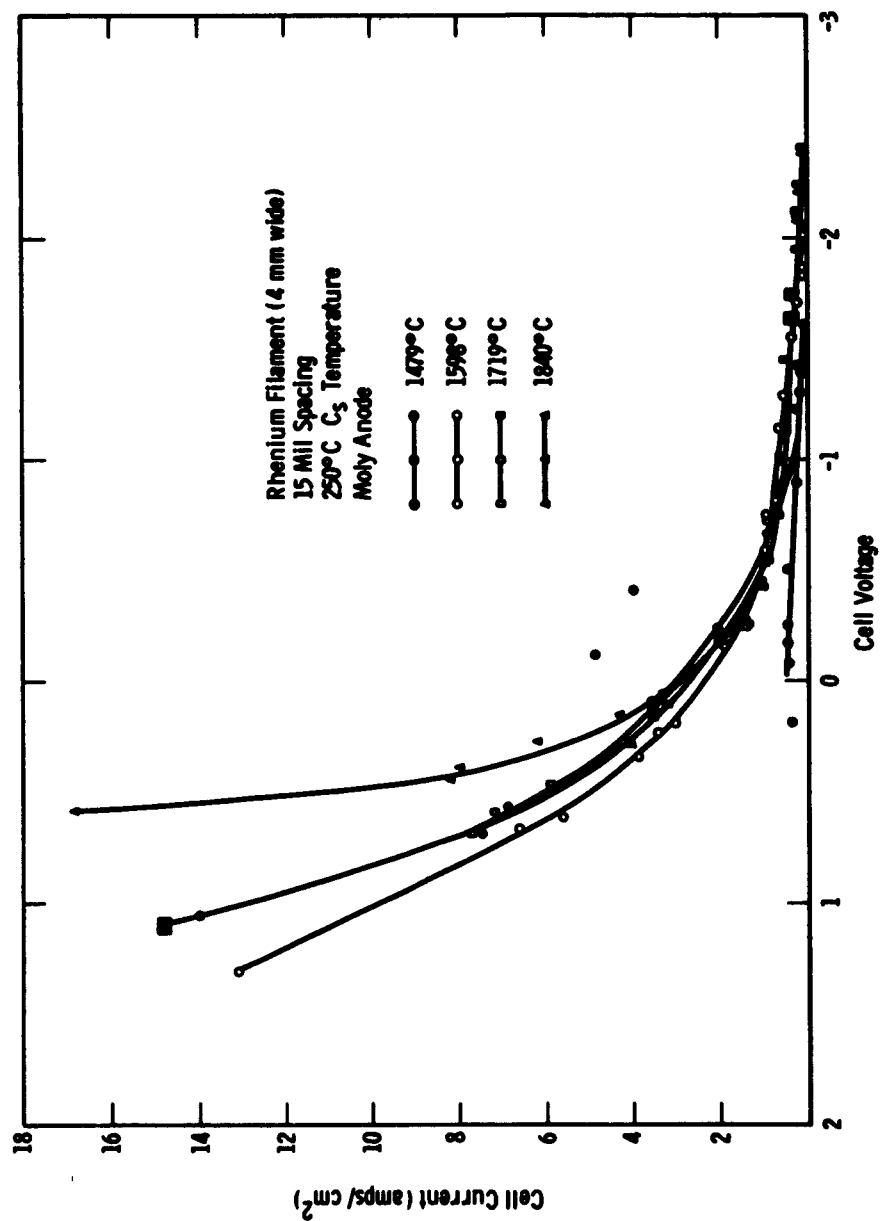


Fig. 1-32. Current Voltage Characteristics with Rhenium Emitter

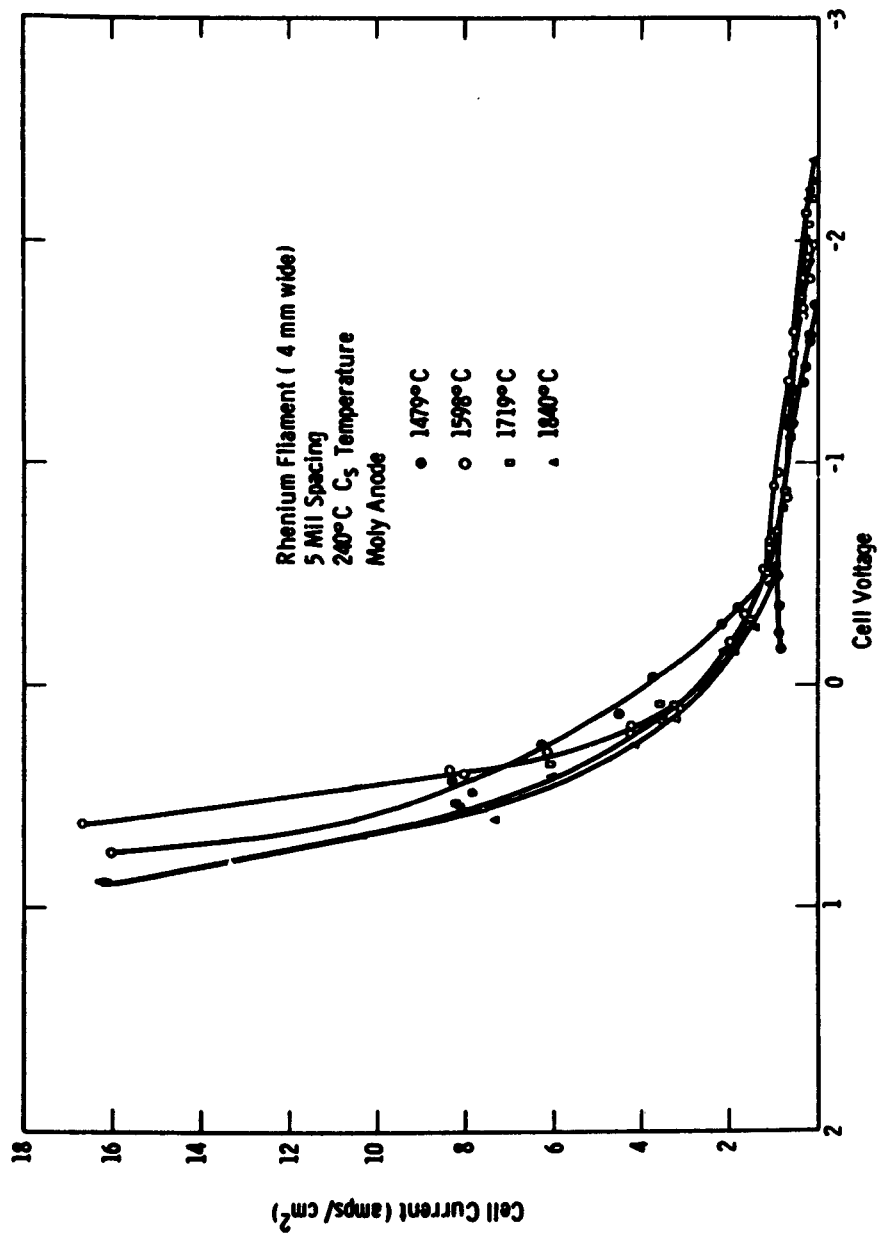


Fig. 1-33. Current Voltage Characteristics with Rhenium Emitter

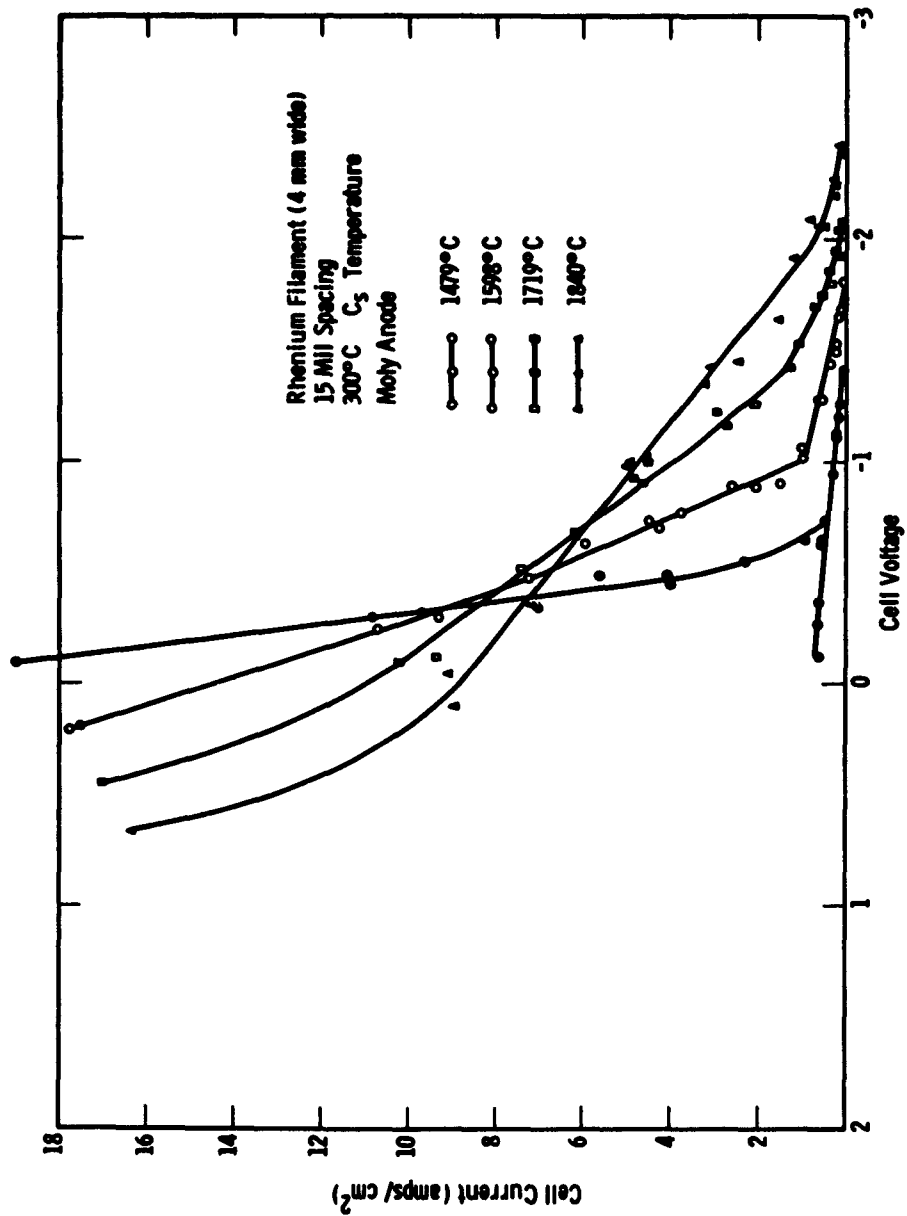


Fig. 1-34. Current Voltage Characteristics with Rhenium Emitter

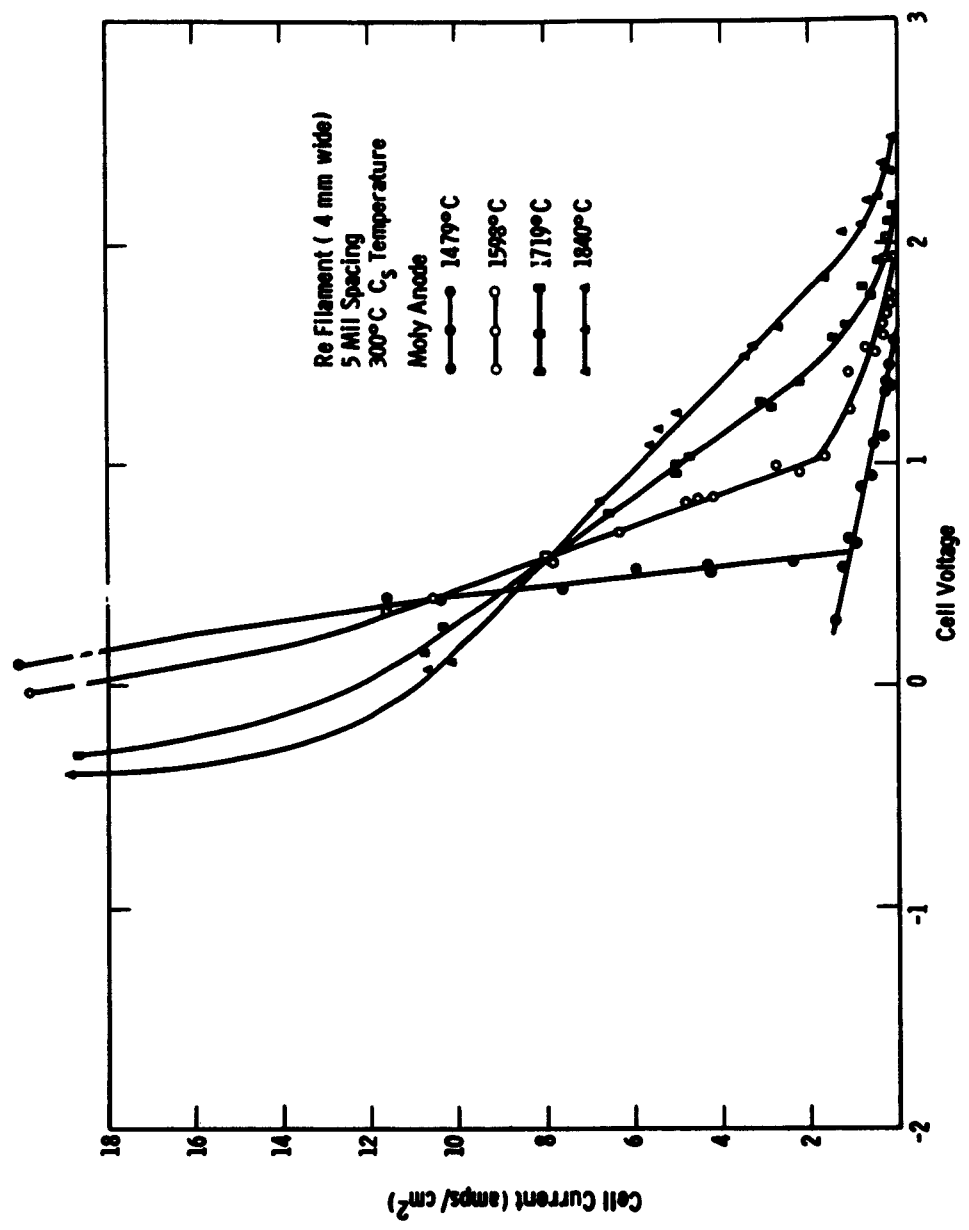


Fig. 1-35. Current Voltage Characteristics with Rhenium Emitter

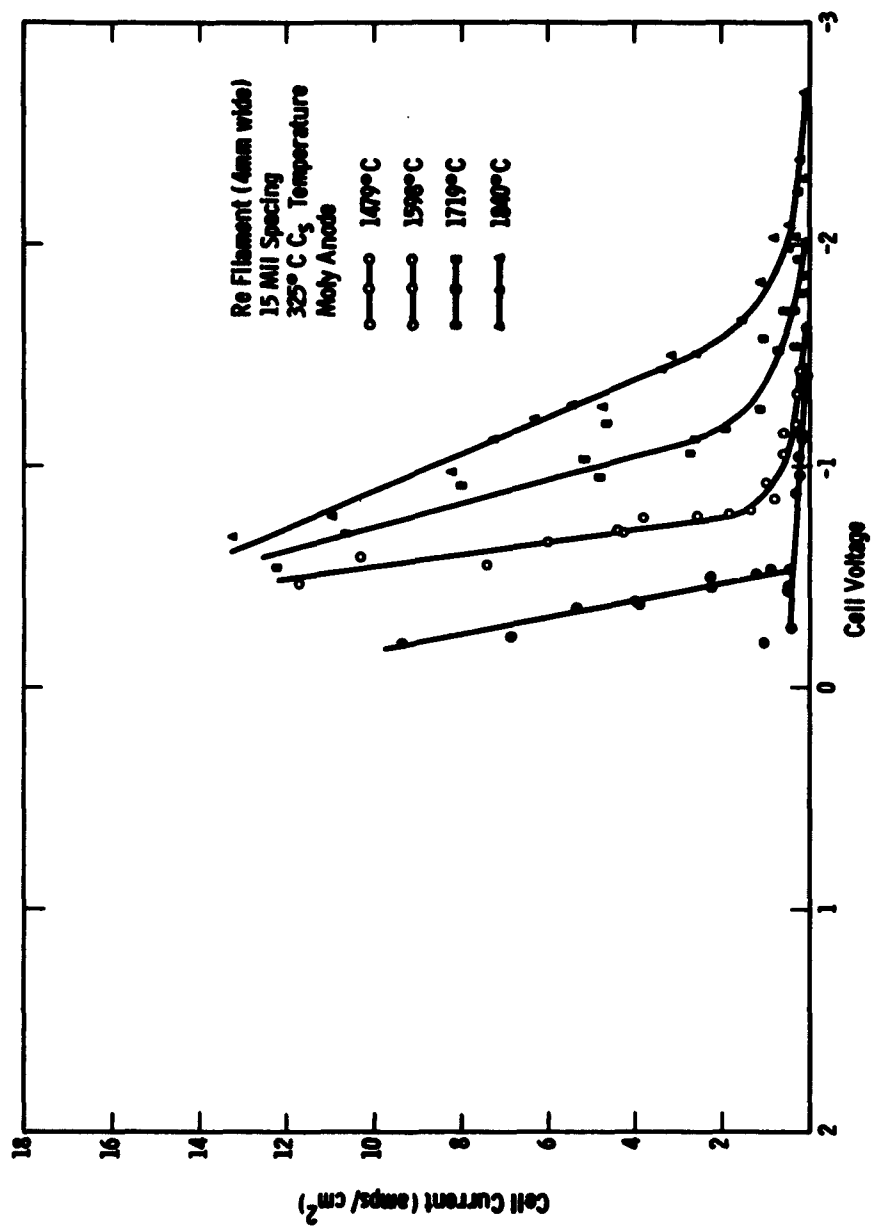


Fig. 1-36. Current Voltage Characteristics with Rhenium Emitter

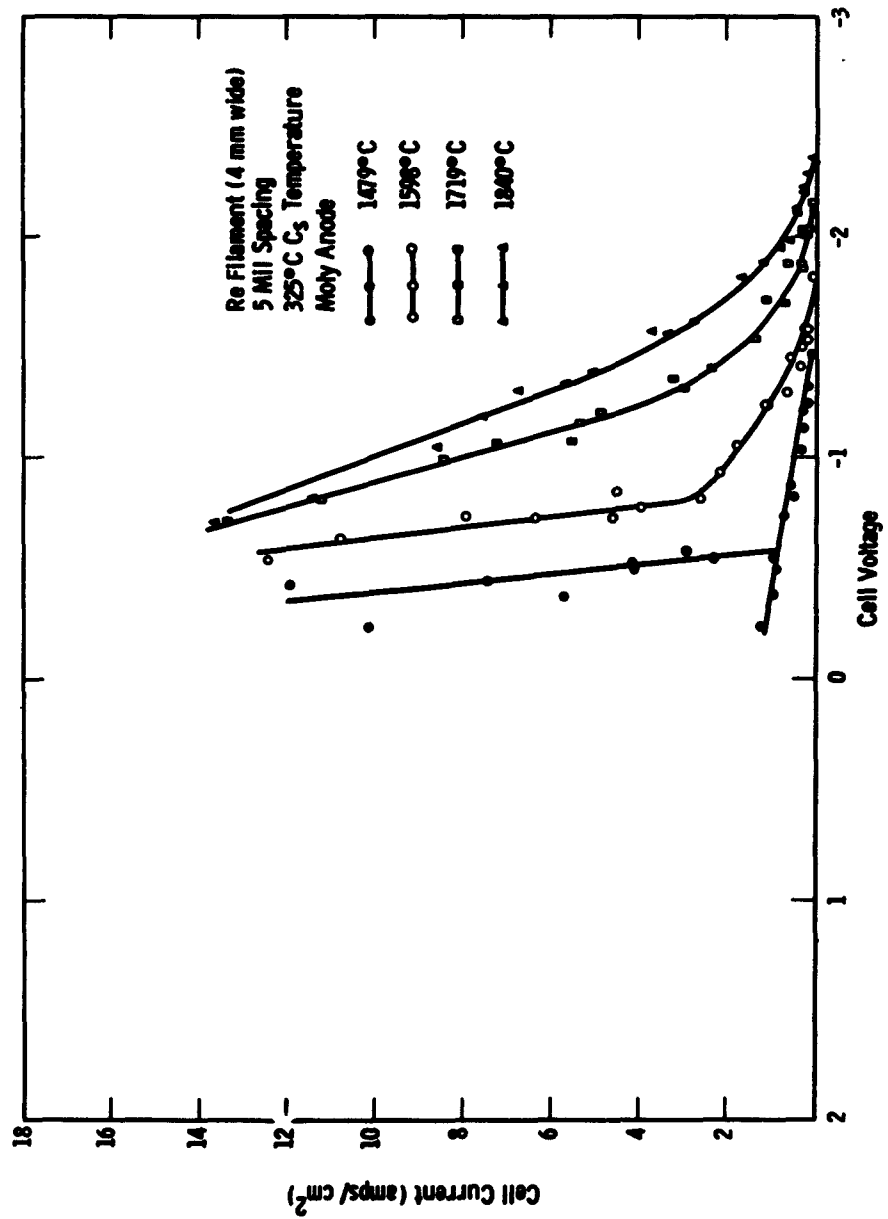


Fig. 1-37. Current Voltage Characteristics with Rhenium Emitter

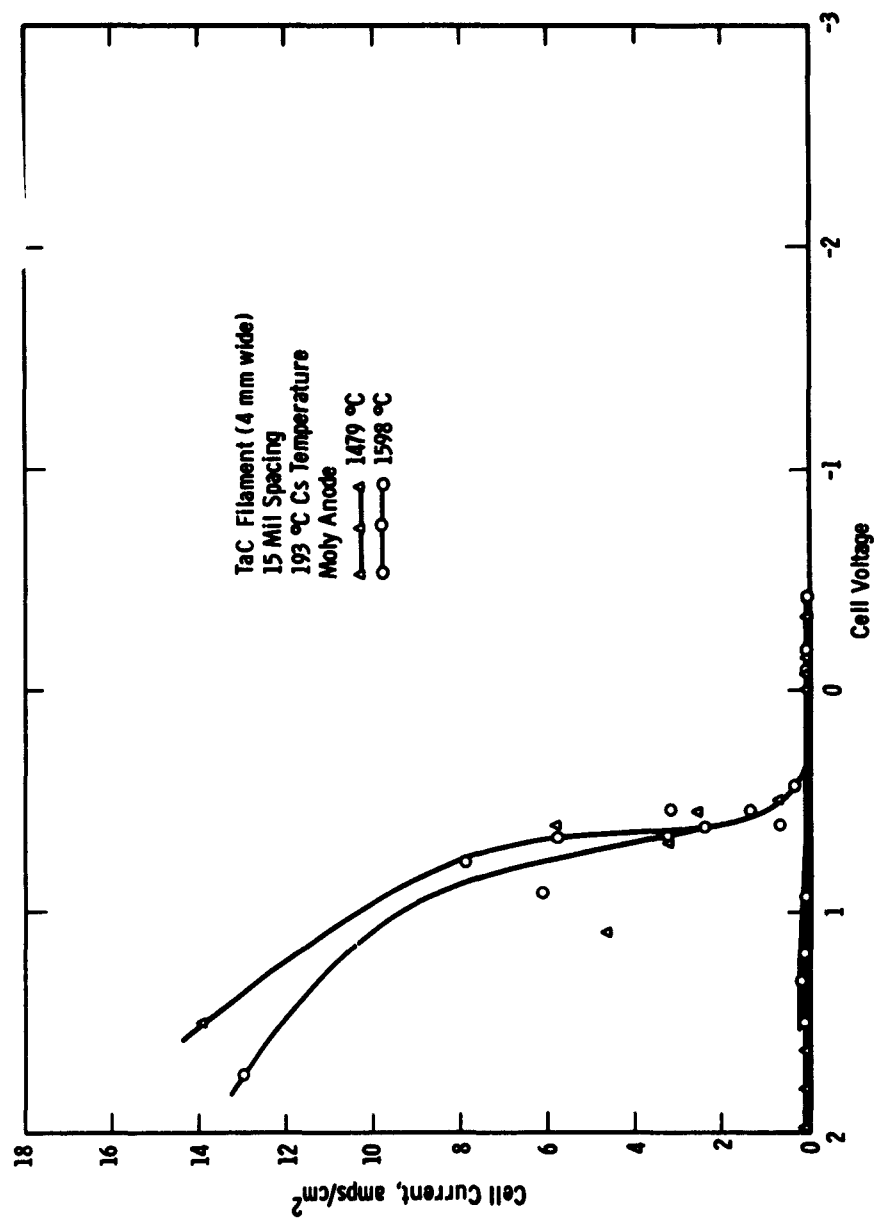


Fig. 1-38. Current Voltage Characteristics with Tantalum-Carbide Emitter

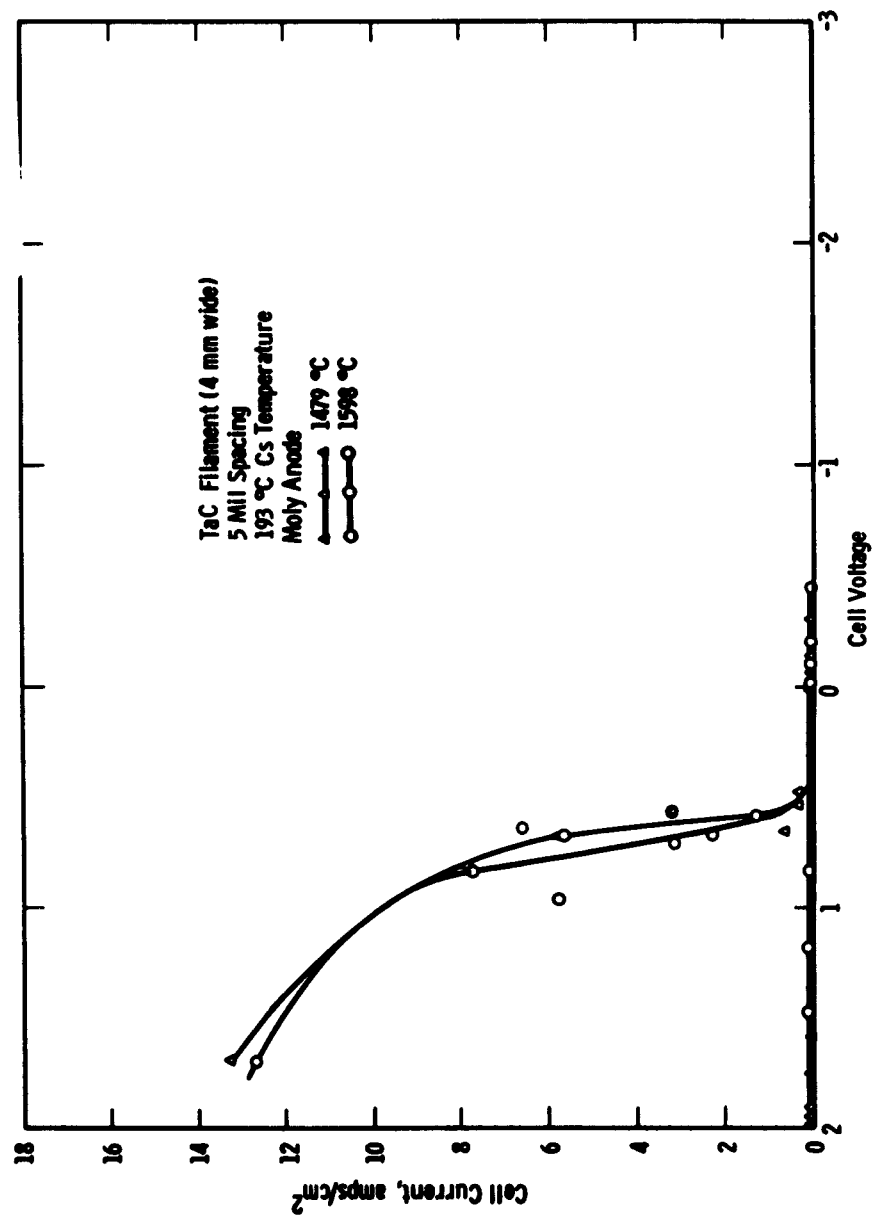


Fig. 1-59. Current Voltage Characteristics with Tantalum Carbide Emitter

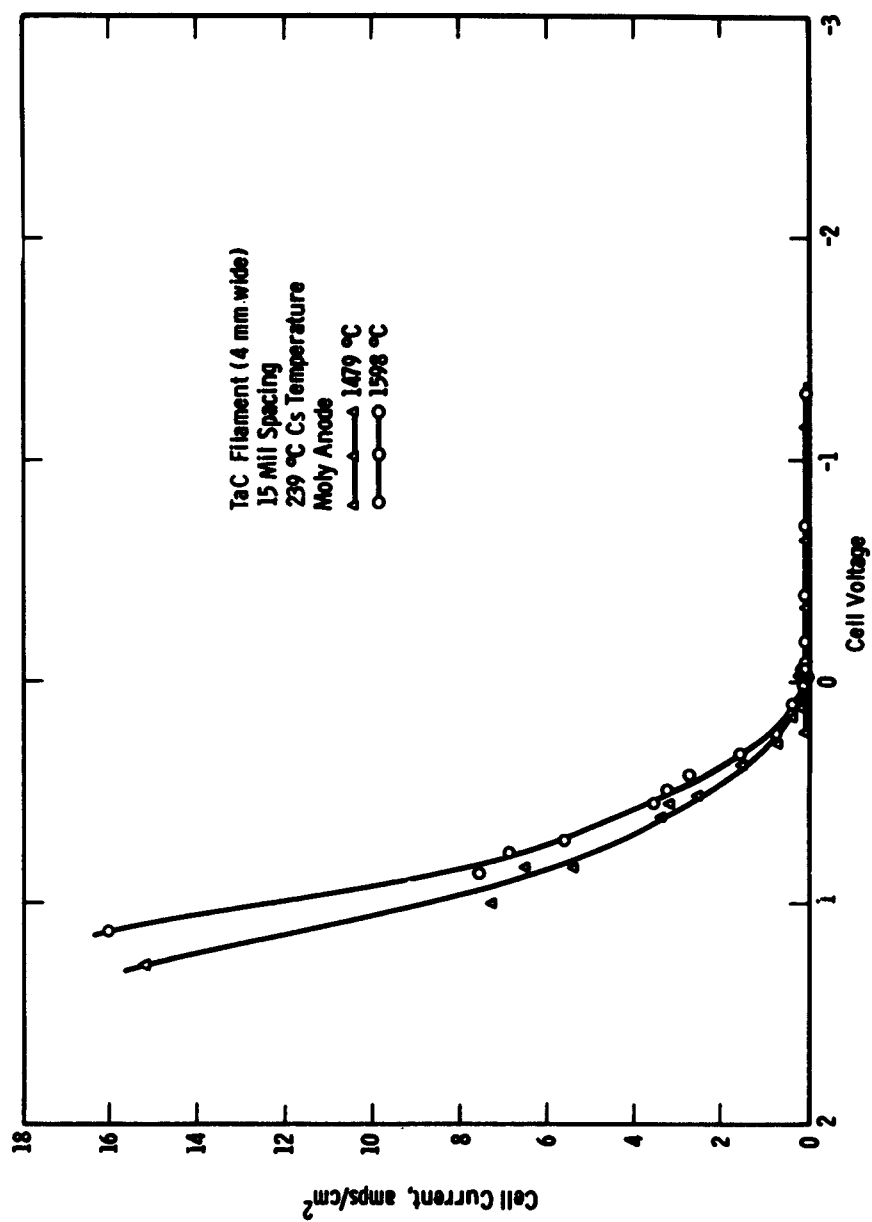


Fig. 1-40. Current Voltage Characteristics with Tantalum Carbide Emitter

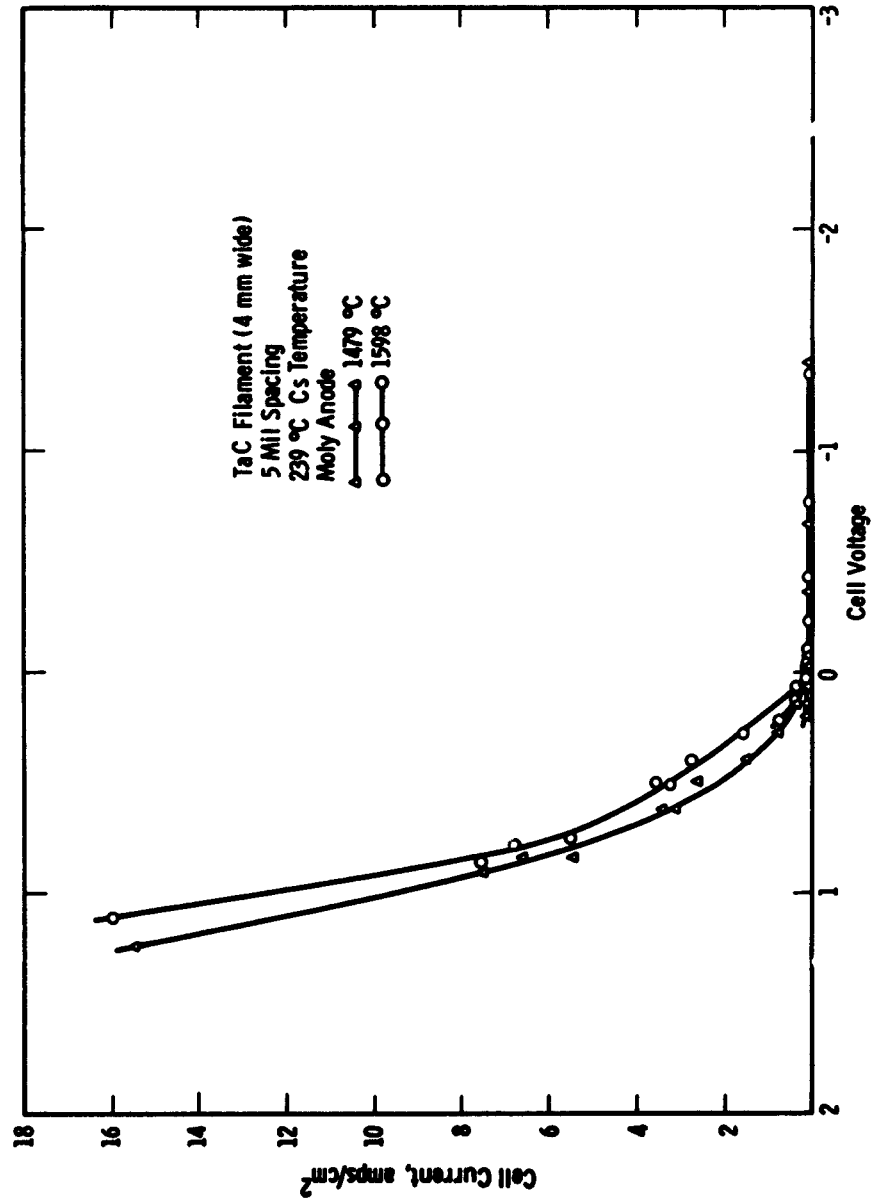


Fig. 1-41. Current Voltage Characteristics with Tantalum Carbide Emitter

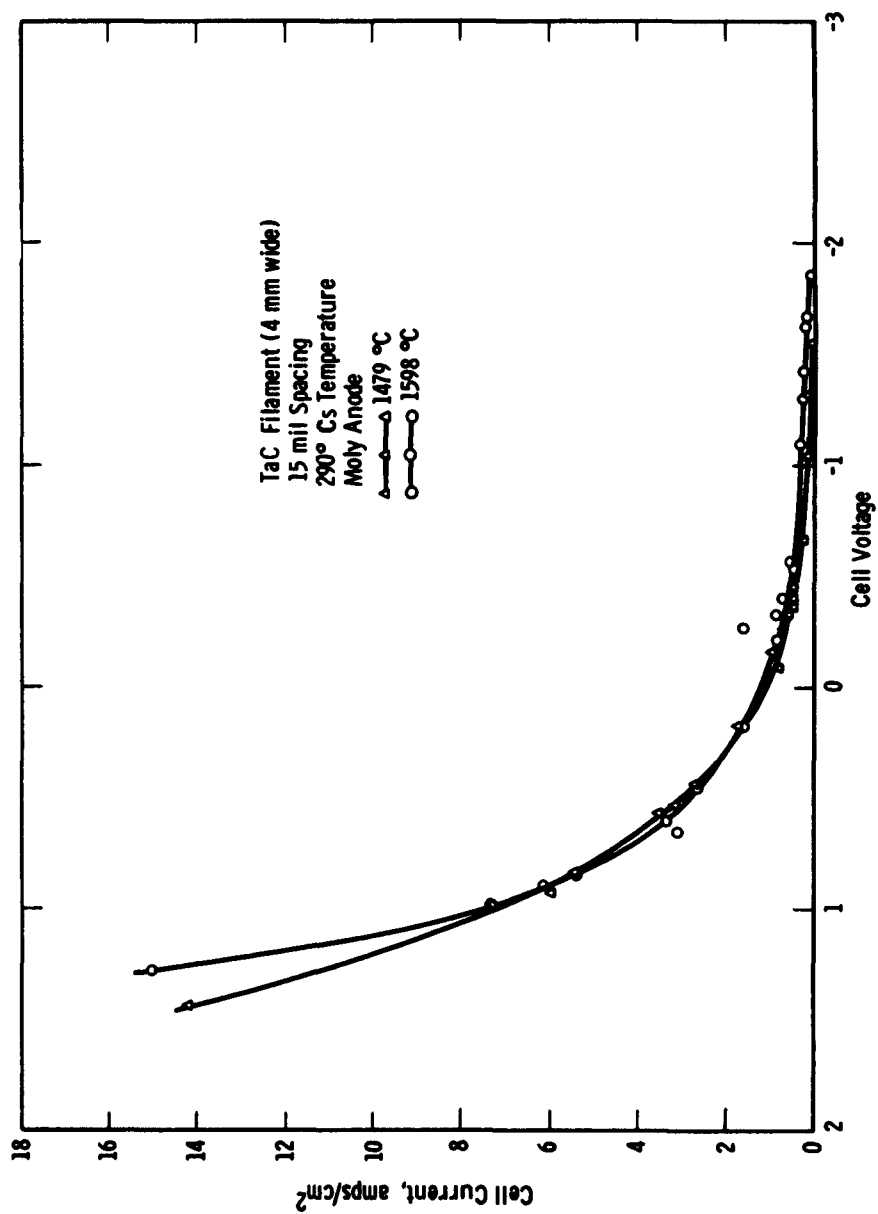


Fig. 1-42. Current Voltage Characteristics with Tantalum Carbide Emitter

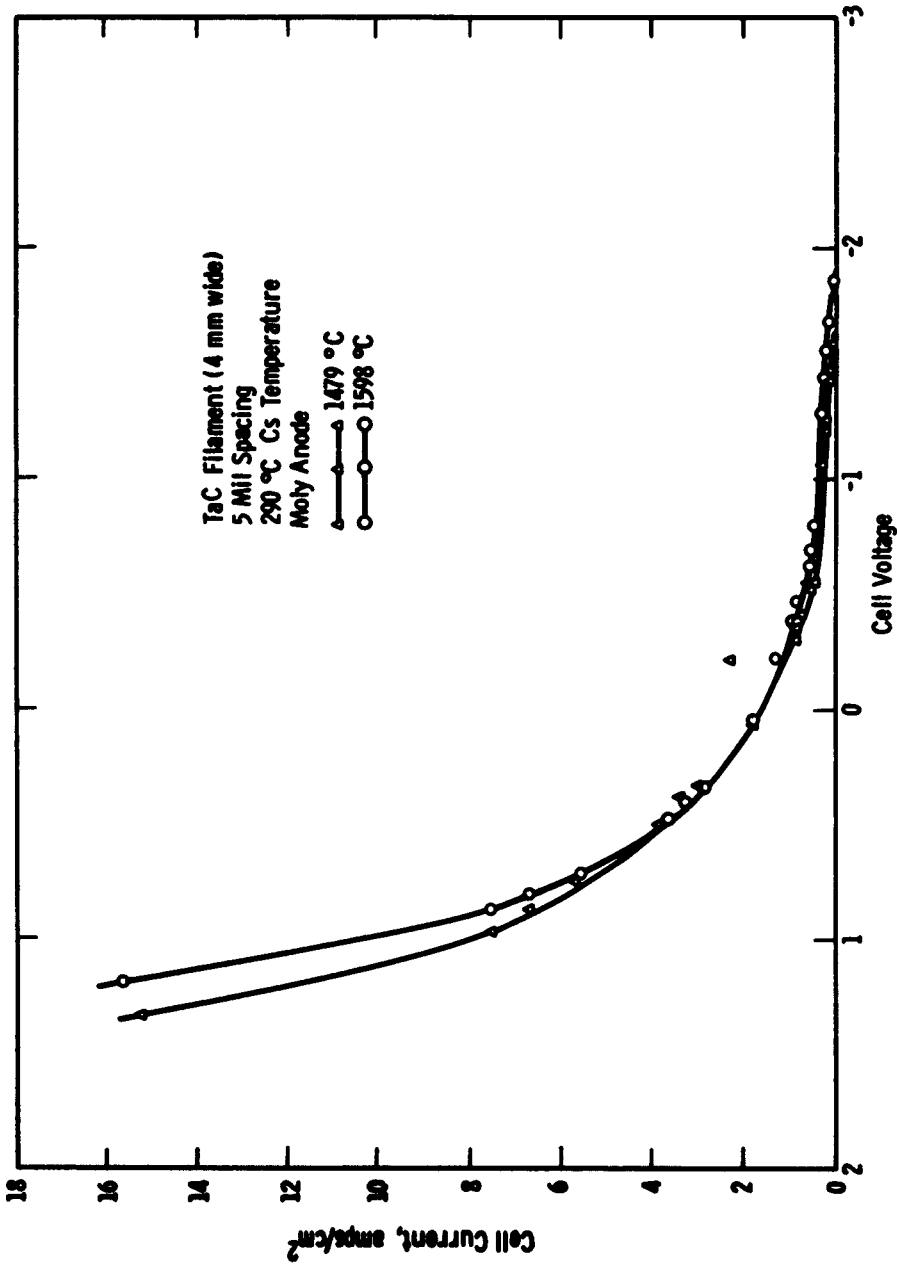


Fig. 1-43. Current Voltage Characteristics with Tantalum Carbide Emitter

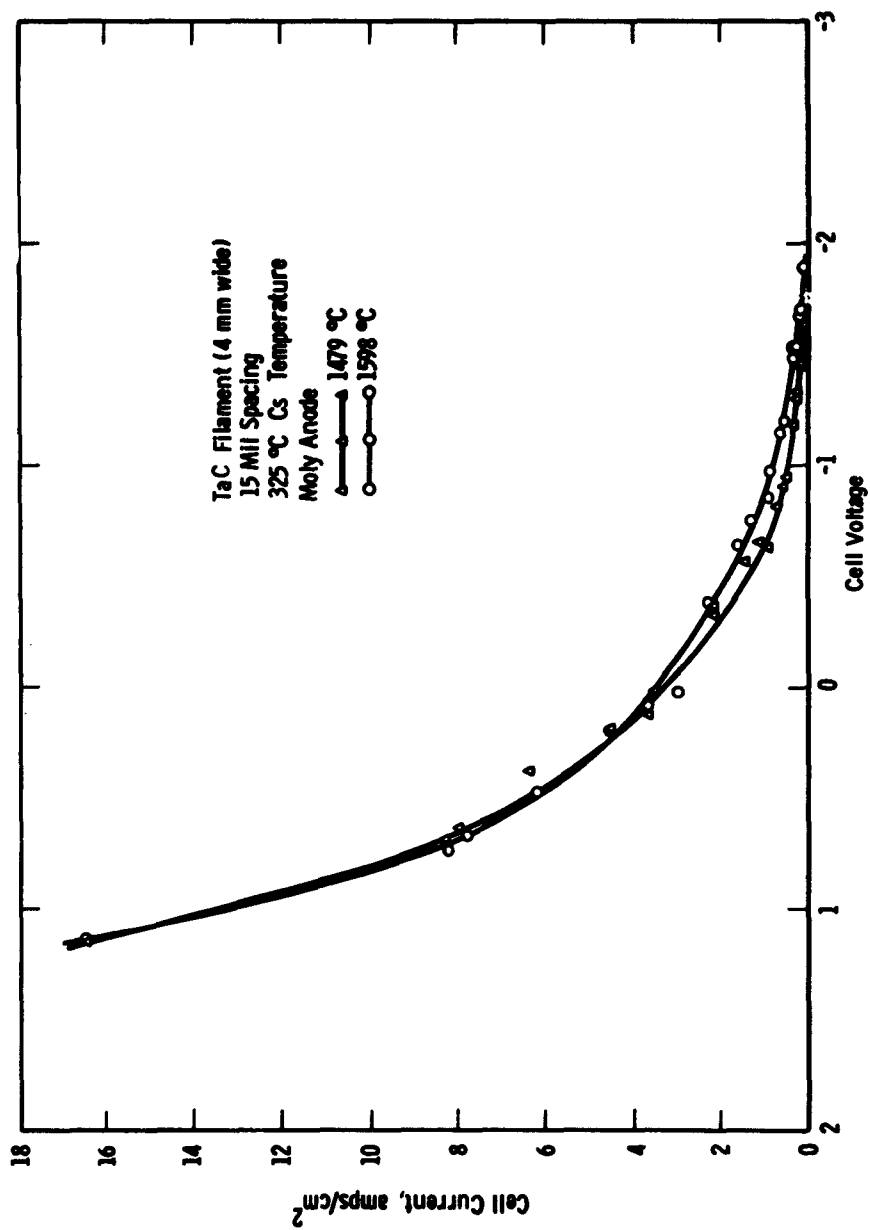


Fig. 1-44. Current Voltage Characteristics with Tantalum Carbide Emitter

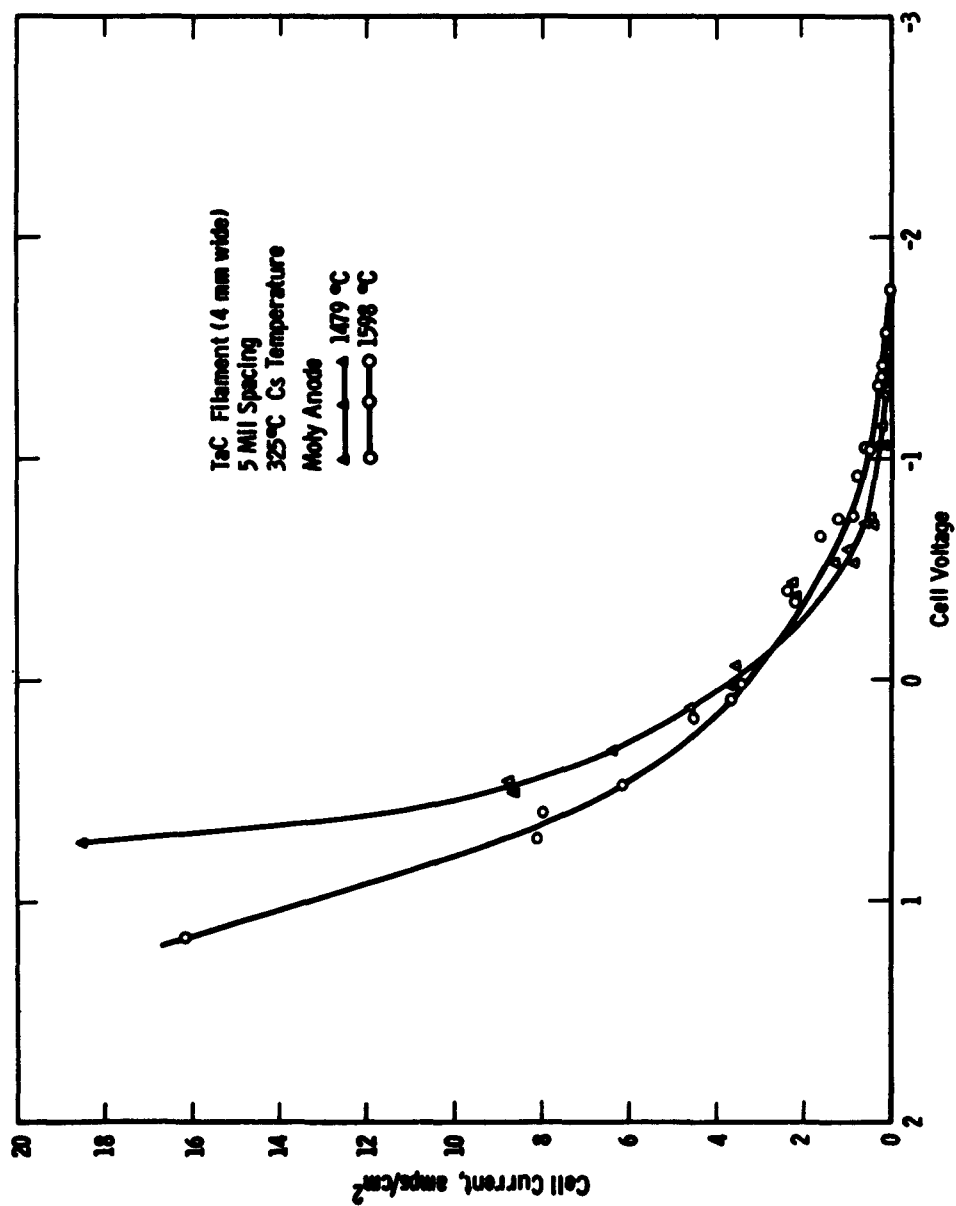


Fig. 1-45. Current Voltage Characteristics with Tantalum Carbide Emitter

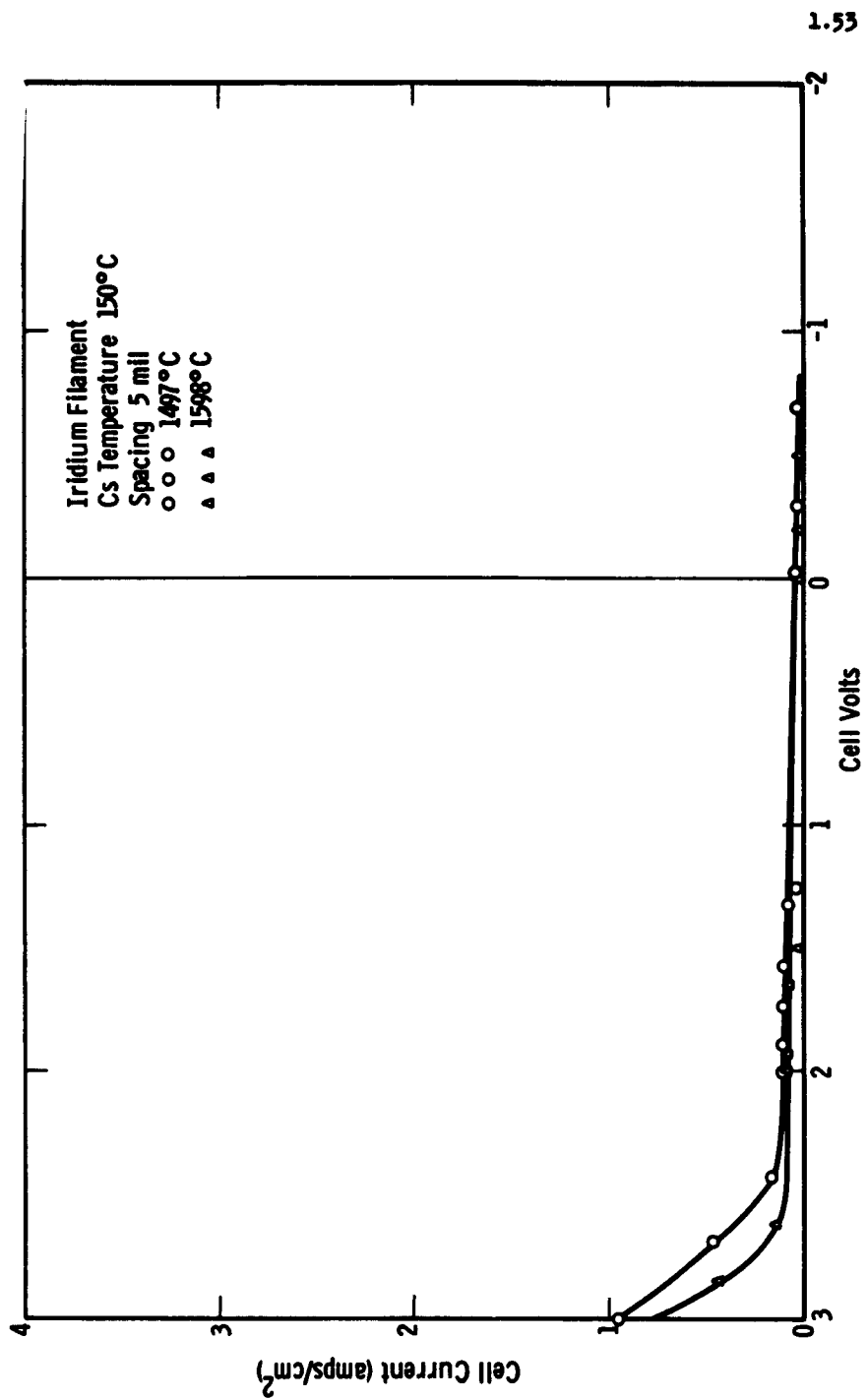


Fig. 1-46. Current Voltage Characteristics with Iridium Emitter

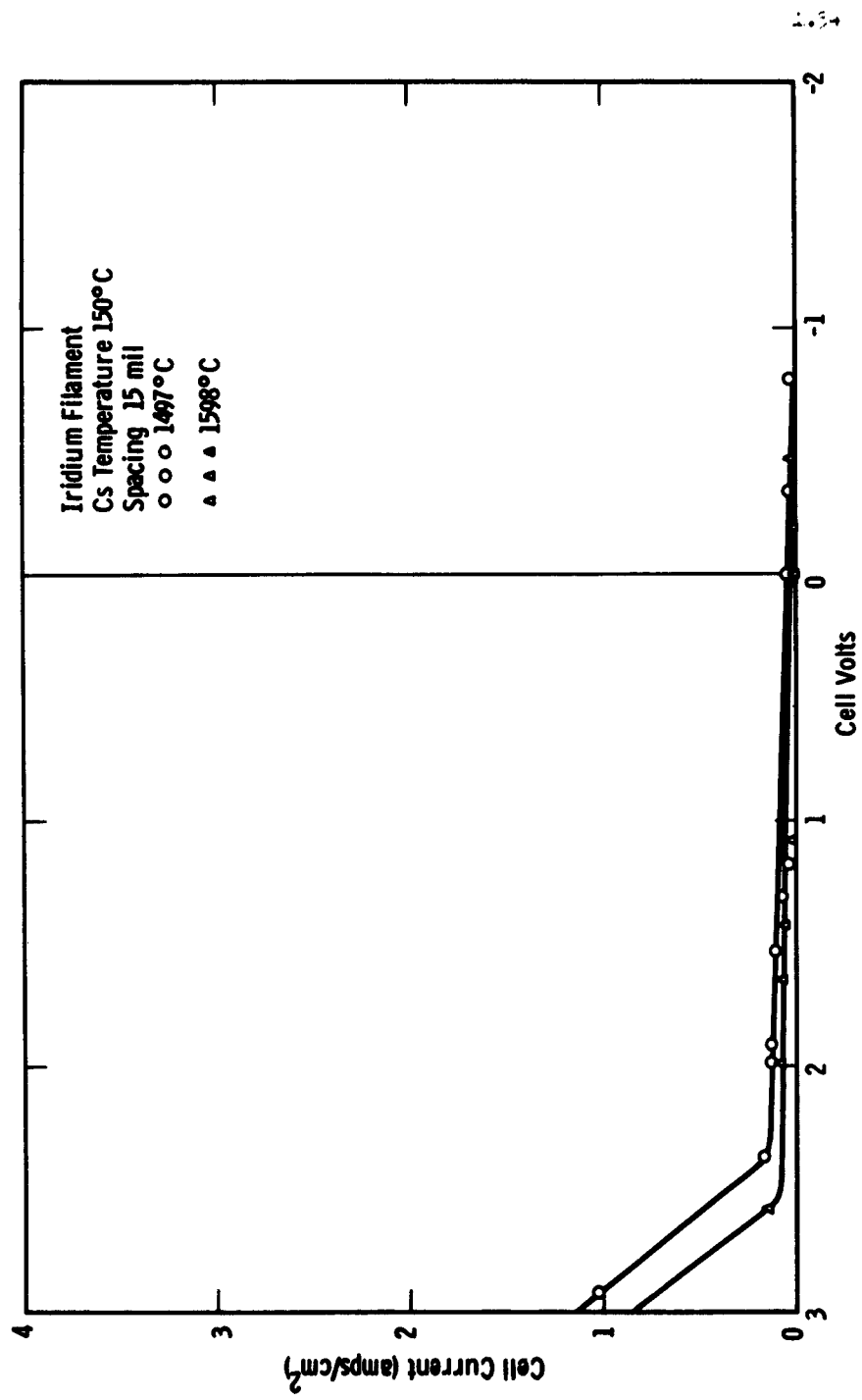


Fig. 1-47. Current Voltage Characteristics with Iridium Emitter

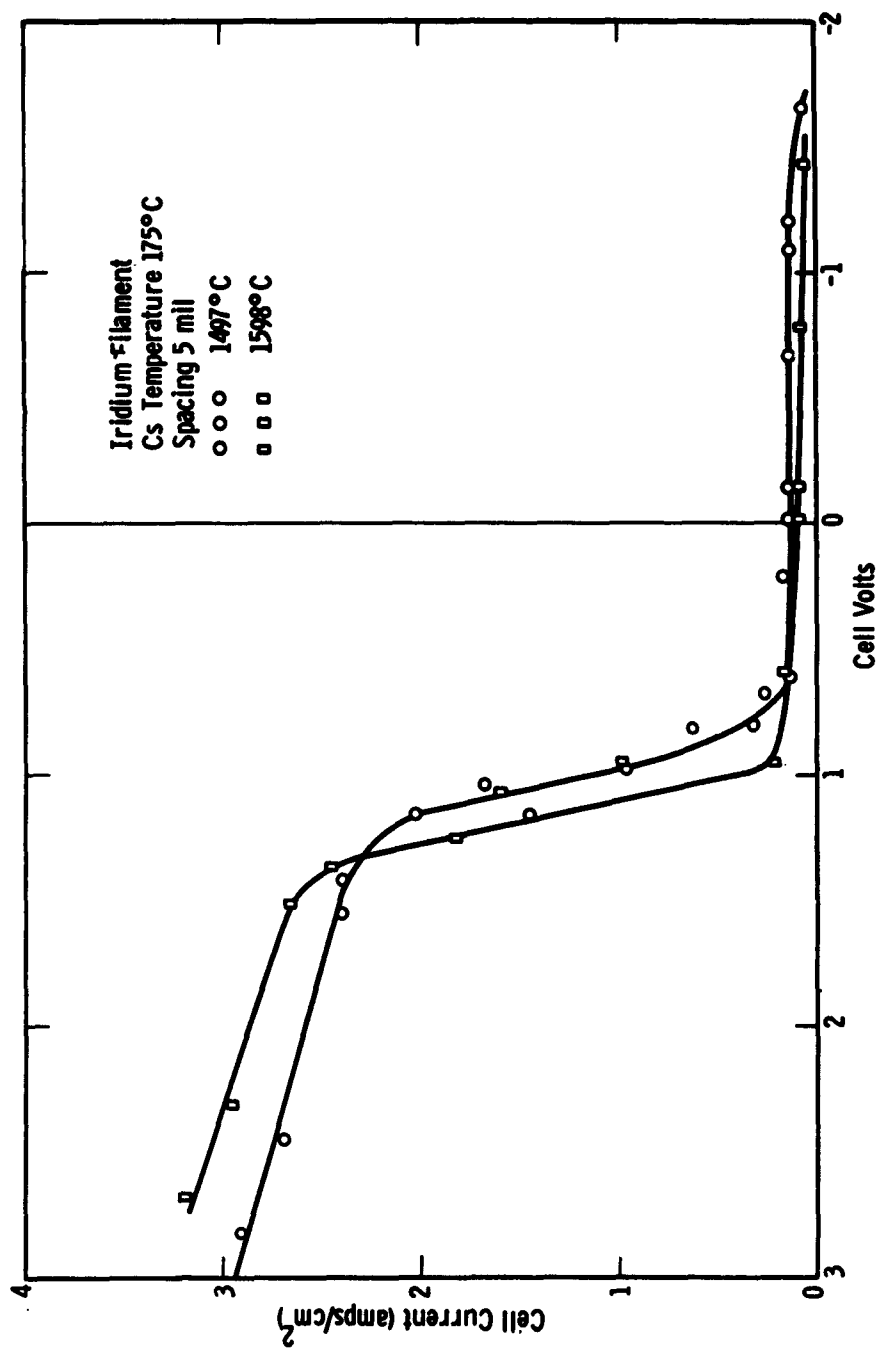


Fig. 1-48. Current Voltage Characteristics with Iridium Emitter

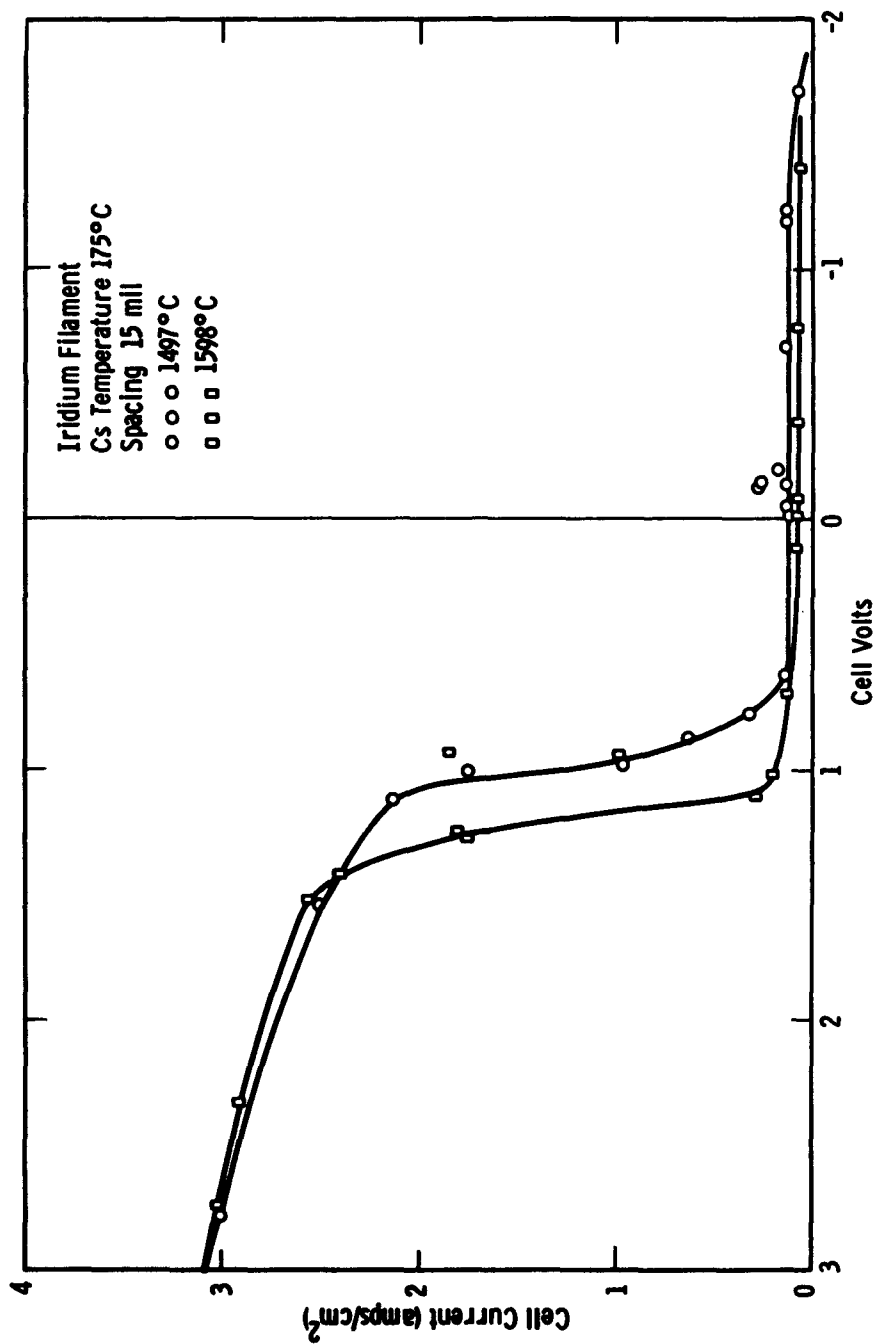


Fig. 1-49. Current Voltage Characteristics with Iridium Emitter

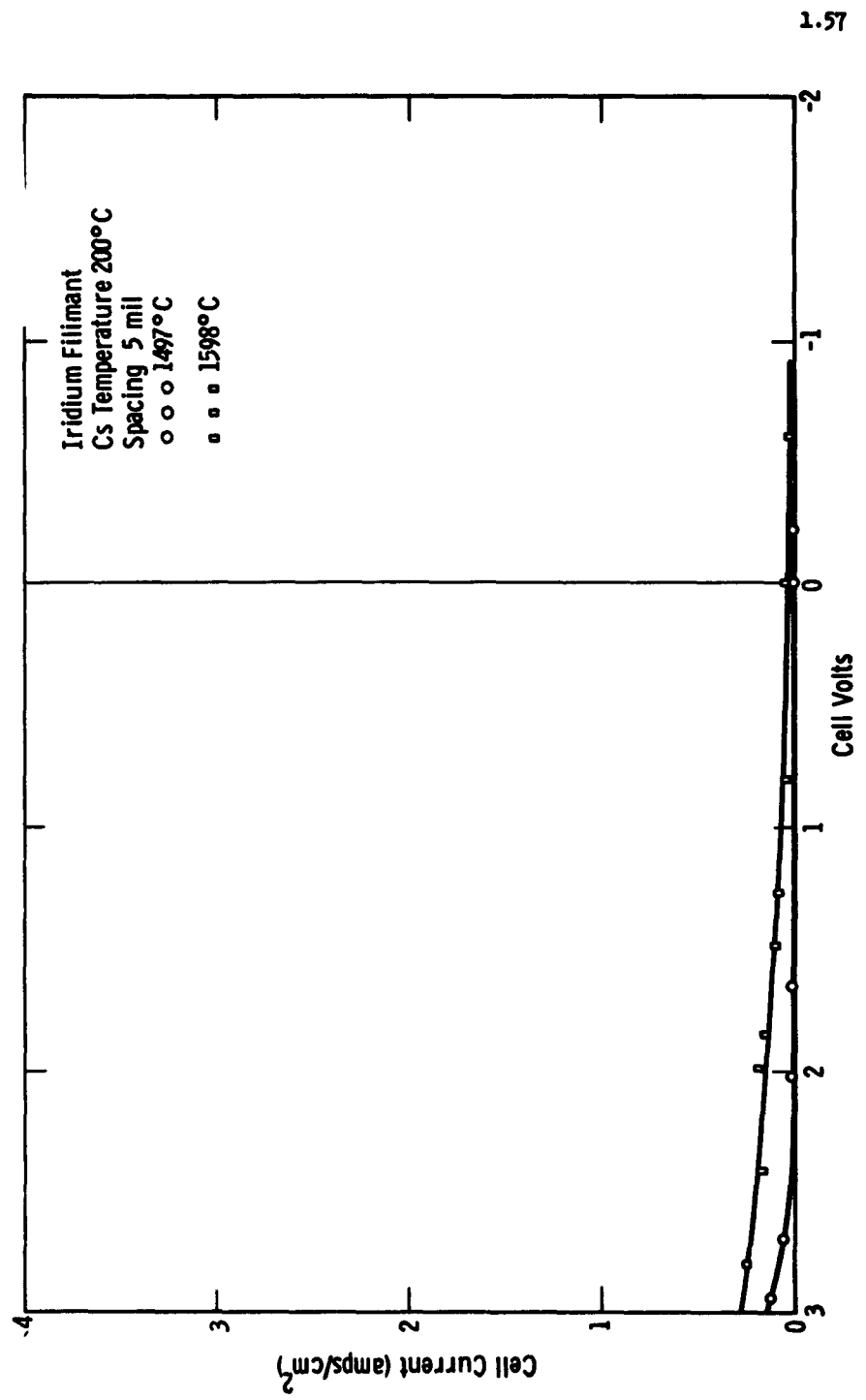


Fig. 1-50. Current Voltage Characteristics with Iridium Emitter

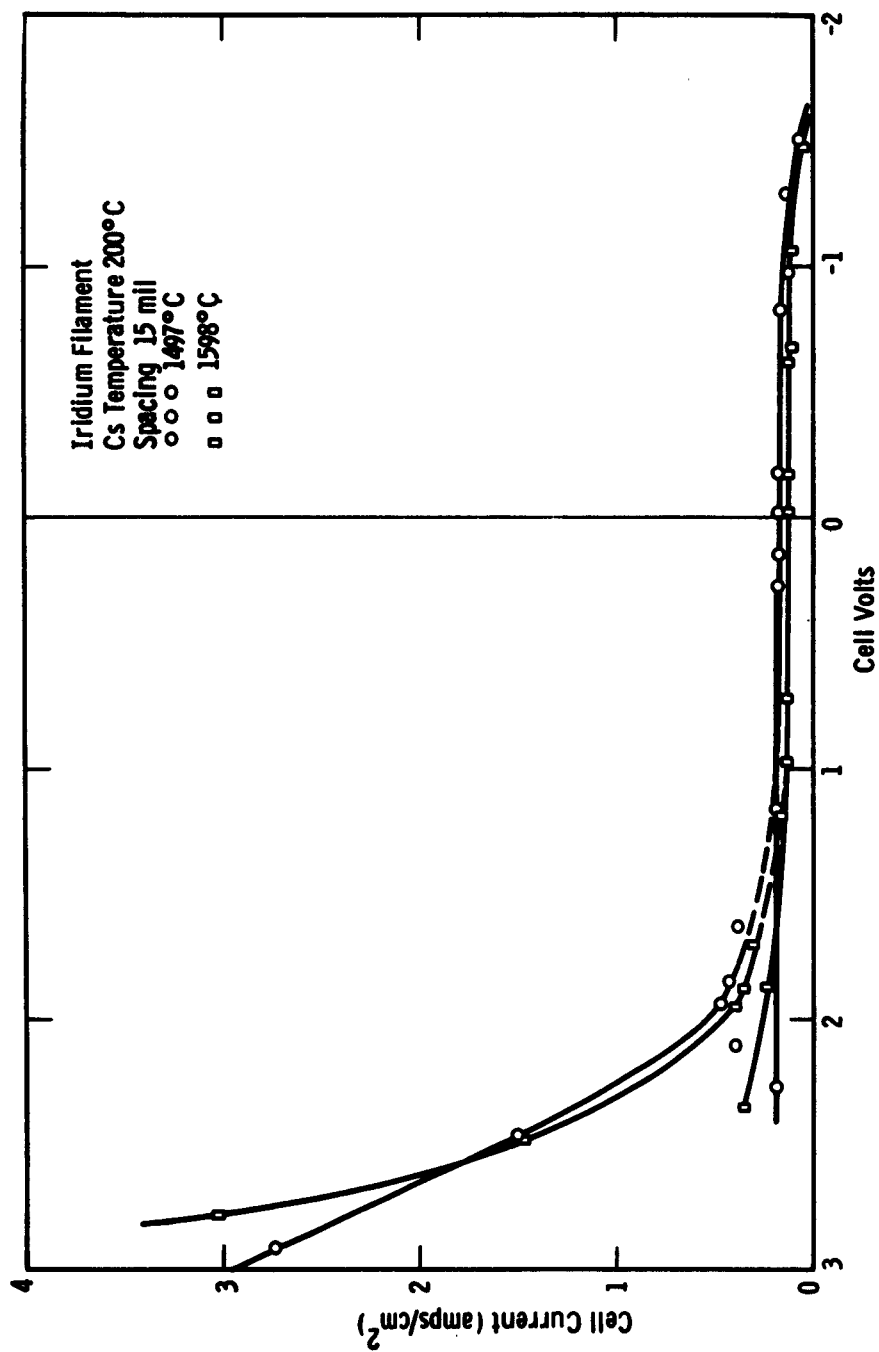


Fig. 1-51 Current Voltage Characteristics with Iridium Emitter

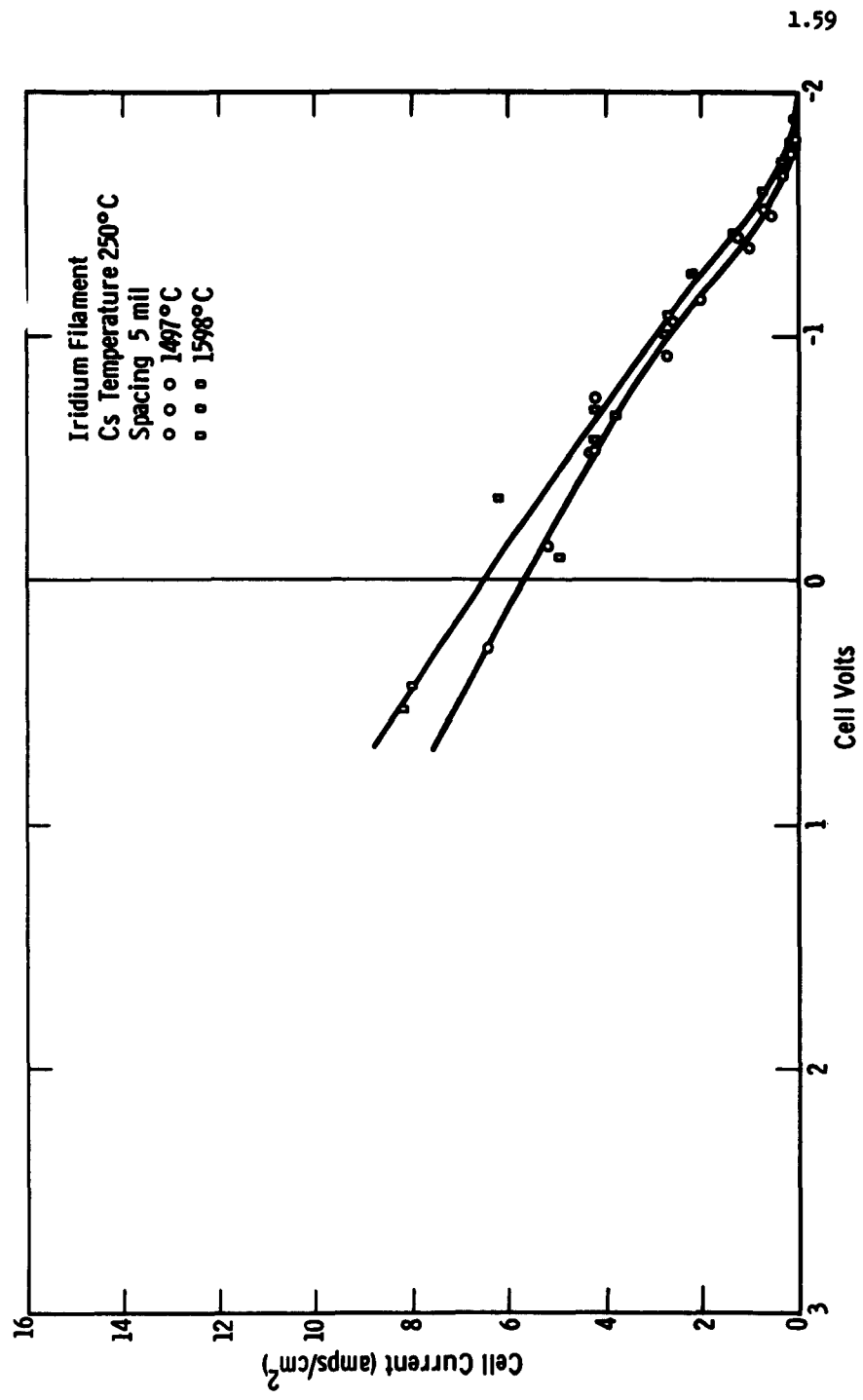


Fig. 1-52 Current Voltage Characteristics with Iridium Emitter

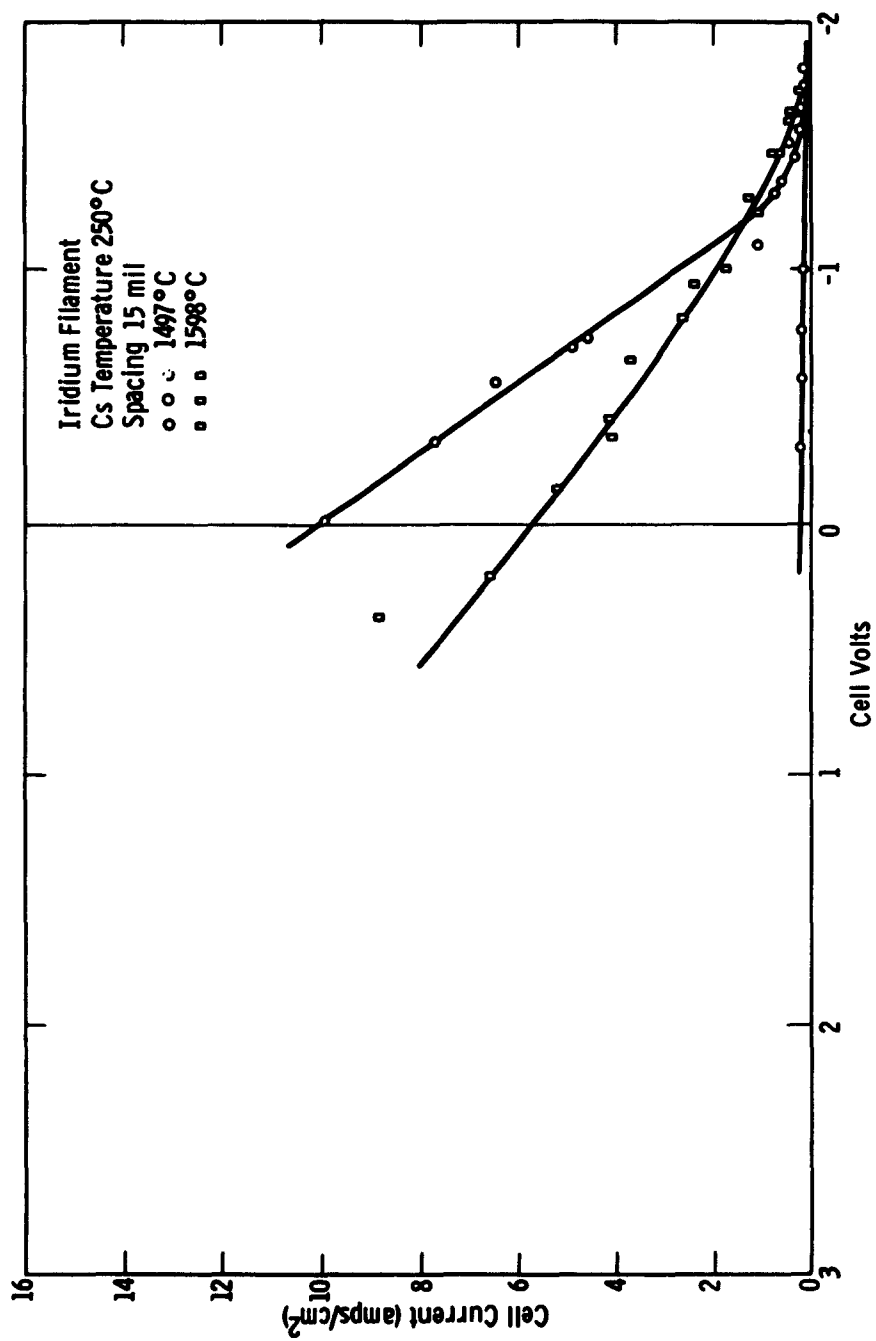


Fig. 1-53. Current Voltage Characteristics with Iridium Emitter

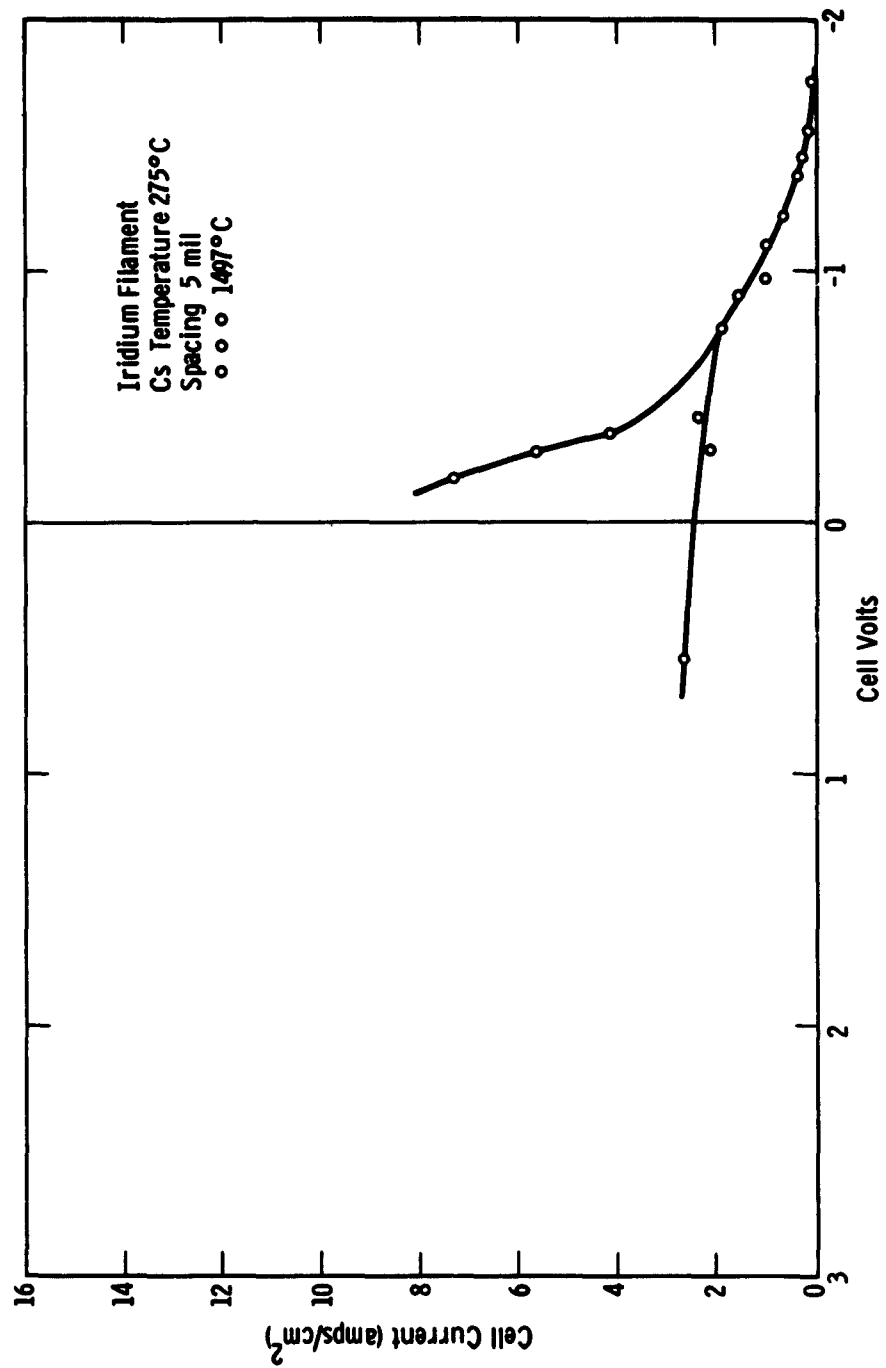


Fig. 1-54. Current Voltage Characteristics with Iridium Emitter

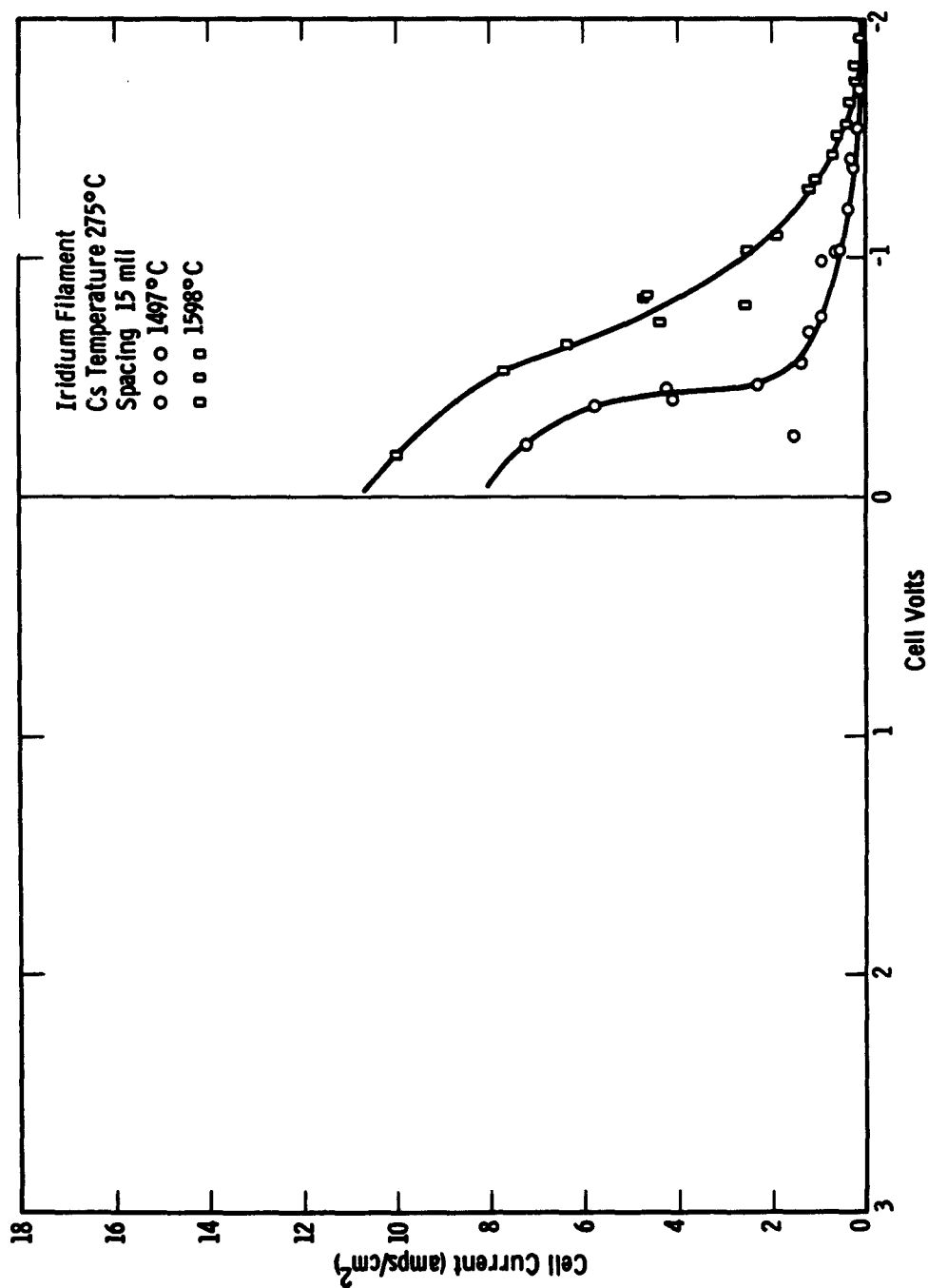


Fig. 1-55. Current Voltage Characteristics with Iridium Emitter.

CHAPTER TWO

SATURATION EMISSION CURRENT MEASUREMENTS ON REFRACTORY MATERIALS
USING "PLASMA ANODE" TECHNIQUE

Measurements of saturated thermionic emission from refractory metals in cesium vapor have been made using the plasma anode technique originated by Marchuk⁽¹⁾ and used by Houston.⁽²⁾ The method uses the test material in the form of a small wire loop emitter, typically 5 mil diameter, passing through insulating ceramic sleeves which expose a short length of the loop to a cesium vapor plasma. The emitter is held slightly negative with respect to the plasma and the resulting positive ion current from the plasma to the test surface neutralizes the emission-retarding effects of the electron space charge at the emitter. The technique has a principal advantage over the diode device, in which an electric field is maintained between the emitter and collector surfaces in order to draw saturation currents. In the presence of Cs vapor there is a strong tendency for a discharge to set in under these conditions and distort the measurements.

A typical experimental cell is shown in Figure 2-1. The sidearm contained an ampoule of liquid Cs, which was broken open by a magnetic hammer after the tube had been processed and sealed off. During a test run, the whole cell was placed in an air oven, thermostatically controlled to within $\pm 1^\circ\text{C}$. The Cs vapor pressure in the cell was then a variable dependent on the temperature of the liquid reservoir. A discharge, created in the vapor between a tungsten helix cathode and a disc anode, was maintained with the anode 40 V to 50 V above the grounded cathode.

Up to six test emitters projected into the resulting plasma, at positions along the tube axis. Preparation of the tube involved evacuation and low temperature bake-out at 325°C for 24 hours. All emitting surfaces were outgassed at temperatures in excess of those reached in the experiments. This was followed by baking at 425°C for 1 hour before sealing off. The pressure of residual gases at room temperature was less than 2×10^{-8} torr before the Cs ampoule was broken.

Figure 2-2 shows the configuration of the measuring circuit. Emission currents from the test surface were observed with an oscilloscope connected across a standard resistor in the emitter circuit. The test filament was heated with half-wave rectified alternating current and a mercury switch was used to short-circuit the input synchronously with the power half-cycle. In this way, emission currents were observed only on the "off" half-cycle, without the superimposition of the voltage generated across the filament by the heating current wave. The potentiometer provided a means of adjusting the potential of the test emitter with respect to the plasma and a variable resistor in the anode circuit was found sometimes useful to stabilize plasma conditions when emission from a test filament became an appreciable fraction of the discharge current.

The temperature of each test emitter was inferred from the heating current at all times, which necessitated an initial calibration. Filament temperatures were observed with an optical micropyrometer above 1000°K . A curve was constructed giving the corrected observed temperature as the ordinate against heating current as the abscissas. The curve was

extrapolated to lower temperatures using resistance measurements. This calibration was carried out with the tube at room temperature when the Cs vapor pressure is of the order 10^{-6} torr, to eliminate possible inaccuracies in temperature measurement due to adsorption of radiation by Cs vapor at higher pressures or the loss of transmittance through the glass envelope due to Cs attack. Each filament was aged before temperature measurements were made, the aging process being monitored by heating current/voltage readings at a suitable temperature. Resistance/heating current calibrations were made at room temperature and at each subsequent oven temperature and were correlated with the micropyrometer readings to yield the emitter temperature under all experimental conditions. The method proved satisfactory in circumstances when no electron cooling occurred locally in the exposed loop. Emission densities generally greater than 10^{-1} A/cm² produced this effect to a degree which destroyed the normal temperature distribution in the filament and therefore rendered the temperature calibration unreliable.

Some detail variations in the system were used during the course of the experimental program. The foregoing descriptions refer to more recent modifications which were suggested by experience with the first cells during the development stage of the technique.

Five discharge tubes^{*} have been used in an experimental period of 12 months. Approximately half this time was employed in development of the system to a level at which meaningful emission data could be measured. The first cell yielded data which deviated markedly from S-curves for a W specimen extrapolated from the work of Taylor and

* References to tubes numbered 1 through 5 apply to the experimental cells in the order of building.

Langmuir⁽³⁾ The chief cause of the distortion was found in the design of the test emitter mounting. The test filament was spot welded to heavier kovar leads only a short distance (about 1 mm to 2 mm) from the end of the ceramic sleeve, where the filament was exposed to the plasma. This arrangement satisfactorily prevented sagging of the filament inside the sleeve, a desirable feature to inhibit contamination of the filament by materials in the ceramic. It had been found previously, in addition, that if contact with the ceramic was allowed a cold spot would develop inside the sleeve which would seriously affect the temperature distribution over the whole exposed area of the loop. On close inspection with a micropyrometer the kovar leads were observed to cool the ends of the loop and establish an appreciable temperature gradient ($5^{\circ}\text{C}/\text{mm}$ to $6^{\circ}\text{C}/\text{mm}$) from the midpoint to the exposed ends of the loop. A new test emitter was designed as a compromise between the need for support as high in the sleeve as possible and the requirement of no temperature variation across the exposed portion of the filament. The resulting arrangement was as shown in Figure 2-3 with the supporting lead protruding about 7 mm into the ceramic. The temperature difference between the ends and midpoint of the loop were then within 4°C to 5°C , the limits of resolution of the micropyrometer.

The very desirable feature of providing guard rings at each test emitter position was not available until the third tube was built. In both the preceding cells failures in the metal-to-glass seals, before emission data could be collected, was in excess of half the total number

produced. As the probability of failure would increase with each additional seal, the number of leads in each tube was kept to a minimum. The cause of failure proved to be mainly temperature cycling fatigue in the rigid kovar-to-glass seals. The leads were chromium plated to prevent attack by Cs, but the seal was also susceptible to mechanical damage when leads to the measuring circuit were being clamped on. The third and fourth tube were fitted with kovar leads, to which flexible stranded copper tails were brazed and this arrangement greatly reduced the amount of mechanical strain imparted to the seal. The reliability of chromium plated tungsten leads was investigated and found to be very good. These leads brazed to flexible tails, similarly as with the kovar, were used to replace some kovar presses in tube No. 3 which failed and were incorporated exclusively in the fifth and later in the fourth tube. In its final condition tube No. 3 was in service for more than 600 hours at elevated temperatures without a single failure. As was mentioned before, in order to maintain the uniformity of temperature over the exposed portion of the test emitter the filament was required to protrude into the insulators for the greater part of their length. The bore of the insulator was reduced in the second and subsequent tubes to minimize the magnitude of error introduced in the regions where the filament entered the sleeves. This combination, unfortunately, caused the temperature of the unexposed filament to exceed the temperature of the exposed surface, at the upper end of the temperature range. Consequently, a number of specimens failed during

outgassing at temperatures which, when observed at the exposed surface, were considered safe. This problem was solved by testing two or three duplicate presses with specimens mounted in a fashion identical to that in the discharge tube. The first specimen was raised in temperature until it failed and the second filament was then life-tested at some lower temperature. Should this temperature still have provided too short a life a third specimen was on hand to allow repetition of the process. Usually just two specimens were sufficient for the determination of a suitable high temperature limit.

Thermionic Emission Data Yielded by the Investigation

The first tube produced no meaningful emission data but was, however, useful in providing a source of experience in cell design and familiarity with the technique. Cell No. 2 although plagued by press failures yielded an S-curve for W and part of the curve for Ta at $T_{Cs} = 373^\circ K$ (Fig. 2-4). The W data deviated considerably from the curve extrapolated from the work of Taylor and Langmuir.⁽³⁾ This may be explained by a combination of emission-enhancing field effects and spurious emission currents, which are discussed below with respect to experiments with rhenium in cell No. 3. The high temperature portion of the Ta curve also appeared displaced to the right of the accepted bare work function line. The maximum of the curve is probably significant in connection with the emission properties of adsorbed oxygen films on refractory metal surfaces (dealt with in the next section of this chapter).

Emission characteristics of Re were investigated with particular attention being paid to the behavior in the region of S-curve emission, where the cesium coverage is some small fraction of a mono-layer. Data for the Re filament are presented in Fig. 2-5 for $T_{Cs} = 398^\circ K$. In regions of high Cs coverage (values of $\phi < 3.2$ eV) the S-curve is of the expected shape. An attempt was made to extrapolate to the true field-free situation by plotting several values of emission current for each emitter temperature against the net positive ion current arriving at the test surface. The resulting curves were extrapolated to values corresponding to zero net ion current. The S-curve of Fig. 2-5 is plotted with points arrived at in this way, in the region free from the anomalous behavior discussed below. This procedure showed that the measured emission currents were slightly sensitive to variations in emitter potential and hence changes in ion current from the plasma to the test surface.

In the domain of low coverage ($\phi > 3.2$ eV) anomalously high emission was observed which indicated a ϕ of 4.3 eV for bare Re instead of the accepted 4.8 eV value. This apparent depression of the bare work function was recorded for both W and Ta specimens used in tube No. 2 (Fig. 2-4). This region of the characteristics was investigated in more detail and the irregularity was found, in the main,* caused by field enhanced emission in which the test material

* Some distortion of the S-curve was traced to spurious emission from an uninsulated tantalum clamp which was heated by conduction through the ceramic sleeves. Points on the curve between the lines $\phi = 4.2$ eV and $\phi = 3.8$ eV probably include this error and are therefore less reliable than points to the left of the line $\phi = 4.2$ eV. This influence was probably also responsible for distortion of the W curve in Fig. 2-4 in the region of the minimum.

was capable of emitting in two principal modes. A discontinuity between the modes was recorded as a sequence of oscilloscope traces shown in Fig. 2-6, when the potential of the emitter was made increasing negative with respect to the plasma in order to draw an increasing positive ion current to the test surface. The potential setting corresponding to the second wave trace allowed a simultaneous view of both modes, possibly because of a periodic small order fluctuation in temperature or plasma conditions. The mode of higher current density was found to be the more stable of the two. Fig. 2-6 is unique because the lower mode of emission could be achieved in a repeatable fashion. Generally the double mode behavior was seen on the oscilloscope as a series of random high frequency "flips" between the two modes with emission finally remaining in the higher mode after about 5 seconds. The magnitude of the lower mode was measureable from the persistent image, during the "flip-flow" behavior. The dependence of emission current in both modes is plotted for one emitter condition in Fig. 2-7 against net positive ion current arriving at the test surface. Extrapolations of the curves become coincident in a single mode value which would fit an S-curve convergent on the $\phi = 4.8$ eV line.

Complete characteristics* plotted from the extrapolated values could not be made with this tube because the spurious emission

* Plotted points of Fig. 2-5 in the domain of low coverage, correspond to data taken with ion currents of the same order as those necessary for saturation emission currents to be measured at higher coverages.

currents observed masked the response of the specimen in some regions of the S-curve minimum. However, there was strong evidence to support qualitatively the suggestions of Zollweg⁽⁴⁾ for an explanation of the anomalous behavior. The double-mode effect was found to diminish with Cs pressure. Part of the Re characteristic at $T_{Cs} = 295^\circ K$ corresponding to a vapor pressure of 10^{-6} torr was measured where the double mode effect appeared negligibly small. These data when plotted showed a curve properly located at the expected $\phi = 4.8$ eV line, which suggested that surface contamination could not be responsible for the behavior at higher pressures. This conclusion was supported by a spark source mass spectrographic analysis of a similar specimen. The test established a negligible surface contamination (about 5 parts in 10^6) by materials which could lower the work function.

Evidence suggested that the double mode effect could be distinguished from the onset of an arc discharge in the vicinity of the test emitter. At no time during the measurements did a discharge become visible near the emitter or insulators. However it should be stated that the light from the emitter made this observation very difficult. The double mode behavior could not be initiated by any change of emitter potential or plasma condition in regions of higher coverage and similar or larger emission densities.

A fine structure multi-mode characteristic was observed randomly superimposed on the two principal modes of emission which

may have been due to differences in response of locally predominant surface orientations in the polycrystalline material.

The S-curves of Figs. 2-8, 2-9, and 2-10 describe the emission characteristics of four materials Ir, Re, Mo and Ta, used in cells No. 4 and No. 5. In these tubes the spurious emission from clamps was eliminated and the emitter potential adjustment was made more sensitive to allow a nearer approach to optimum space-charge neutralization at emission minima. Curves for Ir and Re were constructed from measurements with two filaments of different lengths. The longer filament of each material yielded points on the curve which were within the scatter probably caused by temperature fluctuations and small order effects in the plasma. Although it was not conclusive, it indicated that no serious end error was introduced at the openings of the sleeves. Similar results were suggested earlier with W emitters in cell No. 2. A better arrangement would have been to use loops, the lengths of which differed by a larger ratio than was possible in this experiment. The choice of filament lengths was limited by problems involving the minimum lengths necessary to allow normal construction of the emitter mounting and the maximum length permissible before sagging of the filament occurred, under the weight of the exposed portion. S-curve data for Ir was restricted to temperatures below 2000°K to prevent undue evaporation of the specimens. The dashed lines in the figures describe

portions of the characteristics in which data was collected, but was not as reliable as points on the full-line curves. To overcome electron cooling, when the emitted current density exceeded 10^{-1} A/cm² measurements were made by depressing a switch in the emitter circuit and reading the emission current in the fraction of a second before cooling was observed. It is still unclear whether this method measures a transient condition which is not truly representative of emission under conditions of complete space charge neutralization.

At the low end of the temperature range the curves fall away from the minimum work function line ($\phi \sim 1.7$ eV) with decreasing Cs pressures. This may be neglected as an intrinsic property of the materials but probably arises from a systematic error in the temperature extrapolations below the visible range of the micropyrometer, which is gradually eliminated at higher pressures, as the S-curve maximum occurs progressively at higher temperatures.

For both Ir and Re specimens data were collected at $T_{Cs} = 348^\circ\text{K}$. Curves corresponding to this temperature were not found to be consistent with curves at higher oven temperatures and have therefore been omitted from this report. The possibility exists that condensation of the vapor at a colder part of the cell, resulted in a lower T_{Cs} than was measured by the sidearm thermocouple.

Some Other Experiments

Other materials have been investigated chiefly in the form of coatings on a filamentary substrate of carburized tantalum. Finely powdered lanthanum hexaboride was painted onto one filament in the first experimental cell but no significant measurements were made with the specimen. The painted coating was in itself very unsatisfactory, the method allowing no precise control of the thickness of the deposit. Temperature fluctuations as much as 100°C were observed in adjacent regions along the loop because of the unevenness of the coating. Some work was undertaken to improve preparation of these surfaces. The more direct way to produce TaC was found by heating a Ta wire in a hydrocarbon atmosphere. The conversion process was controlled by monitoring the resistance of the filament. A small amount of data was given for TaC in both tubes 2 and 3 but the investigation was not taken further after emission characteristics were later found to be non-reproducible. It was assumed that a deterioration in the structure of the carbide had taken place, since the reaction



can proceed under conditions similar to those of the experiment, at an appreciable rate⁽⁵⁾ for temperatures in excess of 2500°K. The

temperature of the specimens was kept just below a limit of 1750°K which may still have been high enough to destroy the specimen surfaces in an experimental period lasting over 20 hours. Carbided surfaces may be used again in the future when the conditions of their chemical stability have been determined more precisely.

A NbC surface was prepared by electrophoretic deposition of particles on a TaC filament. A suspension containing particles screened to 44 microns diameter was ineffective, however, a uniform deposit of 1.7 mil average thickness was achieved from a suspension of particles of about 2 microns diameter. The adhesion of the coating was found to be good and it took on a sintered appearance after outgassing. Reproducible data were not obtained for this specimen because of instability in the substrate.

At the time of writing a small amount of work has been completed to study the effects of adsorbed layers on the emitting power of materials. Langmuir and Villars⁽⁶⁾ found that an adsorbed monolayer of oxygen increased the tendency for "sticking" of cesium on tungsten. More recently Aamodt, Brown and Nichols⁽⁷⁾ have demonstrated a similar effect with fluorine. Experiments in the current program have so far involved the W-O-Cs system used by Langmuir. A cell has been built substantially similar to the previous cells differing only by the provision for one test emitter position and a second sidearm containing an oxygen ampoule. Two attempts have

been made to achieve a monolayer of oxygen on the W filament and while there is evidence to suggest the treatment took place, efforts to "activate" the layer at an oven temperature of 373°K have destroyed both specimen surfaces. The total removal of oxygen from the surface was suggested by the curve in Fig. 2-4 which shows emission generally characteristic of bare W. The cell was reusable, it being necessary only to seal new ampoules in the sidearms. There is every reason to expect ultimate success with the plasma-anode technique used in this type of investigation. The S-curve maximum for Ta in Fig. 2-4 suggests a surface other than the pure metal since it involves emission densities nearly 10^2 greater than measurements with the same material in cell No. 5. The minimum work function is shown to be considerably lower than all other pure metal-Cs systems investigated. It is therefore highly probable that oxygen was responsible for the enhanced effect, because a noticeable seal failure occurred shortly after these measurements were taken, which ended the useful life of the cell.

REFERENCES

1. P. M. Marchuk, Trudy Inst. Fiz. Ak. Nauk, Ukraine 7, 17 (1956).
2. J. M. Houston, PIC Proc. Round Table Discussion on Cathode Emission Investigations and Experimental Techniques for Fabricating and Operating Thermionic Cells. Bedford, Mass., June 1961.
3. J. B. Taylor and I. Langmuir, The Evaporation of Atoms, Ions and Electrons from Cesium Films on Tungsten, Phys. Rev. 44, 423 (1933).
4. Chapter 10 of this report.
5. B. H. Eckstein and R. Forman, Preparation and Some Properties of Tantalum Carbide, JAP, 33, 82 (1962).
6. I. Langmuir and D. S. Villars, J. Am. Chem. Soc. 53, 486 (1931).
7. R. L. Asmolt, L. J. Brown and B. D. Nichols (Thermionic Emission from Molybdenum in Vapors of Cesium and Cesium Fluoride) JAP 33, 2080 (1962).



Fig. 2-1 - Plasma-anode discharge tube.

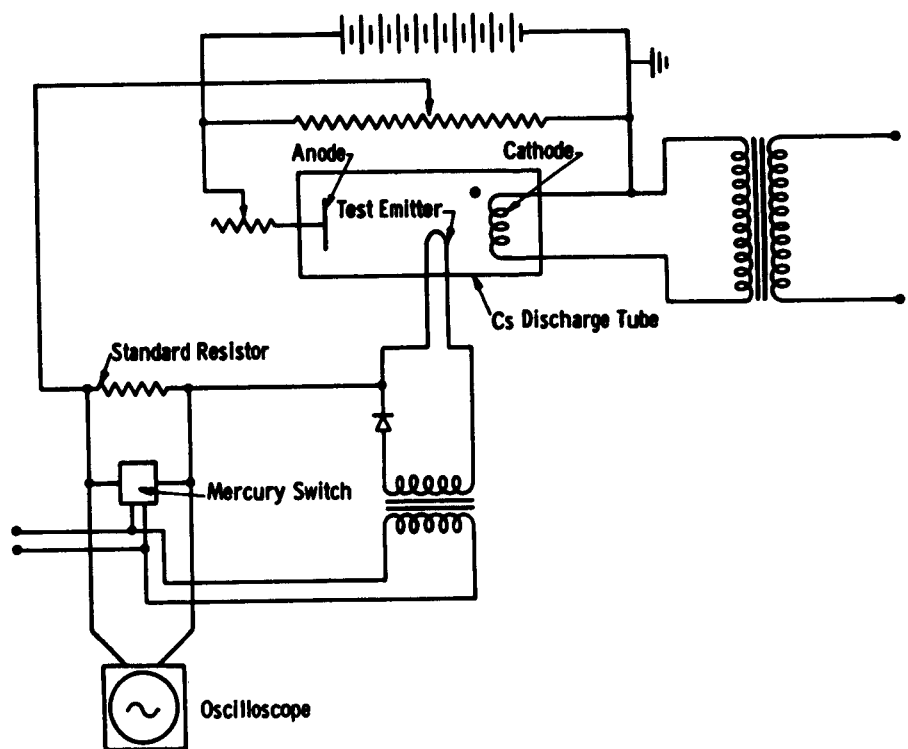


Fig. 2-2 - Measuring Circuit

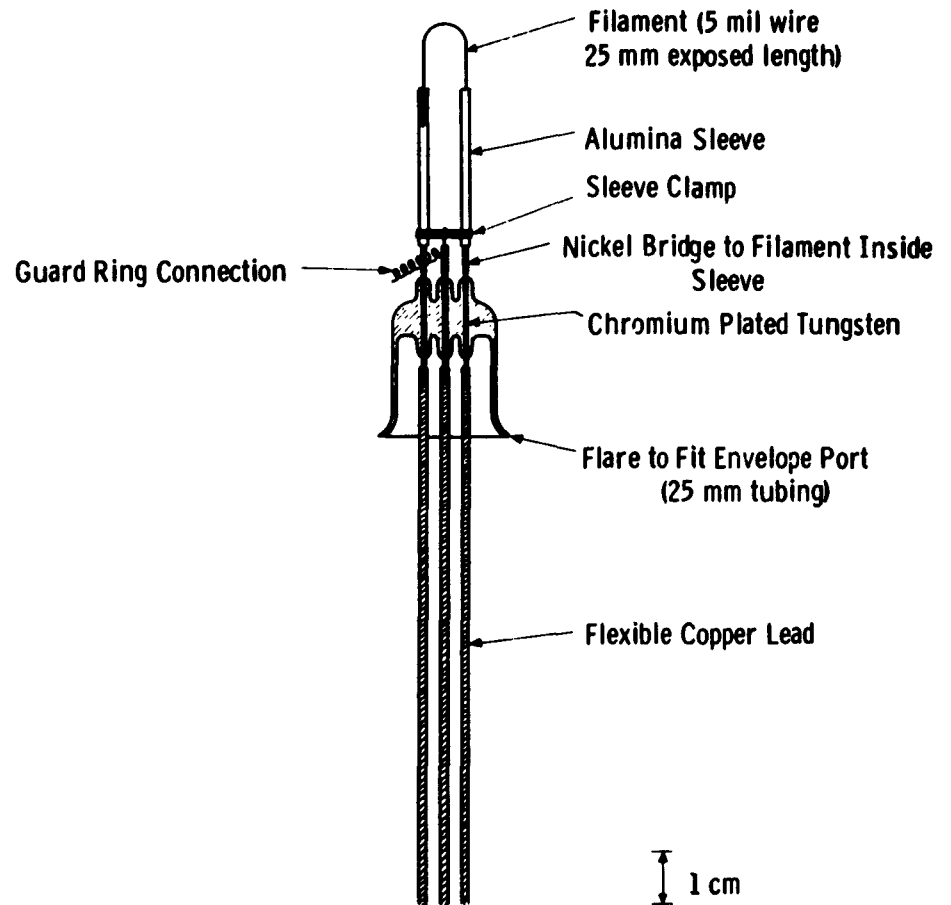


Fig. 2-3 - Mounting Detail of test emitter

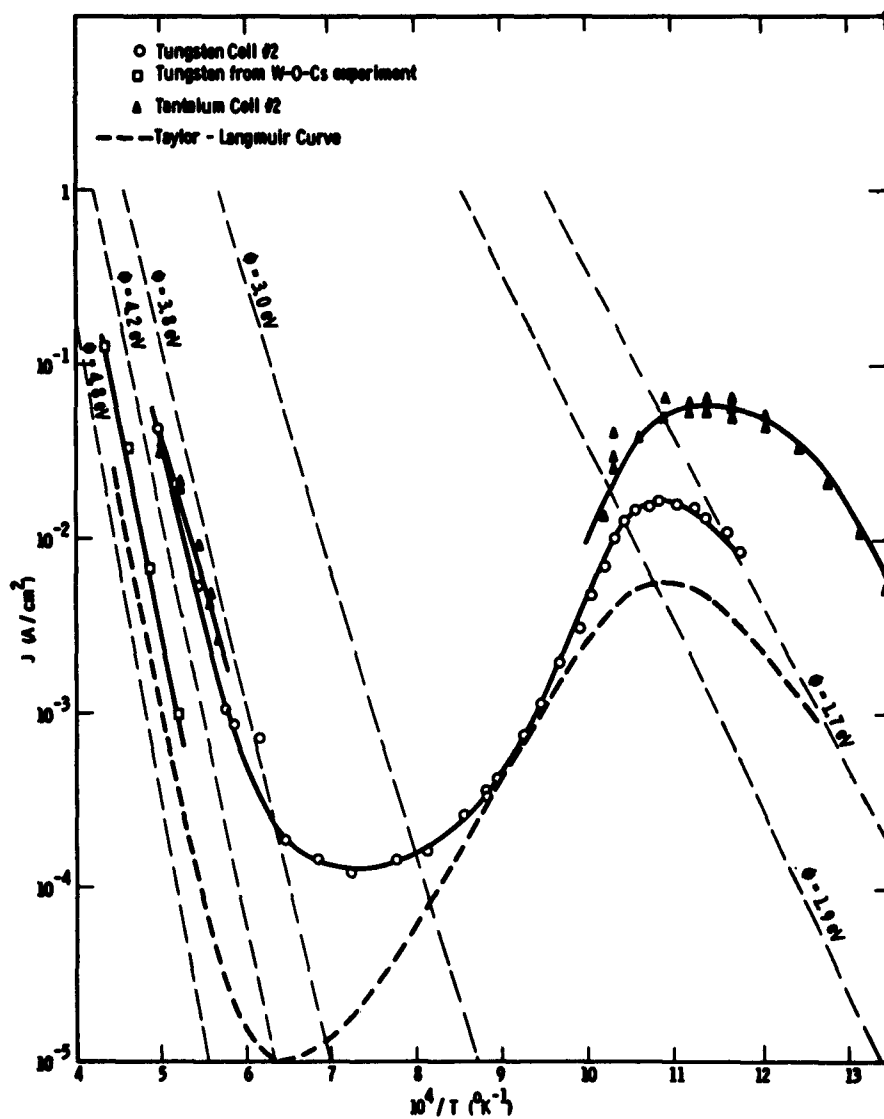


Fig. 2-4 - S-Curve characteristics of tungsten and tantalum
for $T_{Cs} = 373^\circ\text{K}$ ($P_{Cs} = 5 \times 10^{-4}$ torr).

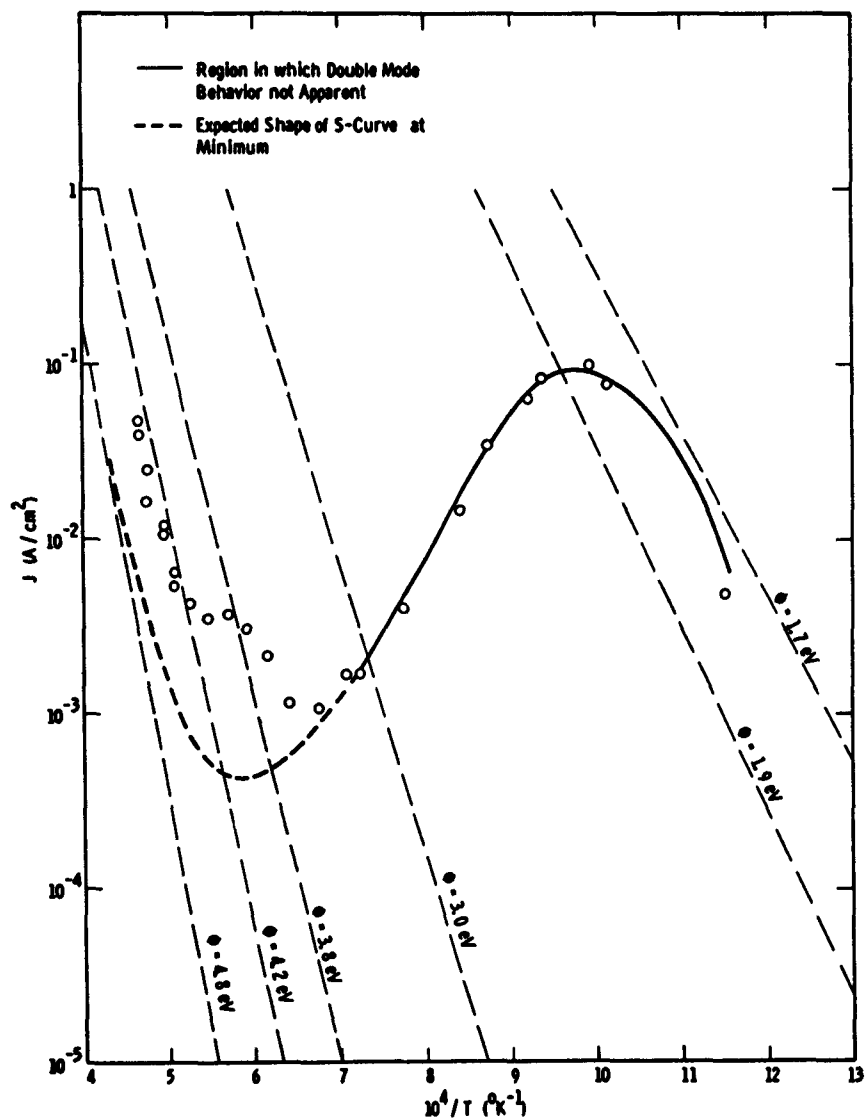
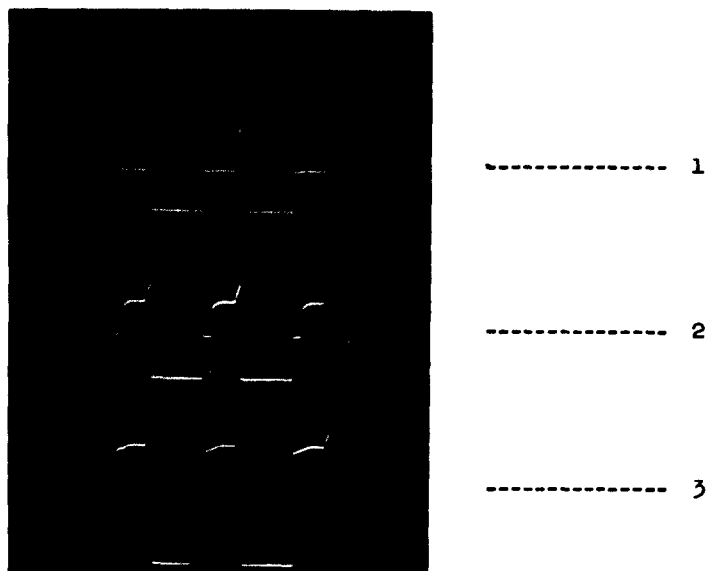


Fig. 2-5 - S-Curve characteristics of rhenium for
 $T_{Cs} = 398^\circ\text{K}$ ($P_{Cs} = 2.3 \times 10^{-5}$ torr).



1. Low Current Emission Mode. Emission Density $1.06 \times 10^{-1} \text{ A/cm}^2$
Positive Ion Current Density $1.25 \times 10^{-3} \text{ A/cm}^2$
2. Simultaneous Appearance of Both Modes
Low Mode Emission Density $1.11 \times 10^{-1} \text{ A/cm}^2$
High Mode Emission Density $2.06 \times 10^{-1} \text{ A/cm}^2$
Positive Ion Current Density $1.38 \times 10^{-3} \text{ A/cm}^2$
3. High Current Emission Mode. Emission Density $2.88 \times 10^{-1} \text{ A/cm}^2$
Positive Ion Current Density $1.50 \times 10^{-3} \text{ A/cm}^2$

Fig. 2-6 - Thermionic emission switched from low current to high current mode with rhenium at 1750°K and $T_{\text{Cs}} = 462^\circ\text{K}$ ($P_{\text{Cs}} = 5 \times 10^{-2} \text{ torr}$).

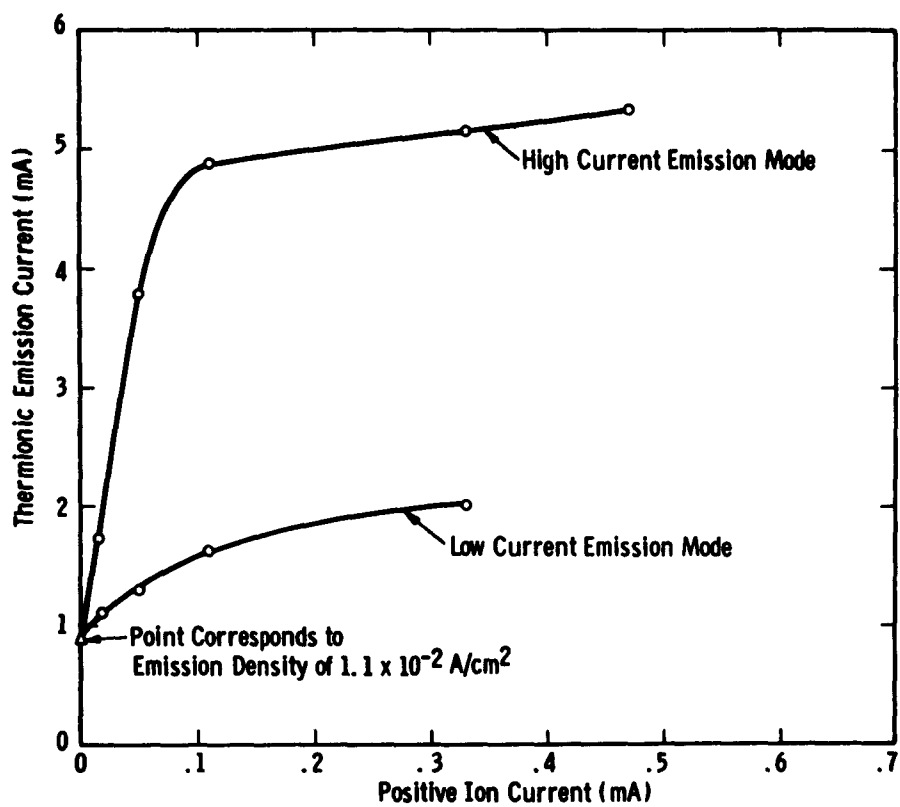


Fig.2-7 Extrapolation of double-mode behavior to zero positive ion current arrival at test emitter for rhodium at 2160°K and $T_{Cs} = 398^\circ\text{K}$

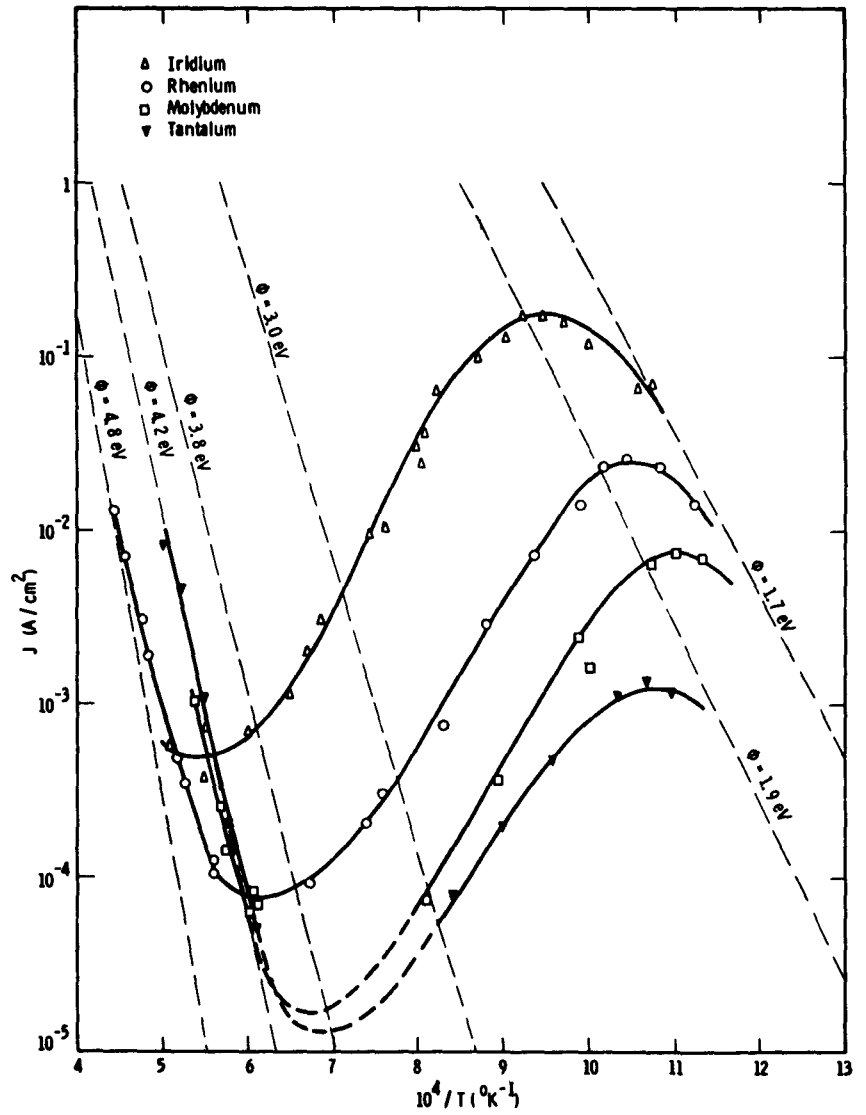


Fig. 2-8 - S-Curve characteristics for $T_{Cs} = 373^\circ\text{K}$
 $(P_{Cs} = 5 \times 10^{-4} \text{ torr})$.

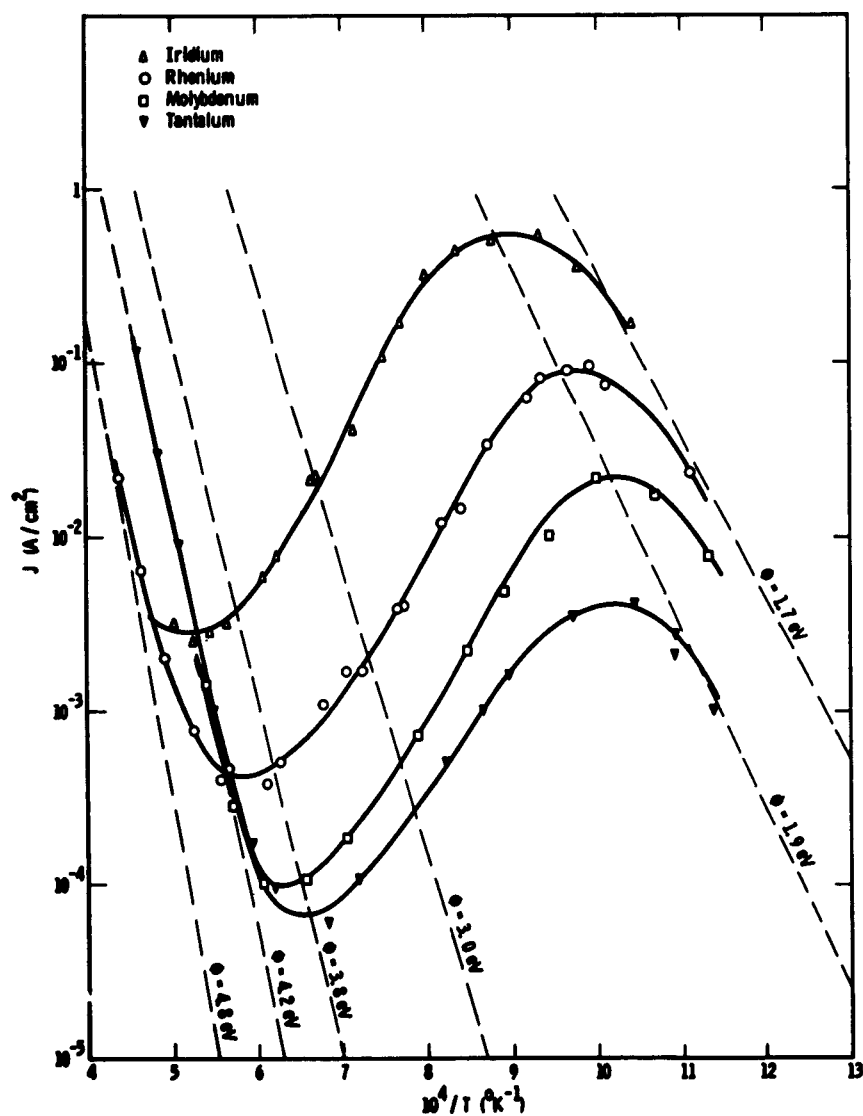


Fig. 2-9 - S-Curve characteristics for $T_{Cs} = 398^\circ K$
 $(P_{Cs} = 2.5 \times 10^{-5} \text{ torr})$.

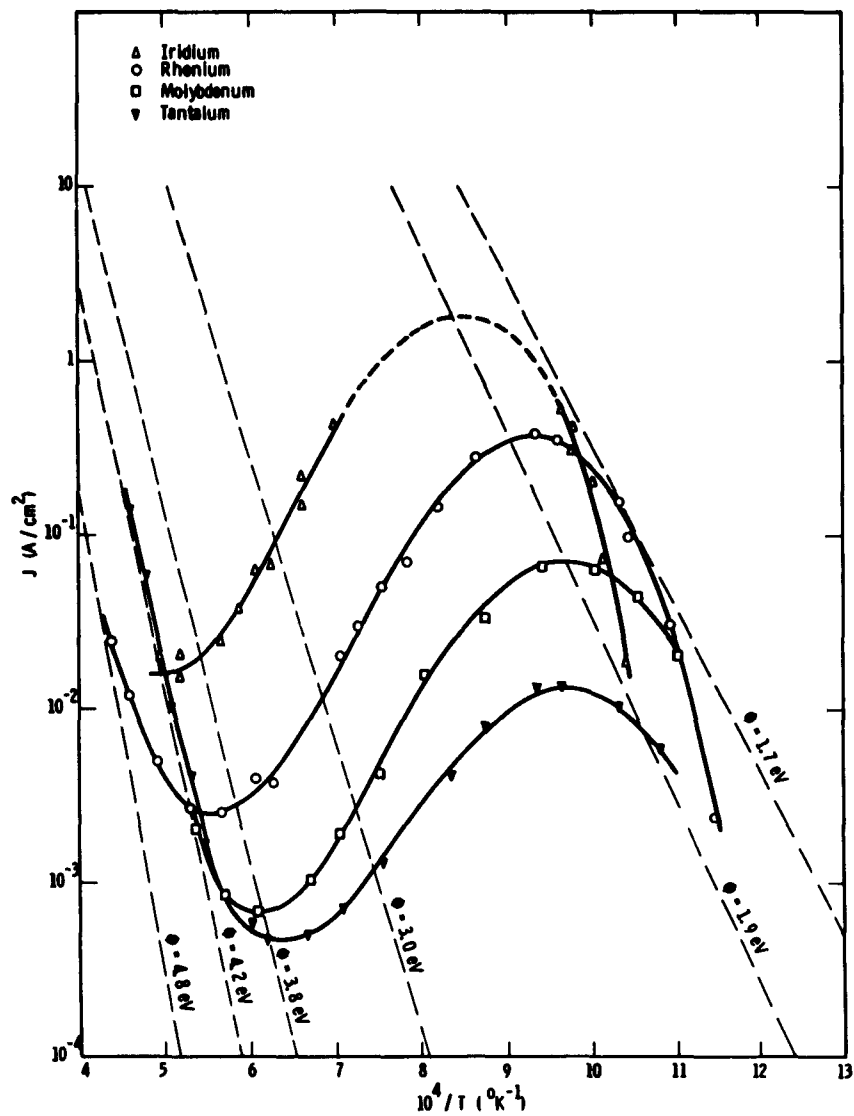


Fig. 2-10 - S-Curve characteristics for $T_{Cs} = 423^\circ\text{K}$
 $(P_{Cs} = 9 \times 10^{-3} \text{ torr})$.

CHAPTER THREE

EVAPORATION OF MOLYBDENUM IN THE
PRESENCE OF CESIUM VAPOR

The use of refractory metals as cathodes for thermionic energy converters is well established.⁽¹⁾ In this use the metals are operating at temperatures high enough that the vapor pressure and the concomitant evaporative loss are a serious problem. A straightforward calculation of evaporative loss in a thermionic converter cannot be made in most cases because of the presence of cesium vapor.

A number of metals and alloys have been proposed for possible use in a thermionic converter. In order of increasing vapor pressure, the most important metals are W, Re, Ta, Nb, and Mo. The data of Edwards, Johnston, and Blackburn⁽²⁾ for the evaporation of Mo are shown in Figure 3-1. An additional measurement⁽³⁾ was made to confirm the extrapolation to lower temperatures of their data.

From the classical kinetic theory of gases⁽⁴⁾ the relationship of evaporative loss R_V to vapor pressure can be expressed in several equivalent ways:

$$R_V = \frac{1}{4} \rho V = P_V \sqrt{\frac{m}{2\pi KT}} \quad (1)$$

where $\rho = \frac{mP}{KT}$ and $V = \sqrt{\frac{8KT}{\pi m}}$ are the density of the saturated vapor and the average velocity of the evaporating atoms (of mass m and temperature T). K is Boltzmann's constant and P_V is the vapor pressure. This equation holds true only for the case where evaporation takes place into an infinite empty space.

When evaporative loss occurs into a surrounding pressure or into a finite container, the relationship of vapor pressure and evaporation rate cannot be so easily calculated. Fonda^(5,6) treated the case of tungsten evaporating into various inert atmospheres and concluded that the effect is to reduce evaporative loss by introducing a diffusion barrier. For the case of evaporation from a cylindrical wire, the rate of loss R could be expressed as

$$R = \frac{C \Delta p}{rp \log \left(1 + \frac{d}{r}\right)} \quad (2)$$

where C is a constant, Δp is the difference in concentration between the evaporating surface and the outer surface of the diffusion barrier, r is the diameter of the wire, p is the pressure of the inert gas and d is the thickness of the barrier. For the plane parallel geometry used for our measurements this becomes

$$R = \frac{C \Delta p}{pd} \quad (3)$$

This equation can also be derived from classical kinetic theory⁽³⁾. In a very general form it can be expressed as

$$R = R_V \left(\frac{4Dp}{V_1}\right) \left(\frac{\Delta p}{p_1}\right) \left(\frac{1}{pd}\right) \quad (4)$$

where D is the diffusion constant, and the subscript 1 refers to quantities evaluated for the evaporating substance at the evaporating

temperature. The quantity $\Delta \rho / \rho_1$ is equal to 1 if the saturated vapor is present at the evaporating surface and the pressure of the evaporating material is zero at the outside surface of the diffusion barrier. Utilizing almost any model of gas-metal atom interaction results in the quantity Dp as constant with change in pressure. Thus, the transport ratio, defined as R_V/R , is directly proportional to pd .

$$\frac{R_V}{R} = a \, pd \quad (5)$$

where a is a constant, the reduction coefficient.

This equation will yield absurd answers for sufficiently small values of pd . This difficulty is avoided by considering the transition from the classical dilute gas treated here to the Knudsen gas, wherein the mean free path is larger than the dimensions of the apparatus.

If this correction is made, equation 5 becomes

$$\frac{R_V}{R} = \beta + a \, pd \simeq 1 + a \, pd \quad (6)$$

where β is a slowly varying parameter whose value is near unity. Both equations 5 and 6 will fit the data presented in this report.

Another effect also changes the evaporative loss from a metal surface. A small amount of surface contamination can be shown to increase or decrease the evaporation rate significantly.⁽⁷⁾ In a thermionic converter the evaporating surface is deliberately contam-

inated with a partial layer of adsorbed cesium, usually for work function modification and/or space charge neutralization. There are several effects which could result in changes in evaporation rate. Fortunately, all of them (in the first approximation) lead to the same form of equation. If θ is the fractional coverage and b is a slowly varying parameter, then

$$R = (1 + b\theta) R_V \quad (7)$$

The simplest assumption is that the metal cannot evaporate through the cesium layer. In this case $b = -1$. A second possibility is that the metal and the cesium react to form a pseudo-compound which then evaporates. $b\theta$ would then be the first term in the series expansion of $e^{-\frac{\Delta F(\theta)}{KT}}$ where $\Delta F(\theta)$ is the change in free energy of vaporization. The same argument would hold if assumptions as to changes in bonding energy because of coverage are made. In this report we have assumed $b = -1$, and have worked only at one value of θ . Further work is necessary to clarify this problem.

The basic equation assumed to hold in this investigation was

$$R = R_V \frac{1 - \theta}{1 + \theta} \quad (8)$$

Only one experimentally determined constant is present in this equation.

In order to determine the magnitude of the effect of cesium on evaporation rate, a series of experiments were performed utilizing the apparatus shown schematically in Figure 3-2.

A molybdenum ribbon filament, 0.2 cm wide and 0.025 cm thick, was heated by passing a current through it. Four nickel collectors (of 0.2 cm² area) were spaced at different distances from this evaporative source. After holding the filament at temperature while a cesium atmosphere was present, the amount of molybdenum deposited on the nickel collectors was determined by a spectrographic technique. The total analysis had a sensitivity of about 1 microgram of molybdenum and a precision of about 15 percent.

The pressure of cesium was maintained at the desired level by placing the entire apparatus within a constant temperature oven. The pressure was calculated from this temperature using Nottingham's equation.⁽⁸⁾

The temperature of the filament was measured at a number of positions by means of an optical pyrometer which had been calibrated against a standard lamp. Corrections were made for the emissivity of molybdenum and for the measured transmittance of the Pyrex envelope. No corrections were made for either the possible absorption of light by cesium vapor (1 inch path) or the possible changes in emissivity due to the fractional cesium coverage.

Spacings were measured with a cathetometer after operating temperature was reached. While the accuracy of measurement was about 1 micron, the spacings did not remain constant during experimental runs. The spacings reported are time averaged, and variations of as much as 25 percent were not unusual.

End effects caused by the finite size of the filaments and collectors were estimated by considering the solid angle covered by the evaporating filament. This is only a first approximation to the true case, because of the fact that the mean free path was smaller than the spacing. The correcting relationship used was

$$R_{\text{corr}} = R_{\text{meas}} \cdot \pi L / (2L \tan^{-1}(L/d) - d \log \left[1 + \left(\frac{L}{d} \right)^2 \right]) \quad (9)$$

where L was the width of the evaporating filament.

The results obtained using the apparatus of Figure 3-2 are summarized in Table I. It is clear that a large reduction in evaporative transfer has taken place. The deposition of molybdenum on the nickel collectors was quite uniform, with no whiskers or similar phenomena detected. In Figure 3-3, the transport ratio R_v/R has been plotted as a function of the product of cesium pressure and spacing. The resulting straight-line relationship is in accordance with theoretical prediction: The average value of the reduction coefficient is $0.074 \text{ (mm of Hg - microns)}^{-1}$ or 0.56 cm/dyne . If the effect of the 15 percent coverage is considered as blockage then the reduction coefficient becomes 0.44 cm/dyne . This corresponds to a collision diameter of 12.7 \AA . (Strictly speaking, " a " should have been calculated for each test separately because of the difference in evaporating temperature. The variation expected from the temperature difference is only about 5 percent, however.)

Table I. Experimental Results of Molybdenum Transport Experiments

Run	1A	1B	1C	1D	2A	2B	2C	2D
Filament Temp., Corrected, °K	2,101	2,101	2,101	2,101	1,993	1,993	1,993	1,993
Time, Seconds	49,200	49,200	49,200	49,200	36,000	36,000	36,000	36,000
Oven Temperature, °K	552	522	522	522	519	519	519	519
Cesium Pressure, Mm Hg	1.0	1.0	1.0	1.0	0.38	0.38	0.38	0.38
Fractional Coverage, (Ref. 8)	0.15	0.15	0.15	0.15	0.16	0.16	0.16	0.16
Amount Evap'd, $\mu\text{g}/\text{cm}^2$	1,260	1,260	1,260	1,260	125	125	125	125
Vacuum, (Ref. 2) Q_V	95	60	31	13	15.1	10	<5	<5
Measured								
Corrected for Solid Angle	119	77.4	48.4	20.3	19.0	13.2	<7.3	<8.3
Corrected for Coverage, G	140	91	57	23.9	22.6	15.7	<8.7	<9.9
Transport Ratio, Q_V/G	9.0	13.8	22.1	52.7	5.5	7.9	>14.3	>12.6
Spacing, Microns	155	225	450	450	195	247	459	538
Reduc. Coefficient, ⁺ (mm Hg - microns) -1	0.052	0.058	0.047	0.115	0.061	0.073	>0.077	>0.062
Reduc. Coefficient, ⁺⁺ ^a	0.058	0.061	0.049	0.117	0.074	0.084	>0.082	>0.067

⁺ Equation 8

⁺⁺ Equation 5

Considering the relative crudity of the experimental techniques, the agreements between different tests was considered quite good. A value of the reduction coefficient was predicted using the Lennard-Jones (6-12) model and the value of 4.0 \AA^0 for the collision diameter. The experimental values were about 10 times this value. The possibility of systematic errors was then explored in some detail. A small amount of oxygen contamination would increase the cesium coverage to values perhaps as high as 0.5, which would cause an apparent increase in the reduction coefficient of about 40%. The absorption of light in the one inch cesium path could increase the true temperature, but this would lead to an underestimate of the reduction coefficient. Convective mass transfer caused by the vertical placement of the evaporating filament could not lead to a large enough loss of molybdenum, particularly since all loss would be equaled by gain from adjacent filament areas. An error in temperature measurement caused by emissivity variations on a cesium coated surface could change the vacuum evaporation rate, but this would also be apparent in the plot of transport ratio versus pressure-spacing (Figure 3-3).

The value of atomic diameter of cesium deduced by Gottlieb and Zollweg⁽⁹⁾ from thermal conductivity measurements was about 9.2 \AA^0 , in reasonable agreement with the 12.7 \AA^0 deduced in this work. The techniques used were very similar in both cases.

The values of transport ratio and reduction coefficient for a typical thermionic converter are given in Table II for 3 different

Table II. Values of Transport Ratio and Reduction Coefficient in a Typical Thermionic Converter

Distance of Closest Approach, σ_{12} in Angstroms	4.0	9.2	12.7
Transport Ratio, R_V/R	2.4	7.3	14.8
Reduction Coefficient, α in cm/dyne	0.084	0.44	0.85
in (mm Hg - micron) ⁻¹	0.011	0.058	0.11
Converter Conditions			
Cathode Temperature	2000°K		
Anode Temperature	1000°K		
Cesium Pressure	1 mm Hg		
Spacing	125 microns		

values of distance of closest approach, using the Lennard-Jones model. Clearly, the amount of material lost from an evaporating surface will be less than that expected from measurements made in vacuum. For the typical conditions of Table II, this reduction will amount to between 60 and 93 percent.

REFERENCES

1. "Materials for Direct Conversion", Proceedings of an AIME Conference of the Electronic Materials committee, presented in Los Angeles, August, 1961. (To be published).
2. J. W. Edwards, H. L. Johnston, and P. E. Blackburn, J. Am. Chem. Soc. 74, p. 1539 (1952).
3. Unpublished Research, L. S. Richardson
4. S. Dushman, "Scientific Foundations of Vacuum Technique", p. 39, Wiley, 1949.
5. G. R. Fonda, Phys. Rev., 21, p. 343 (1923).
6. G. R. Fonda, Phys. Rev., 31, p. 260 (1928).
7. R. C. Haverstraw and P. G. Shewmon, "The Evaporation Rate of Copper", presented at AIME fall meeting, Detroit, October, 1961. (To be published).
8. W. B. Nottingham, Tech. Rept. 373, Res. Lab. of Electronics, Mass. Inst. of Tech. (1960).
9. M. Gottlieb and R. J. Zollweg, "Thermal Conductivity of Cesium Vapor", Symposium on Thermionic Energy Conversion, May, 1962.

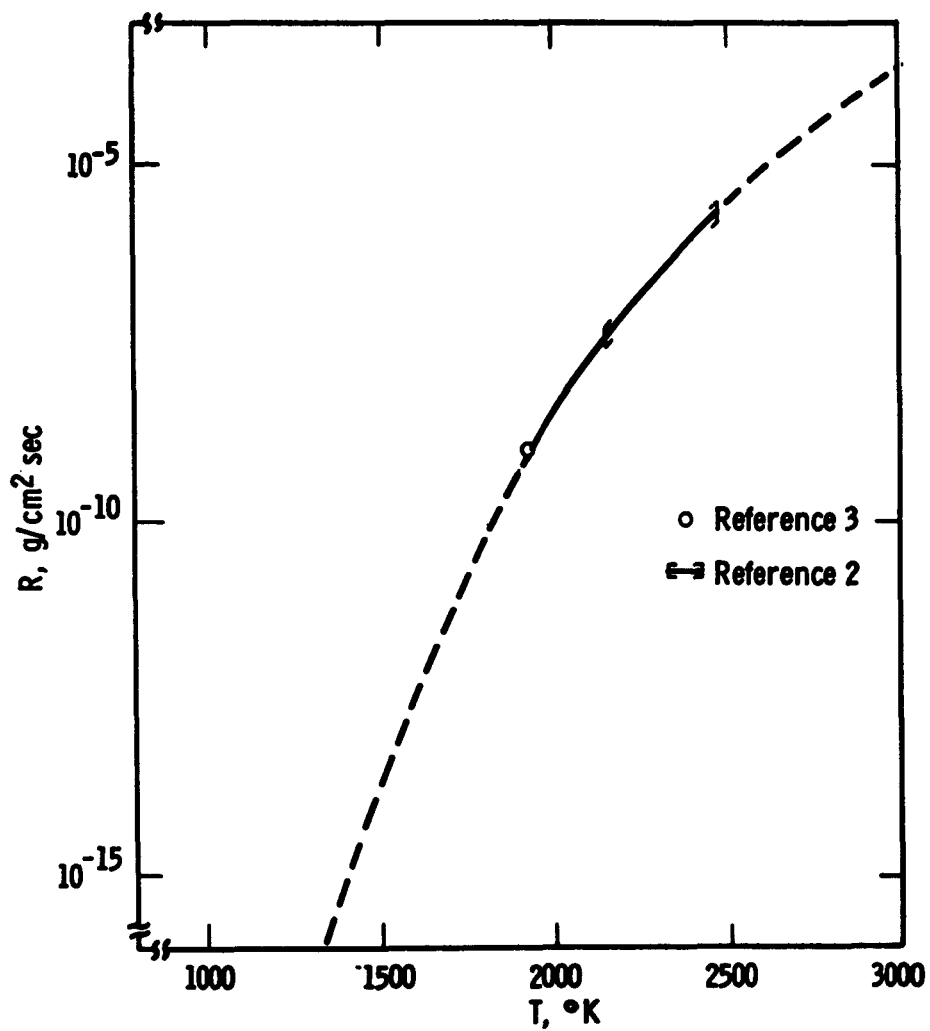


Fig. 3-1. Evaporation of Molybdenum as a Function of Temperature.

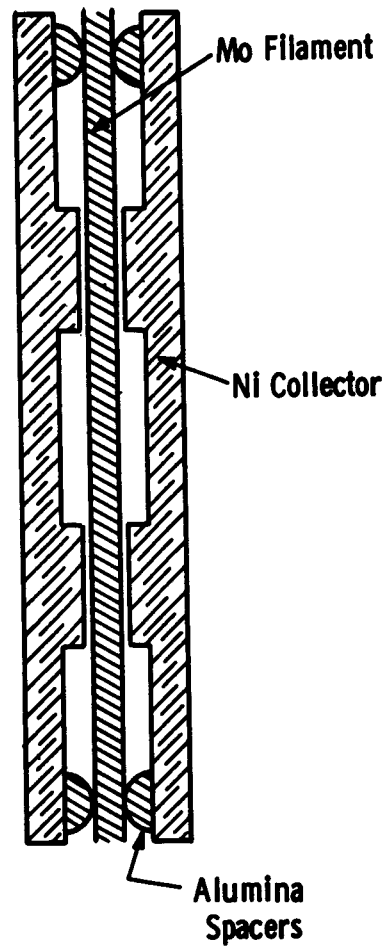


Fig. 3-2. Diagram of Experimental Cell

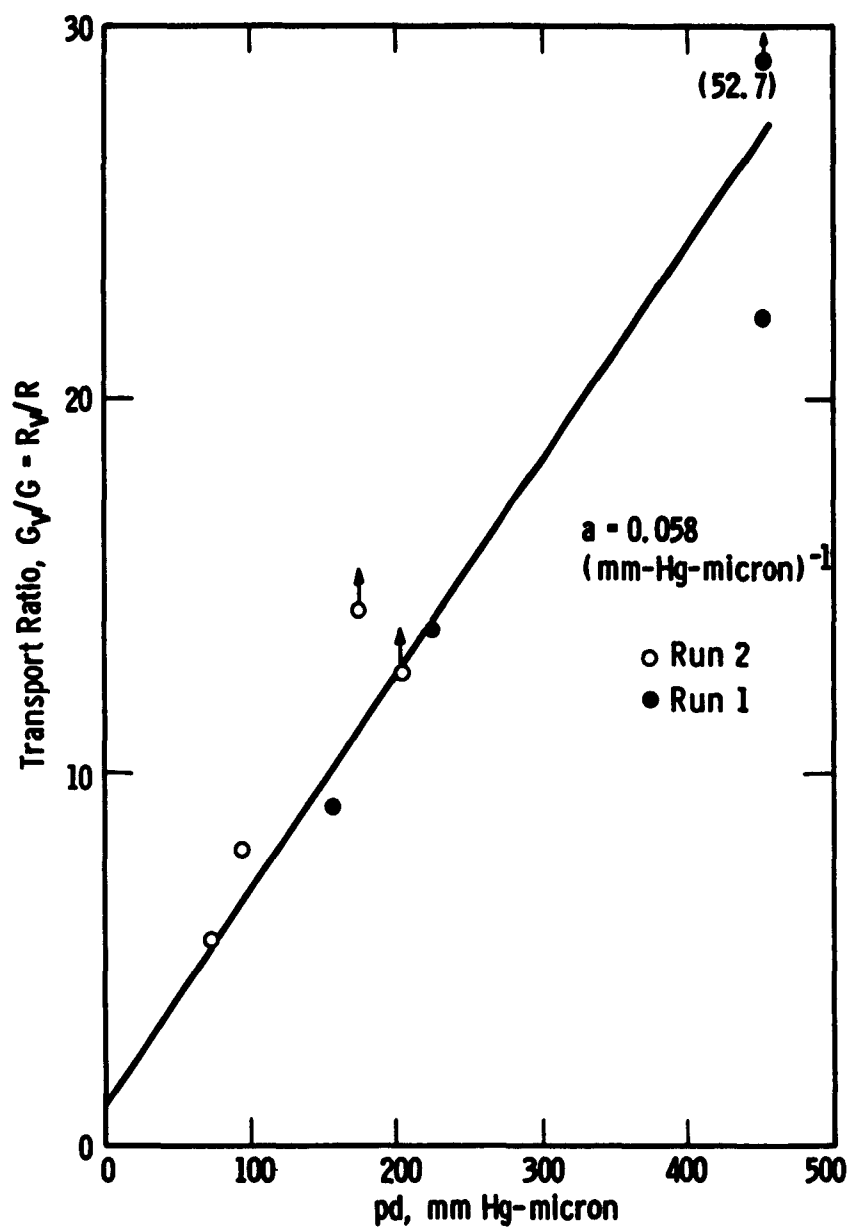


Fig. 3-3. Transport Ratio as a Function of Pressure X Spacing

CHAPTER FOUR

REFLECTION OF ELECTRONS FROM CESIUM COATED SURFACES

The collection of electrons of very low energy is important to the efficient conversion of heat to electrical energy in such devices as the thermionic energy converter and the magnetohydrodynamic generator. Thermionic converter diodes usually use cesium vapor to adjust the emitter and collector work functions and to furnish the positive ions to reduce space charge. MHD generators sometimes use gases "seeded" with alkali metals such as cesium to increase the electrical conductivity at lower gas temperatures.

In order to adequately understand the operation of these devices it is necessary to know quantitatively what fraction of the electrons incident on a cesium coated surface are accepted and what fraction reflected, especially in the thermal energy range, below about 0.2 eV where little experimental data is available for surfaces of any kind.

The current interest in energy conversion has also led to increased interest in the physical properties of cesium vapor. Since experimental tubes designed to measure these properties often collect electrons on cesium coated surfaces and the reflection of electrons may be of the order of 50%, it is useful to have more quantitative data to aid in interpretation of the experimental results.

Theoretical treatments¹ have concluded a low reflection coefficient tending to zero at low primary energies for certain clean metal

surfaces. While Fowler and Farnsworth² have found evidence to support these conclusions for clean metals, they and others³ have found reflection coefficients as high as 50 and 60% for gas covered surfaces. The residual gases ordinarily encountered in vacuum tubes either increase the work function or do not change it greatly, in contrast to Cs which reduces the work function appreciably. Since a monolayer of cesium usually reduces the work function of a metal by about 3 eV, this change in the potential energy of the electron near the surface may have a large effect on electron reflection. With polycrystalline surfaces strong patch fields may also be present giving rise to significant electron reflection. The experimental work described below was designed to obtain more quantitative information in these areas with special emphasis on very low primary electron energies.

Experimental Technique

The experimental tube utilized "monoenergetic" electrons obtained by the ac retarding potential difference technique⁴ with an orthicon-type deflection system.⁵ Figure 4-1 shows schematically the experimental tube, an improvement version of that of ref. 1. Electrons emitted by the filament at the left are accelerated by the next electrode. Those emerging through the circular aperture are retarded by the two dc retarding electrodes and by the center electrode which has a 0.05 v ac retarding potential superimposed upon the dc. This ac potential alternately transmits or reflects electrons in a narrow energy range of the electron distribution while allowing more energetic electrons to be transmitted.

The final electrode accelerates the electrons to the desired primary energy. The electron beam striking the target thus consists of a dc plus an ac component but only the ac component is detected.

An axial magnetic field of 120 gauss collimates the electron beam. Between the target and the collector for reflected electrons, two grids have been provided so that a small transverse dc electric field can be established such that the reflected electrons will be displaced perpendicular to both the electric and magnetic fields and thus be prevented from escaping back to the electron gun. The grids are shaped to minimize the introduction of transverse electron energy.⁶ The ac currents to the target (surface being studied) and to the two collectors for reflected electrons are measured by means of the ac voltage developed across the 1 megohm load resistors, amplified by the Textronic Type 122 preamplifier and White 216A amplifier, (both equipped with 37 cycle twin-T feedback networks), synchronously detected and measured with a dc millivoltmeter. The switch enables the same amplifying system in turn to measure the currents to the various electrodes. A conductive coating on the Pyrex envelope outside the grids collects stray electrons and prevents charging of the glass. All of the electrodes and grids are made of the alloy Advance to reduce the possibility of contact potential differences. Such difficulties persist, however, in the presence of cesium vapor when the parts are at different temperatures. Provision is made to adjust the potentials of the electrodes to compensate for such potential differences.

Figure 4-2 shows a photograph of the experimental tube before being mounted in the Pyrex envelope and evacuated. The electron gun is covered by the grounded shield at the left but the grids and target at the right are visible. In this tube several polycrystalline metals, (copper, molybdenum, stainless steel, monel, inconel, silver plate, tungsten, platinum, tantalum, and Advance) have been provided with an arrangement such that each can be manipulated in turn to the target position. There was no provision for heating the targets internally to provide thorough outgassing or to change the Cs coverage. The aim was to make a survey of several polycrystalline materials with approximately one monolayer coverage of cesium under the degree of cleanliness expected for a thermionic converter or an experimental tube without special efforts to clean the surface. It was found that the leakage resistance between metal leads in the glass press remained greater than 10^8 ohms for the low Cs pressures used so that 10^6 ohm load resistors could be used. Beam currents of about 10^{-9} amps were used.

The purpose of the second collector was to collect those electrons reflected at the target which were reflected for a second time at the main collector. Collector sizes were such that electrons reflected as many as 5 to 6 times were still incident on one of the collectors. To reduce electron reflection the two collectors had their surfaces coated with electrolytically deposited platinum black. Because these surfaces proved to have a very low reflection coefficient it was also possible to measure the longitudinal component of the energy of the reflected electrons.

The distribution of current between the target and collector electrodes as a function of the voltage between the two grids is shown in Figure 4-3 for a primary electron energy of 1 eV. For grid voltage between 10 and 28 volts the fractions of the total current collected at the three electrodes is independent of grid voltage. At higher grid voltage part, and finally all, of the incident beam misses the target and strikes the second collector. The small current to the second collector in the plateau region and the current to collector₁ at high grid voltage indicate that about 8% of the electrons striking the platinum black surfaces are reflected. The rise in target current near zero grid voltage occurs because some reflected electrons having lost part of their longitudinal component of energy in the reflection process are repelled by the retarding potential electrodes in the electron gun and hence return to the target a second time. The retarding potential measurements reported below show that the reflected electrons have a longitudinal energy distribution from zero to the primary electron energy. The knee of the target current curve comes at a lower grid voltage than that for the collector currents because with smaller deflection the reflected electrons strike the final accelerating electrode rather than collector₁. These results illustrate the significant error that results from using the magnetic collimation technique without the electron deflection region for electron reflection measurements.⁷ In this example, with this geometry by using the target current with zero grid voltage one would calculate a reflection coefficient of about 14% in contrast with the correctly measured value of 41%.

Curves similar to that of Figure 4-3 were also obtained for primary energies of 0.1 eV and 5 eV with the average potential between grids about +0.5 V. It was found convenient to vary the primary electron energy by changing the accelerating potential E_k . To cover the entire energy range three values of grid voltage were used. Taking the data in this way means that the primary beam moves somewhat over the target surface and the results are thus an average for the surface. The results with different grid voltages joined smoothly except in a few cases where jumps of 1 to 2% in the reflection coefficient resulted.

The energy spread of the ac component of the electron beam leaving the gun could not be usefully investigated by retarding at the main collector for reflected electrons. This was because field penetration made the potential in the aperture differ from that of the collector surface, depending upon potential difference between the collector and the nearby accelerating electrode.⁸ Indeed, a smaller indicated energy spread of the primary beam was obtained from measurements of target current vs. target potential than from target current vs. collector potential. Primary energy was varied by changing the accelerating potential E_k keeping the target about 1 volt negative and the collectors about 1 volt positive with respect to the final accelerating electrode. Thus information obtained about the spread of electron energy of the incident beam is coupled with the experimental results and discussion of it is deferred to the next section.

Experimental Results

Figure 4-4 shows on a greatly expanded scale the measured target current and reflection coefficient near zero primary energy for the Advance - Cs target with a work function of about 3.14 eV. The reflection coefficient is defined as the current to the two collectors divided by the sum of the target current plus collector currents. The rapid decrease in target current and increase in reflection coefficient at the left occurs when most of the incident electrons are reflected in front of the target because they have insufficient energy to reach the target surface. The fact that the change occurs over a finite energy range is because of the energy spread in the incident beam. The sharp break that occurs at +.02 volts suggests that the number of slower electrons is negligible and that the reflection coefficient measured there is close to the correct one. This cannot be definitely established, however, because if, for example, 10% of the incident electrons were of such low energy that they would all be reflected, then a true reflection coefficient of zero at +0.2 volts would give the measured results. The measurement of +0.02 volts really includes electrons from +.02 to +.12 volts, but because the number decreases so rapidly with increasing energy and the reflection changes relatively slowly the measurement is probably only slightly too high.

We shall now consider the energy spread expected for the experimental tube under ideal conditions--assuming uniform work function emitter, target and retarding potential electrodes and uniform potential across the apertures in the retarding potential electrodes. The ac

retarding potential electrode then alternately passes or rejects electrons with longitudinal energy in a narrow band because of the 0.05 V square wave retarding signal. Then as the target potential is made more negative and becomes retarding the ac target current will decrease exponentially, assuming the electrons have a Boltzmann energy distribution. This decrease should correspond to an emitter temperature of about 1500°K but should be limited to a 0.05 V range beyond which the decrease should be even faster.

Figure 4-5 shows the experimentally measured ac current to the Advance-Cs target plotted on a semilog plot. The expected exponential decrease is observed but the decrease is somewhat faster and occurs over a longer range of voltage than expected, because of a departure from ideal conditions. It was noted that the measured energy spread was less when the initial accelerating voltage E_2 was reduced from 6 volts to about 1.5 volts. At the higher voltage the target current decreased initially at about the same rate but currents about 10% of incident beam persisted to larger retarding voltages.

The observed spread is made up of two components, the energy spread of the initial beam and nonuniformity of the target work function. Actual stopping of the primary electrons in front of the target could lead to a small space charge region which would change the observed spread. It was experimentally verified that this was not the case by measuring the target current vs. target potential for dc beam currents of 2.5×10^{-10} amps, 5×10^{-9} amps and the normally used 1×10^{-9} amps. The results were identical within experimental error. The results with Advance-Cs ($\phi = 3.14$ eV) showed the sharpest change with a few surfaces

showing considerably greater spread. We assume that most of the spread observed in Figures 3 and 4 is that of the primary beam but the greater spread with other targets was introduced by patches of differing work function on the target.

The target work function could be determined from the target current plots in Figures 4-4 and 4-5. The intercept of the two straight lines on the semilog plot could usually be determined to a precision of 0.002 volts. This value combined with any target battery voltage E_T and the assumed work function of the tungsten emitter 4.53 eV allowed a measurement of the work function that is probably correct to within 0.2 eV absolutely with relative accuracy within 0.05 eV. The retarding potential E_3 was always adjusted for a maximum ac target current ($\pm .02$ V) hence the minimum retarding potential at the target would correspond to the potential just outside the tungsten emitter. Even when cesium vapor was present the emitter temperature was sufficiently high that its work function would not be altered by Cs adsorption. The filament was sufficiently distant from the cesium source that at the very slow diffusion rates of cesium vapor at room temperature, the nearby cold retarding potential electrodes did not become cesium coated for several days. Emission data from the tungsten ribbon was obtained using a magnetic field to define the surface area and measuring the current at the target at various filament temperatures. From the slope of a Richardson plot a work function of 4.16 eV with $A = 2.25$ was obtained. Adjusting to $A = 120$ gives $\phi = 4.30$ eV. Using the known area and assuming $A = 120$ a work function of 4.65 eV was obtained at 1500°K.

Although these data were not entirely satisfactory, they do bracket the accepted value and give the limit to the absolute accuracy of the work function determinations of the target surfaces.

Determination of an intercept on the semilog plot was almost always very precise but this emphasizes the low work function areas on the target in the event of nonuniformity. Another value could be obtained by the intersection of two straight lines at the knee of the linear plot of target current vs. voltage in Figure 4-3. This, of course, is more sensitive to the high work function patches. For the present example the difference in these values was only 0.006 eV while in other cases it was as much as an order of magnitude greater. This difference is taken to be some measure of the patchiness of the target surface. In view of the large changes in work function which occur because of cesium adsorption, the relative freedom from patch effect is striking.

The determination of the target work function as discussed above also determines the point of zero primary electron energy.

On logical grounds one might question this procedure since the values obtained depend upon the acceptance or reflection of electrons at the target--the precise properties that are being measured. If the reflection coefficient of the target material were 100% for primary electron energy below +X volts then the primary energy zero as determined here would really be +X volts instead of zero. This possibility, however, seems to be very remote. Even if the incident electron energy and momentum were such that 100% reflection should occur for certain directions at certain crystal faces, the angular spread in momentum of

the incident beam, the polycrystalline nature of the targets and the probability of momentum changing collisions at the surface make it unreasonable to expect reflection coefficients approaching 100% for incident energies greater than zero. 100% reflection of electrons incident upon the surface from the outside would also imply 100% reflection of electrons incident from within, hence no thermionic or photoelectric emission. Thus the zero of primary energy determined here corresponds to the threshold for electron emission at least to within about 0.1 eV.

The possibility of a dependence of the reflection coefficient on magnetic field was considered. Spot checks near minimum reflection were made for several of the targets with the magnetic field adjusted to one half and twice its usual value of 120 gauss. The reflection coefficients obtained were within 1%, approximately the experimental error of the measurements. Since the diameters of the electron helical paths depend upon magnetic field, results obtained with different field strengths will differently average any patch structure on the surface. Thus these results indicate that any prominent patch structure on the surface is smaller than the diameter of the helical path of an electron with transverse energy of about 0.1 eV and a magnetic field of 60 to 240 gauss.

The measured reflection coefficient for several target materials with differing amounts of cesium coverage are shown in Figures 4-6 to 4-40. These include curves showing the measured reflection coefficient over the entire range covered, up to primary electron

energies of 5 eV, as well as plots of the target current and reflection coefficient near zero primary energy on a greatly expanded scale. All of these materials had been mechanically polished and had been subjected to bakeout temperatures up to 350°C while being evacuated but not to further rigorous heating. Measurements were made on Advance and molybdenum targets with 3 degrees of Cs coverage and with one or two degrees of coverage for the other target surfaces. With increasing cesium coverage (lower work function) there is observed a small increase in reflection coefficient yet all the curves are qualitatively similar in shape. A summary of the experimental data is given in Table I. The low work functions given here were obtained from semilog plots of target current vs. the voltage E_1 as discussed above and $\Delta \phi$ gives the difference between this value and that obtained on a linear plot. This gives some measure of the variations in work function of the target surfaces. For the molybdenum target the variation observed was considerably greater than for most of the other targets and the knee on the linear plot was relatively poorly defined. The reflection coefficient for electrons incident on chemically deposited platinum black was measured by applying sufficient grid voltage that the primary beam missed the target proper and struck the second collector. The reflection coefficient given here was calculated as the ratio of the current to the main collector to the sum of the currents to the main and second collectors. If we had plotted the ratio of the main collector current to the second collector current (appropriate for identical surfaces with identical incident energy and reflection

TABLE I. SUMMARY OF MEASURED REFLECTION COEFFICIENTS FOR SEVERAL TARGET MATERIALS
AT VARIOUS DEGREES OF CESIUM COVERAGE:

Target Materials	Low Work Function	$\Delta \phi$ (High v.f. -Low v.f.)	.05	.1	.5	Measured Reflection Coef. - % at Various Primary Energies				
						1	2	3	4	5
Advance	3.14 2.02 1.59 1.50 1.59 1.55	0.006 .025 .016 .007 .008 .005	11.5 19.5 18.3 16.3 16.0 16.4	14.0 19.0 19.3 18.6 18.8 18.7	30.0 33.0 33.5 34.8 35.5 35.5	39.0 43.0 43.3 43.8 45.3 45.2	45.0 49.9 51.3 51.2 52.8 52.0	48.2 53.5 55.7 55.8 57.0 55.7	50.7 56.2 59.4 60.2 60.7 59.1	52.0 57.3 60.5 64.4 64.5 62.5
#301 Stainless Steel										
Inconel										
Monel										
Molybdenum	3.48 2.94	.042 .044-x .10 .097 .043-x	12.7 --- --- --- 20.0 12.1	11.4 19.8 28.9 13.8 20.5 14.5	16.5 26.6 30.2 27.7 30.2 32.8	31.5 34 41.0 39.5 37.2 42.6	43.3 46.3 50.3 48.8 53.2 53.0	52.9 55.0 57.8 55.1 62.1 60.6	58.0 58.6 63.7 59.3 68.5 64.8	58.2 58.2 65.7 60.3 72.8 67.0
Tungsten	1.68 3.56 1.53 1.57	.038 .015 .020	---	---	---	---	---	---	---	---
Tantalum										
7/27 Copper	3.71 3.68 1.63	.034 .043 .014	---	---	---	---	---	---	---	---
8/2 Copper										
Silver Plate	3.15 1.44	.011 .015	9.7 18.4	12.0 20.8	27.4 38.0	36.5 47.0	44.4 54.9	47.9 58.6	49.8 62.0	50.3 65.4
Platinum	1.63	.006	12.0	12.5	20.7	28.8	41.1	48.3	53.2	57.4
Platinum Black	1.76	.034	6.0	5.8	6.9	8.1	8.0	7.4	6.7	6.1

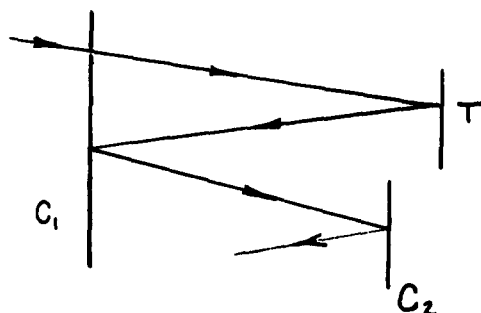
x very poor knee

coefficients) then the reflection coefficient would have been 0.3% to 0.7% higher. The reflection coefficient for platinum black with less cesium coverage was approximately the same as that given here. These results for cesium coated surfaces show considerably greater electron reflection than the values quoted in the literature for clean metals. In the primary energy range below 5 eV the reflection coefficient for clean metals usually obtained is below about 2%.

Retarding Potential Measurements

The small electron reflection coefficient from the collector surfaces coated with platinum black made it possible to measure the longitudinal component of energy of the reflected electrons by retarding at the main collector surface. Because of field penetration of the aperture the potential of the main collector could be adjusted even to the energy of the incident electrons without altering the beam current. The longitudinal energy loss of the reflected electrons whether zero or 100% could be determined to an accuracy of about 1%.

It will be shown that the ratio of the current collected at the main collector C_1 to the sum of the currents to C_1 and C_2 for a given retarding potential E_{C_1} gives very nearly the fractional part of the reflected electrons with longitudinal energy greater than E_{C_1} . Referring to the sketch we let



T = Target

C_1 = Main Collector

C_2 = Auxiliary Collector

R = Reflection Coefficient of Target for the Particular
Primary Electron Energy

R' = Part of the Reflected Electrons with Sufficient
Longitudinal Energy to Reach the Surface C_1

R'' = Part of the Reflected Electrons with Insufficient Longi-
tudinal Energy to Reach the Surface C_1

r = Reflection Coefficient for the Platinum Blacks Surface
of C_1 and C_2 Which by Experiment Has Been Found to be
Relatively Independent of Primary Energy.

Then we have

$$R = R' + R''$$

and of the electrons initially incident on C_1 , $R'(1-r)$ are accepted initially while $R'r + R''$ are reflected. Taking into account additional reflections at C_2 and C_1 the total current collected at C_1 is

$$I_{C_1} = R' (1-r) (1 + r^2 + r^4 + \dots),$$

and

$$\frac{I_{C_1}}{I_{C_1} + I_{C_2}} = \frac{R'}{R' + R''} (1-r) (1 + r^2 + r^4 + \dots).$$

Since r has been found to be between .05 and .08 the last bracket in this equation is between 1.0025 and 1.0064 while $(1-r)$ may vary between 0.95 and 0.92. The results given below will show that the electrons striking C_1 and C_2 have a wide range of energy hence the small observed variation in r with energy is averaged over electron energy. The ratio

$$\frac{I_{C_1}}{I_{C_1} + I_{C_2}}$$

gives then the fraction of the reflected electrons with longitudinal energy greater than the retarding potential C_1 times $(1-r)$.

Figures 4-41 to 4-43 show the relative current collected by C_1 for various primary electron energies when the copper target has a small fractional Cs coverage and a work function of 3.70 eV. Figures 4-44 to 4-46 show similar data for a greater Cs coverage and work function of 1.63 eV. Note that for primary electron energy less than the work function the curves show a nearly linear decrease with increase in retarding potential. This shows that the longitudinal energy of the reflected electrons is equally likely to be any value between zero and the primary energy. In this low energy region one expects the primary electrons to be mostly elastically reflected as found by other investigators,^{9,10} (although not

for Cs coated surfaces). If one makes the assumption that all of the primaries are elastically reflected then these results are consistent with a model in which the primary electrons are either completely absorbed or reflected isotropically over the half plane. A cosine angular distribution of the elastically reflected primaries would yield retarding potential curves quite different from the experimental results.

At primary energies greater than the work function, a departure from the linear character is noted, especially for the lower work function target. These curves show a greater number of low longitudinal energy electrons which may be true secondaries and a relative decrease in part of the more energetic ones. However, the departure from a linear decrease is not great which suggests that elastic reflection is still dominant.

These results obtained with polycrystalline targets cannot distinguish whether the apparent isotropic distribution is obtained from each crystallite or whether the isotropic nature is only the consequence of averaging over several differently oriented crystallites in the target surface. Work in progress using single crystal tungsten targets should answer this question. Jonker¹¹ with 25 eV primary electrons incident on polycrystalline nickel has found an angular distribution for reflected primaries that approaches a cosine function for normal incidence in contrast to the present results. Evtuhov, Smith and Yaggy¹² have obtained normal energy distributions for electrons reflected from a molybdenum target which appear to have some cosine

character at low primary energy. They appear, however, to have confused the normal energy distribution expected for a cosine distribution with that to be expected for an isotropic distribution.

REFERENCES

1. C. Herring and M. H. Nichols, *Revs. Modern Phys.* 21, 185 (1949).
2. H. A. Fowler and H. E. Farnsworth, *Phys. Rev.* 111, 103 (1958).
3. P. Marmet and L. Kerwin, *Can. J. Phys.* 38, 787 (1960).
4. R. E. Fox, W. M. Hickam, D. J. Grove and T. Kjeldaas, Jr., *Rev. Sci. Instr.* 26, 1101 (1955).
5. V. Evtukov, G. F. Smith and L. S. Yaggy, *Rev. Sci. Instr.* 32, 1362 (1961).
6. P. K. Weimer and A. Rose, *Proc. Inst. Radio Engrs.* 35, 1273 (1947).
7. H. Shelton, *Phys. Rev.* 107, 1553 (1957).
8. The preliminary results quoted in ref. 1 are somewhat in error, especially at low energy because the field penetration was neglected there with the result that the collector was held slightly negative instead of at target potential as assumed.
9. H. P. Myers, *Proc. Roy. Soc. (London)* A215, 329 (1952).
10. A. R. Shulman and D. A. Ganichev, *Soviet Physics-Solid State* 4, 545 (1962); *Fizika Tverdogo Tela* 4, 745, (1962).
11. J.L.H. Jonker, *Philips Research Repts.* 6, 372 (1951).
12. V. Evtuhov, G. F. Smith and L. S. Yaggy, *J. Appl. Phys.* 32, 1362 (1961).

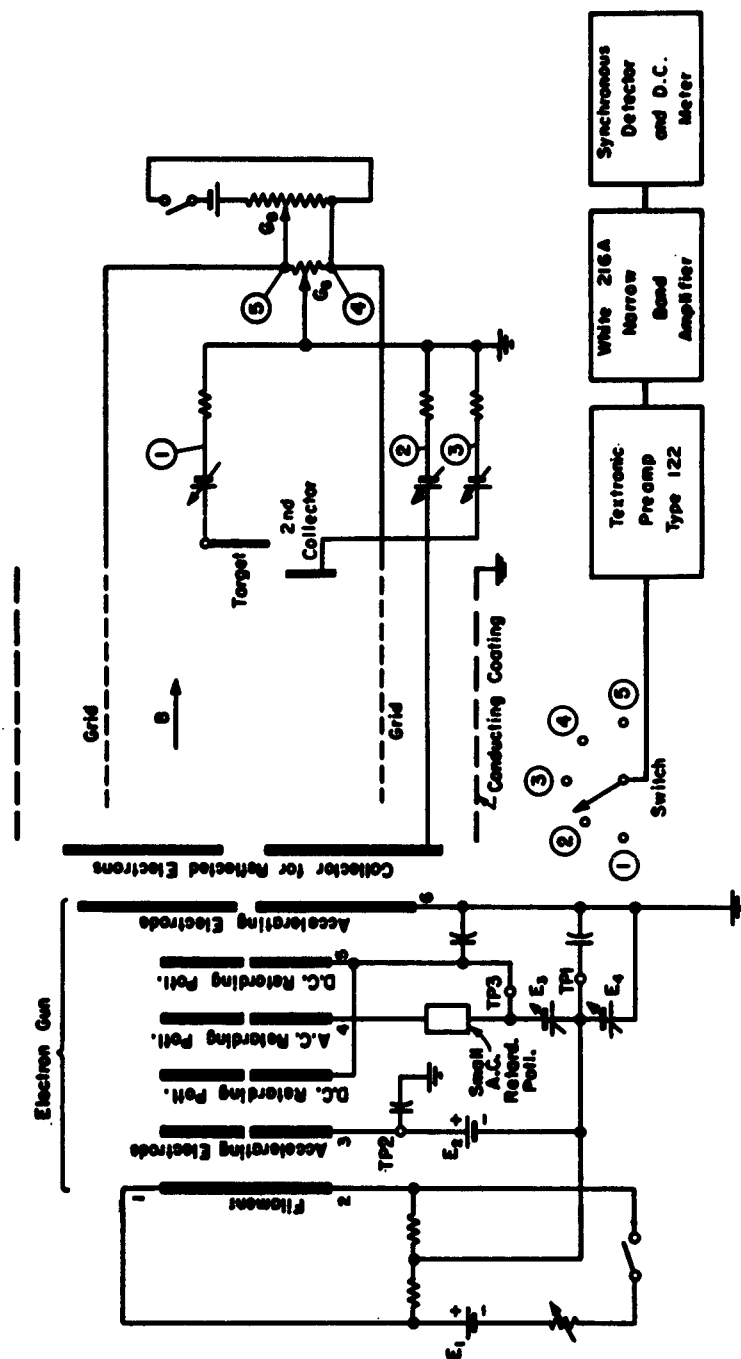


Fig. 4-1. Tube and circuit for electron reflection measurements



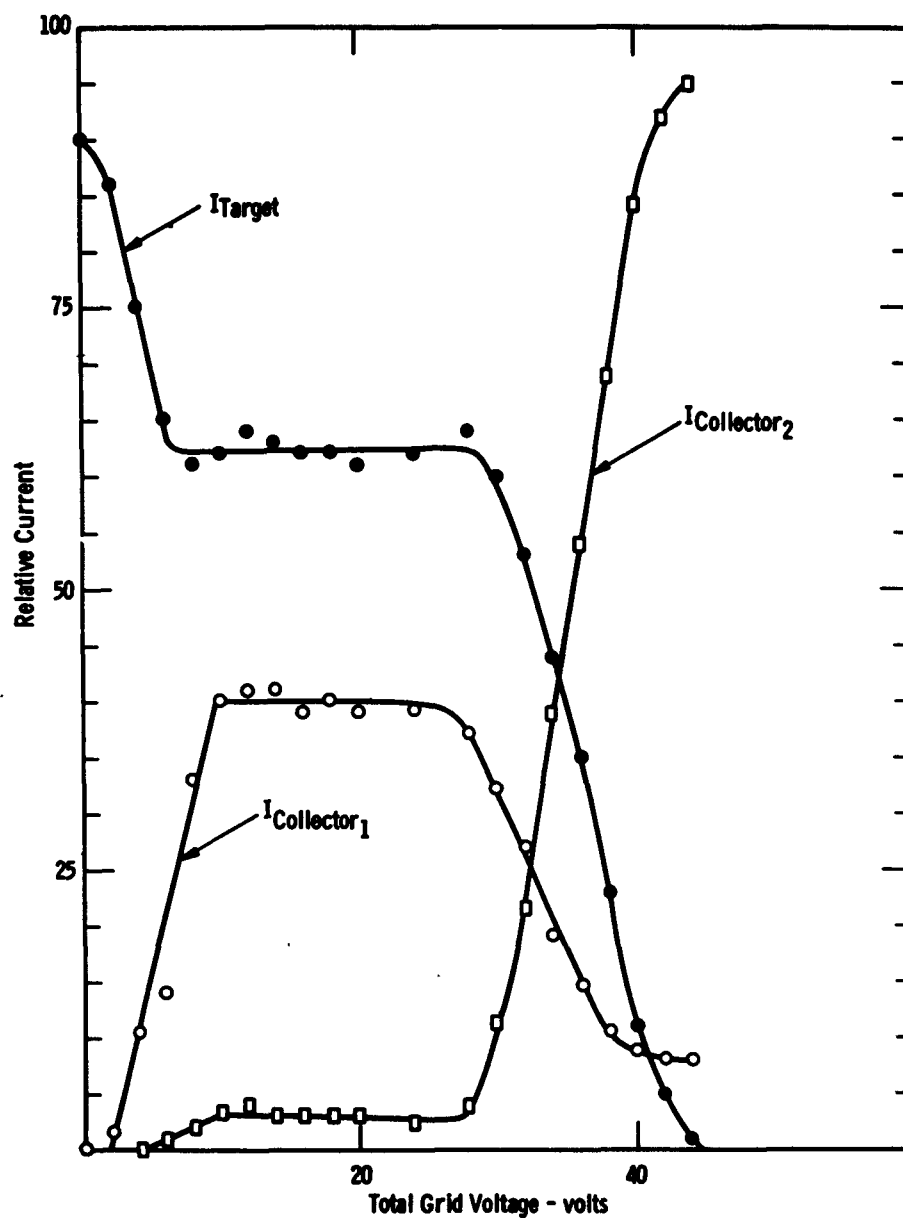


Fig. 4-3. Relative currents to the target and the two collector electrodes vs. deflecting grid voltage. Primary electron energy is 1.0 eV.

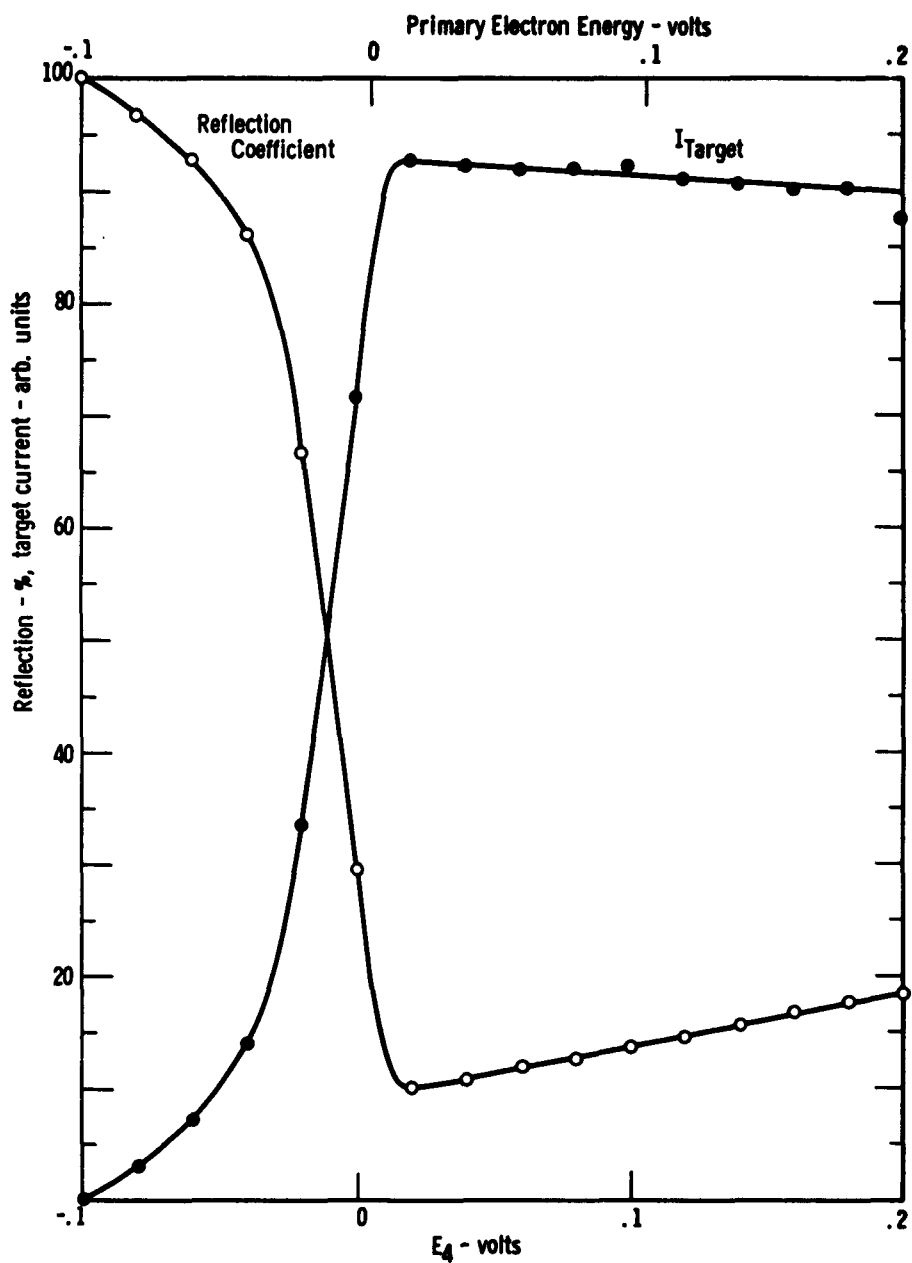


Fig. 4-4. Measured reflection coefficient and target current vs. primary electron energy and potential E_0 for Advance-Cs on a greatly expanded scale near zero primary energy. $\phi = 5.14$ eV.

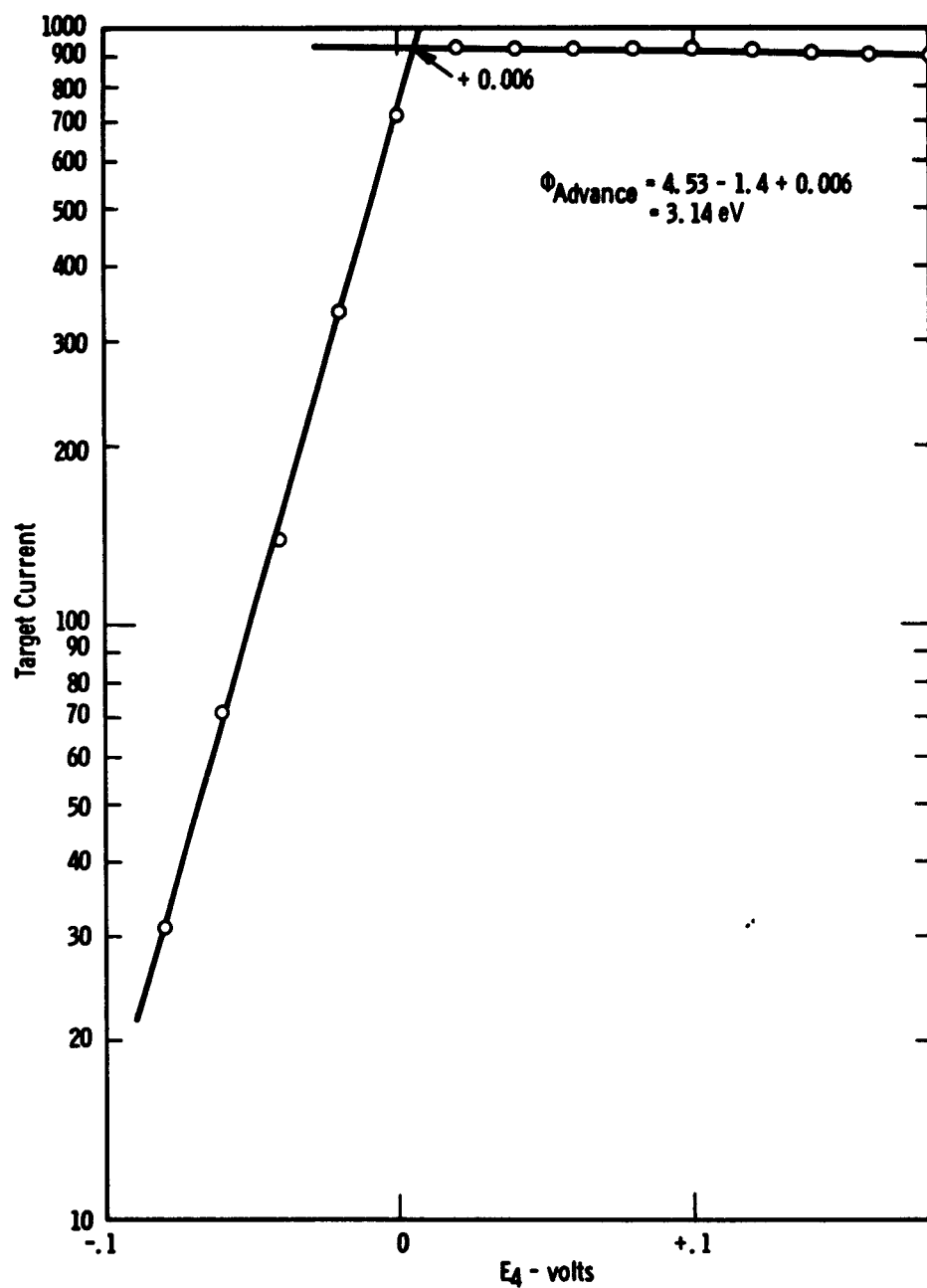


Fig. 4-5. Semilog plot of target current vs. potential E_4 used to obtain zero of primary electron energy and estimate the target work function for Advance-Cs.

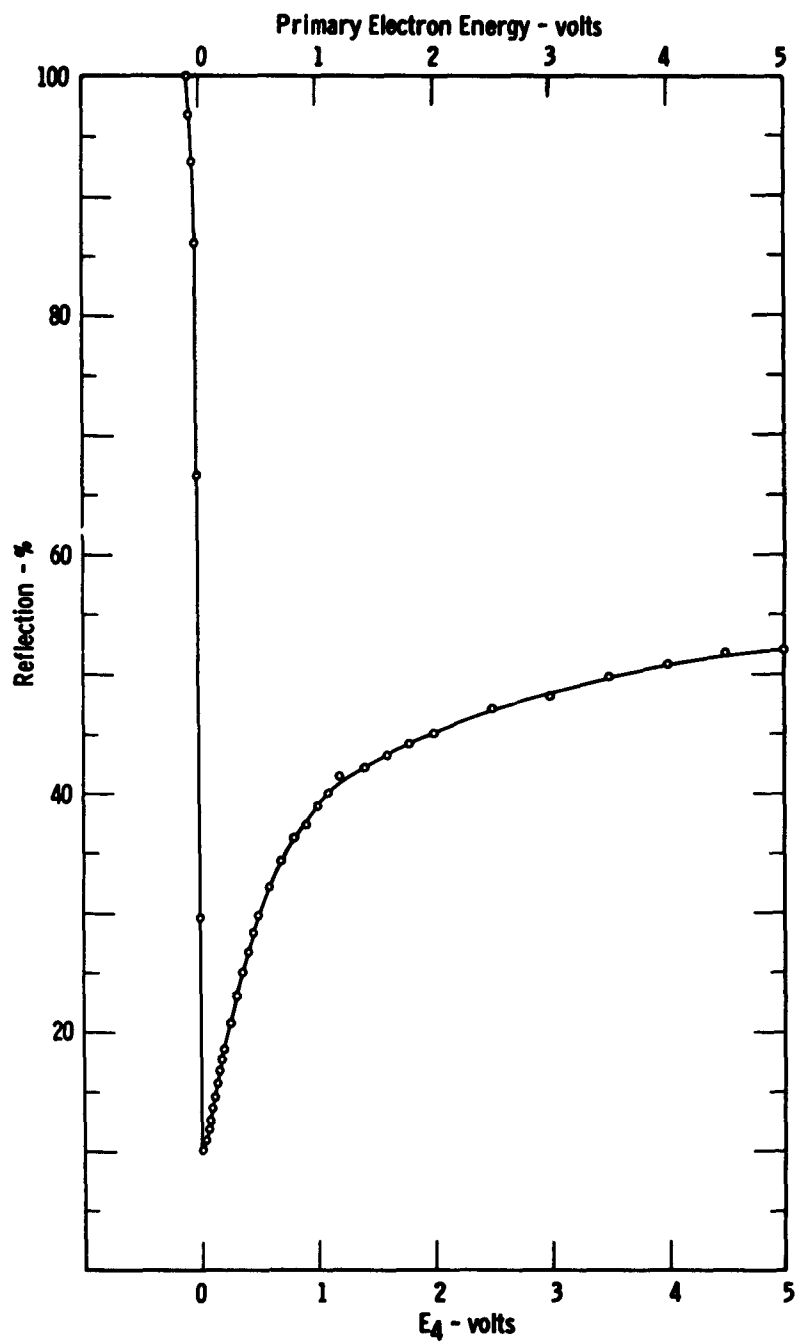


Fig. 4-6. Measured reflection coefficient for Advance-Cs vs. primary electron energy and potential E_4 . $\phi = 3.14$ eV.

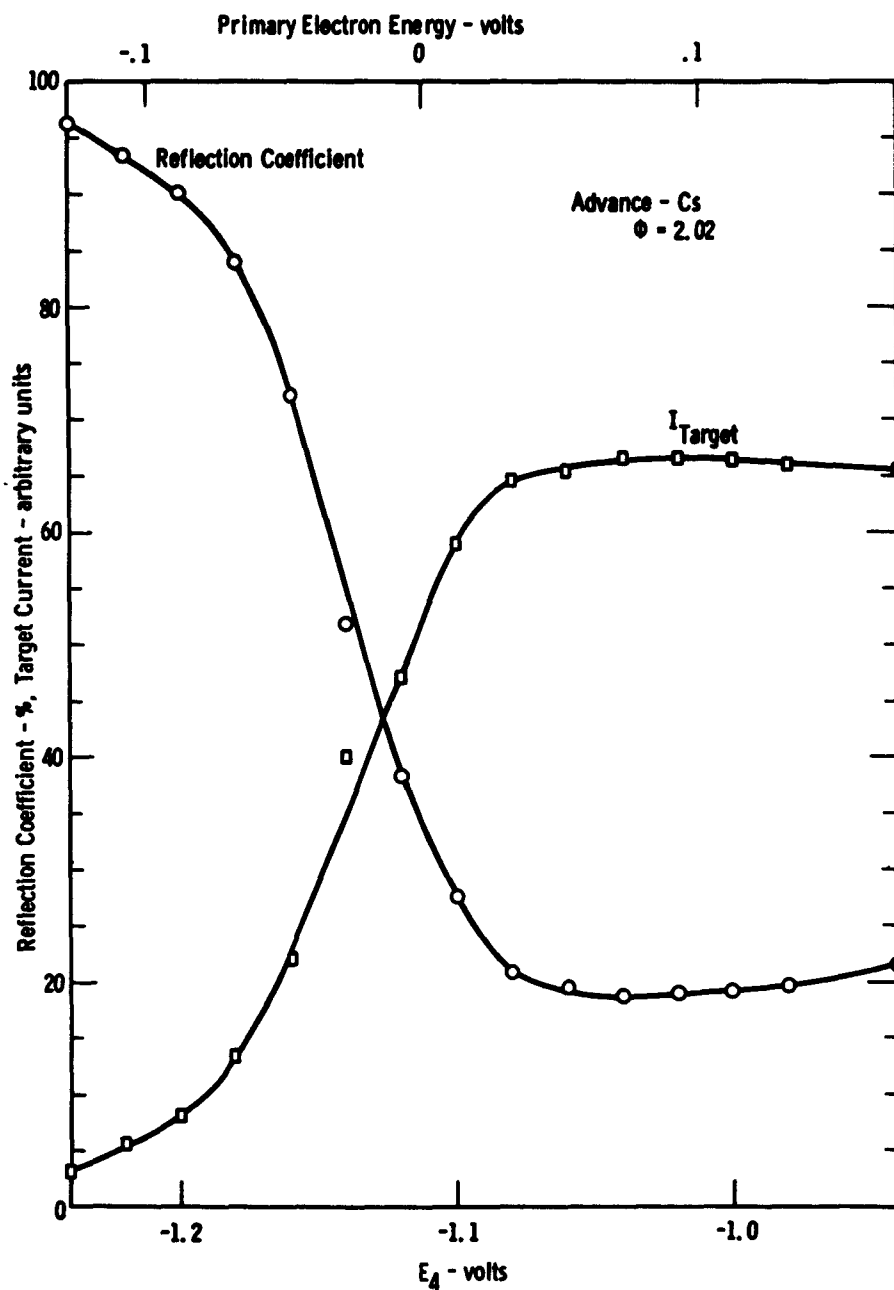


Fig. 4-7. Measured reflection coefficient and target current for Advance-Cs target vs. primary electron energy and potential E_4 near zero primary energy. $\phi = 2.02$ eV.

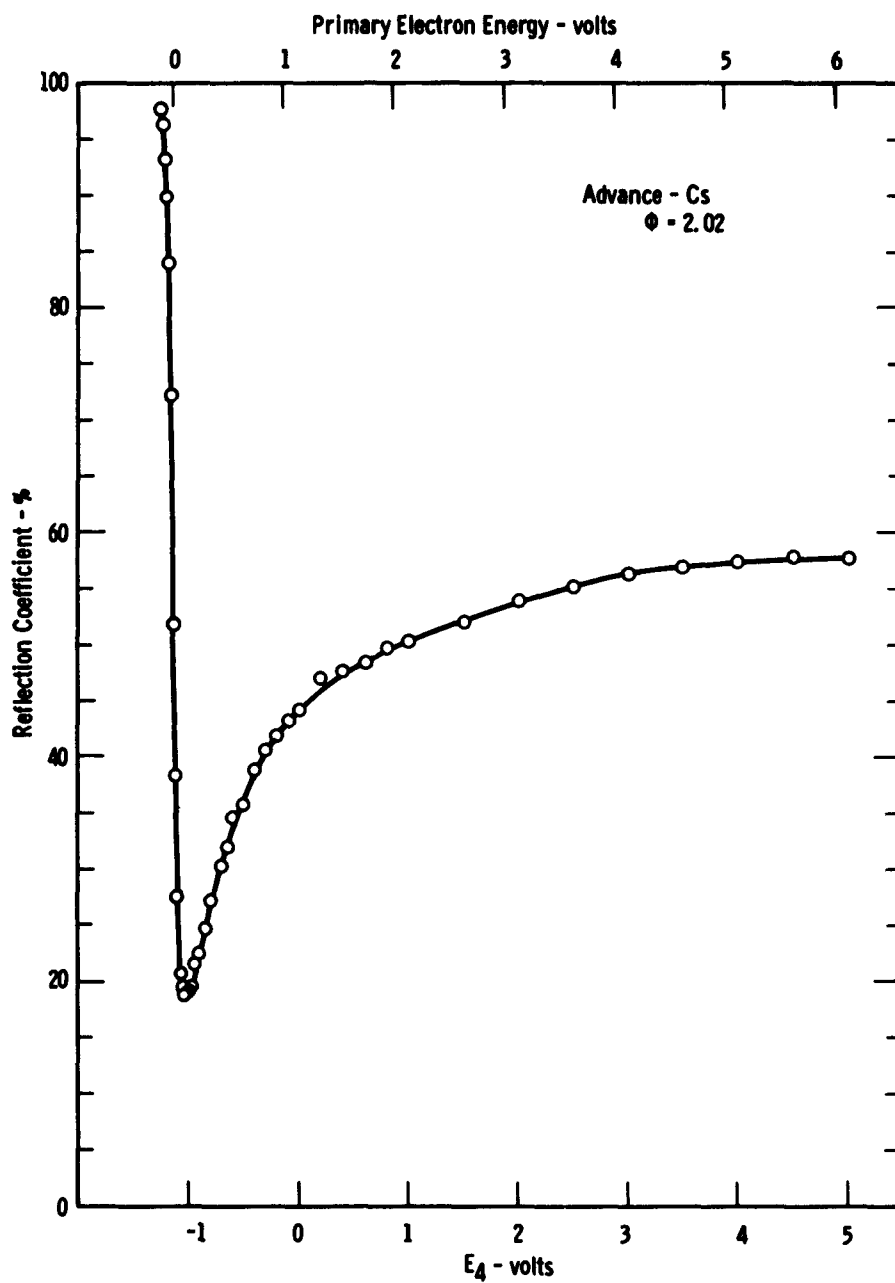


Fig. 4-8. Measured reflection coefficient for Advance-Cs vs. primary electron energy and potential E_4 . $\phi = 2.02$ eV.

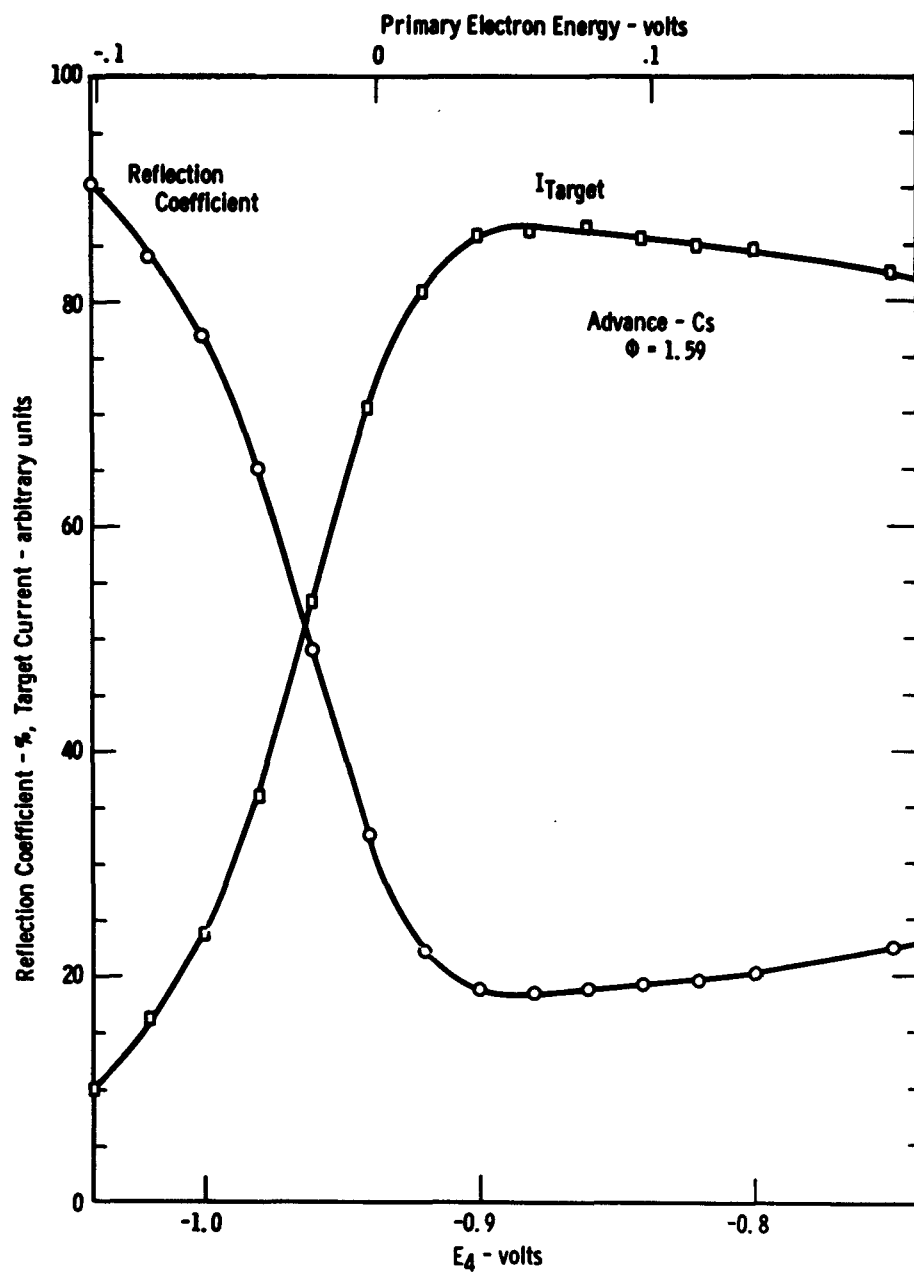


Fig. 4-9. Measured reflection coefficient and target current for Advance-Cs target vs. primary electron energy and potential E_4 near zero primary energy. $\phi = 1.59$ eV.

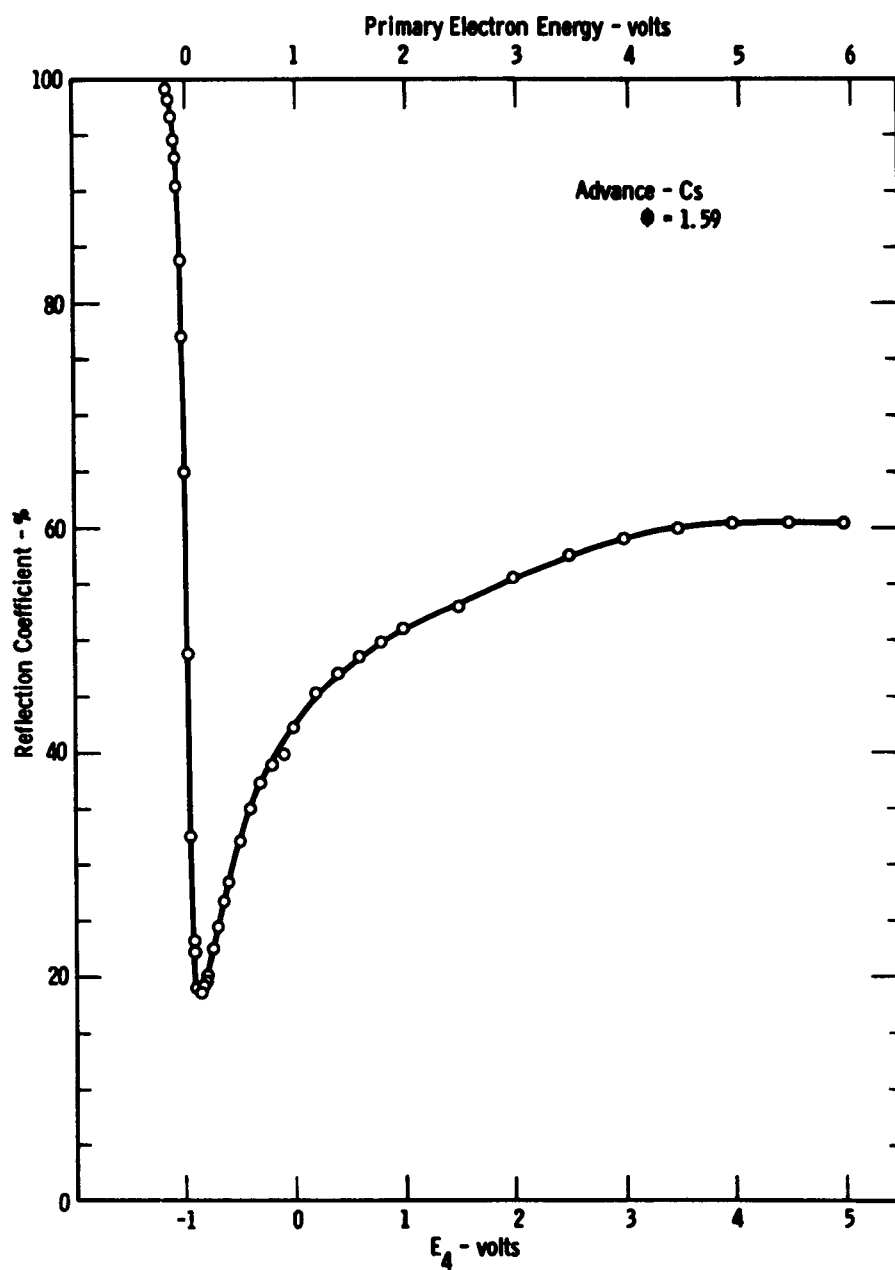


Fig. 4-10. Measured reflection coefficient for Advance-Cs vs. primary electron energy and potential E_A . $\phi = 1.59$ eV.

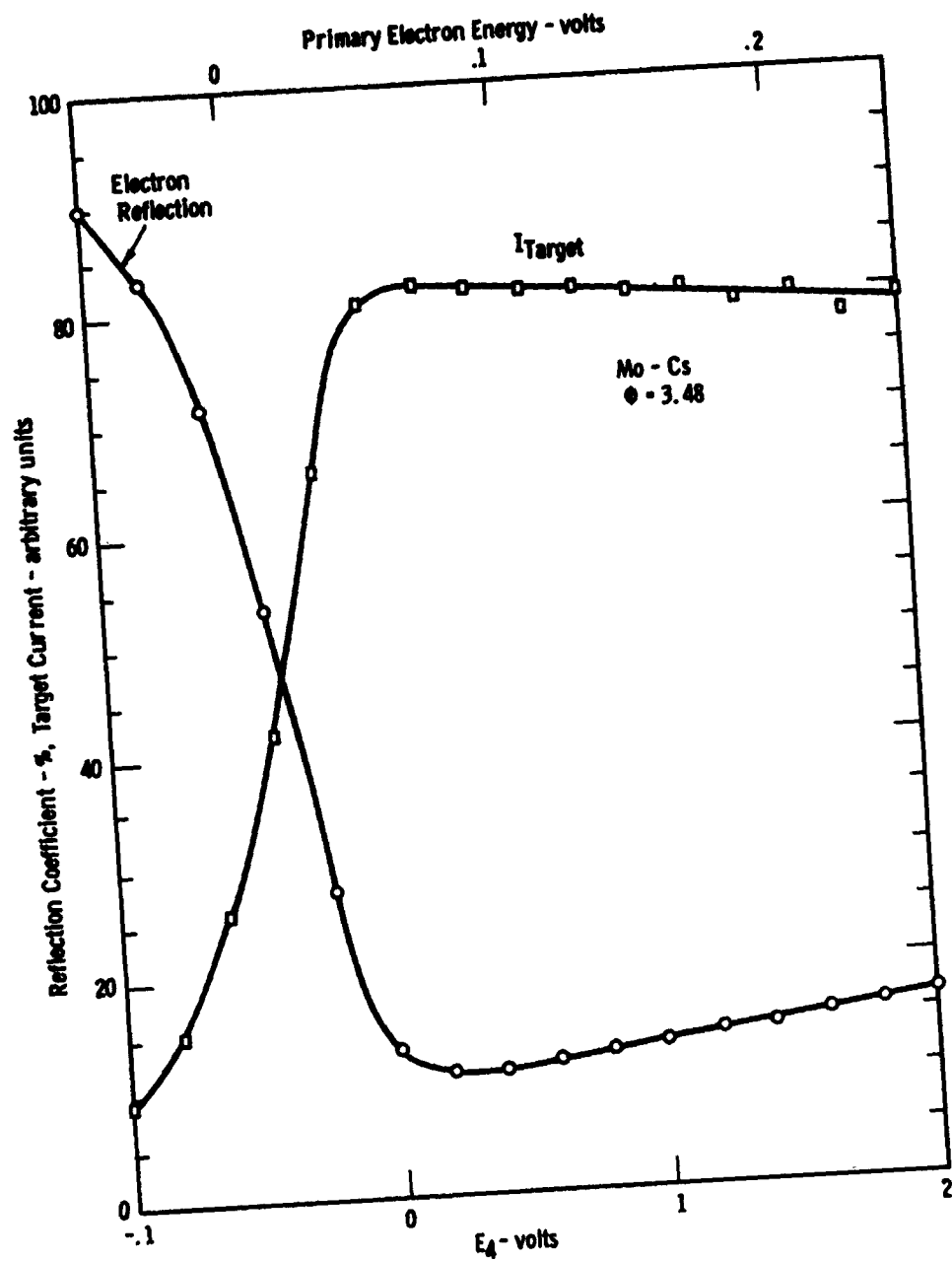


Fig. 4-11. Measured reflection coefficient and target current for Mo-Cs target vs. primary electron energy and potential E_4 near zero primary energy. $\phi = 3.48$ eV.

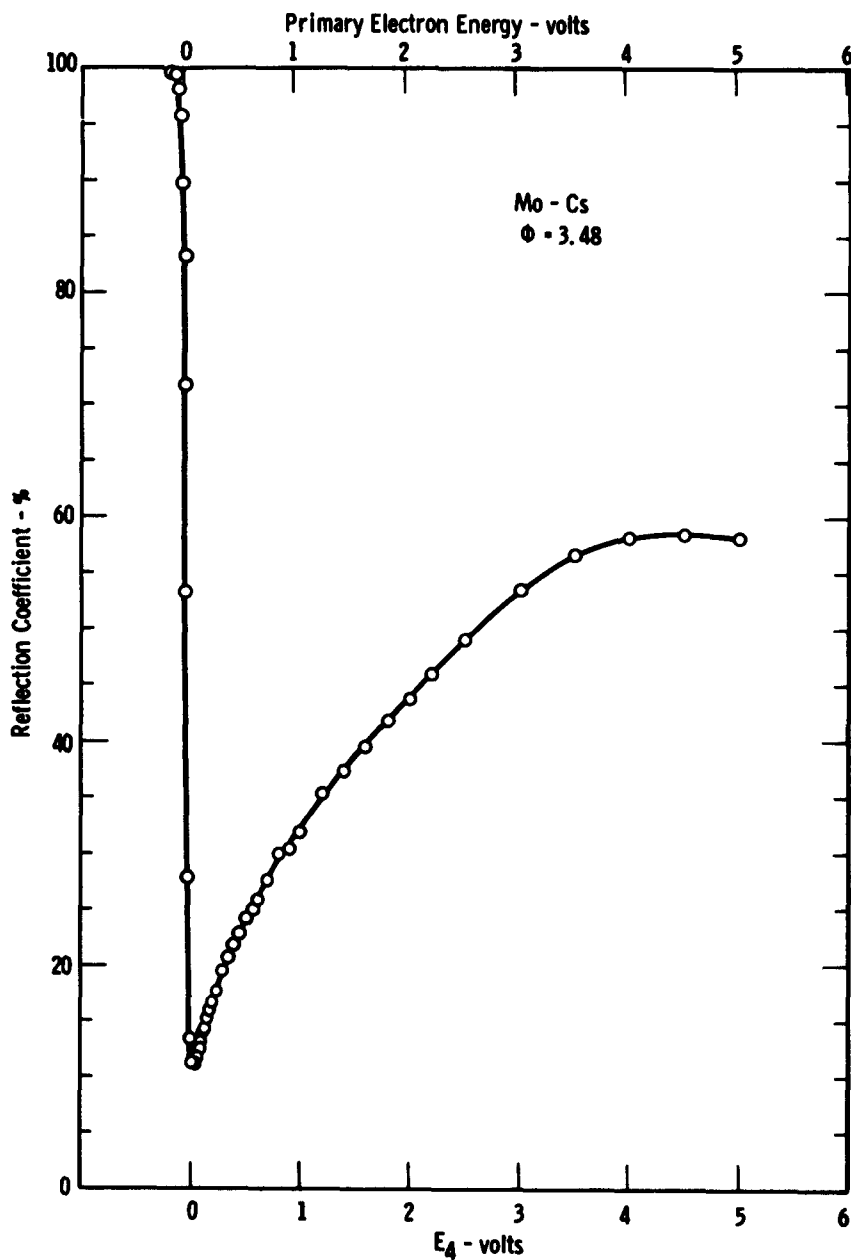


Fig. 4-12. Measured reflection coefficient for Mo-Cs vs. primary electron energy and potential E_4 . $\phi = 3.48$ eV.

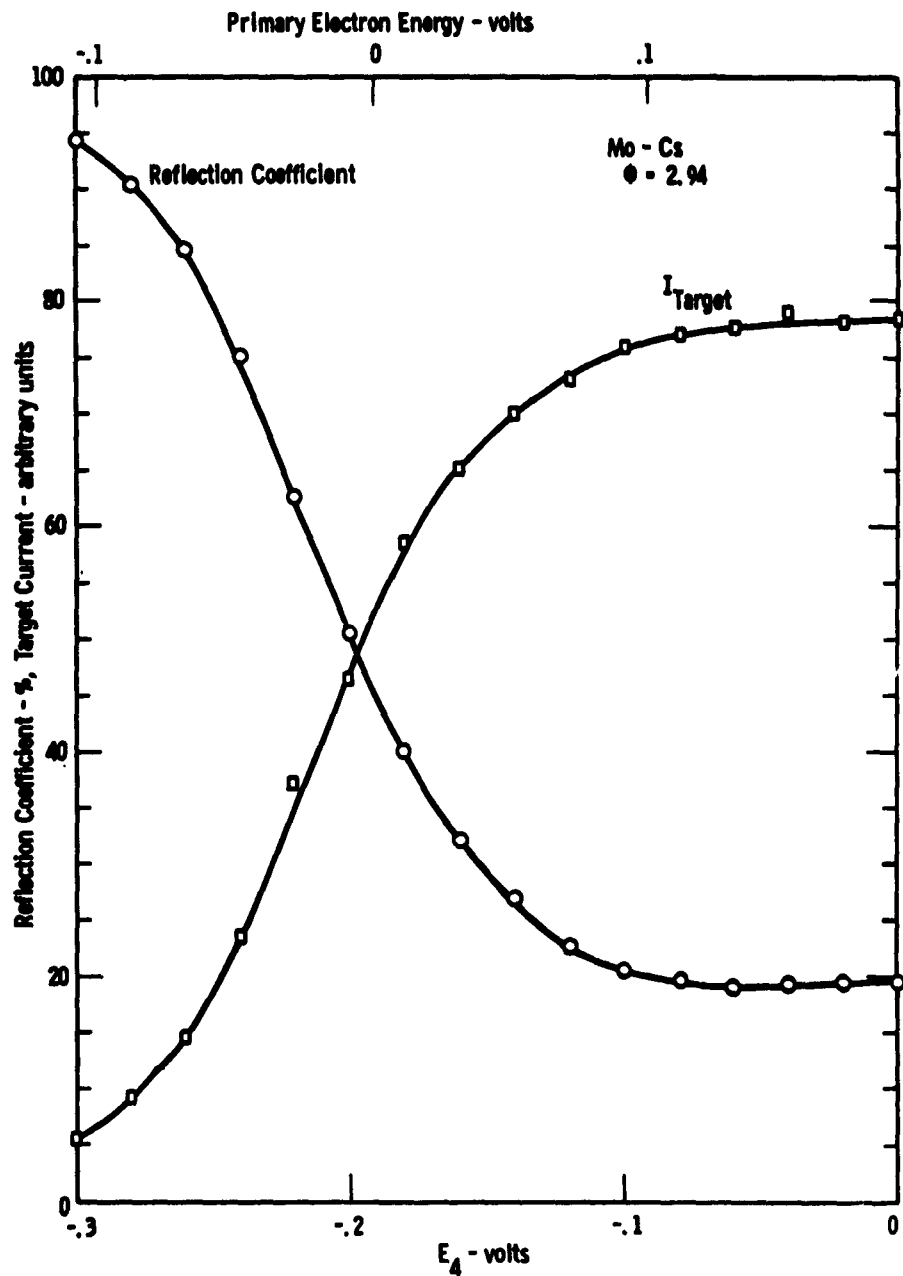


Fig. 4-13. Measured reflection coefficient and target current for Mo-Cs target vs. primary electron energy and potential E_4 near zero primary energy. $\phi = 2.94$ eV.

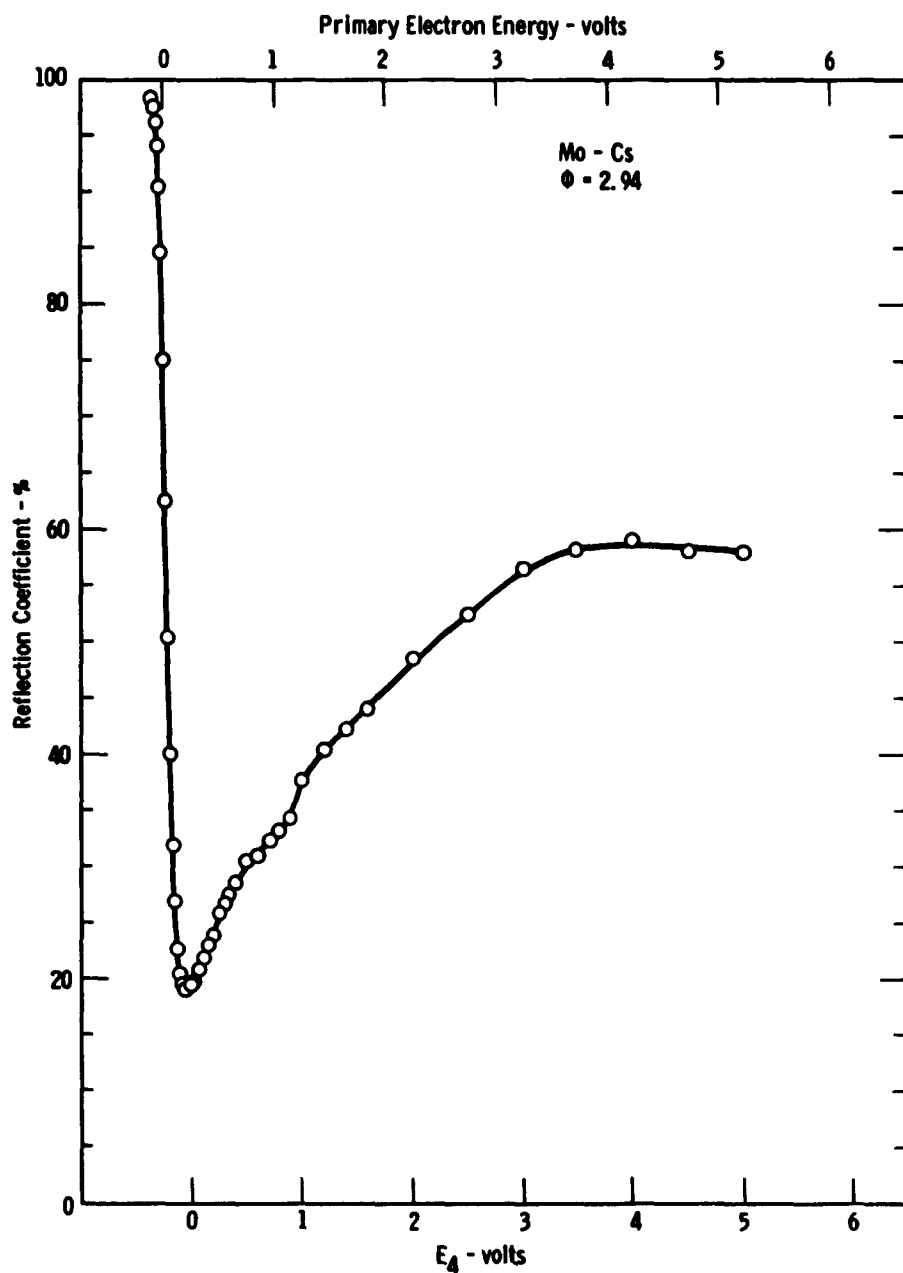


Fig. 4-14. Measured reflection coefficient for Mo-Cs vs. primary electron energy and potential E_0 . $\phi = 2.94$ eV.

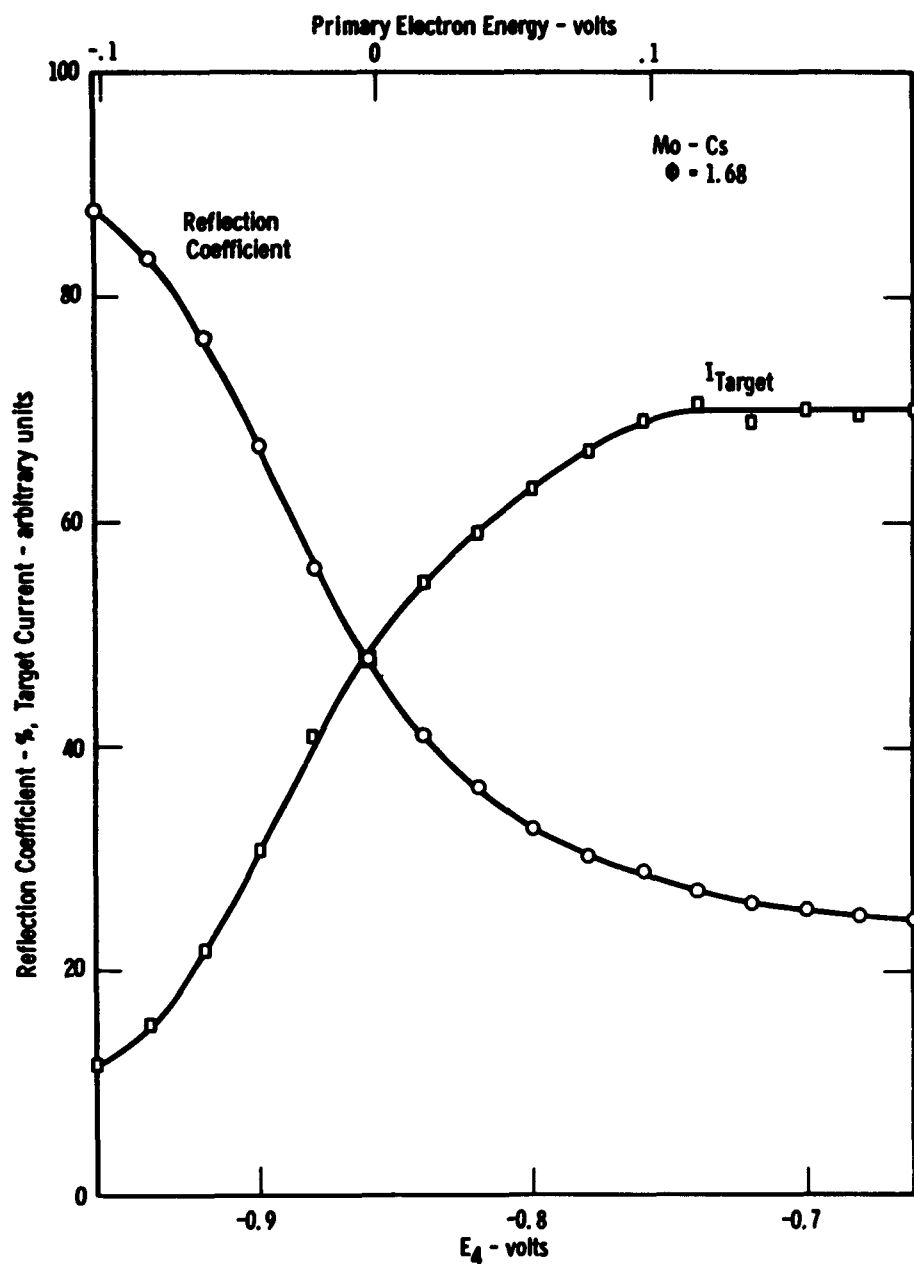


Fig. 4-15. Measured reflection coefficient and target current for MO-Cs target vs. primary electron energy and potential E_4 near zero primary energy. $\phi = 1.68\text{eV}$.

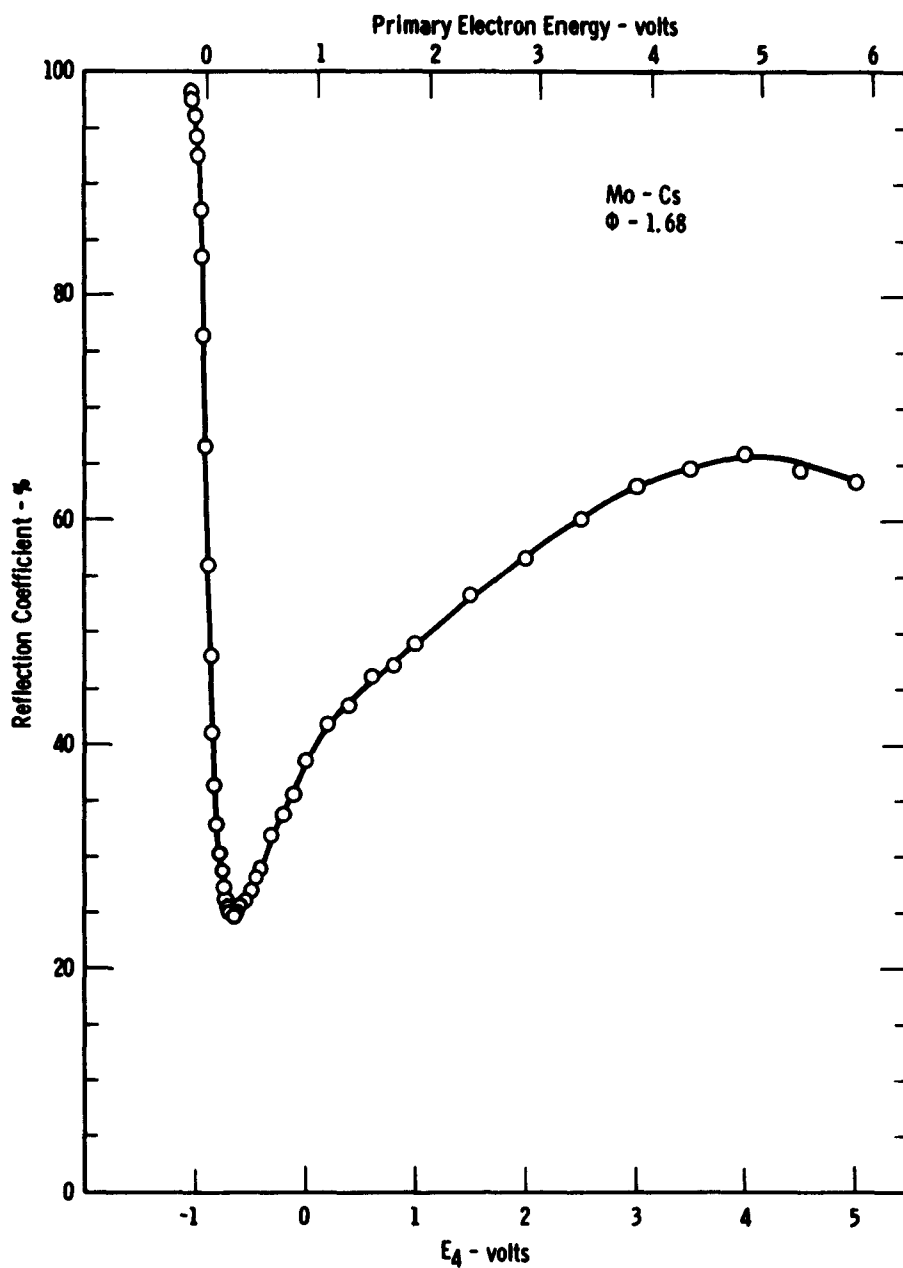


Fig. 4-16. Measured reflection coefficient for Mo-Cs vs. primary electron energy and potential E_A . $\phi = 1.68$ eV.

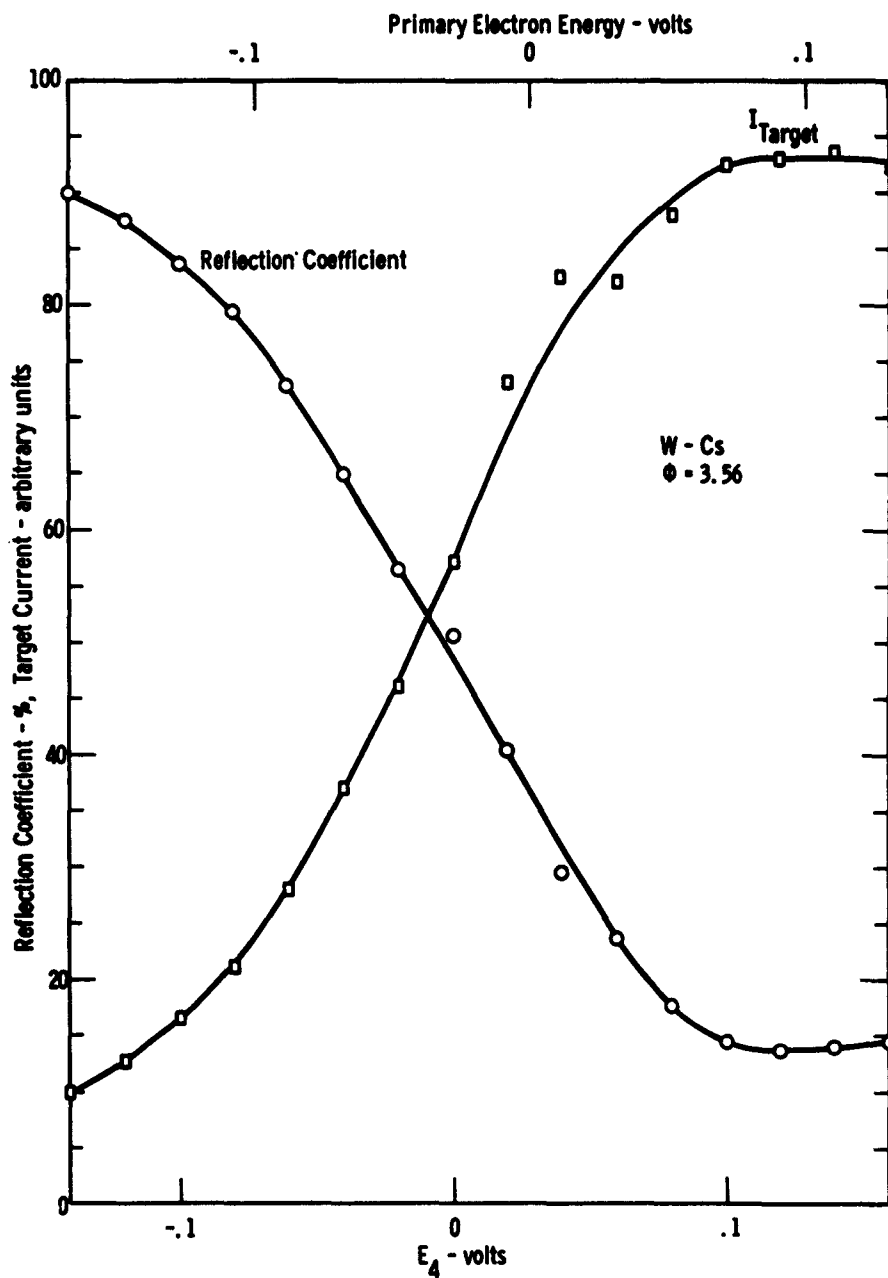


Fig. 4-17. Measured reflection coefficient and target current for W-Cs target vs. primary electron energy and potential E_4 near zero primary energy. $\phi = 3.56$ eV.

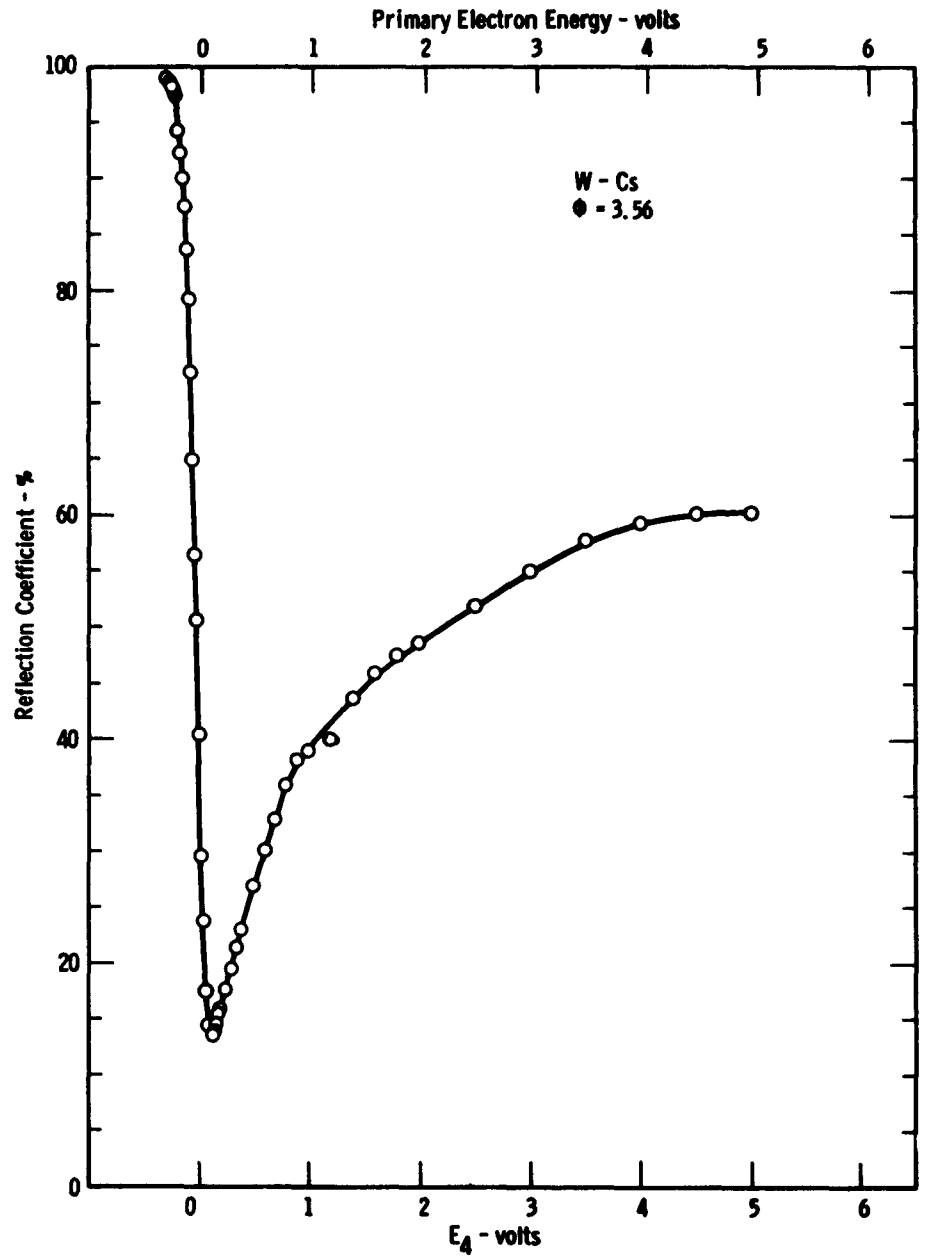


Fig. 4-18. Measured reflection coefficient for W-Cs vs. primary electron energy and potential E_4 . $\phi = 3.56$ eV.

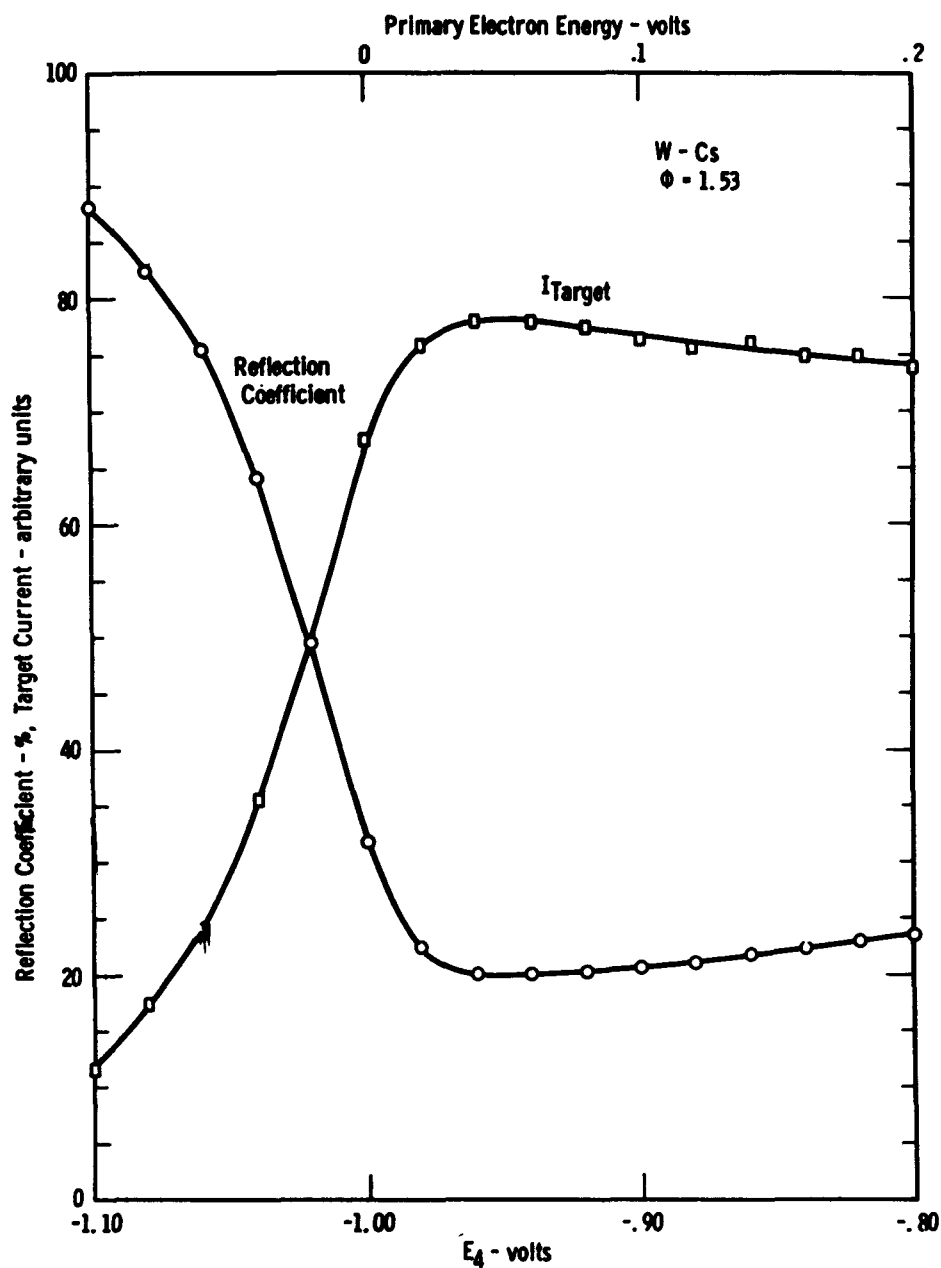


Fig. 4-19. Measured reflection coefficient and target current for W-Cs target vs. primary electron energy and potential E_4 near zero primary energy. $\phi = 1.53$ eV.

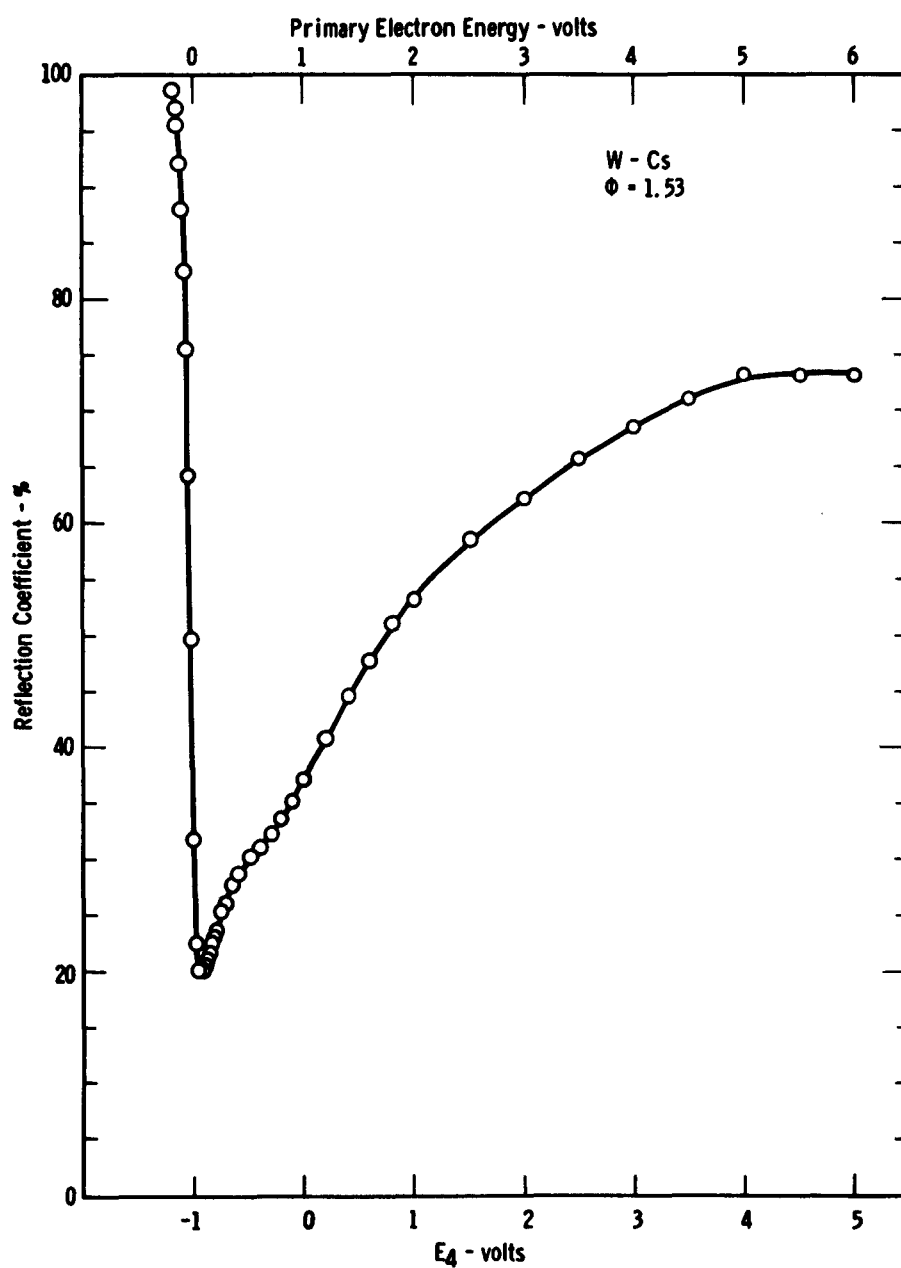


Fig. 4-20. Measured reflection coefficient for W-Cs vs. primary electron energy and potential E_4 . $\phi = 1.53$ eV.

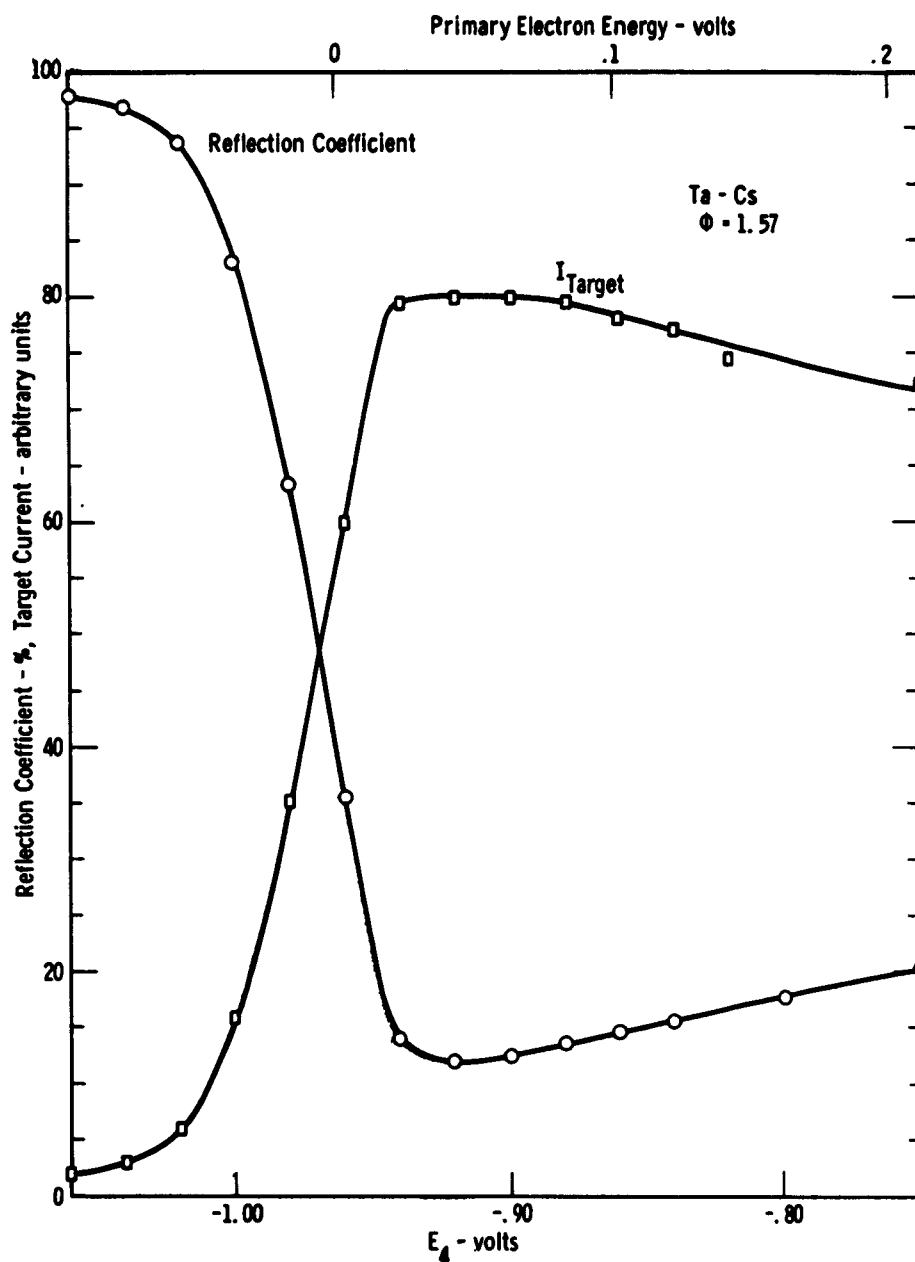


Fig. 4-21. Measured reflection coefficient and target current for Ta-Cs target vs. primary electron energy and potential E_4 near zero primary energy. $\phi = 1.57$ eV.

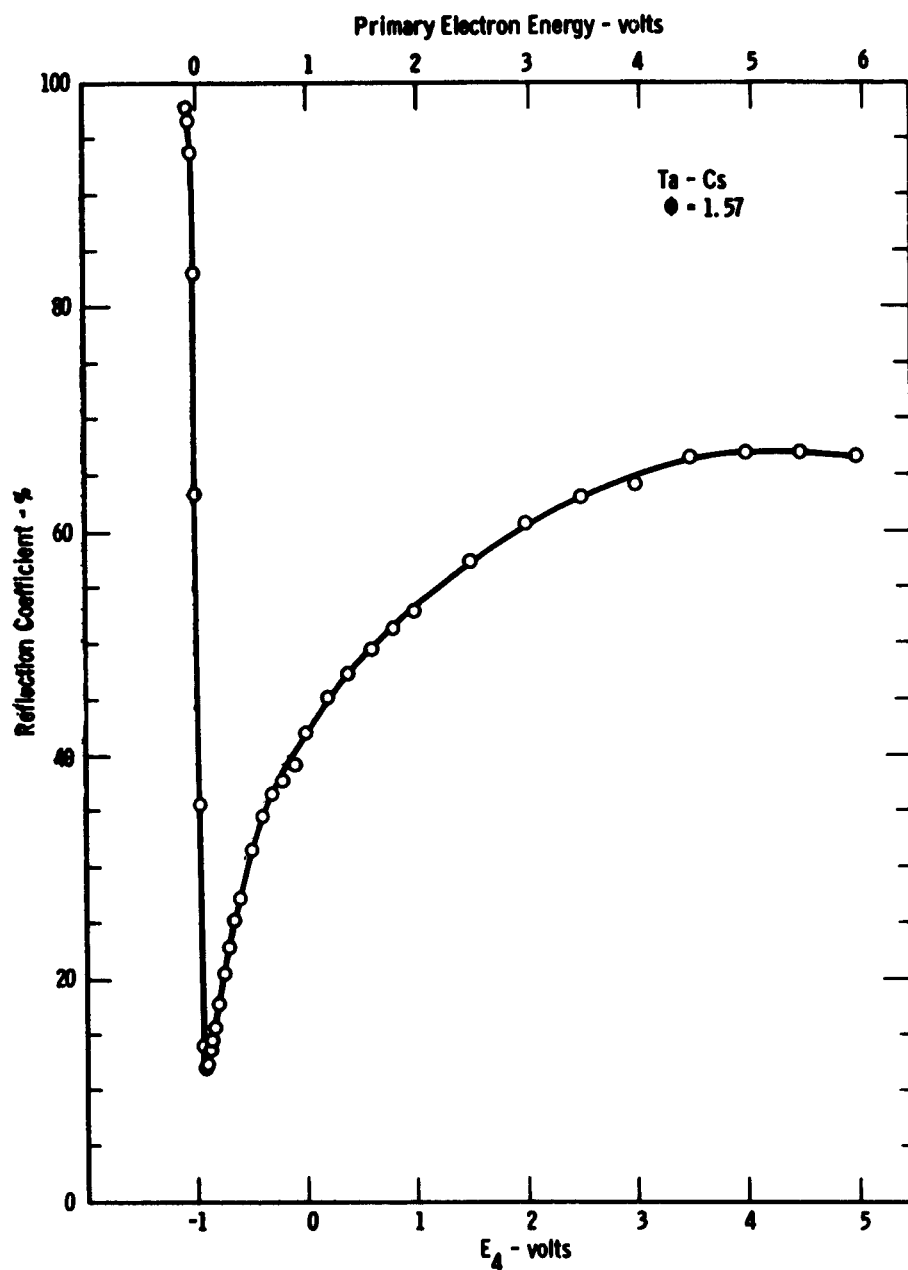


Fig. 4-22. Measured reflection coefficient for Ta-Cs vs. primary electron energy and potential E_4 . $\phi = 1.57$ eV.

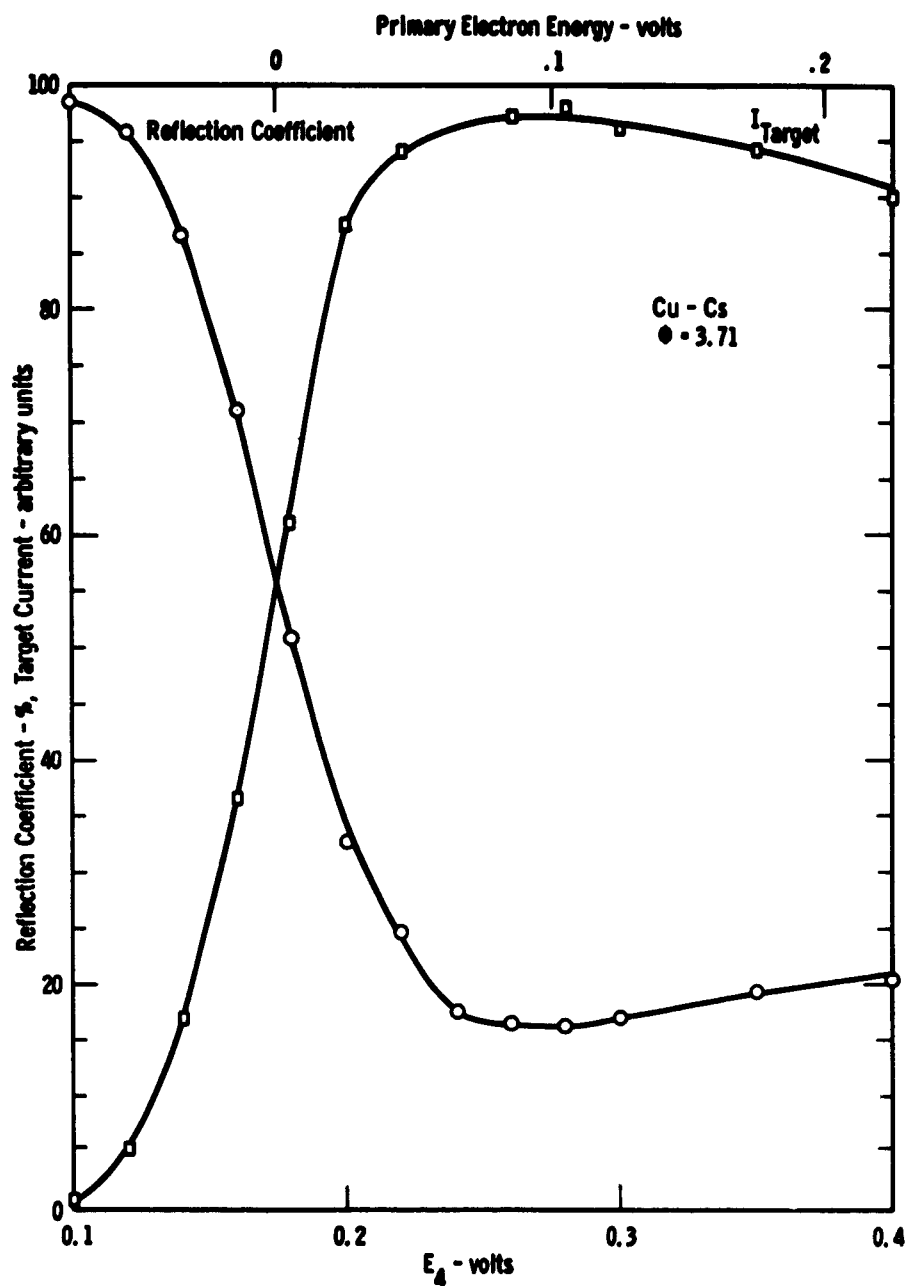


Fig. 4-23. Measured reflection coefficient and target current for Cu-Cs vs. primary electron energy and potential E_4 near zero primary energy. $\phi = 3.71$ eV.

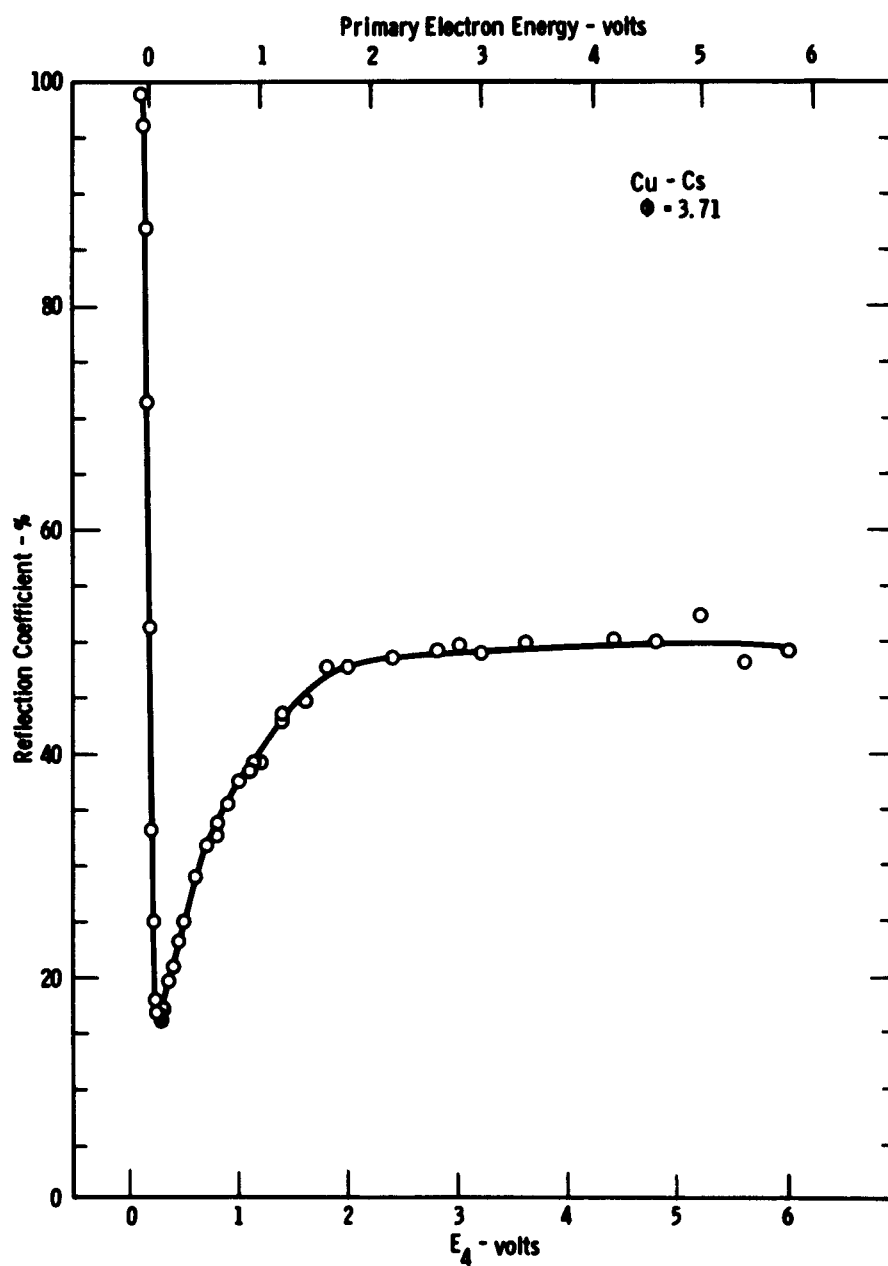


Fig. 4-24. Measured reflection coefficient for Cu-Cs vs. primary electron energy and potential E_k . $\phi = 3.71$ eV.

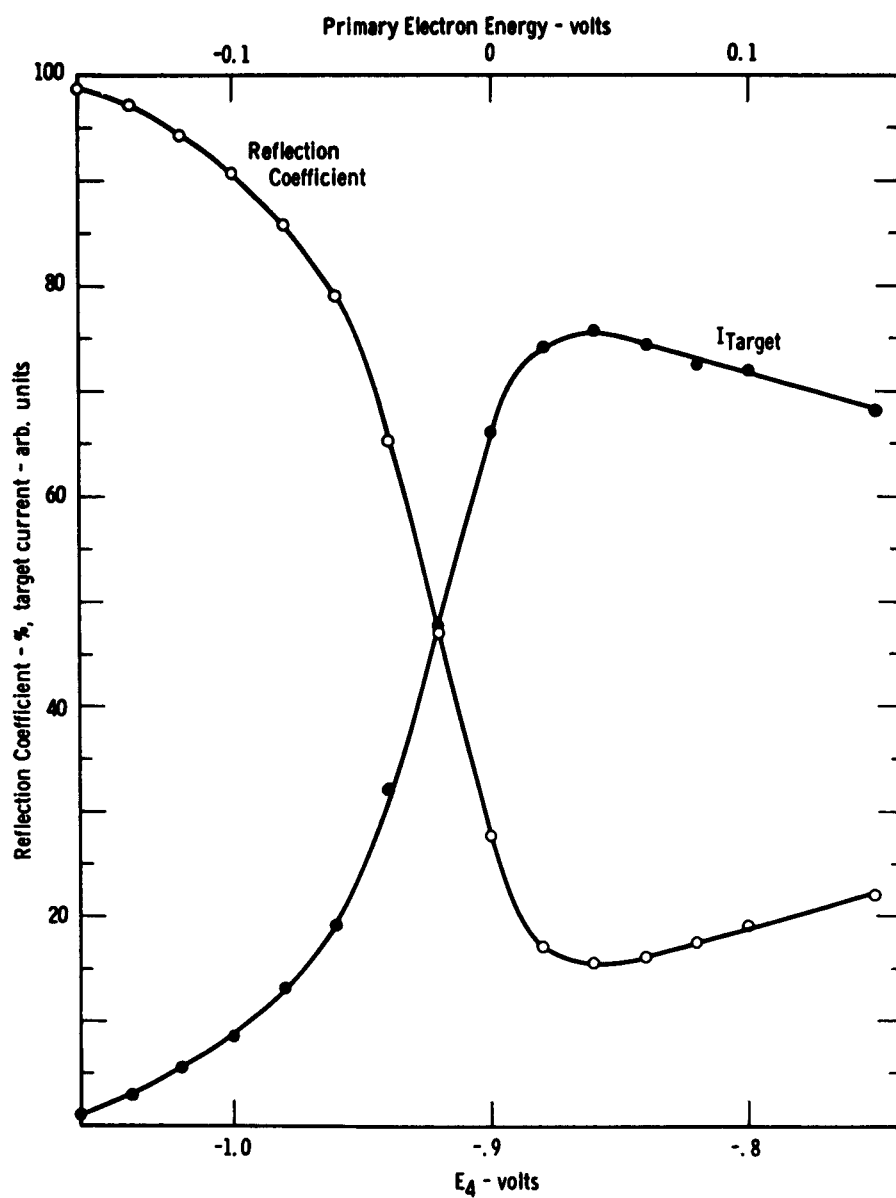


Fig. 4-25. Measured reflection coefficient and target current for Cu-Cu target vs. primary electron energy and potential E_4 near zero primary energy. $\phi = 1.63$ eV.

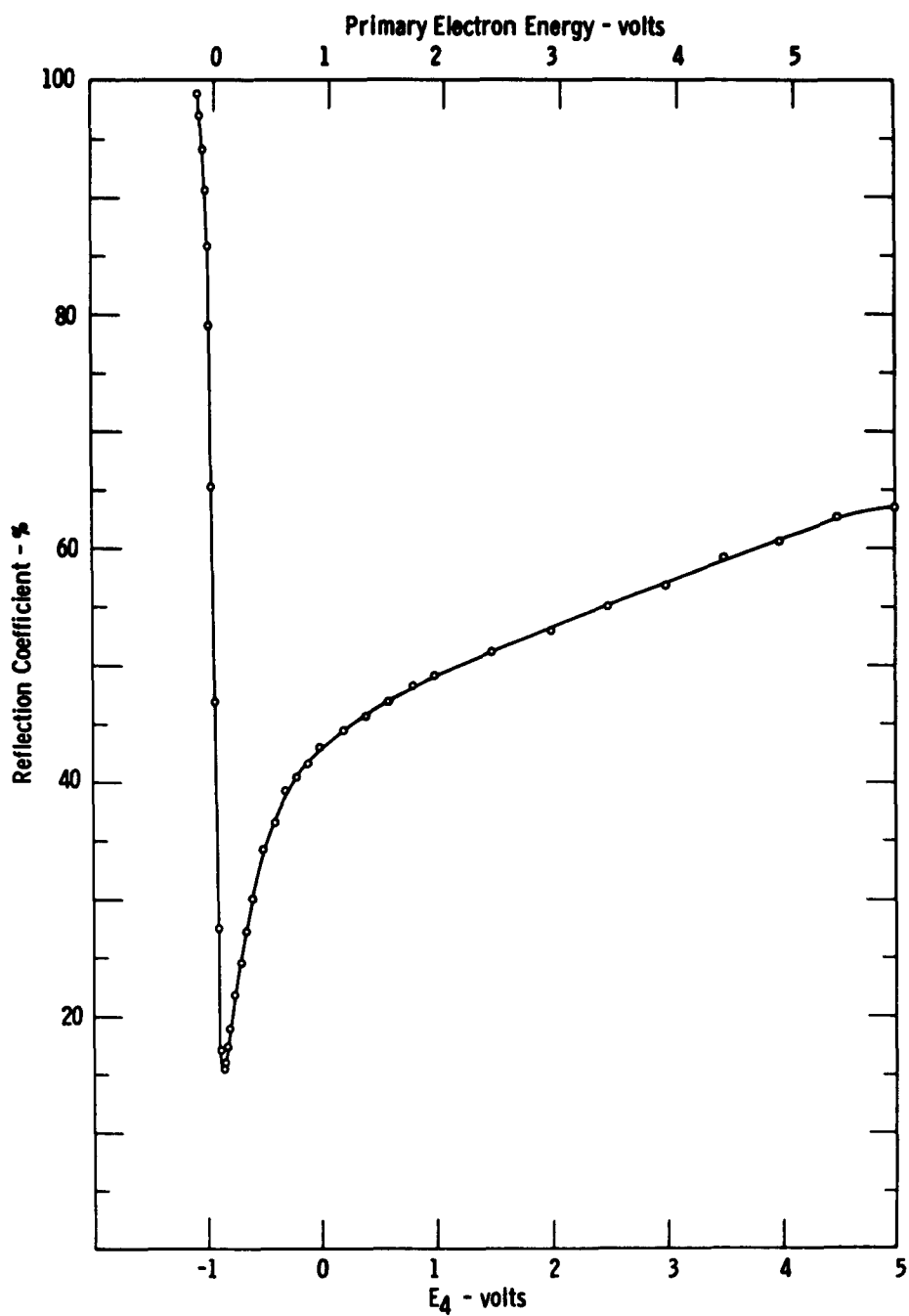


Fig. 4-26. Measured reflection coefficient for Cu-Cs vs. primary electron energy and potential E_4 . $\phi = 1.63$ eV.

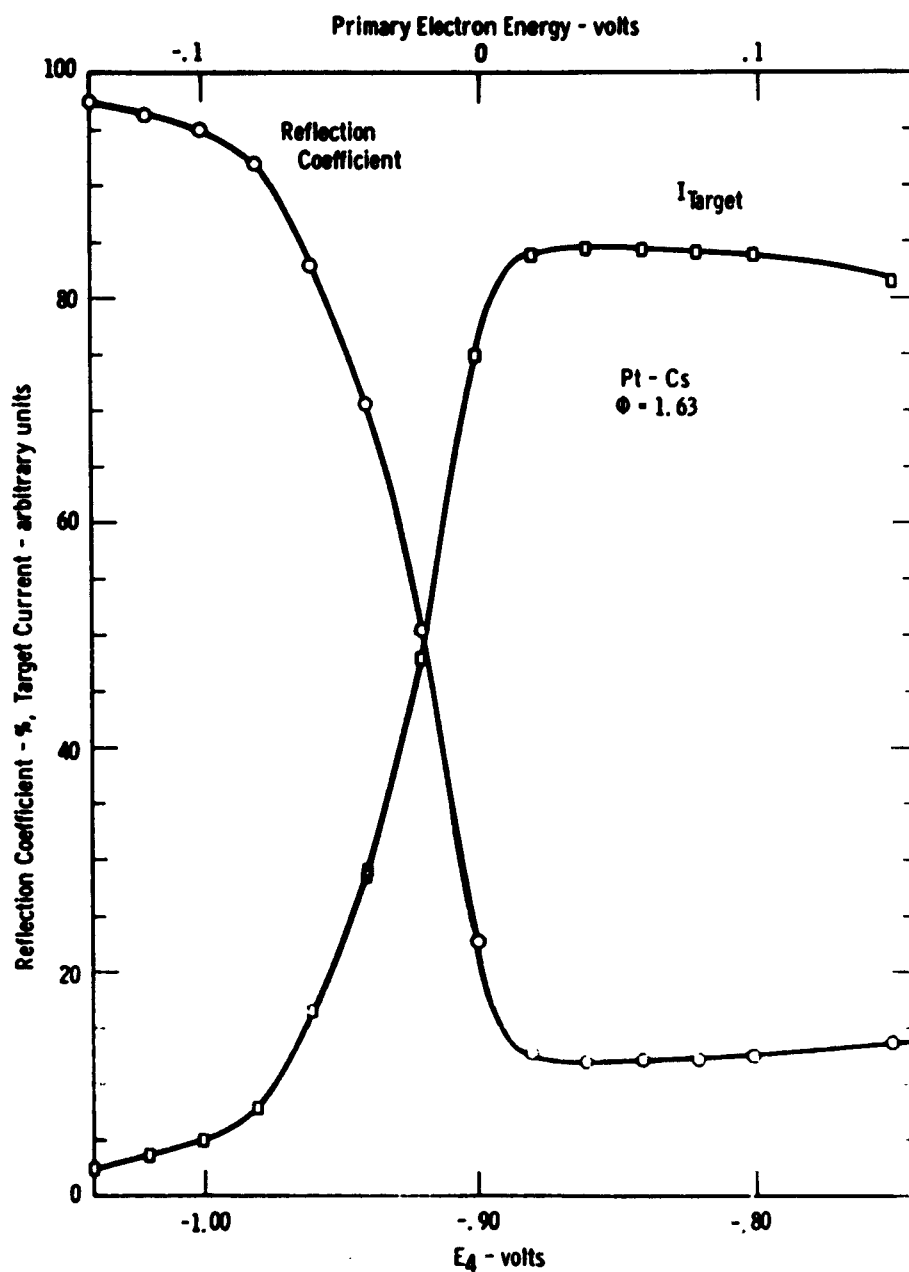


Fig. 4-27. Measured reflection coefficient and target current for Pt-Cs target vs. primary electron energy and potential E_4 near zero primary energy. $\phi = 1.63$ eV.

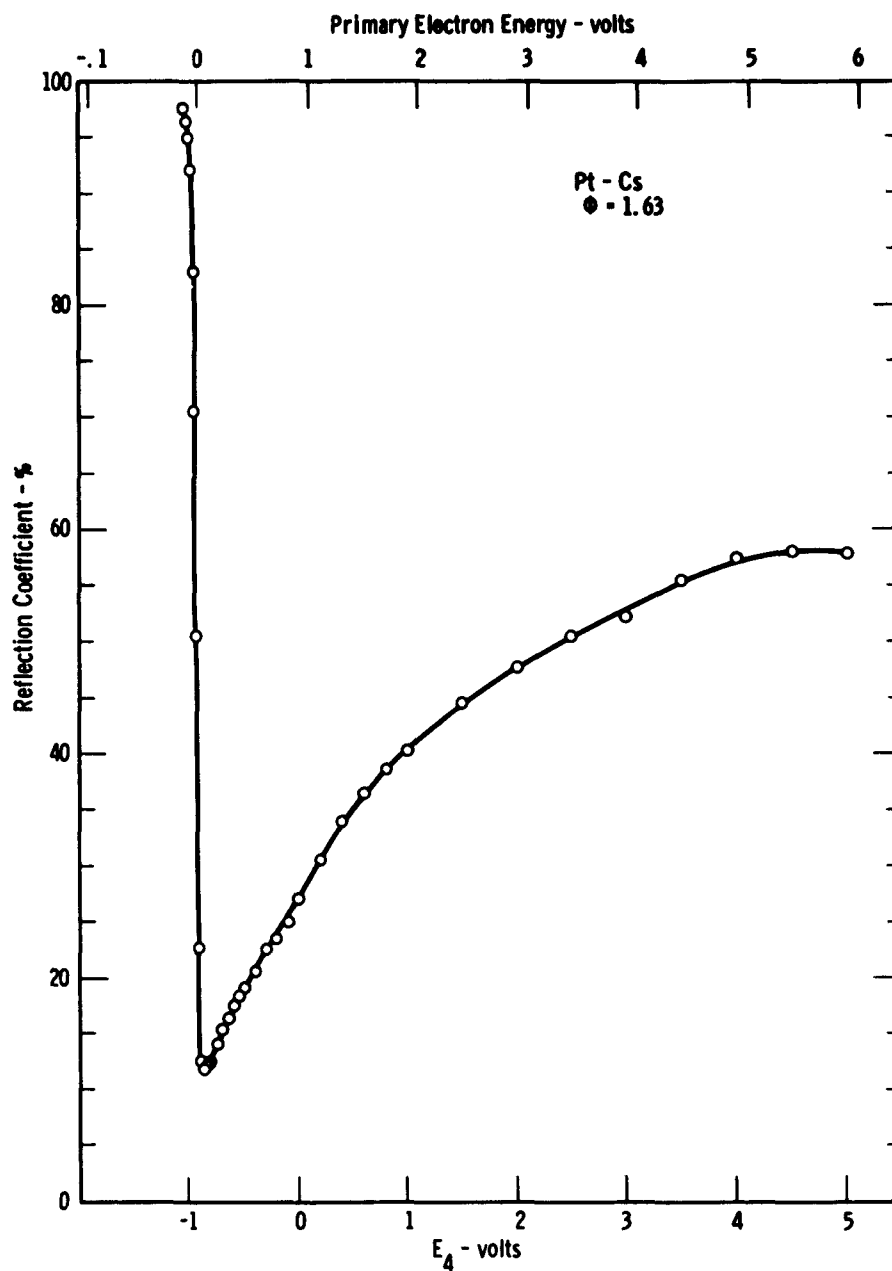


Fig. 4-28. Measured reflection coefficient for Pt-Cs vs. primary electron energy and potential E_4 . $\phi = 1.63$ eV.

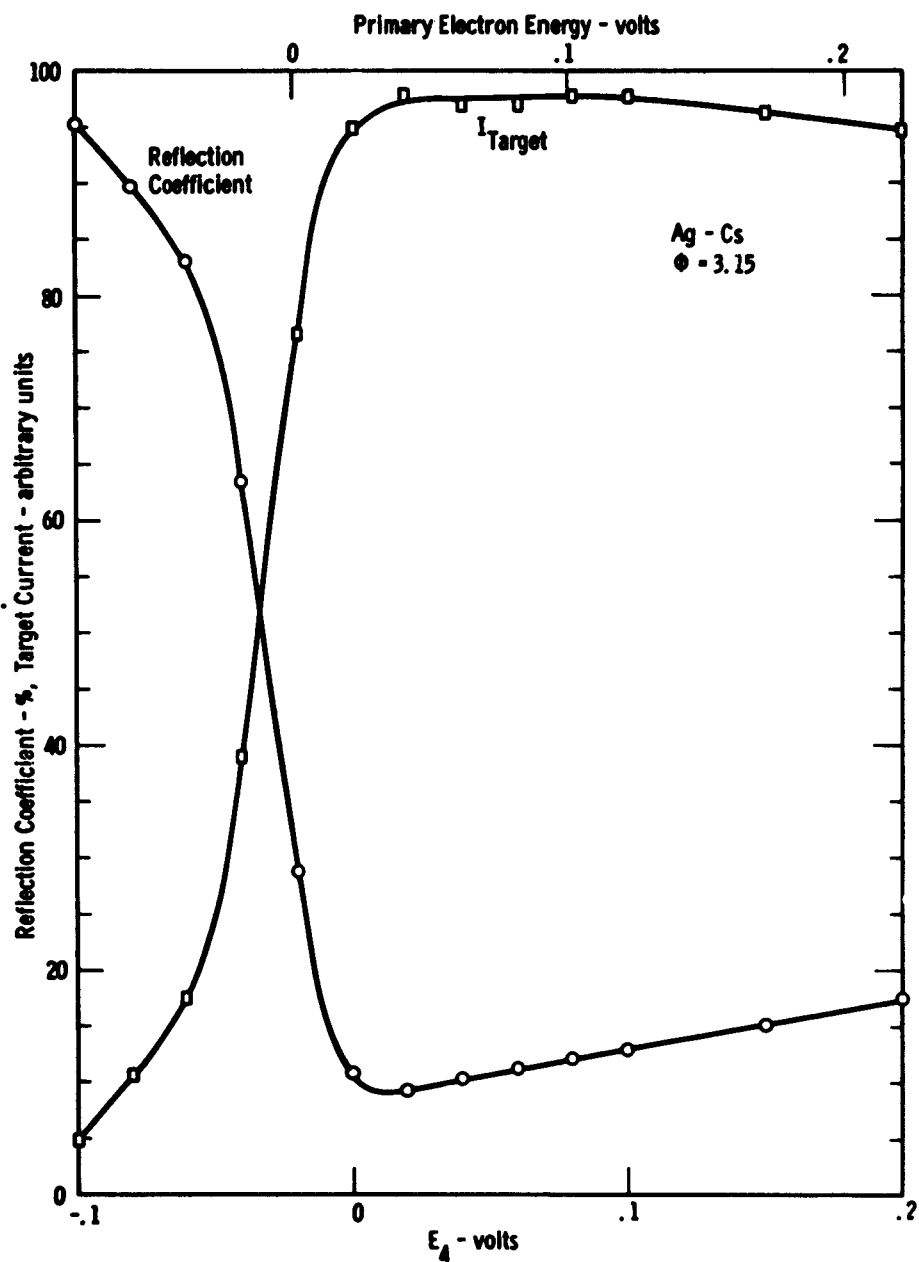


Fig. 4-29. Measured reflection coefficient and target current for Ag-Cs target vs. primary electron energy and potential E_4 near zero primary energy. $\phi = 3.15$ eV.

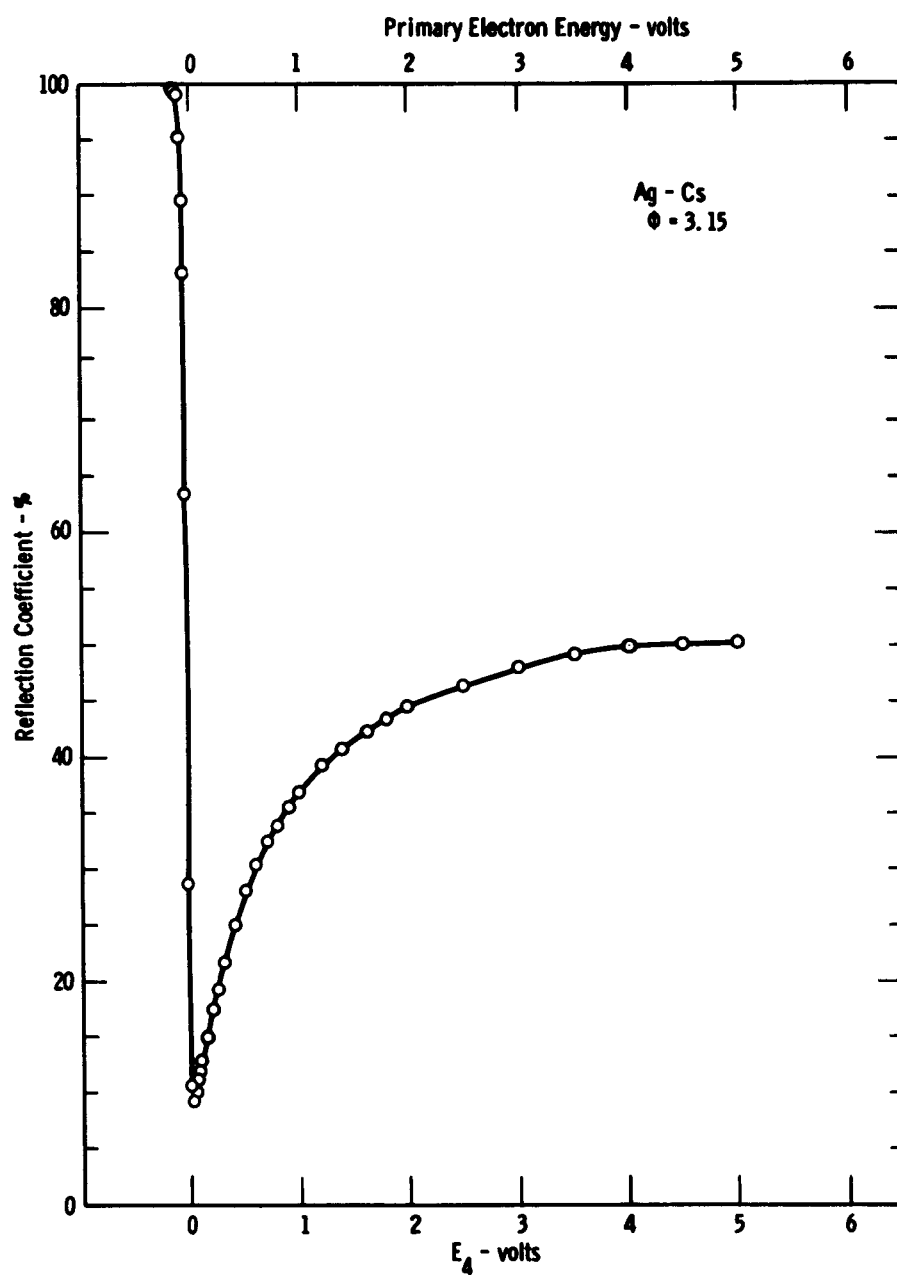


Fig. 4-30. Measured reflection coefficient for Ag-Cs vs. primary electron energy and potential E_4 . $\phi = 3.15$ eV.

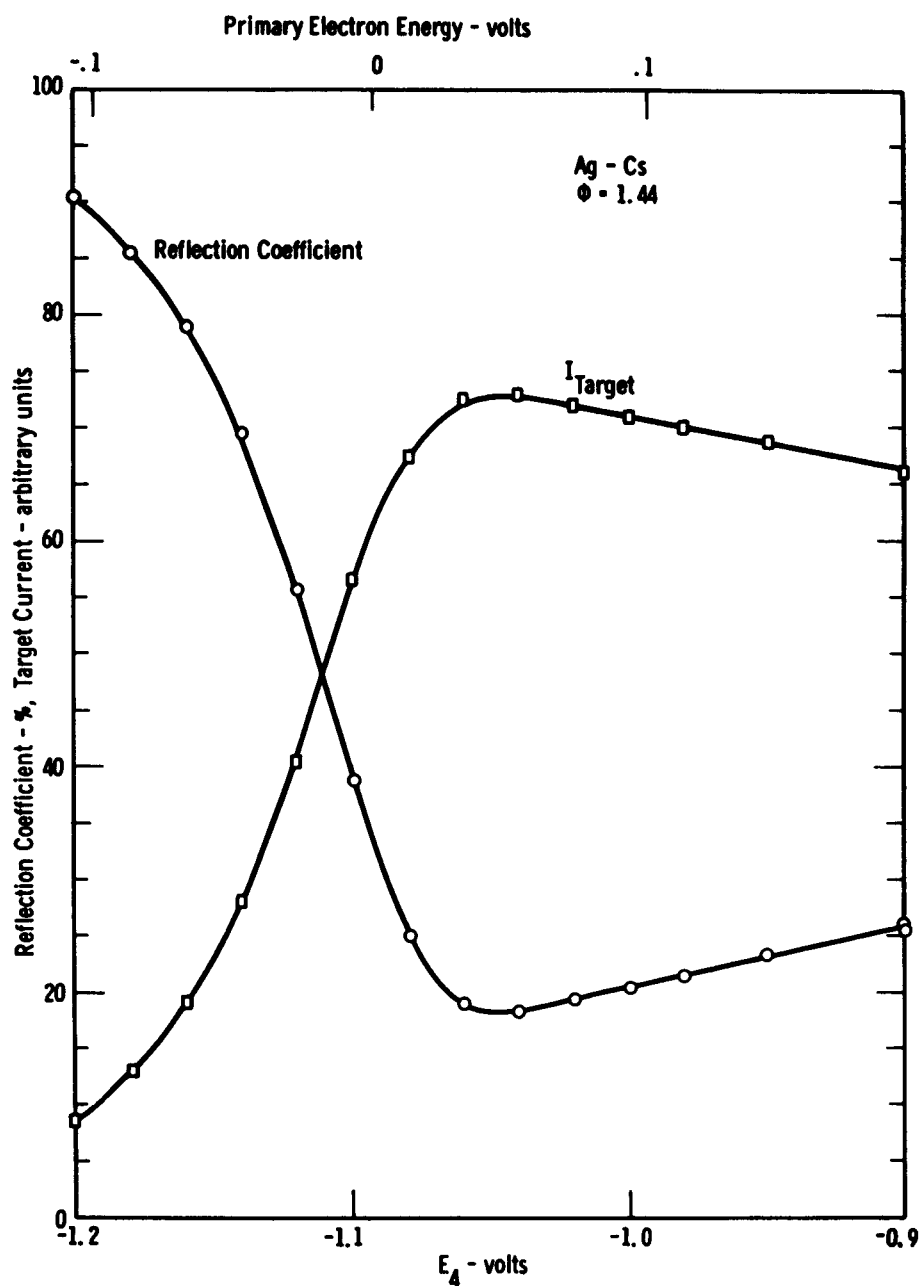


Fig. 4-31. Measured reflection coefficient and target current for Ag-Cs target vs. primary electron energy and potential E_4 near zero primary energy. $\phi = 1.44$ eV.

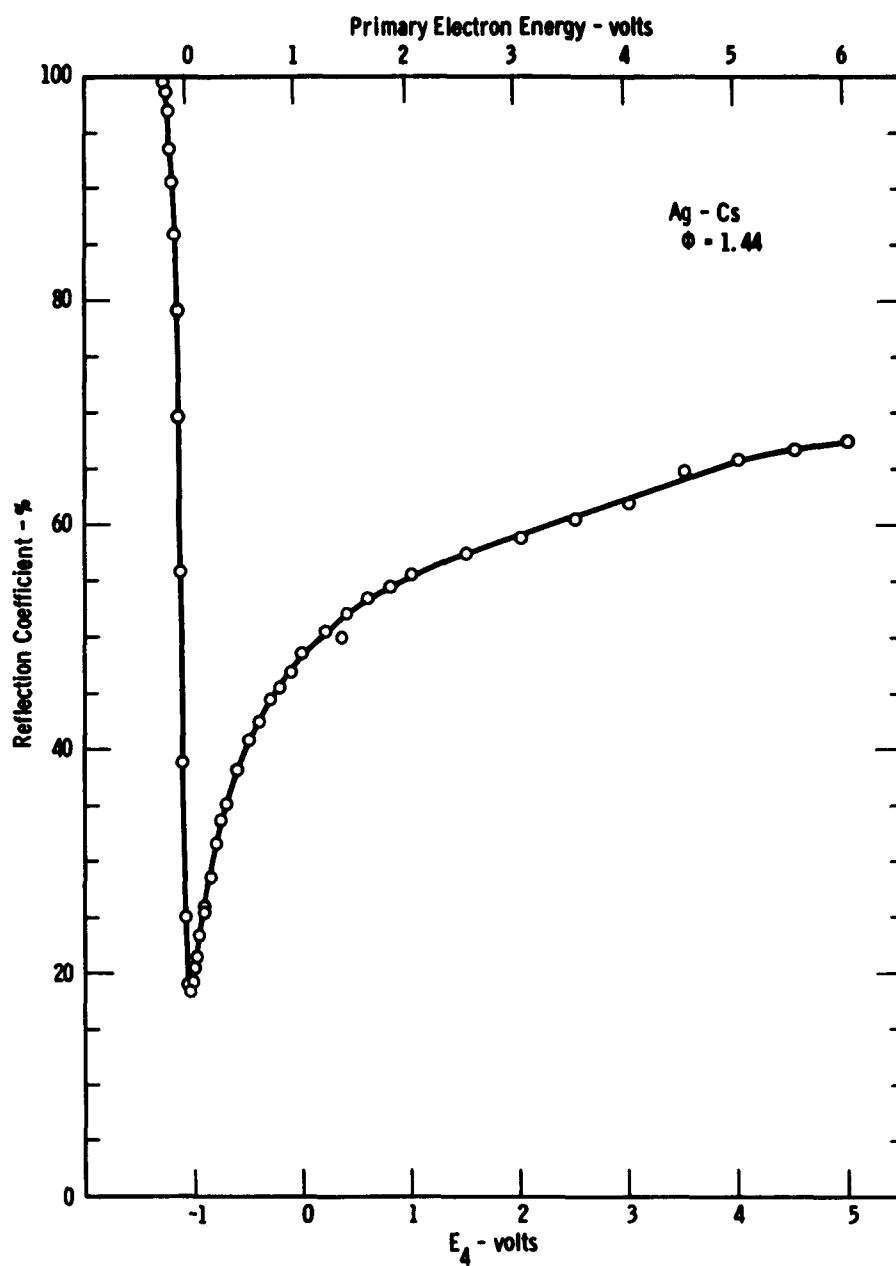


Fig. 4-32. Measured reflection coefficient for Ag-Cs vs. primary electron energy and potential E_4 . $\phi = 1.44$ eV.

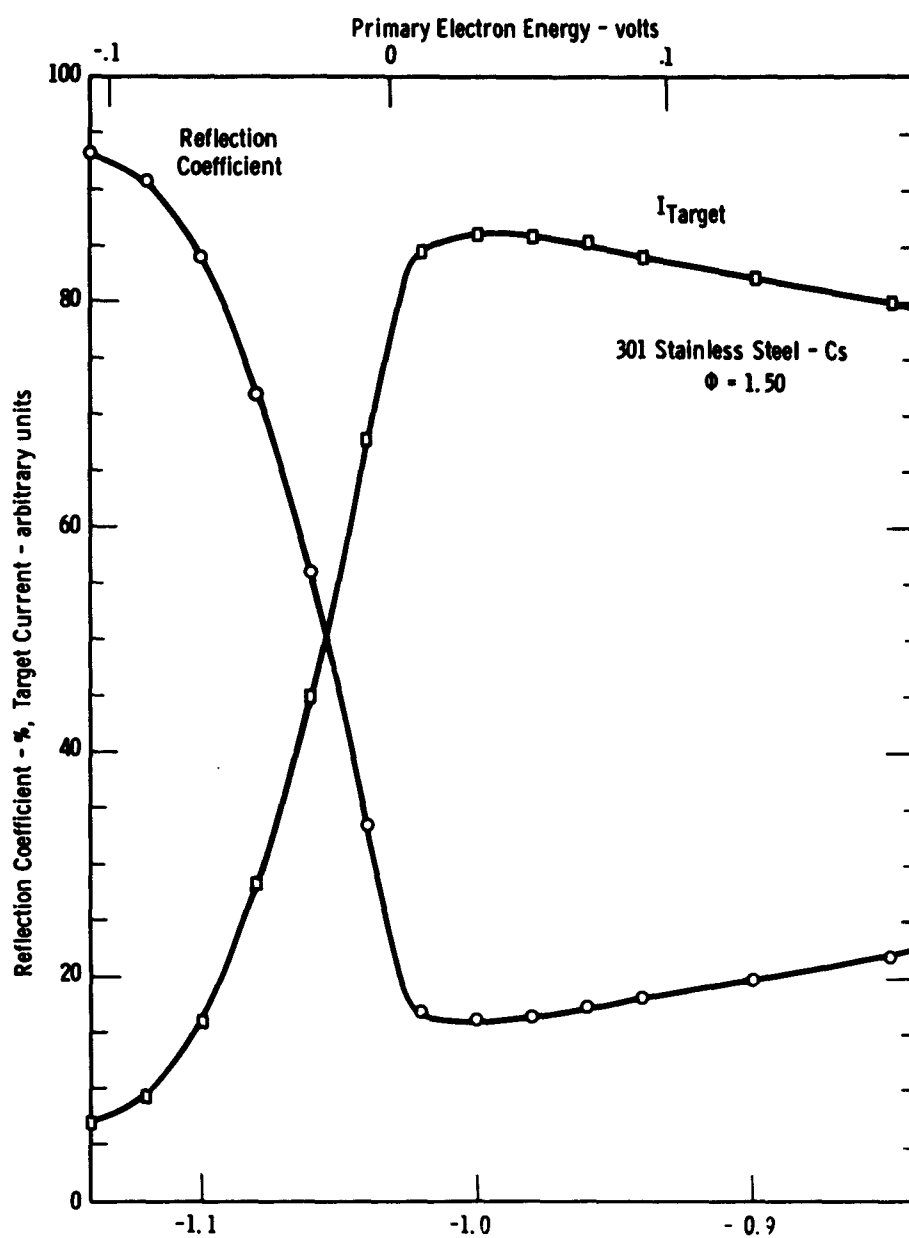


Fig. 4-33. Measured reflection coefficient and target current for 301 Stainless Steel-Cs vs. primary electron energy and potential E_h near zero primary energy. $\phi = 1.50$ eV.

Figure 4-34 withdrawn

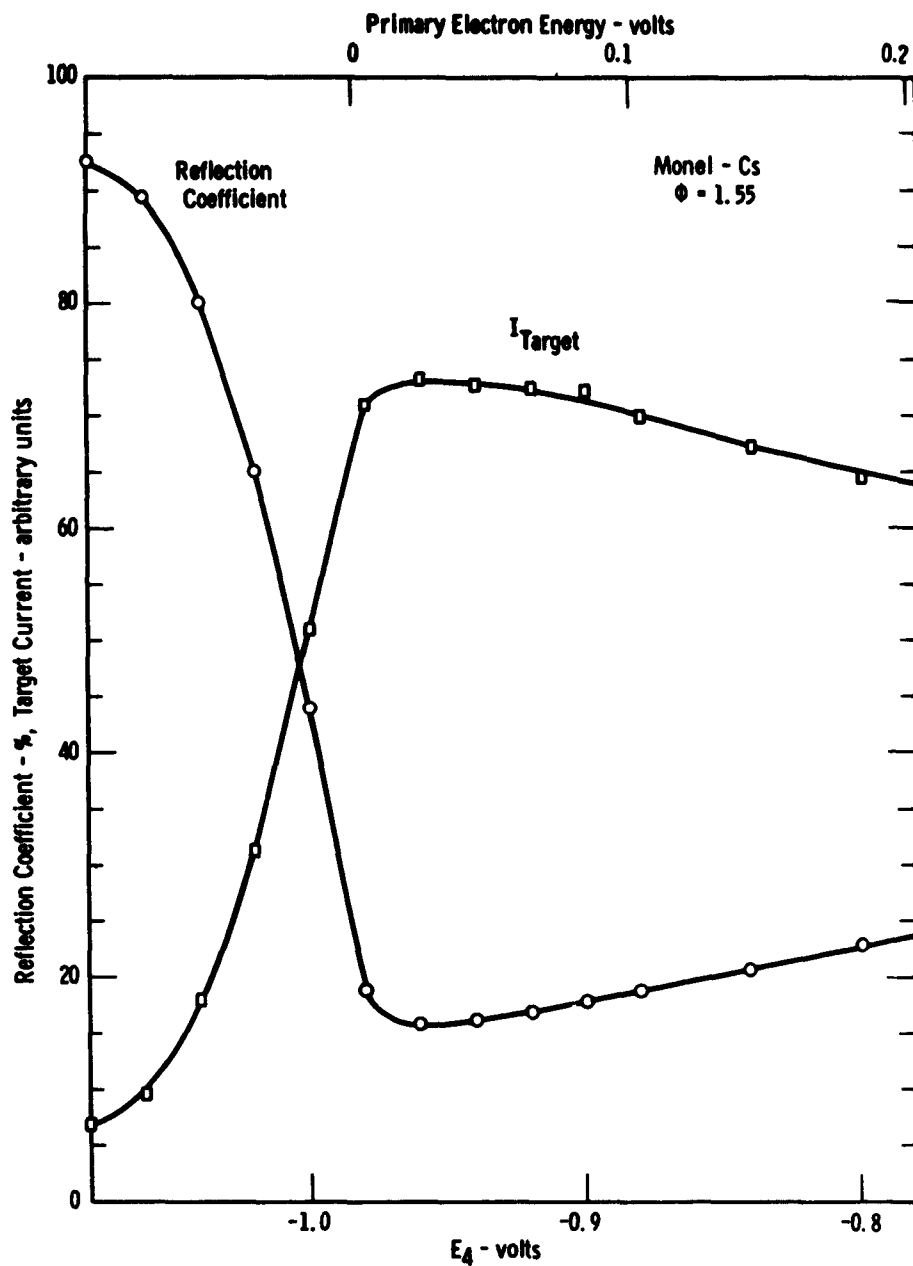


Fig. 4-35. Measured reflection coefficient and target current for Monel-Cs vs. primary electron energy and potential E_4 near zero primary energy. $\phi = 1.55$ eV.

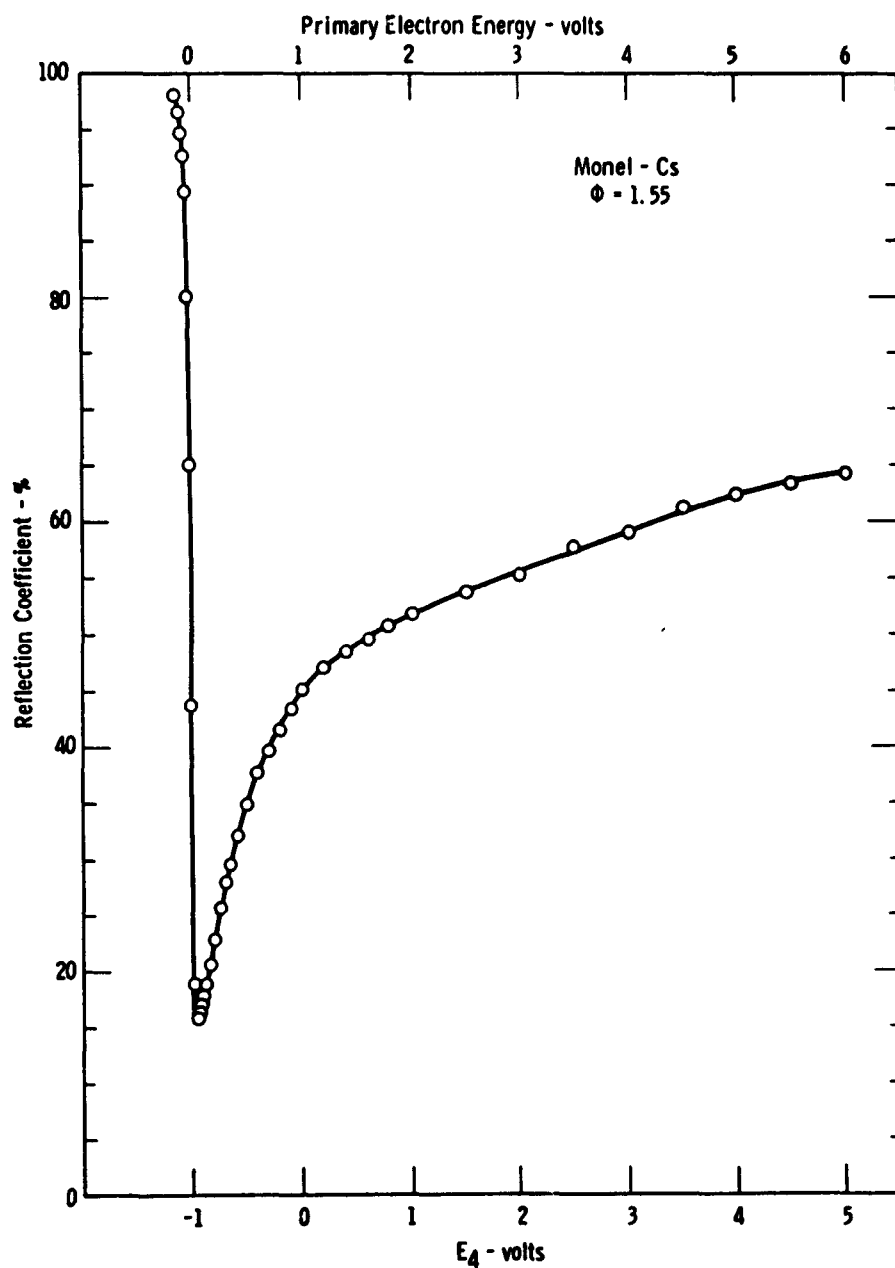


Fig. 4-36. Measured reflection coefficient for Monel-Cs vs. primary electron energy and potential E_4 . $\phi = 1.55$ eV.

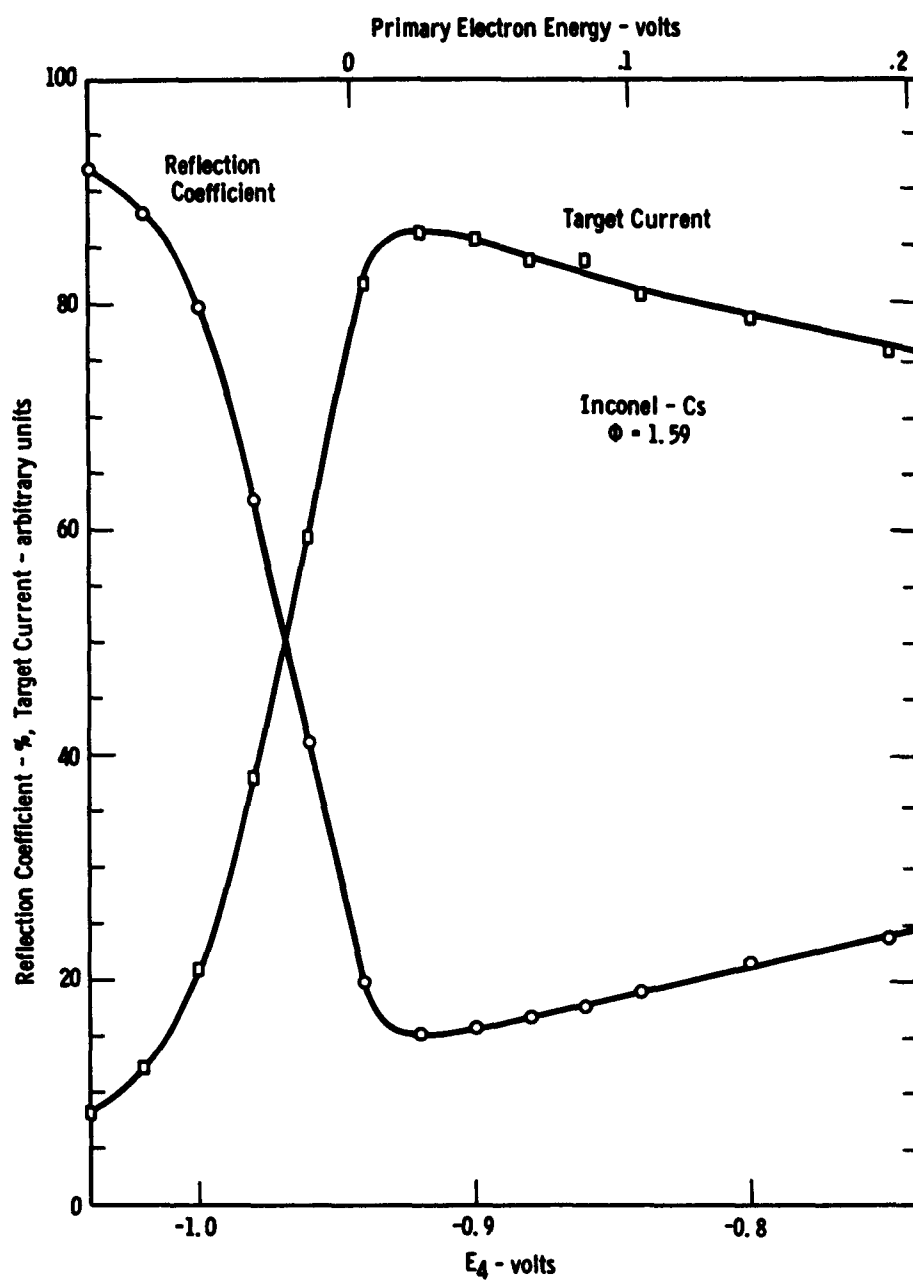


Fig. 4-37. Measured reflection coefficient and target current for Inconel-Cs target vs. primary electron energy and potential E_4 near zero primary energy. $\phi = 1.59$ eV.

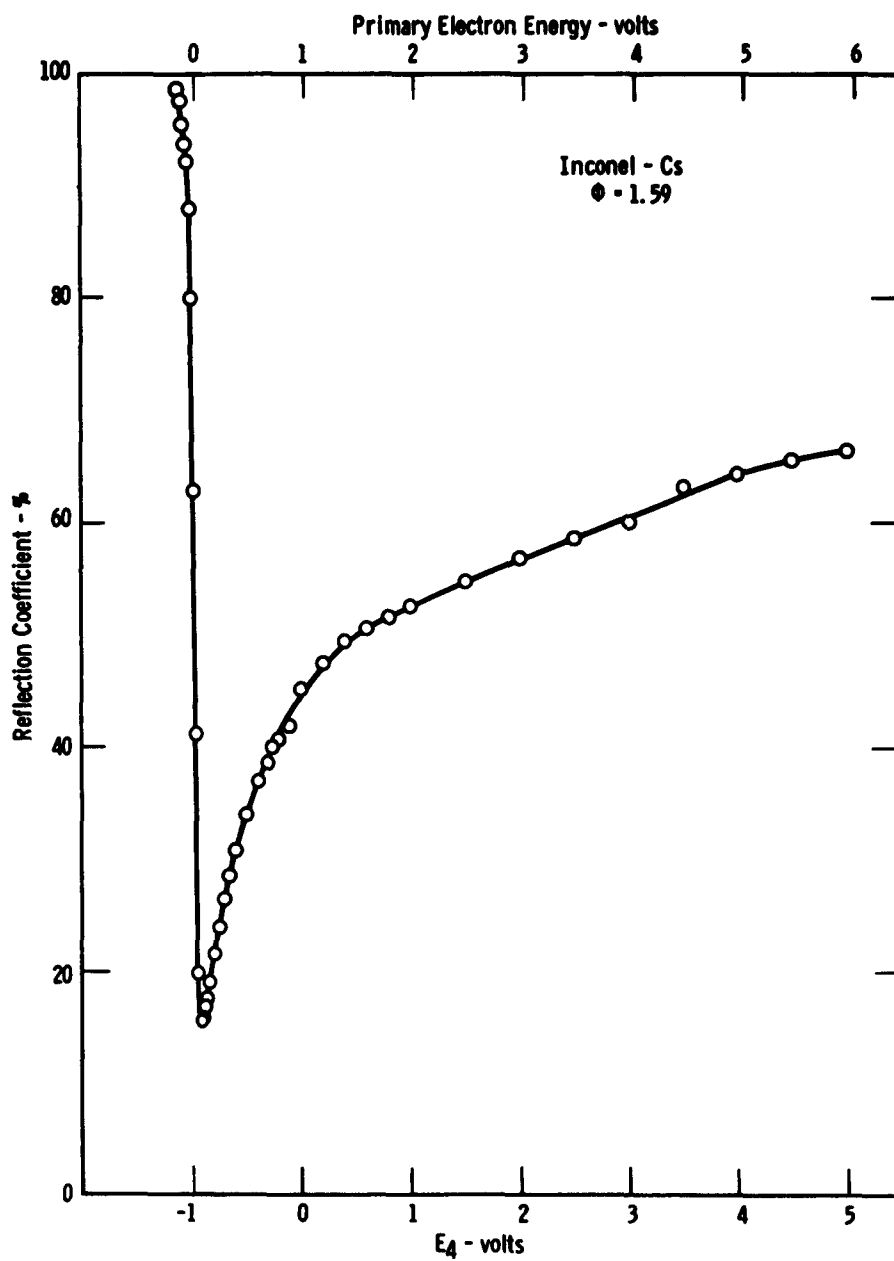


Fig. 4-38. Measured reflection coefficient for Inconel-Cs vs. primary electron energy and potential E_4 . $\phi = 1.59$ eV.

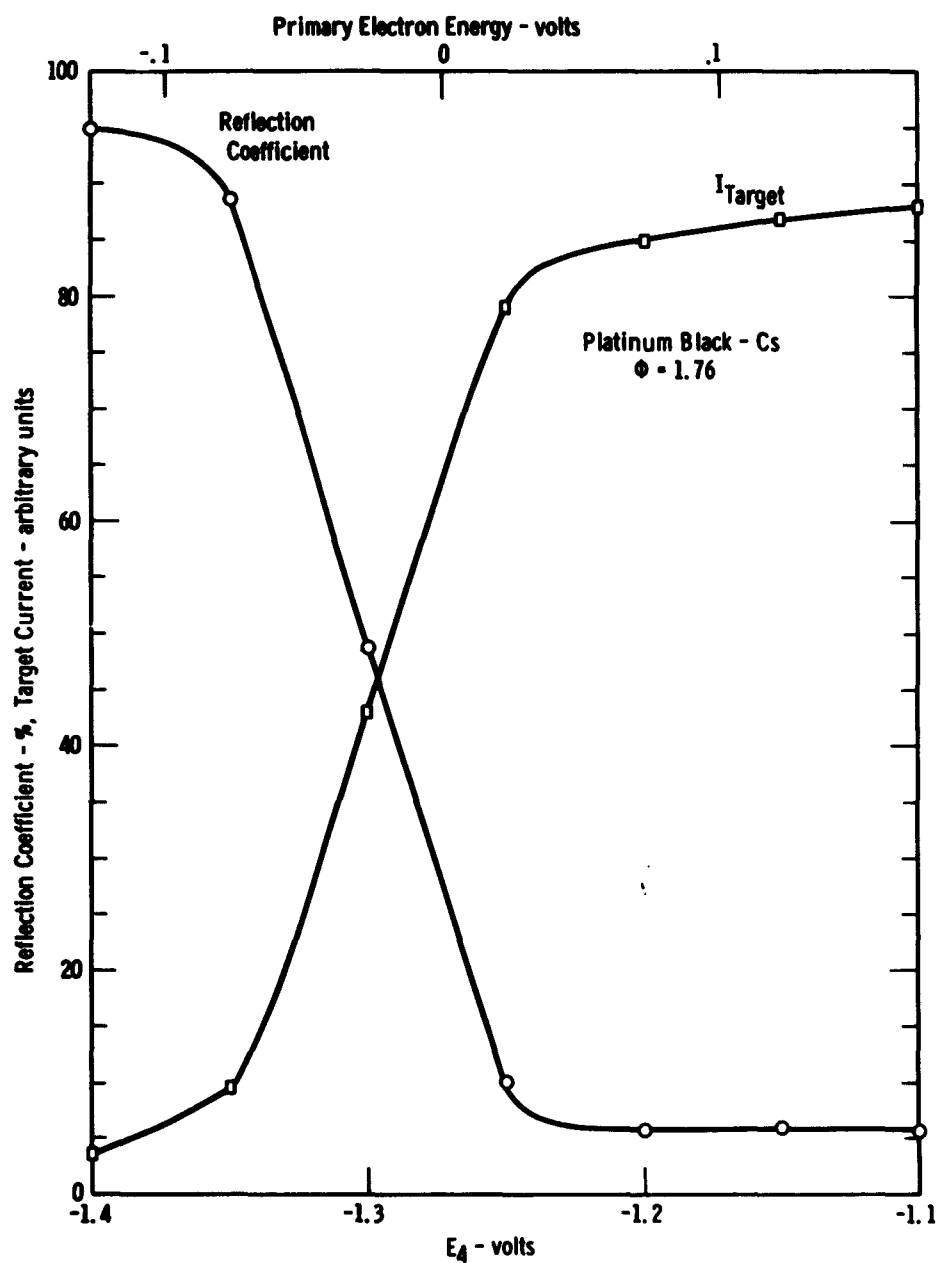


Fig. 4-39. Measured reflection coefficient and target current for Platinum Black-Cs target vs. primary electron energy and potential E_4 near zero primary energy. $\phi = 1.76$ eV.

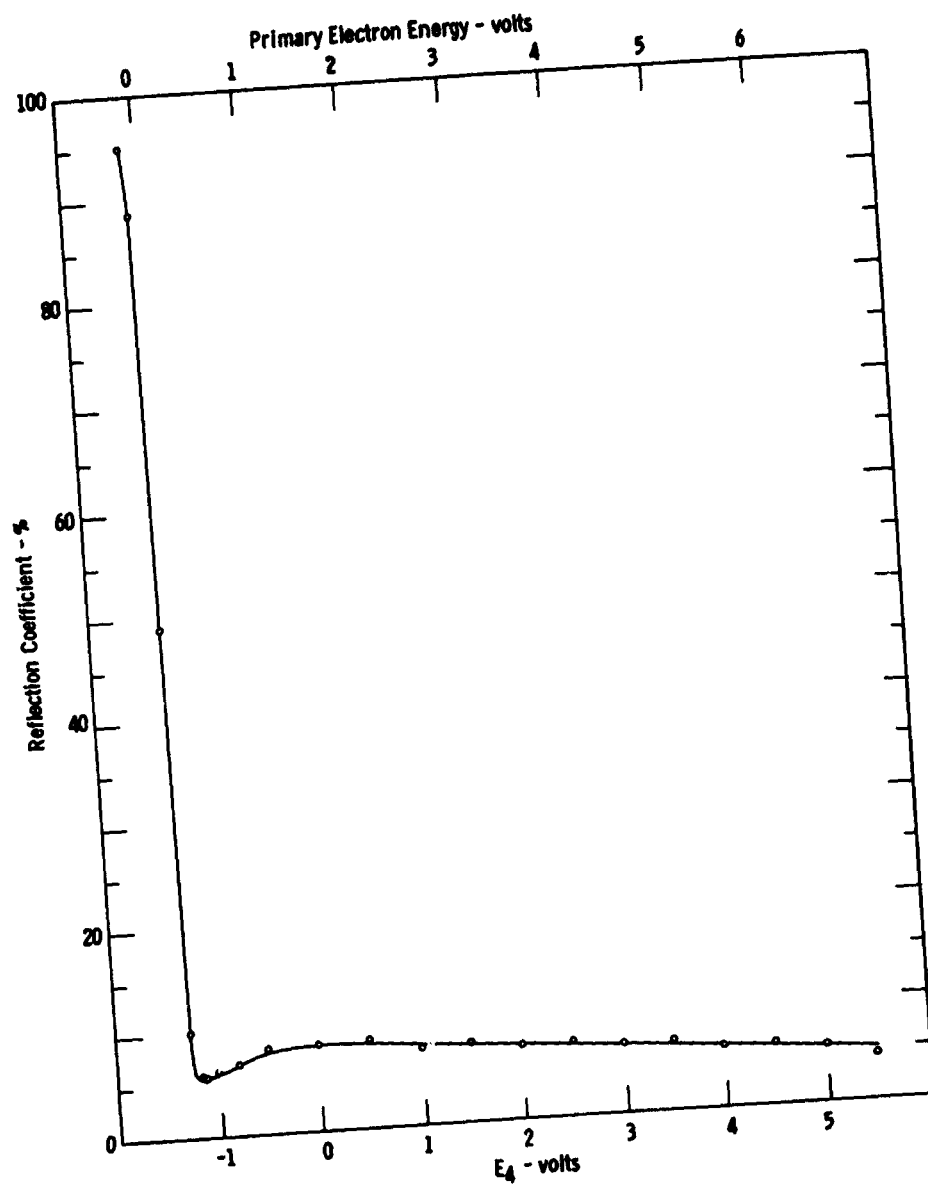


Fig. 4-40. Measured reflection coefficient for Platinum Black-Cs vs. primary electron energy and potential E_4 . $\phi = 1.76$ eV.

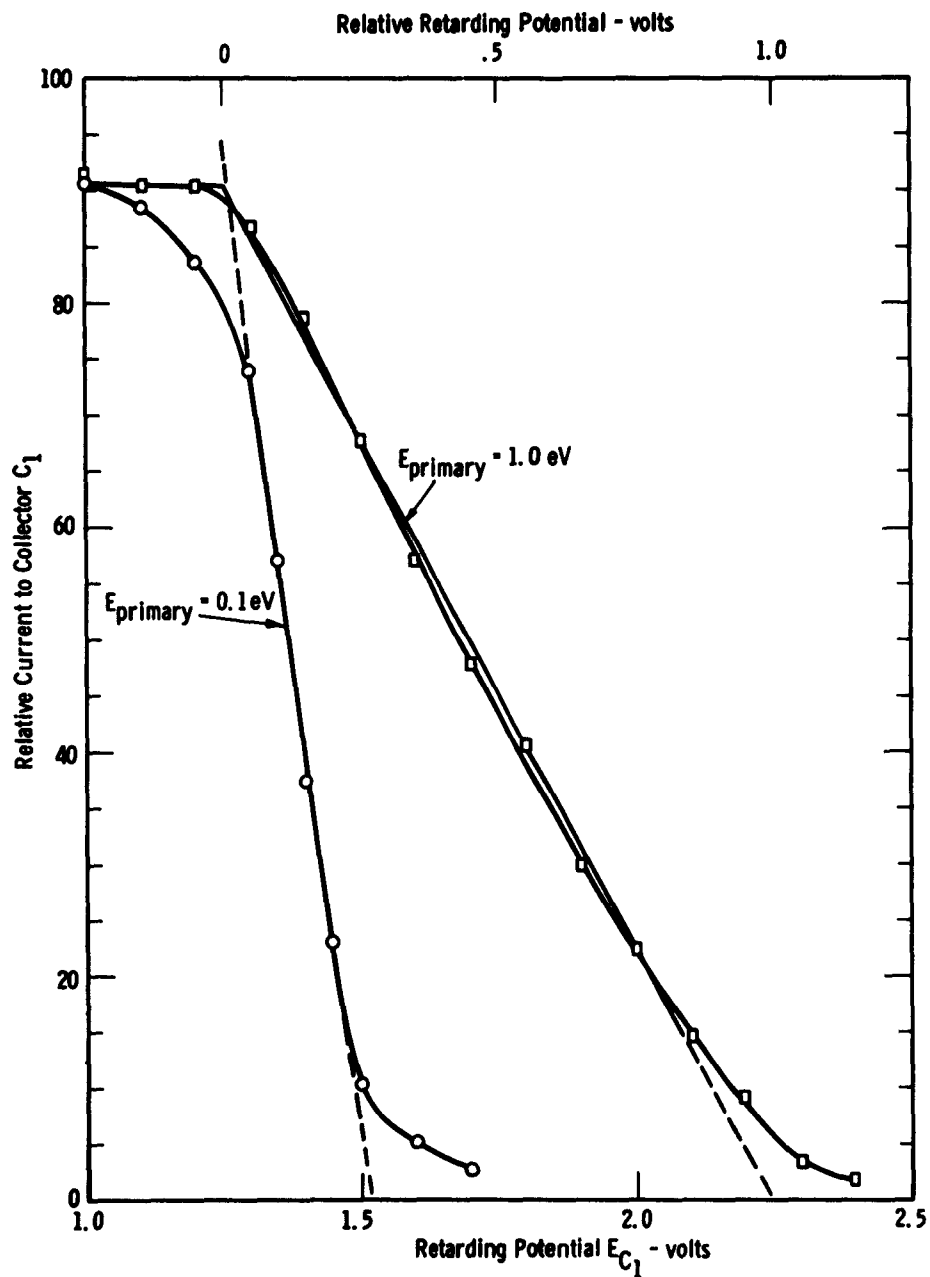


Fig. 4-41. Retarding potential plots showing relative current to collector C_1 vs. retarding potential on C_1 . Target is Cu-Cs with $\phi = 3.70 \text{ eV}$.

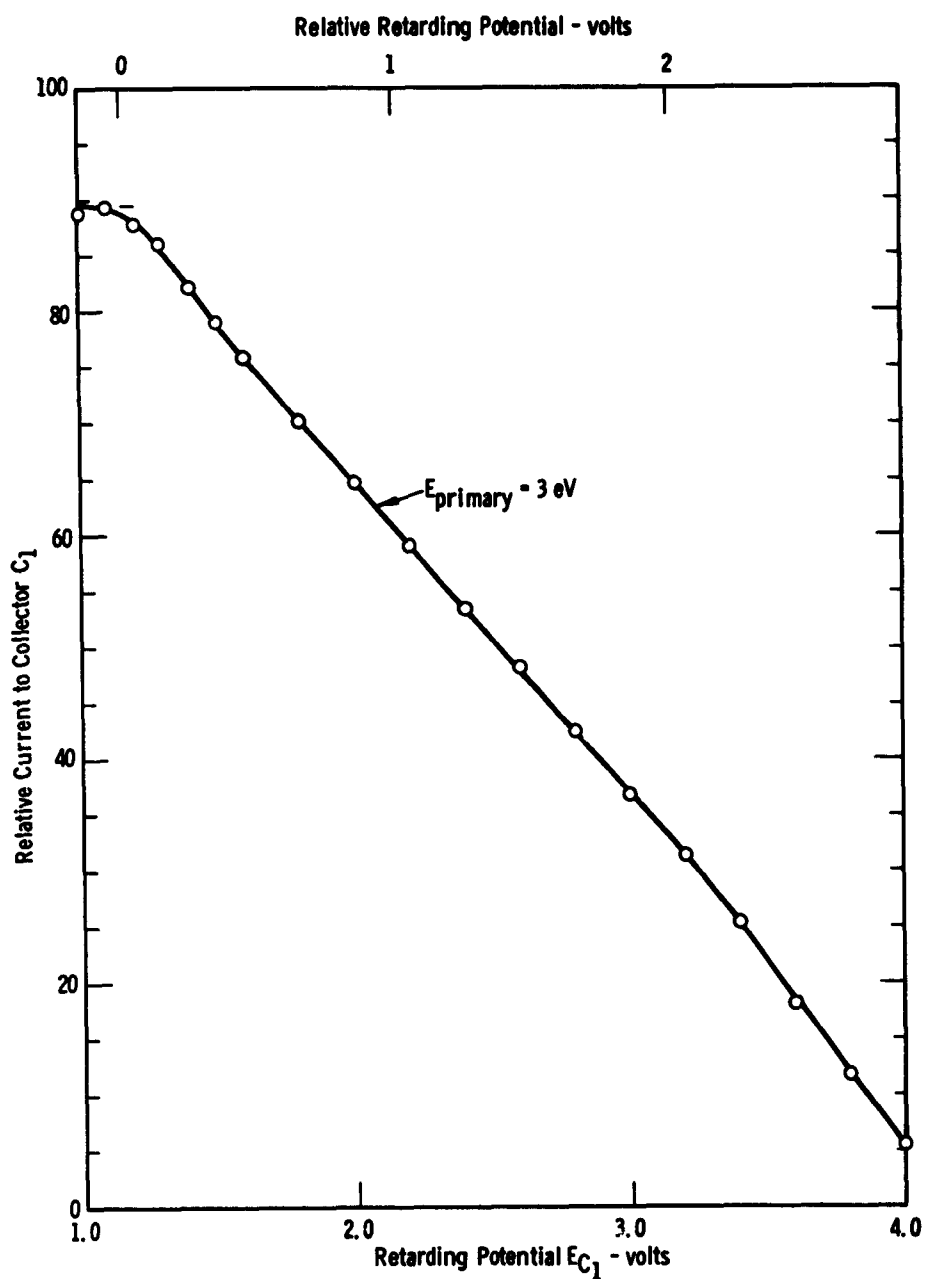


Fig. 4-42. Retarding potential plots showing relative current to collector C_1 vs. retarding potential on C_1 . Target is Cu-Cs with $\phi = 3.70 \text{ eV}$.

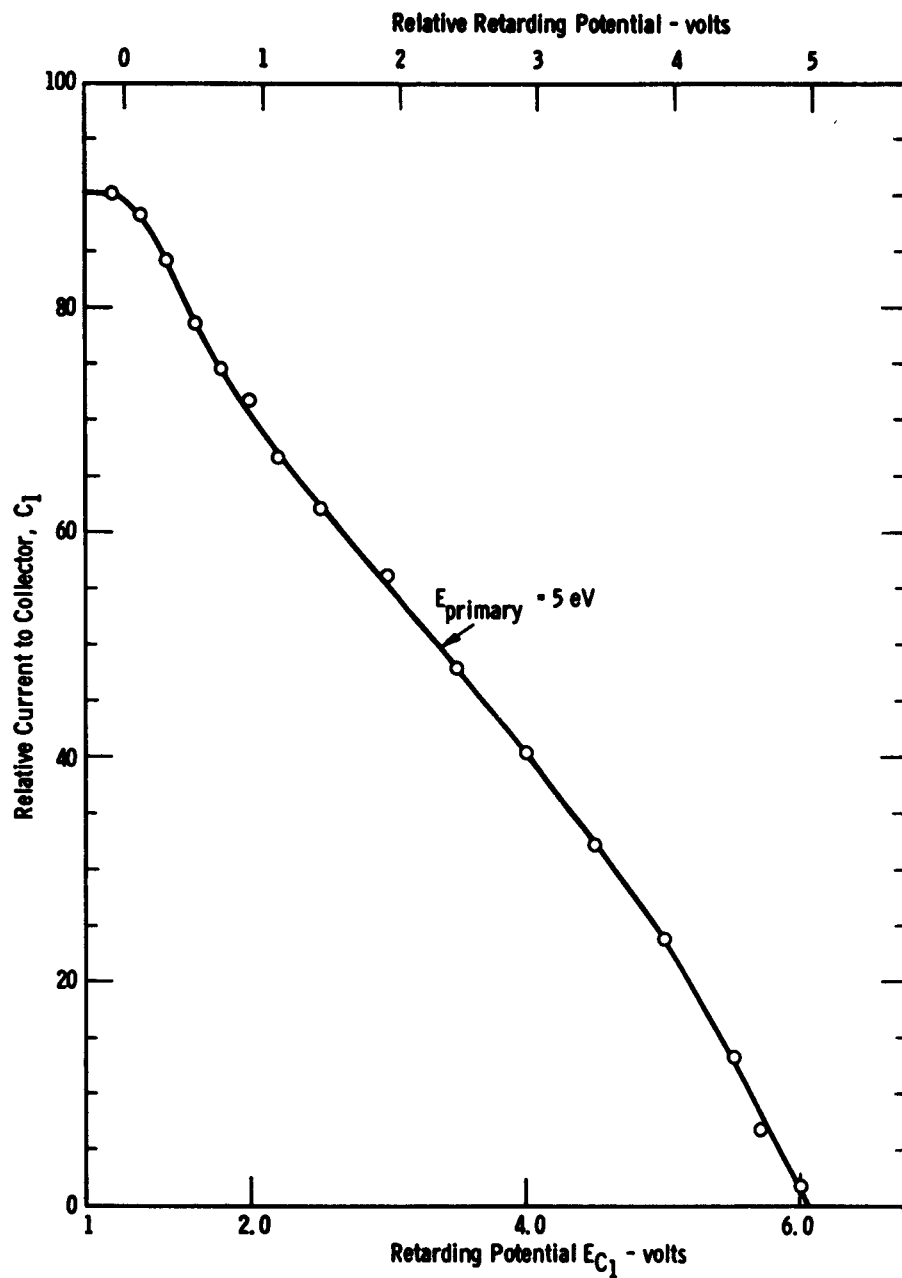


Fig. 4-43. Retarding potential plots showing relative current to collector C_1 vs. retarding potential on C_1 . Target is ^{63}Cu -Cs with $\phi = 3.70 \text{ eV}$.

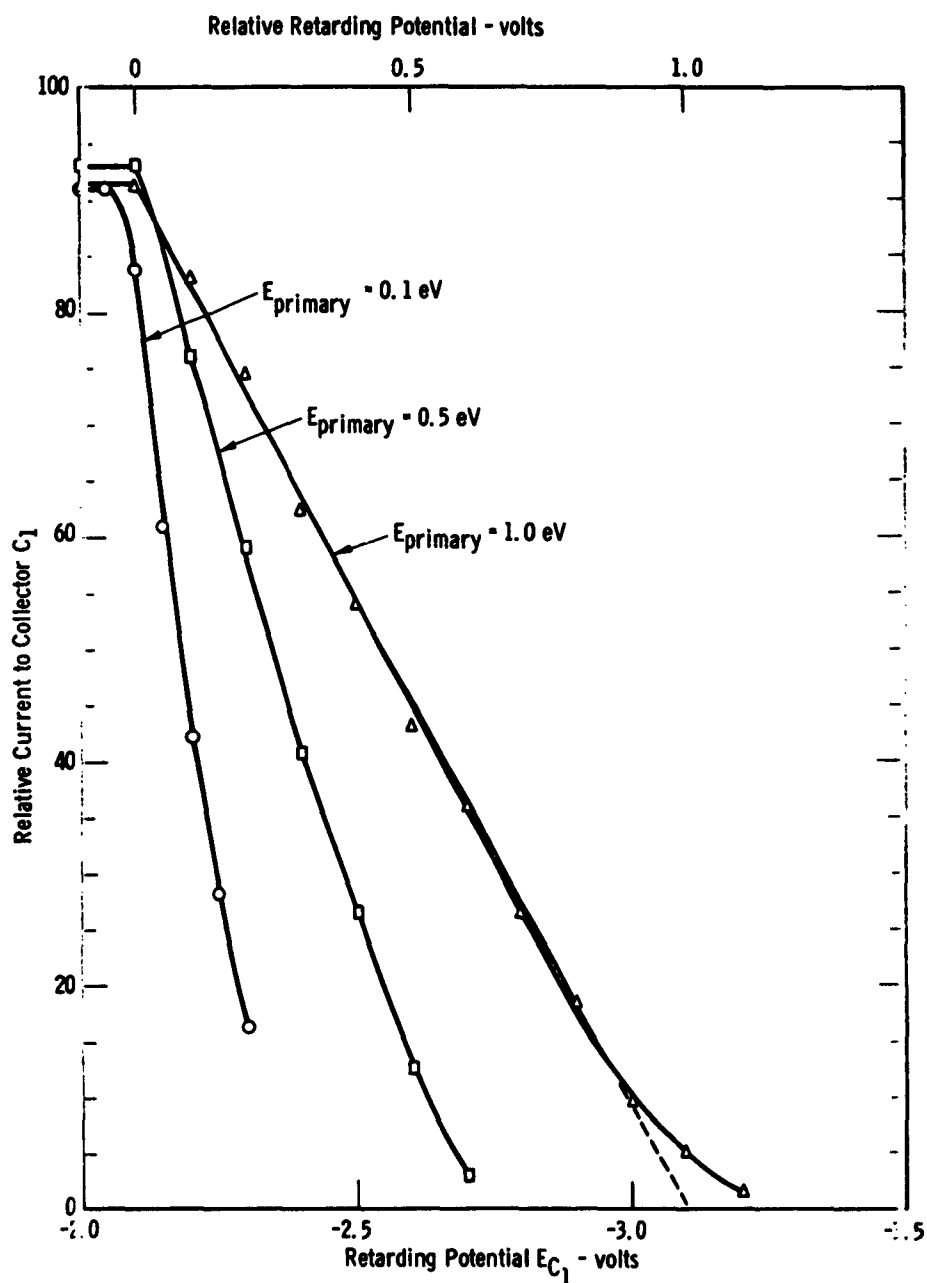


Fig. 4-44. Retarding potential plots showing relative current to collector C_1 vs. retarding potential on C_1 . Target is Cu-Cs with $\phi = 1.63 \text{ eV}$.

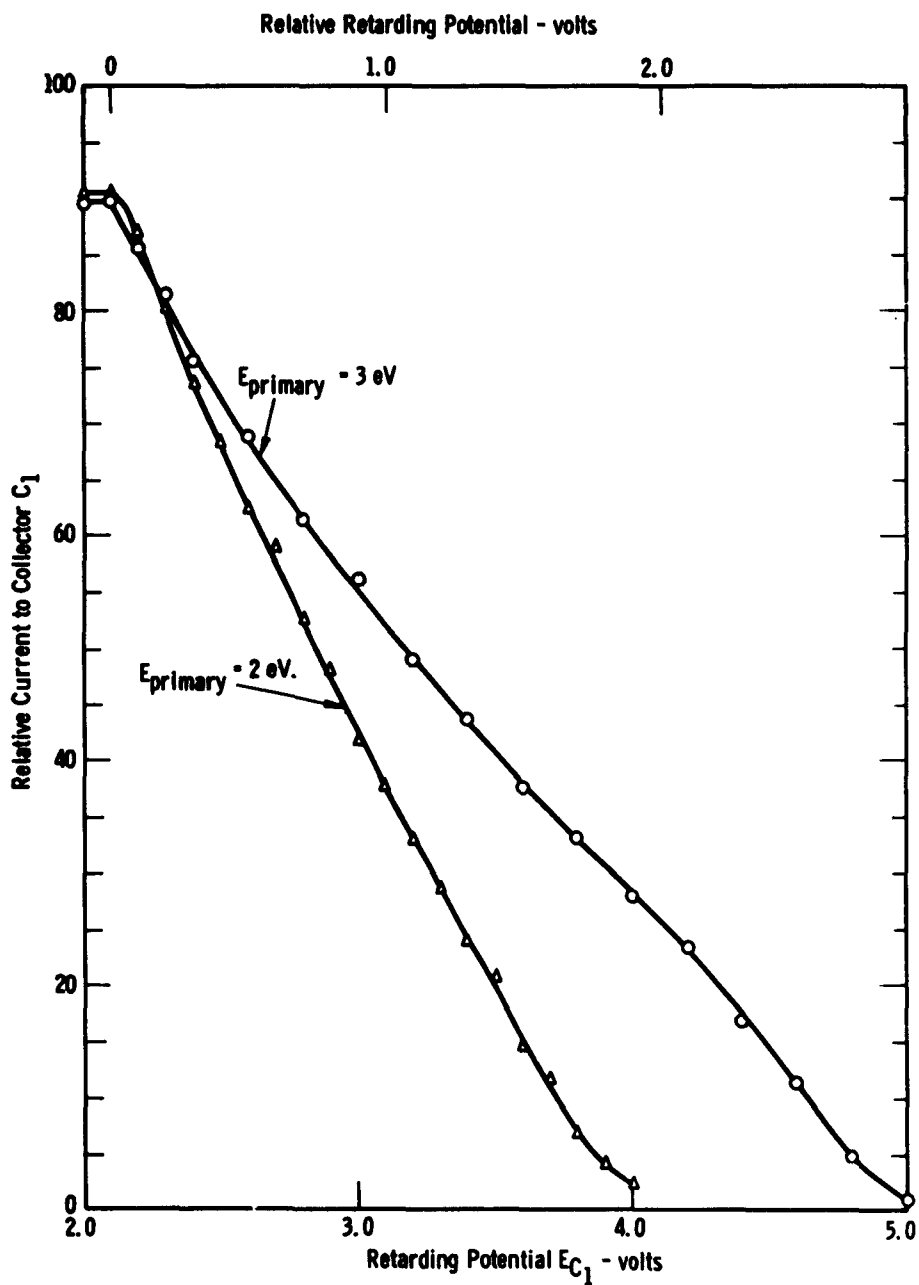


Fig. 4-45. Retarding potential plots showing relative current to collector C_1 vs. retarding potential on C_1 . Target is Cu-Cs with $\phi = 1.63 \text{ eV}$.

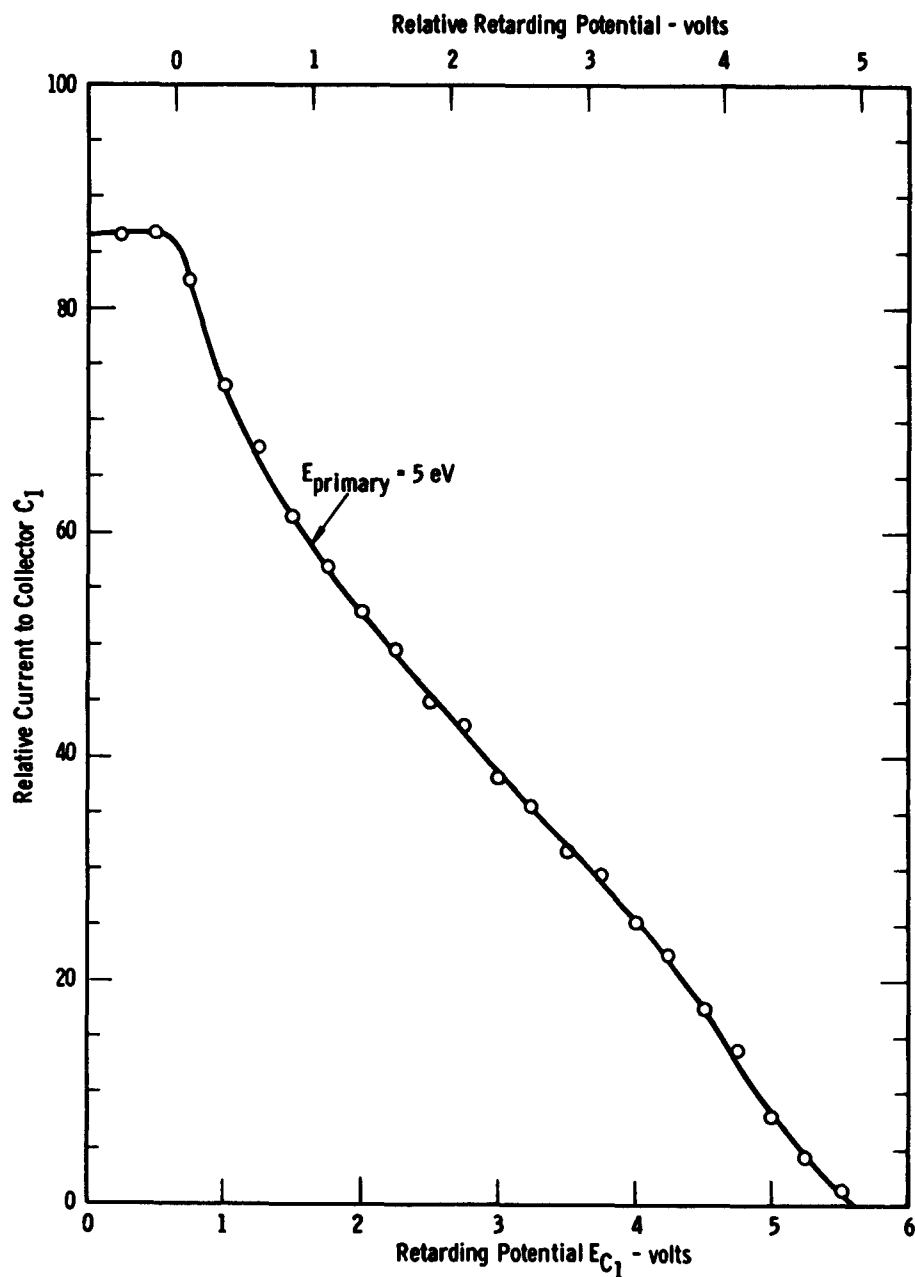


Fig. 4-46. Retarding potential plots showing relative current to collector C_1 vs. retarding potential on C_1 . Target is Cu-Cs with $\phi = 1.63 \text{ eV}$.

CHAPTER FIVE

THERMIONIC DIODE CURRENTS IN TRANSVERSE MAGNETIC FIELDS
AND SCATTERING OF ELECTRONS BY CESIUM ATOMS

The transport of electrons from cathode to anode of a thermionic diode is impeded by the presence of a transverse magnetic field. If the electron flow is in a vacuum the well-known magnetron effect takes place. In a gas the electron diffusion and mobility are not reduced as greatly by the transverse magnetic field because the scattering of electrons by gas atoms randomizes the direction of electron motion with each collision.

For thermionic power converter diodes it has been recognized that the magnetic field induced by the diode current itself can be sufficient to seriously reduce cell current thus producing a practical upper limit to diode current-carrying capacity. Schock¹ has made extensive calculations on the effects of self-induced magnetic fields for thermionic diode currents in a vacuum. Houston² has made a few measurements in cesium vapor. More extensive and precise data are needed for converter design calculations. When this work was undertaken it also appeared that it might be possible to obtain information about the collision frequency and elastic scattering cross section of electrons in neutral cesium since on the basis of relations derived by Langmuir³ and Cobine⁴, the measurement of cell current in a gas should give a measure of the mobility. Our results, however, show that although the calculated cross sections are of the right order of magnitude, difficulties most likely associated with back diffusion of electrons to the emitter prevent the precise determination of scattering cross sections. Nonetheless the

data should be of considerable value in connection with converter design since the combined effects of electron transport and back diffusion in a transverse magnetic field in cesium vapor are not at present calculable from first principles.

An empirical result useful for converter design is obtained as follows:

$$\frac{I_0}{I} = 1 + \frac{4.8 \times 10^{-3} d^{1.7} B^2}{p^{1/2}}$$

where I_0 is the current in the absence of the magnetic field, I with magnetic field, d is emitter-collector spacing in inches, B is magnetic field in gauss and p is Cs pressure in mm Hg.

Cell current measurements were made with cells of two different structures as shown in Figure 5-1. Both cells utilized a 0.005 inch by 0.080 inch by 1 inch tungsten ribbon filament heated directly with halfwave rectified A.C. power. The anode in one case consisted of plane parallel copper plates with cathode-anode spacings of 0.020 inches. The anode in the other case was a 0.500 inch diameter stainless steel cylinder which thus had an average cathode-anode spacing of 0.225 inches, about an order of magnitude larger than the first cell. The tubes were mounted in an oven inside a solenoid magnet the field of which could be continually varied up to about 350 gauss.

The circuit shown in Figure 5-2 was used for the measurements. Cell currents were determined by the voltage drop across a known resistance during the time that the filament voltage was zero, using a calibrated oscilloscope. To reduce the scatter of the data associated with changes in filament emission a switch was used that simultaneously closed the

magnet current circuit and replaced the cell load resistance by an alternative resistance box. Thus the load resistance when the magnetic field was present could be increased to compensate for the reduced cell current. In this way the cell voltage and internal fields remained constant. A Clare Hg-wetted relay synchronously opened the anode lead during the filament heating pulse. A battery was added to the circuit to supply positive potentials to the anode. The required cesium vapor pressure was established by immersing a side tube containing the cesium ampule in a Sn-Pb eutectic bath which could be controlled to within about 1°C . The rest of the envelope was heated to a higher temperature to prevent Cs condensation. The communicating apertures between the diode and the tube envelope were sufficient that estimates of the thermal transpiration effect lead to the conclusion that appreciable pressure differences do not exist between the cathode-anode region and the cesium reservoir over most of the region of interest.

The results of the measurements were found to depend upon filament temperature and cell potential as well as expected dependence upon cesium pressure and magnetic field strength. With the larger spacing cell the results with lower filament temperatures and higher filament temperatures were not far different while intermediate temperatures gave a greater reduction in cell current with magnetic field. Since at the higher temperature used one would expect sufficient ions to be formed by contact ionization at the cathode to neutralize the electron space charge and since the space charge is not as severe a problem at the lowest cathode temperatures where electron emission is smaller, the higher current reductions from intermediate temperatures

appear to be associated with additional space charge effects associated with the reduced electron mobility in a magnetic field. In Figure 5-3 are plotted some of the results for the larger spacing cell. We have plotted data only for the higher emitter temperature (2000°K) where the effects of space charge should be negligible. It should be remembered, however, that the magnetic field greatly decreases the electron mobility without a comparable decrease in the cesium ion mobility. The ratio of the current in the absence of the magnetic field to that with the magnetic field has been plotted vs. the square of the magnetic field strength for three cesium reservoir temperatures and two cell potentials. Note that the current reductions are somewhat less for higher anode potentials. Included is the curve for the cesium reservoir at room temperature--where electron-cesium atom scattering is negligible. Because of the contact potential difference, the curve obtained with a battery potential of 1.56 volts probably corresponds to approximately a zero field condition between the electrodes.

Figure 5-4 shows the results for the closer spacing cell. All of the I_0/I vs. B^2 curves in Figure 4 are linear, except the one corresponding to $T_{\text{Cs}} = 250^{\circ}\text{C}$ with a filament temperature of 609°K and +8.8 volts cell potential. Most of the results with this cell were independent of cell potential as shown in Figure 5-5 until potentials sufficient to cause inelastic scattering and perhaps volume ionization are reached. It is evident that there is considerable variation in the slopes. The decrease in slope with increase in cesium pressure is less than might be expected as discussed in the next section.

In the low magnetic field region where qualitative comparison is possible the results are in reasonable agreement with those of Houston².

The calculations of Schock¹ for electron transport perpendicular to the magnetic field in a vacuum grossly overestimate the effect of the magnetic field when cesium vapor is present. One expects the electron transport in this case to be dominated by the relations for the mobility and diffusion in the magnetic field.⁵

$$\mu = \frac{\mu_0}{(1 + \omega^2 \tau^2)}, \quad D = \frac{D_0}{(1 + \omega^2 \tau^2)} \quad (1)$$

where μ_0 and D_0 are the values in the absence of the magnetic field, $\omega = \frac{e}{m} B$ and τ is the period between collisions. Equations (1) are strictly valid only if the collision frequency is independent of electron velocity but are also a good approximation in other cases for sufficiently high magnetic fields.

In cases where there is no space charge and only elastic collisions Langmuir³ found that

$$I = \frac{4}{3} I_{\text{sat}} \frac{\lambda}{x} \frac{V_1/V_0}{\ln(1 + V_1/V_0)}$$

where I_{sat} is the saturation current, λ is the electron mfp, x is plate separation, V_1 is cell potential and V_0 is the initial electron energy. Since both the diffusion constant and mobility are proportional to the mean free path one would expect in this case that

$$\frac{I_0}{I} = \frac{\mu_0}{\mu} = 1 + \omega^2 \tau^2 \quad (2)$$

where I_0 , μ_0 are the values without and I , μ in the presence of a

transverse magnetic field. The question of space charge limited currents in the presence of a scattering medium has been considered by Cobine⁴ and in greater detail by Shockley and Prim⁶. Where initial velocities can be neglected they obtain

$$I = \frac{9K\epsilon_0\mu V^2}{8x^3} \quad (3)$$

for the plane parallel case with electrode spacing x , a result analogous to the Langmuir-Child's Law for the vacuum diode. If Equation (3) were to apply then Equation (2) would also be valid. Equation (3) does assume that the electron mobility is independent of energy, as has recently been pointed out by Forman⁷ who derives another expression valid for rare gases under certain conditions.

Our measurements shown in Figures 5-3 and 5-4 are approximately consistent with a relation of the form $\frac{I_0}{I} = 1 + K B^2$ as expected from Equation (2). But there is some scatter in the data and some departure from linearity. Furthermore, the slope K of the curve $\frac{I_0}{I}$ vs B^2 , which should be proportional to τ^2 and hence to $\frac{1}{\text{pressure}^2}$, is found not to

vary in the proper way with pressure. There is also a dependence on electrode spacing. The most likely source of this discrepancy would appear to be the back diffusion of electrons from the plasma to the electrodes which might reasonably be expected to depend upon pressure, magnetic field and spacing. While, in principle, measurements of this sort might be used with an assumed mobility dependence to determine the back diffusion contribution, it is felt that the results are not sufficiently precise to merit this.

For converter operation the results, of course, are directly applicable. The results in Figures 5-3 and 5-4 should give reasonable estimates within perhaps a factor of 2 of the magnitude of the effect. For other spacings and pressures, estimates can be made by use of the empirical result

$$\frac{I_o}{I} = 1 + \frac{4.8 \times 10^{-3} d^{1.7} B^2}{p^{1/2}}$$

where d is the emitter-collector spacing in inches, B is in gauss and p is the pressure in mm Hg. The reduction in cell current should be diminished somewhat at higher ion concentrations because of the larger scattering cross section of Cs^+ compared to neutral Cs .

A summary of the available data on electron scattering by Cs atoms is shown in Figure 5-6. The solid curve shows Brode's⁸ data. The circles show the results as originally given by Boeckner and Mohler,⁹ but in a later paper they indicated that their electron density measurements were in error at the higher pressures and the squares show these results corrected by Phelps¹⁰ using the results given by Mohler's paper. Steinberg's¹¹ data was also used to calculate collision frequencies and his values at the two lower Cs pressures are shown here although his electron densities presumably also may be in error. It should be noted that the data of Brode need not necessarily agree with that of Mohler since Mohler's results are for a mobility measurement while Brode's measurements would be sensitive to very small angle scattering. One might expect Brode's results to yield a larger collision frequency than Mohler's contrary to Figure 5-6.

REFERENCES

1. A Schock, J. Appl. Phys. 31, 1978 (1960).
2. V. C. Wilson ARS Space Power Systems Conf., Santa Monica, California, September 27-30, 1960. Data of Houston.
3. I. Langmuir, Phys. Rev. 38, 1656 (1931).
4. J. D. Cobine, Gaseous Conductors, McGraw-Hill Book Co., Inc. New York (1941).
5. W. P. Allis, Handbuch der Physik XXI, 383, Springer-Verlag, Berlin (1956).
6. W. Shockley and R. C. Prim, Phys. Rev. 90, 753, (1953).
7. R. Forman, Phys. Rev. 123, 1537 (1961).
8. R. B. Brode, Phys. Rev. 34, 673 (1929).
9. C. Bochner and F. L. Mohler, Bur. Stand. Jour. Res. 10, 357 (1933).
10. A. V. Phelps, Private Communication.
11. R. K. Steinberg, Jour. Appl. Phys. 21, 1028 (1950).

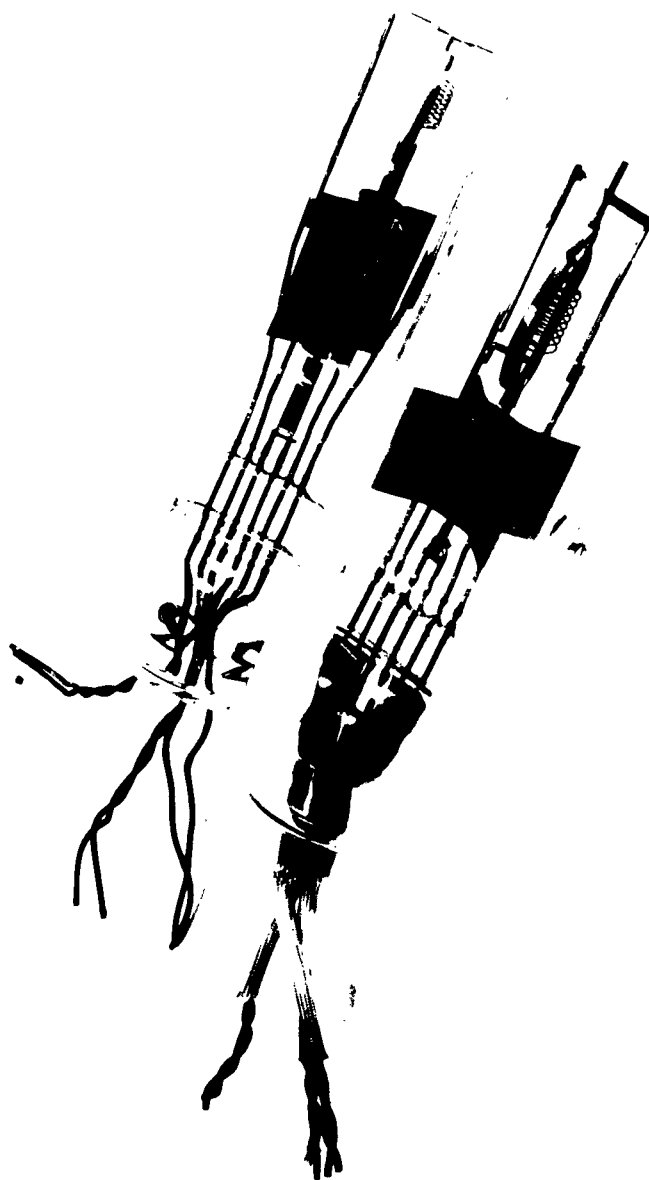


Fig. 5-1. Photograph of the Cells Used for Measurements

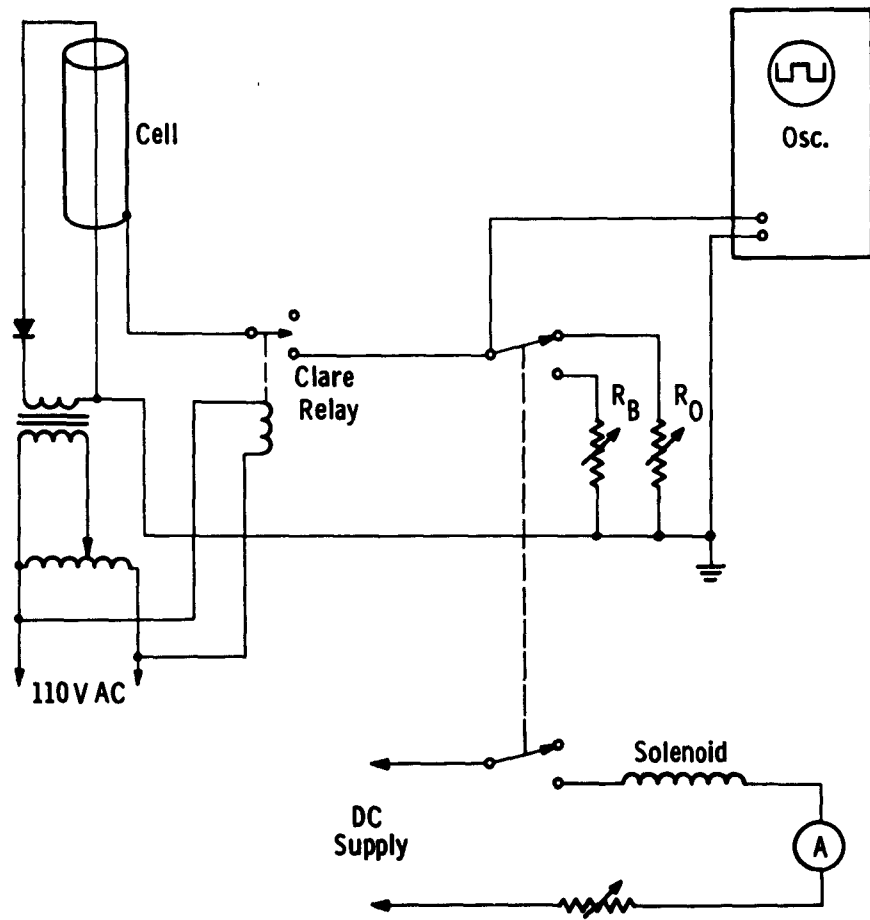


Fig. 5-2. Measuring Circuit

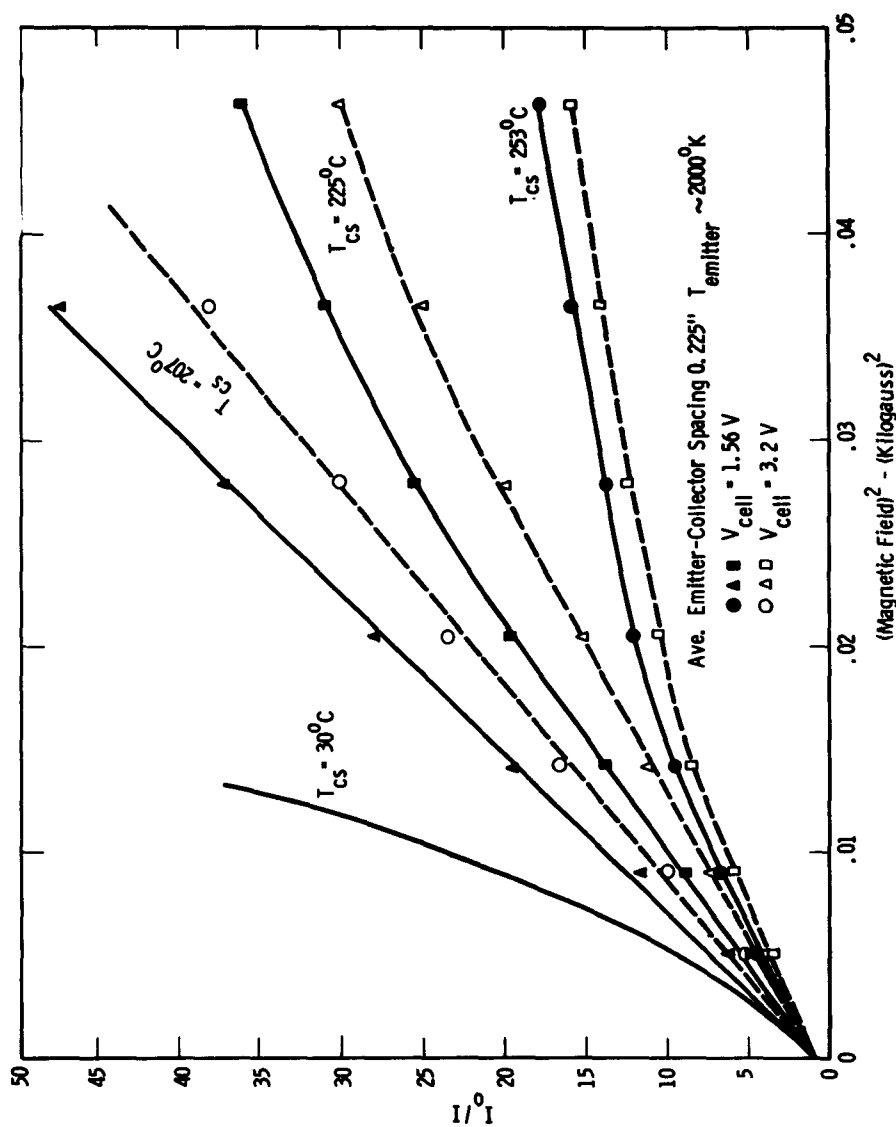


Fig. 5-3. I_0/I vs $(\text{Magnetic Field})^2$ for 0.225 " Spacing

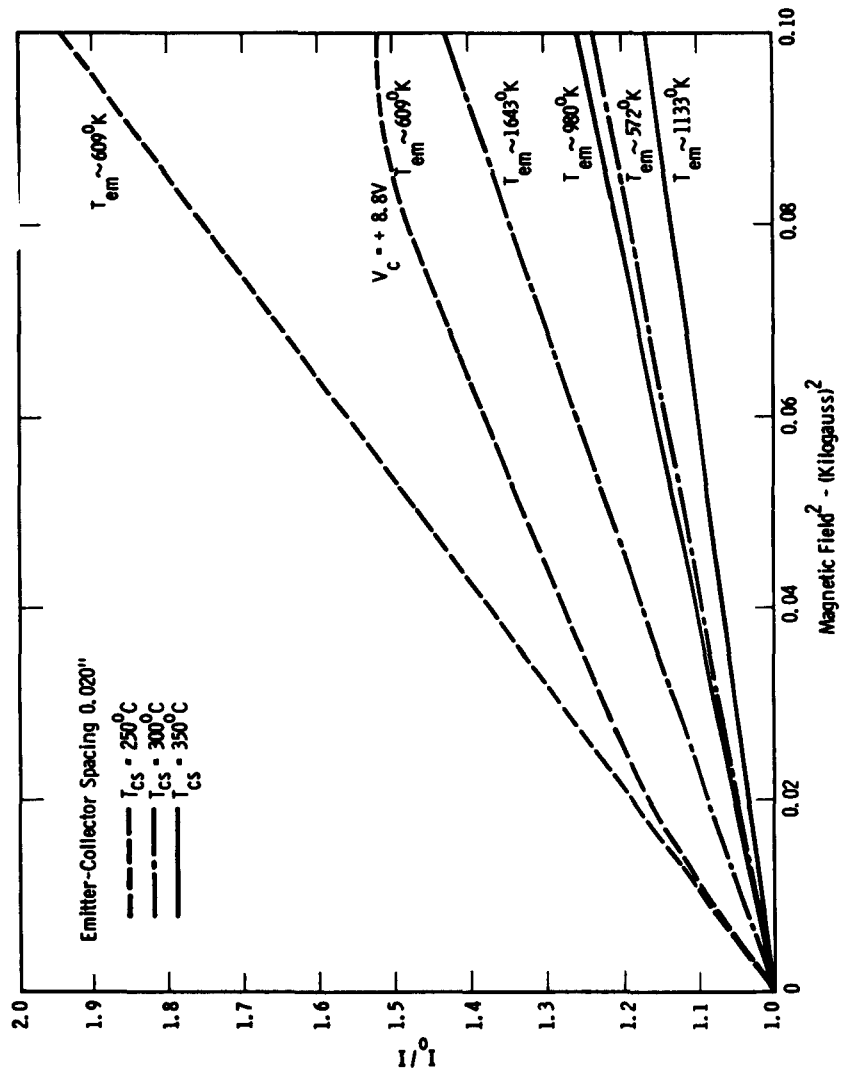


Fig. 5-4. I_0/I vs $(\text{Magnetic Field})^2$ for 0.20" Spacing

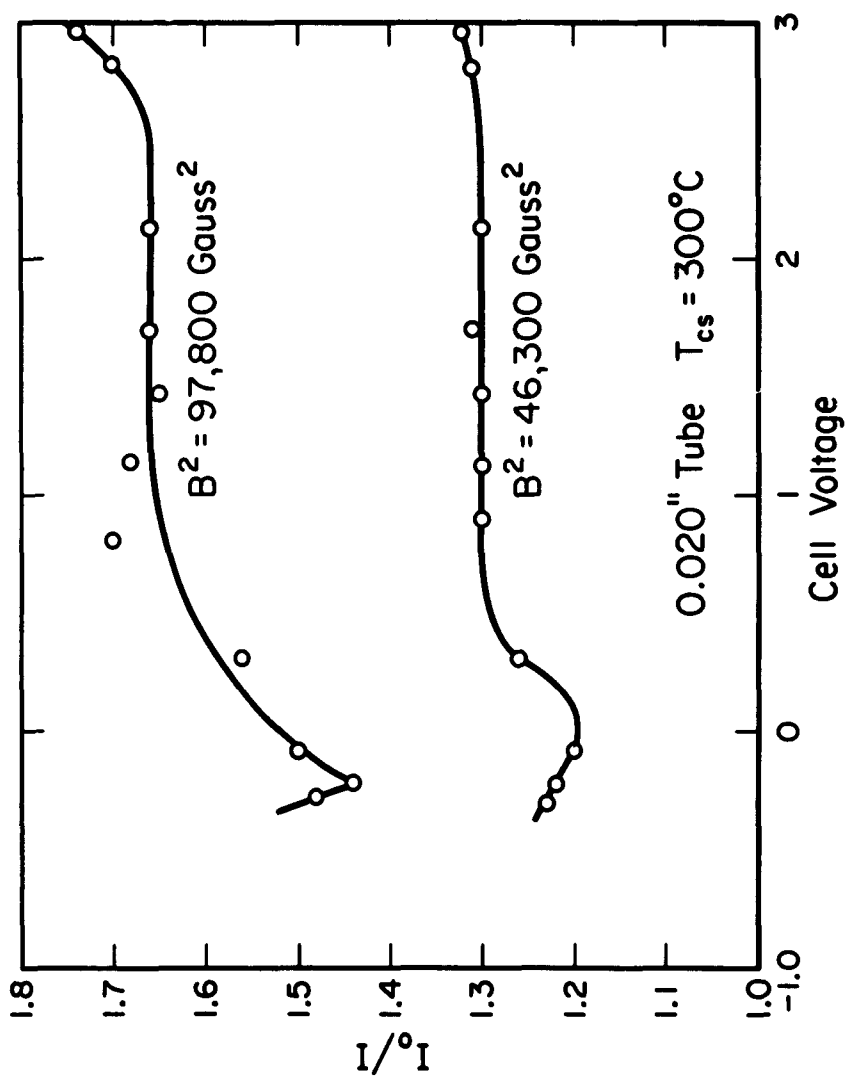


Fig. 5-5. Dependence of Current Ratio on Cell Potential

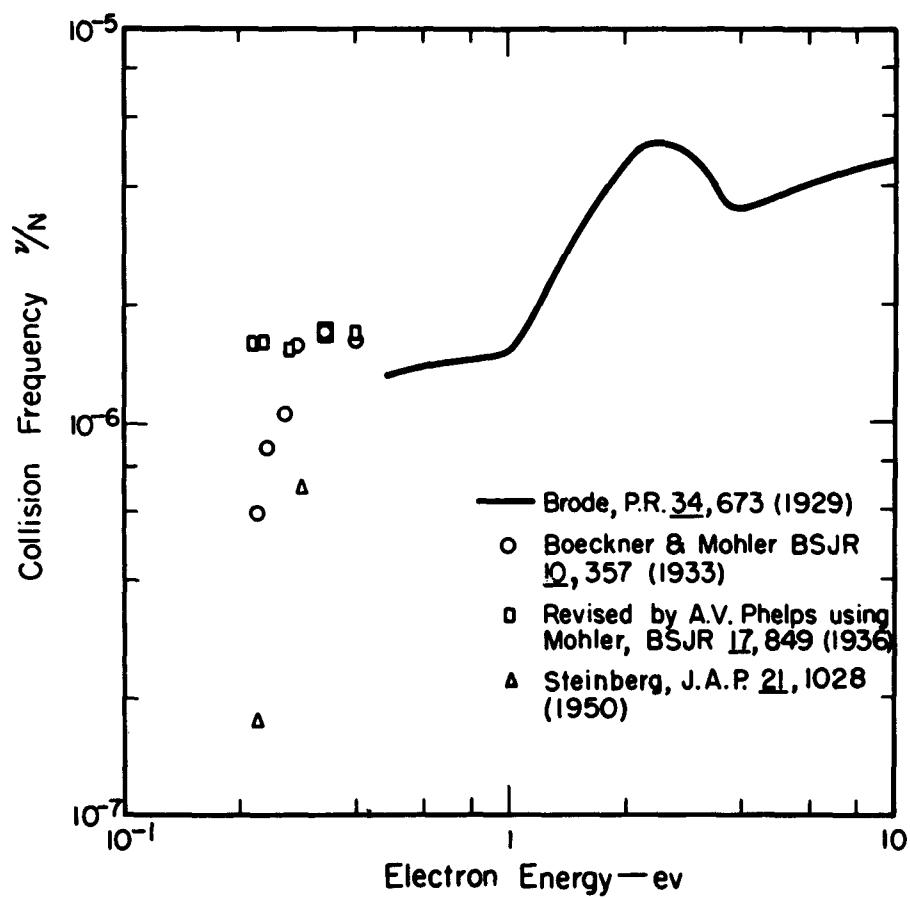


Fig. 5-6. Available Data on Electron Scattering

CHAPTER SIX

THERMAL CONDUCTIVITY OF CESIUM AND RUBIDIUM VAPOR

Recent developments in thermionic conversion have indicated that a favorable regime of operation is one of high cesium pressure and rather small emitter-collector spacings. High converter efficiencies have been demonstrated for pressures around 1 mm Hg. and spacings around 0.005". Under these conditions thermal conduction through the cesium vapor may be a significant irreversible energy loss. Very little data is available in the literature concerning the transport properties of alkali vapors, so that the work described here should be useful in improving the estimates of thermionic converter efficiency.

The heat transfer by thermal conduction was determined by measuring the additional power required to maintain a hot ribbon filament at a fixed temperature with increasing cesium pressure. The filament was a 2 mm wide tungsten strip and the collector was a pair of nickel plates. One of the difficulties encountered with this type of cell was the effect of undetermined conduction losses at the ends of the filament into the supporting structures. This problem was overcome by incorporating two filaments in the cell, one of which is twice the length of the other. A photograph of this cell is shown in Figure 6-1. A double width collector accommodates both filaments. Both filaments have identical ends, so that for the same temperatures, the end losses are the same for both. If the measured power increments are ΔP_L and ΔP_{2L} for the filaments of length L and $2L$ respectively, and the cesium thermal

conduction losses are K_L and $2K_L$ respectively, then

$$\Delta P_L = K_L + \text{end losses}$$

$$\Delta P_{2L} = 2K_L + \text{end losses}$$

Since the end losses are the same, the difference between these two expressions is

$$\Delta P_{2L} - \Delta P_L = K_L,$$

thus canceling the error due to end effects, to first order.

The power supply for the filaments consisted of six volt storage batteries assisted by battery chargers, so that there was very little problem with drifting currents. All of the electrical measurements were made to four place accuracy with a $1\frac{1}{2}$ N K-2 potentiometer. The measuring circuit is shown in Figure 6-2. The long and short filaments are indicated as R_{f_1} and R_{f_2} , respectively. The potentiometer leads were built into the cell and put directly across the filaments, eliminating possible error due to voltage drops in the supporting structure. For any given temperature, the shorter filament required a greater current than the longer filament and this was supplied by the battery in the auxiliary circuit. By this means, the temperature of both filaments was kept the same at all times. The heating currents were measured with the potentiometer as the voltages across the standard resistors R_{S_1} and R_{S_2} .

The filament temperature measurements were made by calibrating the resistance of each filament against its temperature as measured with

6.3

an optical micropyrometer before cesium was admitted to the tube. All subsequent temperature determinations were made with these calibrations. The temperatures of the filament refer to that measured at the center of each through the small holes in the collector plate. However, the temperature was not uniform along the filaments because of end effects. In order to correct this, temperature profiles were made with the pyrometer for both filaments. The appropriate average temperature was then used in all thermal conductivity calculations.

A set of thermocouple leads was built into the tube and the junction welded at the center of the collector plate, so that its temperature could be measured. A calibration was made of the plate temperature with cathode temperature under vacuum conditions and at a cesium pressure of 2 mm Hg.

The cesium reservoir temperature was maintained constant to within one half a degree by immersion in a liquid metal bath of lead-tin eutectic.

A set of filament power measurements vs filament temperature for a spacing of 0.005" was made for cesium reservoir temperatures of 28°C, 226.5°C, 250°C, 280°C and 306.5°C. The most reliable data was in the filament temperature range from 1300°K to 1600°K, and this is plotted on an expanded scale in Figure 6-3. The thermal conductance was computed for each pressure at 1300°K, 1400°K, 1500°K and 1600°K, and an average value over this range for each pressure was obtained. A similar set of measurements for a gap spacing of 0.010" was also made. The thermal

conductance determined in this way is independent of pressure and varies inversely with spacing at high pressures, as expected from kinetic theory.

The accuracy of the measured variation of thermal conductance with filament temperature may be doubtful, but a regular variation was observed and this is presented here. The thermal conductance vs pressure for the 0.005" spacing as measured at five filament temperatures is plotted in Figure 6-4.

The result of the most simplified calculation of the thermal conductivity of a gas⁽¹⁾ is

$$\lambda = \frac{1}{3} \bar{v} \frac{1}{n} C_v = \xi \frac{\sqrt{m kT}}{\pi \sigma^2} \frac{C_v}{m} \quad (1)$$

in which

$$\bar{v} = \left(\frac{8kT}{m\pi} \right)^{1/2}, \text{ mean velocity}$$

$\frac{1}{n}$ = mean free path

C_v = heat capacity at constant volume

σ = molecular diameter

ξ = numerical constant, dependent upon rate of collisions.
It is taken here as 25/32.

For a monatomic gas, using the model in which the atom is considered a rigid sphere,

$$\lambda = 8.34 \times 10^{-4} \frac{\sqrt{T/M}}{\sigma^2} \text{ watts/cm}^2\text{-}^\circ\text{K}, \quad (2)$$

where M is the molecular weight of the gas and σ is expressed in angstroms.

The hard sphere model is a useful approximation but a more realistic description of the molecular potential is required for more refined results. A commonly used one is the Lennard-Jones potential, whose form is

$$\phi(r) = 4\epsilon \left[\left(\frac{\sigma}{r}\right)^{12} - \left(\frac{\sigma}{r}\right)^6 \right] \quad (3)$$

The significance of the constants is that σ is the distance of closest approach of two colliding molecules of zero kinetic energy, and ϵ is the maximum energy of attraction of the two molecules. The methods for carrying out the calculations of the transport properties are very involved, and are discussed in some detail in Reference 1.

The expression for thermal conductivity, to a first approximation, based upon an arbitrary potential is very similar to that for hard spheres, with the additional involvement of a parameter known as the collision integral,

$$\Omega^{(2,2)}(T) = \sqrt{\frac{kT}{2\pi m}} \int_0^\infty e^{-\gamma^2} \gamma^7 Q^{(2)}(v) d\gamma \quad (4)$$

in which $\gamma = \frac{1}{2} \frac{mv^2}{kT}$

v = relative velocity of two colliding atoms

$Q^{(2)}(v)$ = collision cross section between two atoms of relative velocity v .

For rigid spheres,

$$Q_{\text{rig. sph.}}^{(2)} = \frac{2}{3} \pi \sigma^2$$

$$\Omega_{\text{rig. sph.}}^{(2,2)} = \sqrt{\frac{2kT}{\pi m}} \pi \sigma^2$$

The formulas are more conveniently expressed in terms of the reduced quantities

$$T^* = \frac{kT}{\epsilon}$$

and

$$\Omega^{(2,2)*} = \frac{\Omega_{\text{rig. sph.}}^{(2,2)}}{\Omega_{\text{rig. sph.}}^{(2,2)}}$$

The collision integral ratio is then a measure of the departure from the rigid sphere model. A table of values of $\Omega^{(2,2)*}$ is presented in Reference 1, (p. 1126), for the Lennard-Jones potential. The variation of $\Omega^{(2,2)*}$ is as $(T^*)^{-1/2}$. The thermal conductivity in terms of the collision integral is

$$\lambda = 8.34 \times 10^{-4} \frac{\sqrt{T/M}}{\Omega^{(2,2)*} (T^*) \sigma^2} \text{ watts/cm}^{\circ}\text{K} \quad (5)$$

Methods of calculating the interaction potential, ϵ , are discussed in Reference 1, p. 245, for the Lennard-Jones potential. The result is

$$\epsilon/k = 1.15 T_{\text{Boiling Point}},$$

$$\epsilon/k = 1.92 T_{\text{Melting Point}}$$

or
$$\epsilon/k = 0.77 T_{\text{Critical}}$$

The interaction energy constant for cesium from the boiling point temperature is

$$\epsilon/k = 1108^{\circ}\text{K}$$

and

$$T^* = \frac{T}{1108^{\circ}\text{K}}$$

Estimates of σ may be made from measurements of the atomic volume in the solid phase, and a value of 5.40 \AA is obtained for cesium.⁽²⁾ It may be expected, however, that such a determination of the atomic diameter in the gas phase will not be very accurate. The product of thermal conductivity times σ^2 from Equation (5) is plotted vs T in Figure 6-5 for cesium. A best fit to the experimental data is obtained by choosing $\sigma = 9.17 \text{ \AA}$. Using this value of σ , the theoretical thermal conductivity is compared in Figure 6-6 with the experimental values obtained over a range of temperature from 945°K to 1188°K . The experimental variation of thermal conductivity appears to be greater than the variation expected from theory, but it may be that the accuracy of the measurements is not good enough to warrant this conclusion.

The mechanisms governing thermal conduction in a gas at low pressure are different than those at high pressure. If the distance between the hot boundary and the cold boundary is less than the mean free

path of the gas atoms, then the atoms make almost no collisions with each other in crossing the space. In this case, all of the energy picked up by an atom at the hot surface is deposited on the cold surface, provided the accommodation coefficients are unity. Since no collisions occur in the space, the transport of energy will be independent of the spacing, but will be proportional to the number of atoms filling the space, and to their velocity. It is easily shown from kinetic theory⁽³⁾ that the thermal conductance at low pressure, for plane parallel geometry, is

$$\lambda = \alpha K p$$

in which K depends only upon the gas temperature and atomic velocity, and α is the accommodation coefficient. Using an accommodation coefficient of unity, and assuming a cosine law of evaporation from the surfaces, a value of $K = 2.7 \times 10^{-3}$ watts/cm²-°K-mm Hg is calculated for cesium.

The mean free path of a gas is given by*

$$\frac{1}{\lambda} = \frac{K T}{\xi p \pi \sigma^2} = 5.05 \times 10^{-6} \left(\frac{T}{P} \right) \text{ cm}$$

For a gas temperature of 1100°K, a mean free path of 0.005" is calculated to occur at a pressure of 0.28 mm Hg. using the atomic diameter of 9.17 \AA , obtained from the high pressure conductivity. This is in good agreement with the experimental results, where the high pressure behavior begins at about 0.5 mm Hg. The knee of the conductance curve as the high pressure value is reached is, however, much sharper than expected.

*See Ref. 1, p. 10.

The slope of the measured conductance curve in the low pressure region is $1.52 \times 10^{-3} \frac{\text{watts}}{\text{cm}^2 \cdot ^\circ\text{K} \cdot \text{mm Hg}}$, which is 56 percent of the theoretical value. This difference can be explained by an accommodation coefficient which is less than unity. If the accommodation coefficient of both surfaces were the same, then from the formula for the effective accommodation coefficient, α , of a pair of plane parallel surfaces whose coefficients are α_1 and α_2 ,

$$\alpha = \frac{\alpha_1 \alpha_2}{\alpha_1 + \alpha_2 - \alpha_1 \alpha_2},$$

the experimental results correspond to a surface accommodation coefficient of 0.72. On the other hand, if the cold surface, which is heavily coated with cesium, is assumed to have a coefficient of unity, then the surface accommodation coefficient of the hot surface would be 0.56, which seems rather low. Since there is no available data in this area, it is not possible to resolve this uncertainty here.

The large value of the scattering cross section obtained from the cesium thermal conductivity measurements suggested that the theory upon which this evaluation is based, might not be valid in the region of interest. A similar series of measurements was completed for rubidium vapor, which permits an independent comparison with the theory. The atomic structure and physical properties of rubidium and cesium are very similar. The transport properties of these two vapors would be expected to differ to the extent of the differences in their atomic mass and atom-atom interaction. The measurement techniques are very similar, since their vapor

pressure curves differ by only about 15°C . The two vapor pressure curves are shown in Figure 6-7.

The experimental methods and apparatus were the same as used for the cesium measurements. A 0.005" spacing was maintained between the tungsten filaments and the collector plates. Measurements of filament power vs filament temperature were made for rubidium pressures of 0.2, 0.3, 0.42, 1.0, 2.2 and 3.2 mm Hg. Data was taken in the range of filament temperature from 1200°K to 1600°K . The resulting power curves for the long filament and the short filament are shown in Figure 6-8 and Figure 6-9. The thermal conductance was computed for each pressure at filament temperatures of 1200°K , 1300°K , 1400°K and 1500°K , and the results are shown plotted in Figure 6-10. The knee in the curve, between the high and low pressure behavior, occurs at very nearly the same pressure for rubidium as for cesium. The high pressure value for rubidium is 8.6×10^{-4} watts/cm²- $^{\circ}\text{K}$, as compared to 1.36×10^{-3} watts/cm²- $^{\circ}\text{K}$ for cesium. A small dependence on filament temperature was observed and is indicated by the individual points. The thermal conductivity of rubidium is shown in Figure 6-11. There is no significant change with temperature in the region between 940°K and 1120°K . This is in distinction to the variation observed for cesium, which is also shown in Figure 6-11.

The atomic diameter, σ , can be estimated as for cesium. If ϵ/k is evaluated as $\epsilon/k = 1.15 T_{\text{Boiling Point}}$, the value calculated for σ is 12.7 \AA . However, the value for the dissociation energy of rubidium, obtained from optical data, is $\epsilon = 0.49$ electron volts. This gives a

value of $\sigma = 8.82 \text{ \AA}$. From X-ray measurement of the atomic volume in the solid state, $\sigma = 5.02 \text{ \AA}$. The following table gives the corresponding values for cesium.

Table 1
Atomic Diameter

	ϵ/k from T_B	ϵ from V_d	from atomic volume
Cs	9.17 \AA	7.05 \AA	5.4 \AA
Rb	12.7 \AA	8.82 \AA	5.02

This analysis of the thermal conductivity measurements yields a larger value for the atomic diameter of rubidium than for cesium, which is an unexpected result. This suggests that the Lennard-Jones interaction potential may be seriously deficient as applied to the transport properties of the alkali vapors.

REFERENCES

1. Hirschfelder, Curtiss and Bird, "Molecular Theory of Gases and Liquids," Wiley, New York, 1954.
2. American Institute of Physics Handbook, McGraw-Hill, New York, page 7-10, 1957.
3. S. Dushman, "Scientific Foundations of Vacuum Technique," Wiley, 1949.

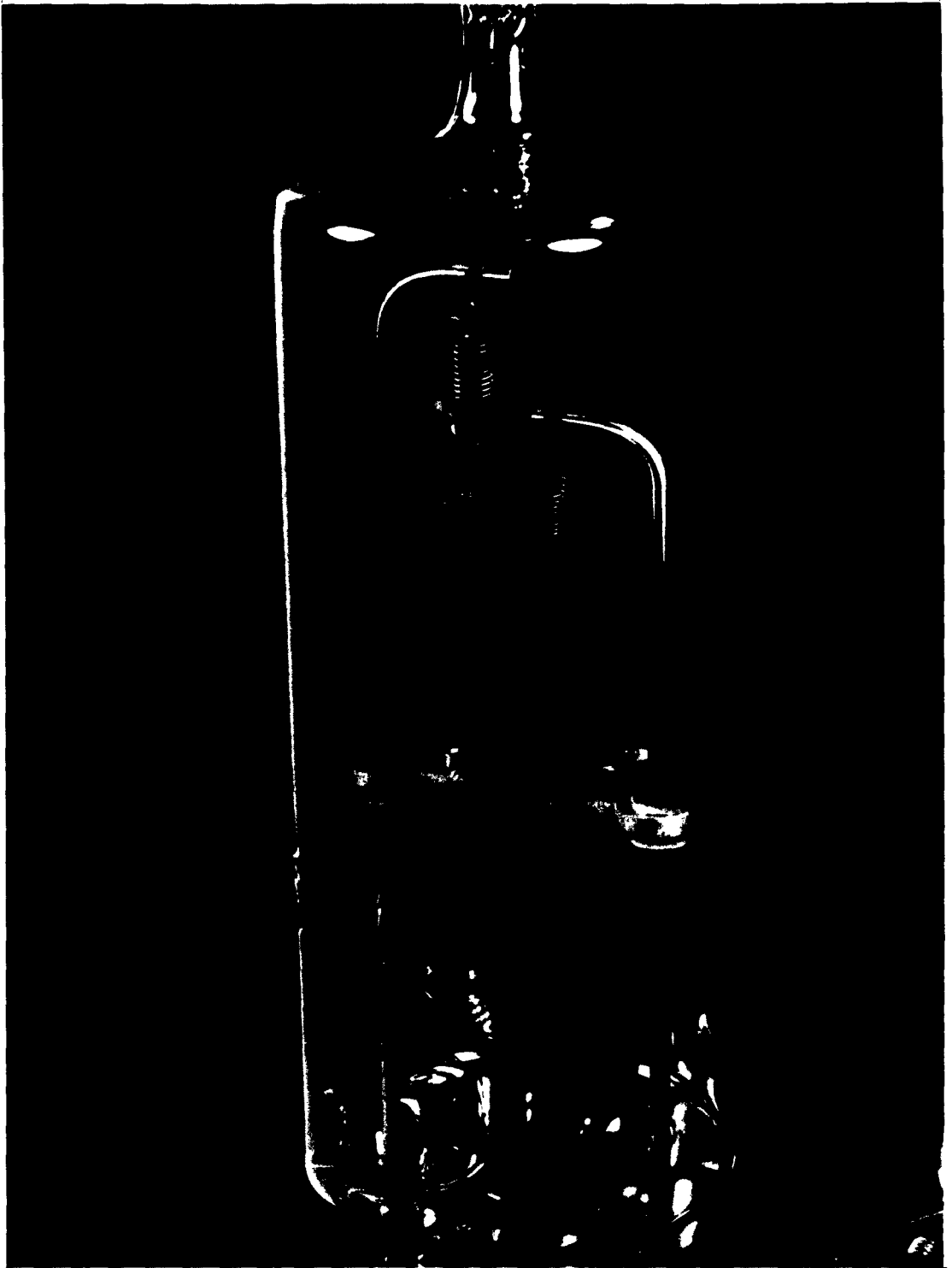


Fig. 6-1. Thermal Conductivity Measurement Cell

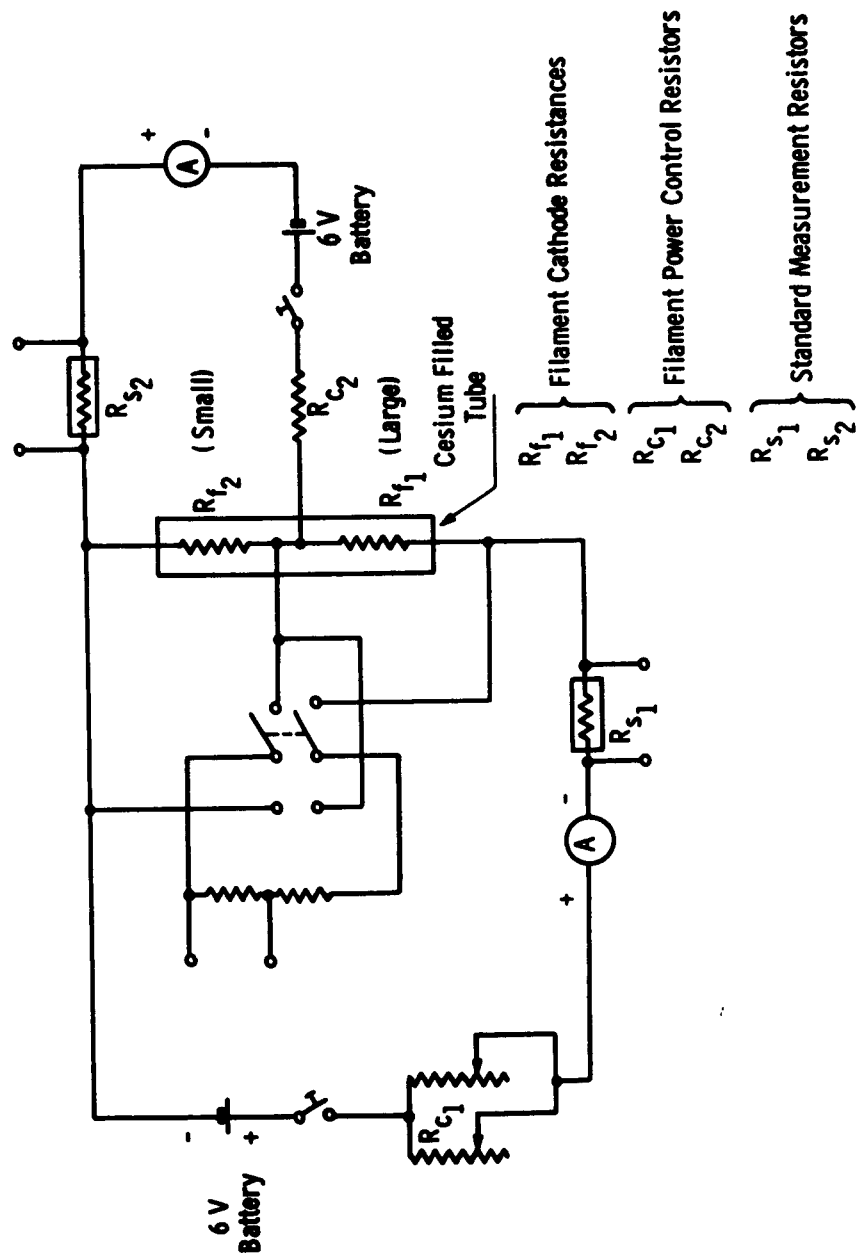


Fig. 6-2. Measuring Circuit

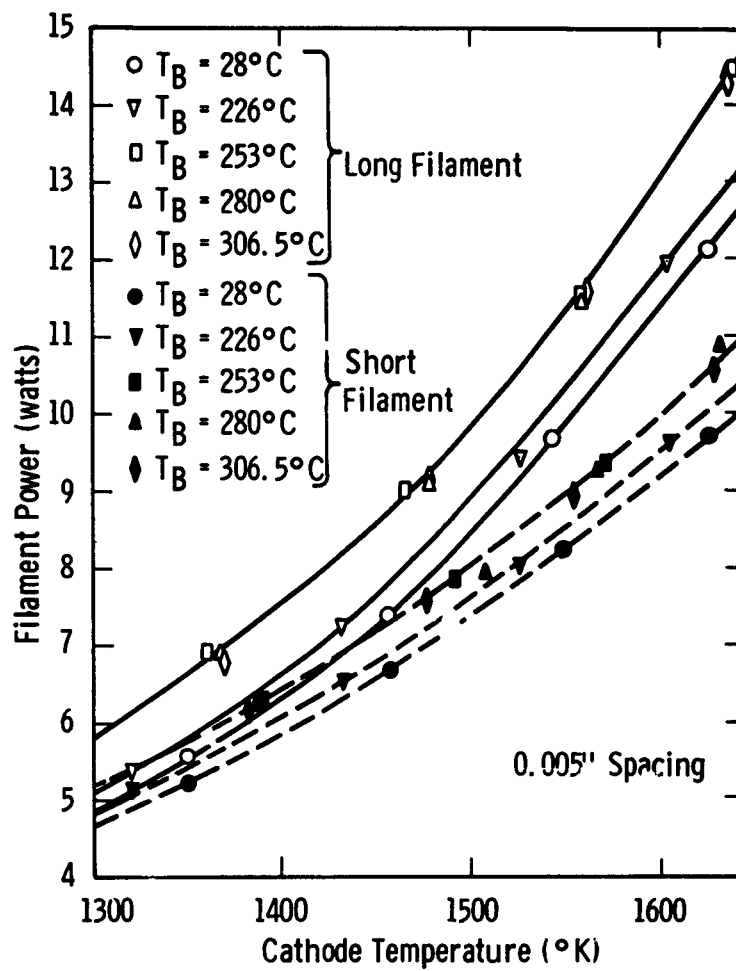


Fig. 6-3. Filament Power vs. Temperature

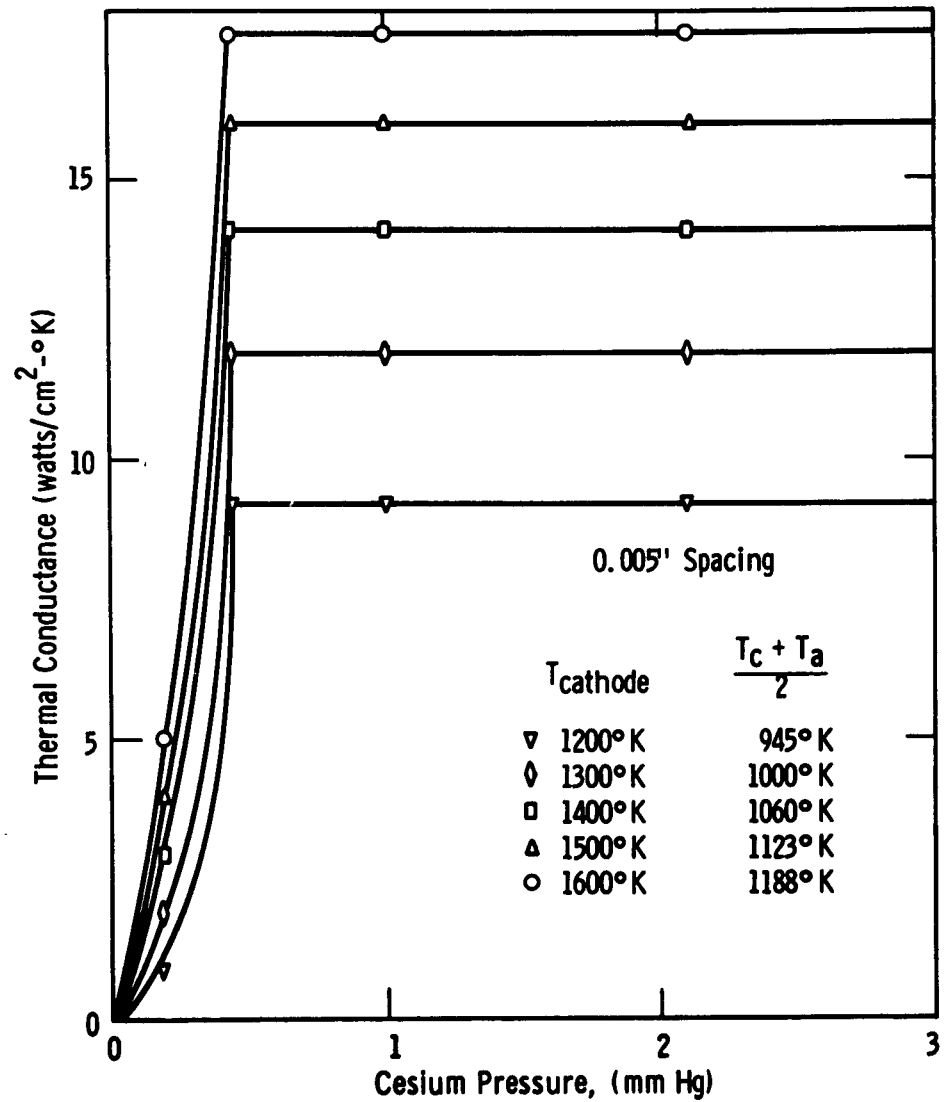


Fig. 6-4. Thermal Conductance vs. Pressure

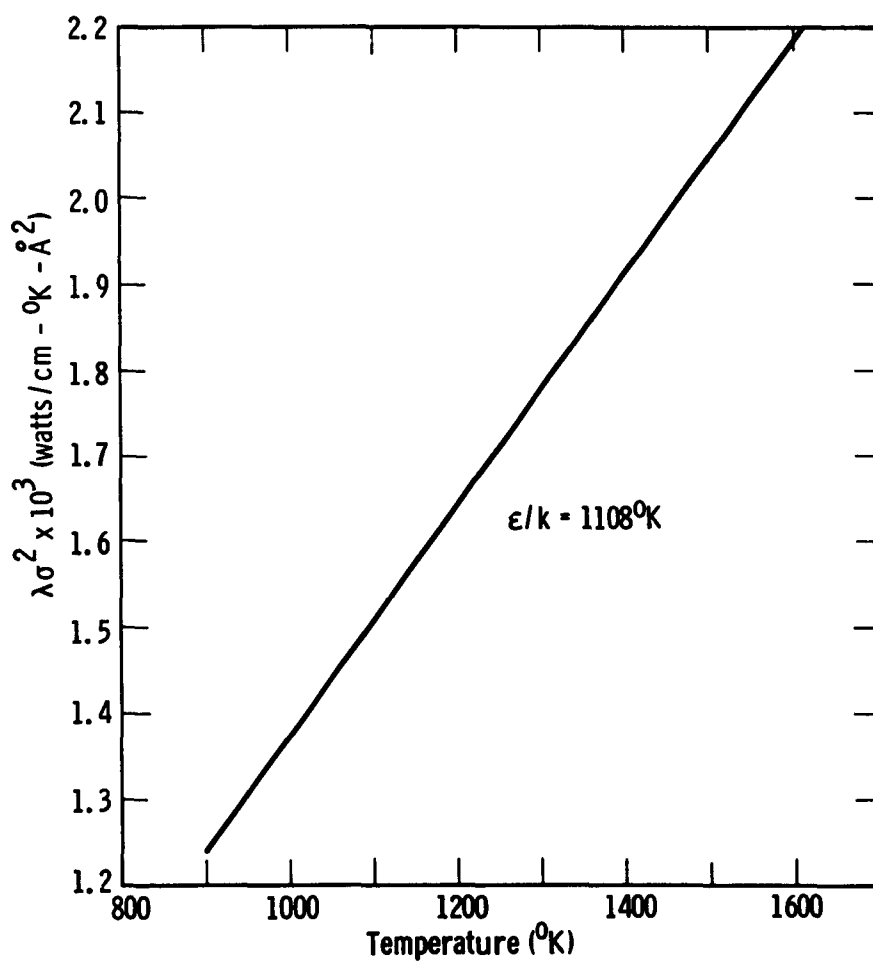


Fig. 6-5. $\lambda\sigma^2$ vs. Temperature from Theory

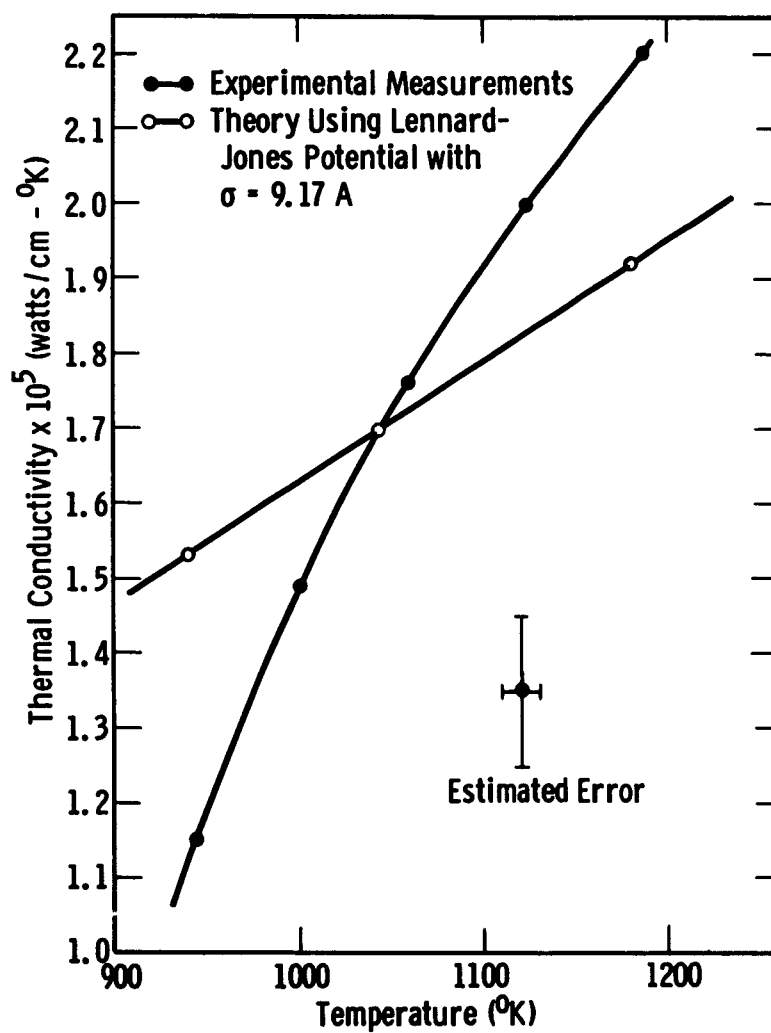


Fig. 6-6. Experimental and Theoretical Thermal Conductivity vs. Temperature

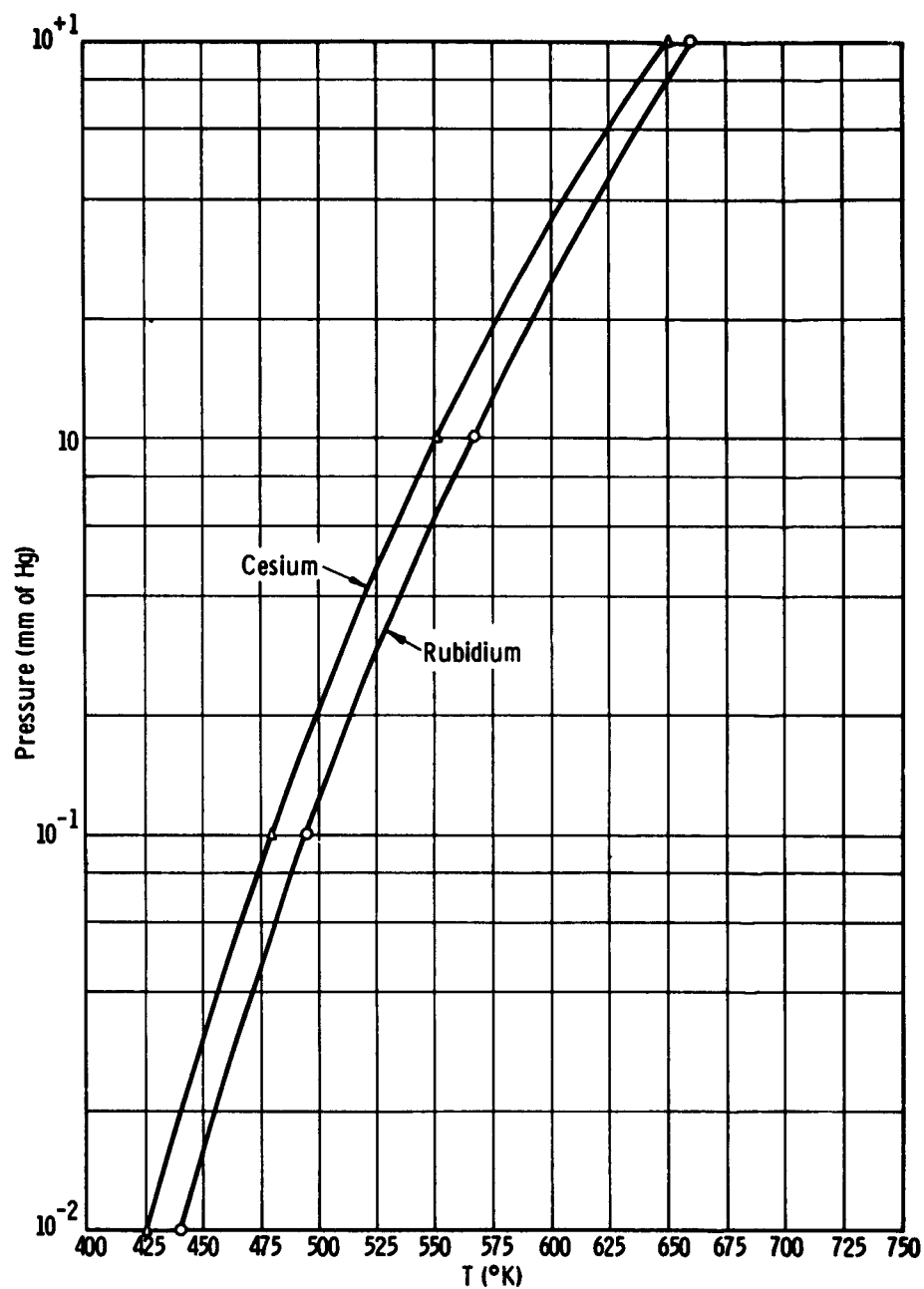


Fig. 6-7. Vapor Pressure of Cesium and Rubidium

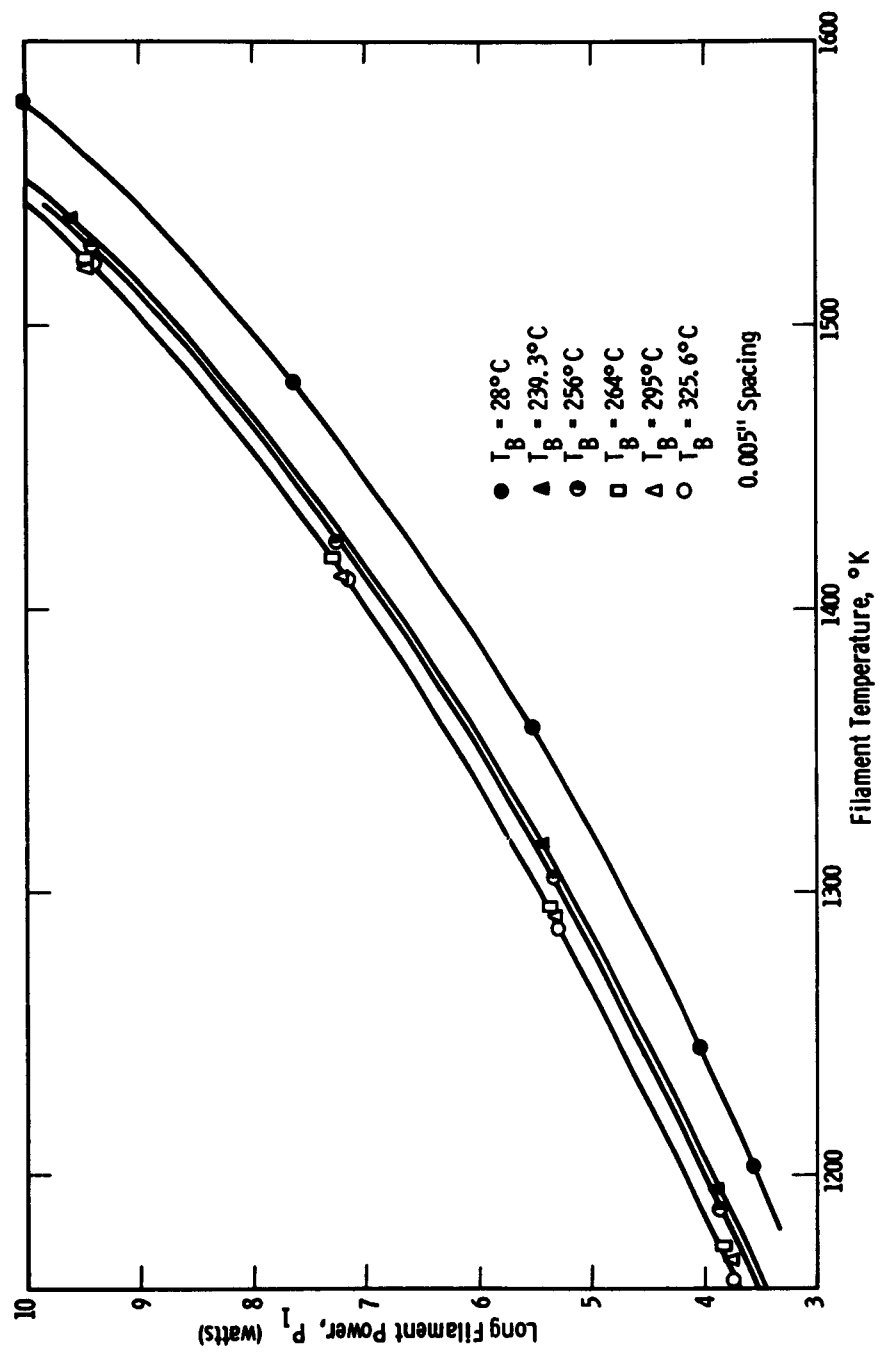


Fig. 6-8. Filament Power vs. Temperature for Long Filament

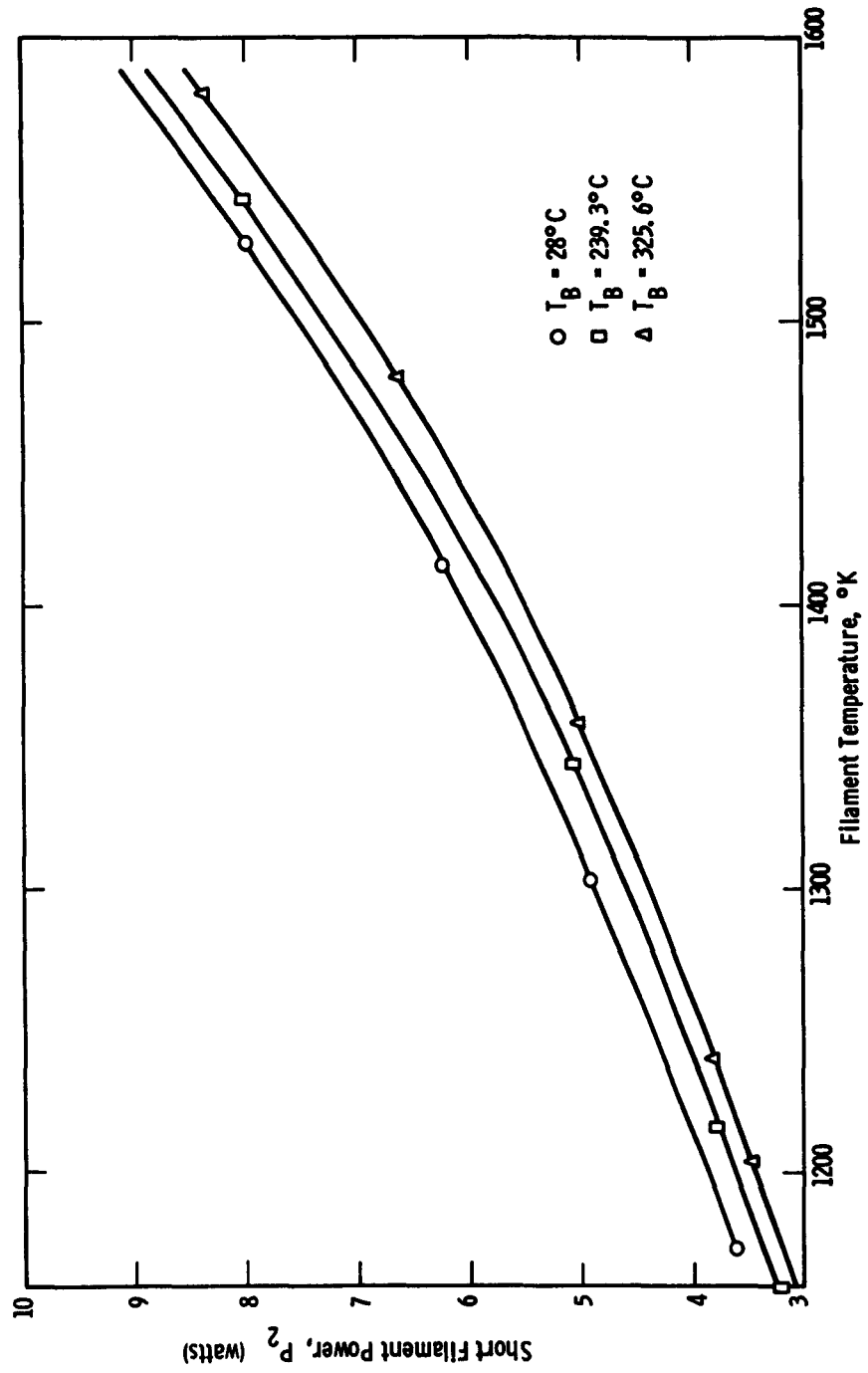


Fig. 6-9. Filament Power vs. Temperature for Short Filament

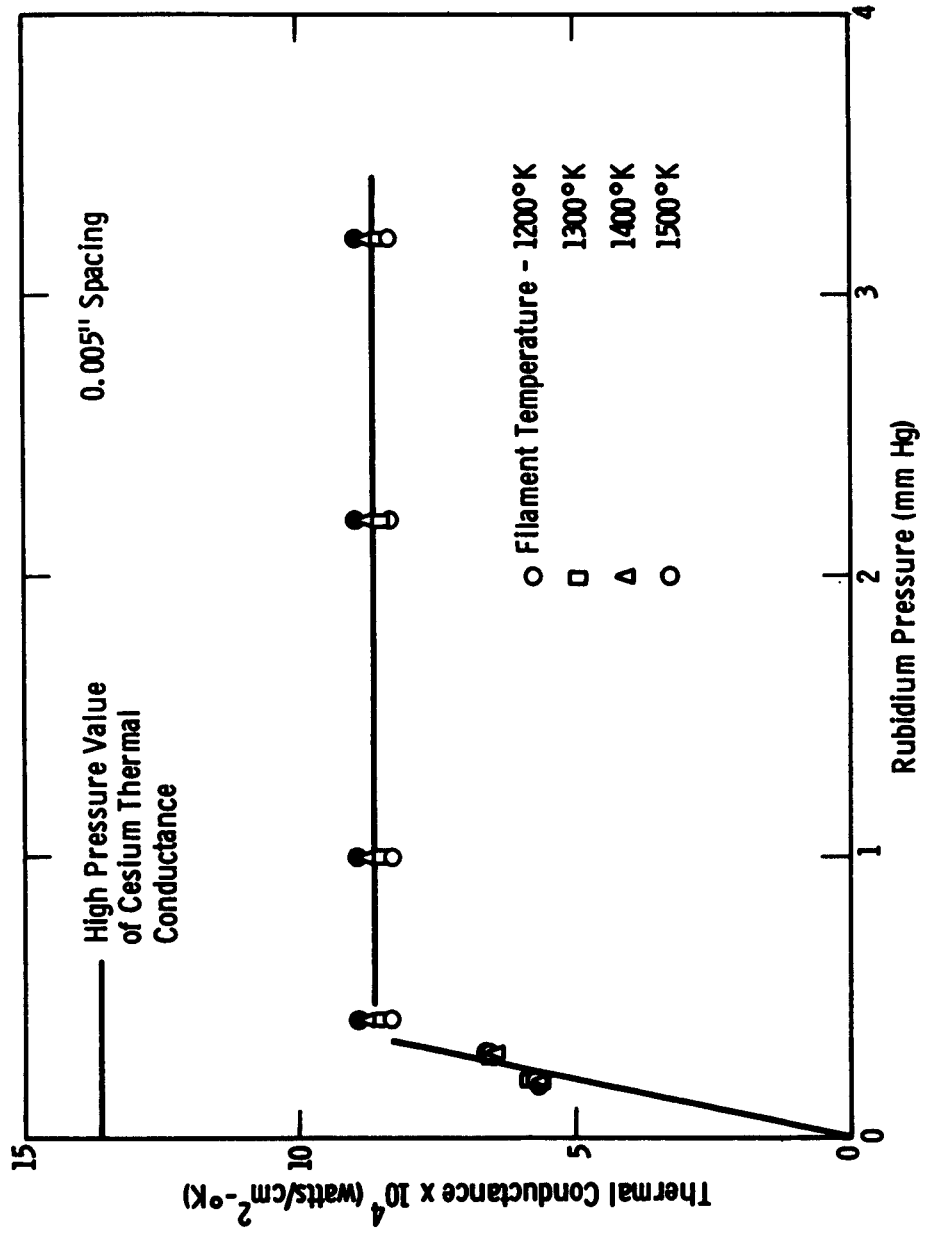


Fig. 6-10. Thermal Conductance vs. Pressure for Rubidium

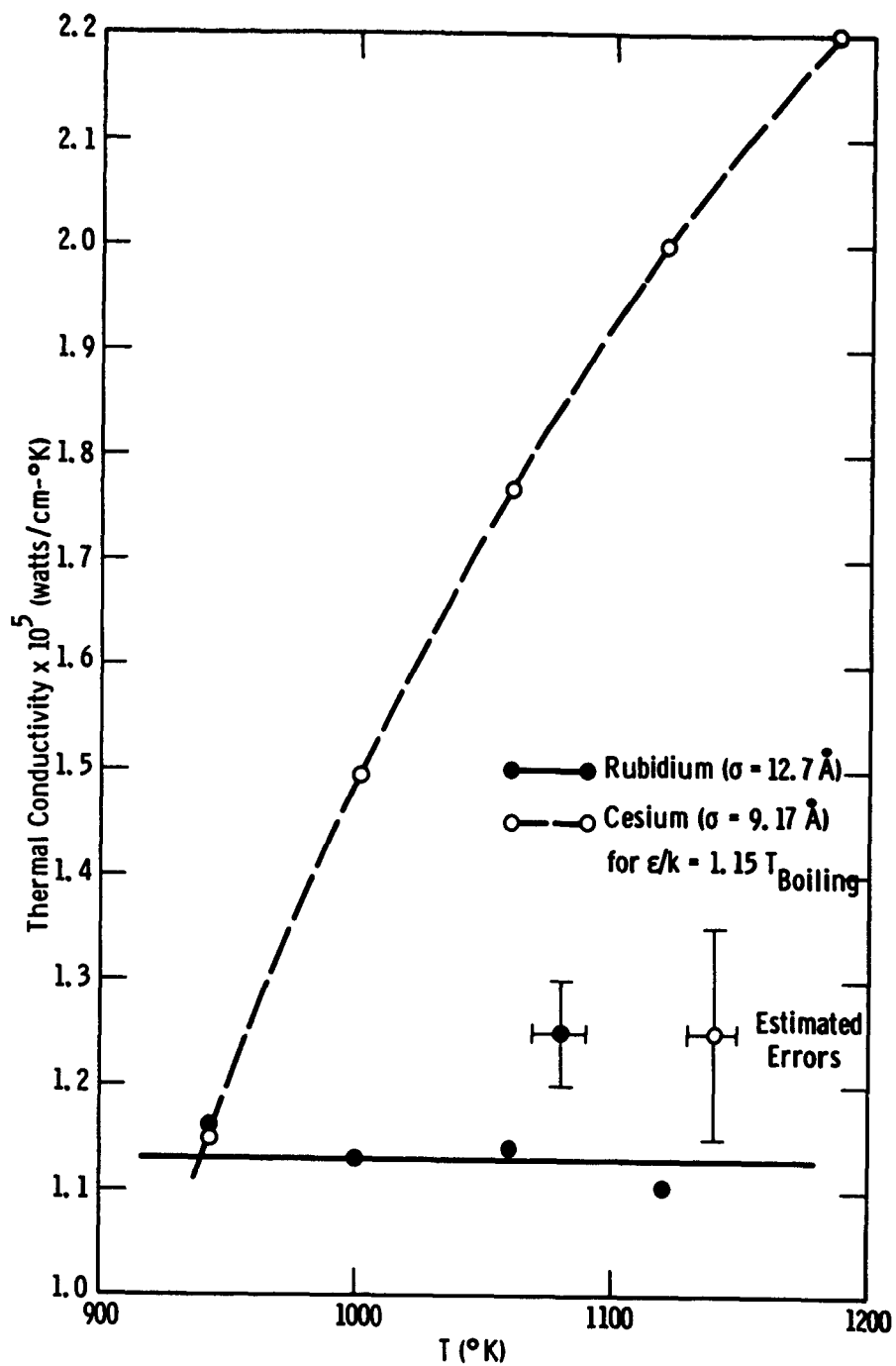


Fig. 6-11. Thermal Conductivity vs. Temperature

CHAPTER SEVEN

THEORETICAL EFFICIENCY OF A THERMIONIC ENERGY CONVERTER

As early as 1955, the possibility of using thermionic emission as a means of converting thermal energy directly into electrical energy was discussed.⁽¹⁾ Since that time, a number of papers have appeared in the literature describing the operation of devices utilizing this means of energy conversion.⁽²⁾ These papers have used the efficiency of the device as a criterion of comparison with other energy converters. While many of the authors have described the effects of varying some of the many parameters governing the operation of a thermionic converter, none have considered all of the effects simultaneously. Certain important effects, such as back current and varying load resistance, have not been analyzed carefully, if at all. In this work, an attempt is made to maximize efficiency by simultaneously optimizing cesium pressure (including the effects on work function), anode temperature, load resistance and lead resistance. The effects of varying cathode temperature and anode-to-cathode spacing are also included. It is the purpose of this work to construct a model predicting the behavior of a thermionic converter for the use of designers or experimenters. Results of numerical computation of efficiency are also presented.

While many properties are of importance in the operation of a thermionic converter, once the materials for construction of cathode and anode have been chosen, only a few independent parameters remain. The

geometrical configuration, the electrode temperatures, the means of space charge neutralization, and the resistances of the lead and load are the only variables which can be adjusted. The most common means of space charge neutralization is the use of a cesium atmosphere in the inter-electrode gap. Most of the experimental cells and almost all of the converter designs use geometry which is equivalent to plane parallel electrodes. Since the lead and load resistances can be simultaneously optimized to yield maximum efficiency, the four independent variables in a conventionally designed thermionic converter are the cathode and anode temperatures, the cesium pressure, and the interelectrode spacing. A later section will show that the anode temperature and cesium pressure can also be simultaneously optimized. Thus, once the basic design of a converter has been made, the choice of materials, spacing, and cathode temperature will fix all other parameters, if maximum efficiency is sought.

Description of the Operation of a Thermionic Diode

In this section, a mathematical model describing the behavior of a thermionic diode will be set up and used to evaluate the efficiency of such a device. For the sake of mathematical convenience, the operation will be expressed in terms of variables which are not all independent. (For example, thermal emissivity is a function of surface temperature.) This will not affect the derivations described below. Before numerical calculations can be performed, however, the actual interrelationships among the physical parameters must be taken into account. A description

of the manner in which this will be done will be deferred until the analysis of the operation of the thermionic diode has been presented.

Description of Model Used

Stripped of the numerous parts necessary in its construction, the thermionic diode can be basically represented by the schematic of Figure 7-1. A cathode surface in contact with a heat reservoir at an absolute temperature T_c thermally emits electrons across a gap to an anode in contact with a heat reservoir at a temperature T_a . The electrons are returned from the anode to the cathode through an external load.

In practice, certain effects take place which tend to prevent the flow of a reasonable current. The most serious of these is the formation of a space charge in the space between the cathode and anode. This space charge forms a potential barrier for the electrons leaving the cathode and can reduce the number of electrons reaching the anode (and therefore the current through the load) by many orders of magnitude. Two different methods are presently in use to overcome the problem of space charge. The simplest of the two, in theory, is the method of close spacing. It is known⁽⁴⁾ that the reduction of current flow by space charge is very sensitive to the distance between the cathode and anode. For separations of 0.0002 in. or less, the detrimental effects of space charge can be made almost negligible.⁽⁵⁾ The second common method of reducing or eliminating space charge is by the use of a positively ionized vapor (usually cesium) in the gap between the anode

and cathode. The electrostatic potential set up by the ions will then counteract the retarding potential of the electronic space charge and permit an increased flow of electron current.

The introduction of the plasma results in a loss of energy available to the load by conducting heat from the cathode to the anode and by scattering electrons in the region between the cathode and the anode. In addition, the plasma may modify the values of the chemical potential of both the anode and cathode.

In this paper, it will be assumed that the space charge in the region between the anode and cathode has been eliminated by using a plasma. It will be assumed that the sole effect of the plasma on the behavior of the diode is to introduce a "plasma electrical resistance," R_p , and a "plasma thermal conductance," K_p . The former will contribute to an internal voltage drop inside the diode, and the latter to a thermal conduction of energy across the cathode-anode gap. Also, only the case of plane parallel plates one square centimeter in area* will be considered.

Let $\bar{\phi}_c$ and $\bar{\phi}_a$ be the work functions of the cathode and anode respectively. (When similar quantities are defined for both the cathode and anode, a subscript "c" will refer to the former and "a" to the latter.) The potential seen by an electron in going from the cathode to the anode will then be represented by one of three possible cases depicted

*In this regard, it must be remembered that the value of resistance must correspond to electrodes of unit area, and that net current densities calculated will be numerically equal to currents.

by Figure 7-2. The mode of operation will be classed as uphill if $V > \bar{\phi}_c - \bar{\phi}_a$ (Figure 7-2a), downhill if $V < \bar{\phi}_c - \bar{\phi}_a$ (Figure 2b), and flat if $V = \bar{\phi}_c - \bar{\phi}_a$ (Figure 2c).

The saturation emission current densities will be denoted by J_{cs} and J_{as} . By Richardson's equation

$$J_{cs} = AT_c^2 \exp(-\bar{\phi}_c/KT_c) \quad (1)$$

$$J_{as} = AT_a^2 \exp(-\bar{\phi}_a/KT_a) \quad (2)$$

where A is Richardson's constant, equal to $120 \text{ amp cm}^{-2} \text{ deg K}^{-2}$; and, if k is Boltzmann's constant, and e the electronic charge, $K = k/e = 8.616 \times 10^{-5} \text{ volts deg K}^{-1}$. In the flat mode, the net current density, J, from the cathode to the anode is simply the net saturation current density, J_s

$$J = J_{cs} - J_{as} = J_s \quad (3)$$

In general, this is not true, and the net current must be written

$$J = J_c - J_a \quad (4)$$

where in the uphill mode

$$J_c = J_{cs} \exp \left[-(V - \bar{\phi}_c + \bar{\phi}_a)/KT_c \right] \quad (5)$$

and in the downhill mode

$$J_c = J_{cs}$$

$$J_a = J_{as} \exp \left[- (\bar{\phi}_c - V - \bar{\phi}_a) / kT_a \right] \quad (6)$$

The heat input to the cathode and power output to the load must be known in order to calculate the efficiency of operation of a thermionic generator. The power output is simply the load voltage times the current, where the load voltage is equal to the emf, V , generated by the diode minus the voltage drops due to plasma resistance (R_p) and lead resistance (R_L).

$$P_{out} = J(V - J(R_L + R_p)) \quad (7)$$

By the first law of thermodynamics, the total heat input to the cathode is equal to the total energy leaving the cathode. The latter can be expressed as the sum of several terms:

- 1) Heat radiated from cathode to anode, W .
- 2) Support and end losses, X .
- 3) Heat absorbed by electrons leaving the cathode and reaching the anode, H_c .
- 4) Heat conducted from cathode to anode by lead wires and plasma, H_K .
- 5) Heat returned to the cathode by electrons arriving from the anode, H_a .
- 6) Heat returned to cathode from the Joule heating of lead wires and plasma, H_J .

The first four effects carry heat away from the cathode while the last two bring heat to the cathode.* The total heat input, H_{in} , to the cathode can be evaluated.

$$H_{in} = W + H_c + H - H_a - H_J + X \quad (8)$$

The individual terms are readily calculable. The thermal radiation term W is given by the Stefan-Boltzmann law**

$$W = \sigma F (T_c^4 - T_a^4) \quad (9)$$

where, if ϵ_c and ϵ_a are the total emissivities of a parallel cathode and anode, the view function F is⁽⁶⁾

$$F = (\epsilon_c^{-1} + \epsilon_a^{-1} - 1)^{-1} \quad (10)$$

and σ is the Stefan-Boltzmann constant (5.67×10^{-12} watts cm^{-2} deg K^{-4}). The heat carried by thermal conduction away from the cathode is

$$H_K = (K_p + K_L) (T_c - T_a) \quad (11)$$

where K_p and K_L are the thermal conductances of the plasma and the leads respectively. It will be assumed that the Joule heat returned to the cathode is simply one-half the total Joule heat produced in the leads and in the plasma.*** Thus

*Minor losses due to thermoelectric effects and the energy required to ionize the plasma will be ignored.

**It is here assumed that both the anode and the cathode are gray bodies.

***This result is obtained rigorously in reference 2d.

$$H_J = (1/2) (R_L + R_p) J^2 \quad (12)$$

In order to compute H_c and H_a , the mode of operation must be considered. From Figure 7-2, it is seen that in the downhill mode an electron leaving the cathode must have absorbed an amount of heat at least equal to $\bar{\phi}_c$. Similarly, an electron arriving at the cathode from the anode must also have absorbed at least that amount of heat. For the uphill mode, this minimum amount of absorbed heat is $V + \bar{\phi}_a$. Define

$$\bar{\phi} = \text{Max} (\bar{\phi}_c, \bar{\phi}_a + V) \quad (13)$$

The value of $\bar{\phi}$ is thus the minimum heat absorbed by an electron traversing the diode in any mode. In addition to this minimum heat $\bar{\phi}$, there is some kinetic energy which the electron may possess. If the electrons immediately outside the cathode or anode have a Maxwellian distribution characteristic of the temperature of the surface which they have left, it can be shown that, on the average, this additional kinetic energy will be $2KT$ where T is the temperature of the emitting surface. Thus

$$H_c = J_c (\bar{\phi} + 2KT_c) \quad (14)$$

and

$$H_a = J_a (\bar{\phi} + 2KT_a) \quad (15)$$

The efficiency, defined as the ratio of output power to heat in, is then given by

$$\eta = \frac{J [V - J (R_L + R_p)]}{W + J_c(\bar{\alpha} + 2KT_c) + (K_L + K_p)(T_c - T_a) - J_2(\bar{\alpha} + 2KT_2) - J^2(R_L + R_p)/2 + X} \quad (16)$$

In practice, the load resistance, R_{load} , is a quantity which can be varied at will. However, mathematically the internal voltage

$$V = J(R_L + R_p + R_{load}) \quad (17)$$

is much more convenient to use. Therefore, in lieu of R_p , R_L and R_{load} being considered as three independent variables, R_p , R_L and V will be used, the transformation being non-singular. It must be kept in mind, therefore, in the following analysis that, if, for example, a variation of R_L at constant V is considered, a variation in R_p and/or R_{load} is necessary. The value of the variable V is not completely optional. There are limits on V , and values outside of these limits are not physically obtainable. It is only the load resistance which can be physically varied from zero to infinity, short and open circuit respectively. Each case yields an equation which may be solved for the internal voltage. The minimum value for V , V_{sc} , is obtained from the short circuit equation

$$0 = V - J (R_L + R_p) \text{ at } V = V_{sc} \quad (18)$$

Equation (18) is transcendental and cannot be solved analytically. The open circuit voltage V_{oc} is determined by the condition

$$J = 0 \text{ at } V = V_{oc} \quad (19)$$

An analytic solution to (19) for V_{oc} can be obtained from (4), (5) and (6)

$$V_{oc} = \bar{\phi}_c - \bar{\phi}_a + KT \ln (J_{cs}/J_{as}) \quad (20)$$

where

$$T = T_c \text{ if } J_{cs} > J_{as}, \text{ and } T = T_a \text{ if } J_{as} > J_{cs}.$$

B. Optimization of Lead Resistance

The efficiency (16) can be optimized with respect to the lead resistance at fixed V as follows:

If A_c , L , ρ , and κ are respectively the cross-sectional area, length, electrical resistivity, and thermal conductivity of the leads

$$R_L = \rho L/A_c \quad (21)$$

$$K_L = \kappa A_c/L \quad (22)$$

By the Wiedemann-Franz law ρ and κ of a metallic conductor at a temperature T_0 are related by the equation

$$\rho = \lambda T_0/\kappa, \quad \lambda = 2.44 \times 10^{-8} \text{ watt-ohm-deg } K^{-2} \quad (23)$$

If T_0 is assumed to be the average of T_c and T_a

$$K_L = (\lambda/2 R_L) (T_1 + T_2) \quad (24)$$

Thus K_L can be replaced in (16) by its value in terms of R_L from (24) and obtain an expression which can be reduced to

$$\eta = \beta \eta_0 \quad (25)$$

where η_0 is the efficiency of an identical diode with ideal leads (i.e., $R_L = 0$, $K_L = 0$)

$$\eta_0 = \frac{J [V - JR_p]}{W + J_c (\bar{a} + 2KT_c) - J_a (\bar{a} + 2KT_a) + K_p (T_c - T_a) - J^2 R_p / 2 + X} \quad (26)$$

and

$$\beta = (1 - \gamma) \left\{ 1 - \frac{\eta_0}{2} \left(\gamma - \frac{1}{G\gamma} \right) \right\}^{-1} \quad (27)$$

$$G = (V - JR_p)^2 \left[(T_c^2 - T_a^2) \right]^{-1} \quad (28)$$

$$\gamma = \frac{JR_L}{V - JR_p} \quad (29)$$

From (17) therefore

$$\gamma = \frac{R_L}{R_L + R_{load}} \quad (30)$$

Thus physically the parameter γ is the fraction of the external emf of the diode which appears across the leads; or equivalently, it is the ratio of the lead resistance to the total external resistance. Its range therefore is from 0 to 1.

The efficiency can then, in principle, be maximized with respect to the lead resistance R_L . Using the representation of (25) and noting that R_L enters only through the dimensionless parameter γ , it is found that the efficiency optimized with respect to R_L is (quantities evaluated at that value of R_L giving maximum efficiency will be denoted with an overhead bar)

$$\bar{\eta} = \eta_o \bar{\beta} \quad (31)$$

where

$$\bar{\beta} = \frac{\sqrt{1+B} - 1}{\sqrt{1+B} + 1 - \eta_o} \quad (32)$$

$$\bar{R}_L = \left[(V - JR_p)/J \right] \left[(\sqrt{1+B} - 1)/B \right] \quad (33)$$

$$\bar{\gamma} = JR_L / (V - JR_p) \quad (34)$$

$$B = G(2 - \eta_o) \eta_o \quad (35)$$

As the value of B ranges from zero to infinity, the value of $\bar{\gamma}$ will range from $1/2$ to zero. Thus under no conditions will more than half the external emf appear across the leads when they are optimized.

Obviously, $\bar{\beta} < 1$. The quantity $\bar{\beta}$ is the fraction to which the efficiency of the ideal diode with ideal leads (zero electrical resistance and zero thermal conductivity) has been reduced when the physical leads have been optimized. Considered as a function of η alone (V , T_c , T_a

fixed), $\bar{\beta}$ can be shown to be monotonically decreasing. Thus the tendency of the leads to decrease the efficiency is greater for an ideal diode with a large efficiency. This can be explained qualitatively from the fact that the higher efficiency diodes have in general the larger electric currents and that the larger the current, the larger the voltage drop in the leads. However, $\bar{\eta}$ is still a monotonically increasing function of η_0 .

If non-optimum leads are used, a decrease in efficiency will result. This effect will be considered for the most pessimistic case by adjusting the parameters so that β is as small as possible. This can be done by making G as small as possible. For the values $T_a = 0^\circ\text{K}$, $T_c = 3000^\circ\text{K}$, and $V - JR_p = 1$ volt, G is equal to 4.55. Figure 7-3 shows the results of calculations of β as a function of η_0 and γ . Also shown in that figure is the locus of the maximum of the curves, $\bar{\beta}$. Several features of these curves are of interest. At a critical value of γ equal to $G^{-1/2}$ (0.47 in this case), the curves for different values of η_0 intersect. For γ greater than this critical value, β is a monotonically decreasing function of η_0 , but very weakly dependent upon η_0 . For γ less than this critical value, β is a strong monotonically increasing function of η_1 .

Curves of $\bar{\gamma}$, $\bar{\eta}$, and $\bar{\beta}$ as functions of η_0 are presented in Figure 7-4 for the values of T_c , T_a and V used above.

Empirical Evaluation of Parameters

In order to be able to calculate the quantities discussed, it is necessary to know the values of many parameters such as work functions and emissivities. In reality, quantities such as these are not independent, but depend on the pressure of cesium and the temperatures of the electrodes. This section is devoted to describing the relation which exists among these quantities.

The relationship of effective work function to cesium pressure and surface temperature has not been well determined. The pioneering work of Langmuir⁽⁷⁾ provided the basis for the present empirical equation. While no theoretical justification of the equation can be given, the results are in close agreement with the original data and with the extrapolations of other investigators.^(2d)

The effective work function of cesium-coated tungsten was assumed to be a function of only the fractional coverage, θ . The data of Langmuir and Taylor⁽⁷⁾ are plotted in Figure 7-5. The empirical equation

$$\begin{aligned}\bar{\phi} &= 4.52 - 8.59 \theta + 6.3 \theta^2, \quad \theta \leq .86 \\ \bar{\phi} &= 1.81, \quad \theta \geq .86\end{aligned}\tag{36}$$

was fitted to this data. The results of this equation are also plotted in Figure 7-5.

The estimation of the fractional coverage as a function of cesium pressure and surface temperature was also made by the use of a

set of empirical equations. Figure 7-6 shows the relation between surface temperature and coverage for two particular cesium temperatures.⁽⁷⁾ Figure 7-7 shows the relationship of work function to cesium pressure and surface temperature.

The thermal emissivities of tungsten is given by several references as a function of temperature. The data used here are those of Forsythe and Watson.⁽⁹⁾

Values of plasma electrical resistance and thermal conductance are not available in the literature. Gottlieb and Zollweg⁽¹⁰⁾ have recently measured the thermal conductance of cesium plasma. An empirical fit to their results is shown in Figure 7-8. These data were fitted well by the empirical equation.

$$p = 1.5 \times 10^{-4} \quad 1 - \exp(-40 Pd) \quad (37)$$

where P is the cesium pressure in mm of Hg, d the spacing in cm and p the thermal conductivity of the plasma in watt-cm/deg K. The electrical resistance was estimated from J-V curves taken by Gottlieb and Zollweg. The results are quite preliminary in nature. For the calculations discussed hereafter, the plasma resistivity, ρ_p , was estimated by the equation

$$\rho_p = 2.67P \quad (38)$$

where P is the cesium pressure in mm Hg and ρ_p is in ohm cm.

Results of Numerical Calculations

Because empirical data concerning the effect of cesium coverage on the thermionic properties of materials is well known only for tungsten, calculations were made only for a device in which both the anode and cathode were made of tungsten.

Calculations of the optimum operating point according to the method described above were carried out on a high speed digital computer for more than 5000 different combinations of spacing, and cathode, anode, and cesium bath temperatures. At the values of load and load resistance which yielded the maximum efficiency for each of the given combination of parameters, some forty different properties, such as power delivered to load, external voltage, net current, etc., were tabulated in addition to the efficiency. As already shown, for given materials of construction, the efficiency η , optimized with respect to load and load resistance is a function of only four variables - cathode-anode spacing, and the temperature of the cathode, anode, and cesium reservoir. Because of the number of independent variables, it is possible to plot lines of constant efficiency in a large number of ways. By keeping two of the parameters constant, efficiency contours can be plotted as a function of the other two. Figures 7-9, 7-10, and 7-11 show respectively sample result of keeping fixed cesium temperature and spacing, anode temperature and spacing, and cesium temperature and anode temperature. It was found, however, that the most useful type of plot was obtained by fixing the spacing and cathode temperature and drawing curves of constant efficiency

as a function of anode and cesium reservoir temperatures. A typical set of such plots is shown in Figure 7-12. It should be noticed that in each case, the efficiency has a maximum occurring at a unique combination of cesium and anode temperatures. This maximum is a general occurrence for all of the possible combinations of spacing and cathode temperature, although its precise location will depend upon the particular values of spacing and cathode temperature considered. It should be mentioned that these maxima may only be local and that higher efficiencies may be obtainable at lower anode temperatures. However, anode temperatures less than 600°K were not considered to be reasonable from a design standpoint. Further, the anode temperature can never be less than the temperature of the cesium reservoir, for the latter must be the lowest temperature in the diode so that it will determine the pressure of the cesium vapor. Curves of the type in Figures 7-9, 7-10, and 7-11 do not display a maximum of efficiency since higher efficiencies can always be obtained by going to a sufficiently higher cathode temperature. If Figure 7-11 is considered at a fixed value of cathode temperature, it can be shown that an optimum value of spacing exists. However, these spacings are extremely small (less than 2.5 microns) and not realizable. Therefore, for spacings larger than this, the efficiency decreases with increasing spacing.

A summary of the maxima obtainable from plots of the type of Figure 7-12 is shown in Figures 7-13 and 7-14. In these figures are shown three sets of curves as functions of cathode temperature - maximum

attainable efficiency and the anode and cesium bath temperatures necessary to attain that efficiency. Each set consists of five curves corresponding to five different spacings. There are several important features of these curves which should be noted. There is, for a fixed spacing, a wide range of cathode temperatures in which the ultimate efficiency is relatively independent of cathode temperatures. Thus, a small improvement in the temperature capability of most existing materials does not produce a large improvement in efficiency of operation. Further, the anode temperature required for maximum efficiency is seen to be within the range 900°K to 1100°K regardless of the cathode temperature or spacing.

It should be reemphasized at this point that the numerical results presented in the figures and in the above discussion refer to a device with tungsten anode and cathode. For other materials, the numerical values might change considerably, but it is believed that the qualitative nature of the results should be the same.

It must also be recalled that these calculations are based on the assumption that space charge has been eliminated. Since there is a minimum cesium temperature at which this is true, certain areas of the curves presented (particularly at the lower cesium temperatures) are inaccurate. Fortunately, from the limited data available in the literature, the optimum operating points do not appear to be in this excluded area.

If accurate emission data were available, calculations of the type discussed here could be carried out for other materials. While

experimental investigations of these data are presently being made by various laboratories, little information is available in the literature.

Conclusions and Recommendations for Further Study

The following are some conclusions we have drawn from this study and some recommendations for further work.

When for a fixed spacing and cathode temperature all other parameters are optimized using efficiency as the criterion, the resulting optimum efficiency is a relatively insensitive function of the cathode temperature in the temperature range 1600 to 2200°K. Clearly, a small improvement in temperature capability will not result in a significant improvement in efficiency. Only a large increase in operating temperature provides a marked improvement. In order to operate a thermionic converter of the type discussed here at 25% efficiency, a cathode temperature above 2200°K is necessary. A thermionic converter using tungsten electrodes operating with a cathode temperature of 1600 to 2200°K would have an efficiency between 15 and 20%.

The introduction of cesium into a thermionic energy converter has two opposing effects upon the efficiency. Thermal and electrical losses occur in the cesium, while the reduction of cathode and anode work functions allows more efficient operation. As the pressure of cesium is increased from zero, the efficiency is increased reaching a maximum. Above this critical value of cesium pressure, the efficiency decreases because of the increasing electrical and thermal losses in the plasma.

The attainment of maximum efficiency depends critically upon establishing the optimum cesium pressure. The use of a cathode material possessing a larger affinity for cesium would make possible lower cesium pressure to obtain a given work function. The plasma losses would then be lower. The net result would be a higher efficiency of operation. In short, the use of a cathode material of higher affinity for cesium will result in increased efficiency. It can be shown that the converse is also true. Thus, consideration of the cesium affinity is of considerable importance in the selection of a cathode material.

From examination of the operating characteristics of thermionic converters (such as Figure 7-12), it is seen that efficiency is a relatively insensitive function of anode and cathode temperature and of spacing. The cesium pressure, on the other hand, is quite a critical parameter and should be controlled very closely. The lead and load resistances are also critical parameters. Operation away from these critical values can decrease the efficiency by a sizeable fraction. These relationships should be carefully considered in the design of thermionic converters.

The calculations of efficiency have been checked against the results of the few experimental devices available in the literature. Where sufficient information is given to allow comparison, the agreement has been quite reasonable. While the calculations are not to be considered as exact theoretical results, the values are probably quite close to reality. While the model of the plasma is not entirely realistic and the effect of space charge has been largely ignored, the errors introduced

are small in the regions of interest. Devices of 35% efficiency are clearly impractical, while a 20% efficient device can probably be built with present techniques and materials.

REFERENCES

1. D. K. Coles, Westinghouse Research Report 60-94469-2-R1, June 16, 1954.
2. (a) N. S. Rasor, J. Appl. Phys. 31, 163 (1960);
 (b) J. M. Houston, J. Appl. Phys. 30, 481 (1959);
 (c) J. H. Ingold, J. Appl. Phys. 32, 769 (1961);
 (d) A. Schock, J. Appl. Phys. 32, 1564 (1961);
 (e) G. N. Hatsopolous and J. Kaye, Proc. I.R.E. 46, 1574 (1958);
 (f) "Direct Conversion of Heat to Electricity," edited by J. Kaye and J. A. Welsh, John Wiley and Sons, Inc.; New York (1960).
3. U. S. Patent No. 2,980,819 issued to G. R. Feaster, April 18, 1961.
4. W. B. Nottingham, "Thermionic Emission," HANDBUCH DER PHYSIK 21, Springer-Verlag, Germany (1956).
5. H. F. Webster, J. Appl. Phys. 30, 488 (1959).
6. (a) M. Jakob, Heat Transfer, John Wiley and Sons, Inc.; New York (1957), Vol. II, Chap. 31.
 (b) A. E. Fein, Rev. Sci. Inst. 31, 1008 (1960).
7. J. B. Taylor and I. Langmuir, Phys. Rev. 44, 432 (1933).
8. W. B. Nottingham, Tech. Rept. 373, Research Laboratory of Electronics, The Massachusetts Institute of Technology (1960).
9. W. E. Forsythe and E. M. Watson, J. Opt. Soc. of Amer. 24, 114 (1934).
10. Unpublished Research, M. Gottlieb and R. Zollweg.
11. L. S. Richardson, A. E. Fein, M. Gottlieb, G. A. Kemeny, and R. J. Zollweg, paper presented at Technical Conference of the AIME, Los Angeles, California, August 30 - September 1, 1961. Proceedings to be published. Also, see Westinghouse Scientific Paper 918E901-P2 (October 13, 1961).

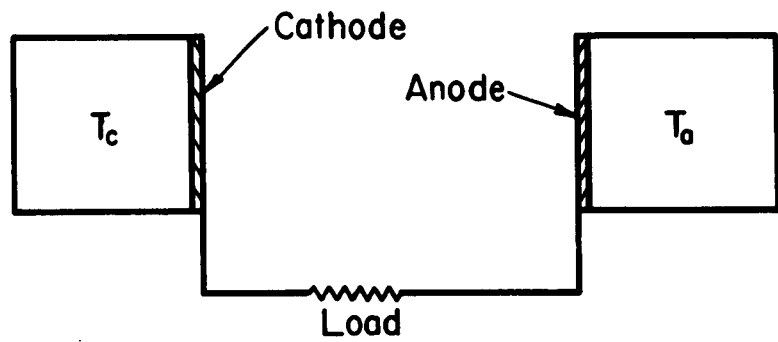


Fig. 7-1

Basic Thermionic Diode

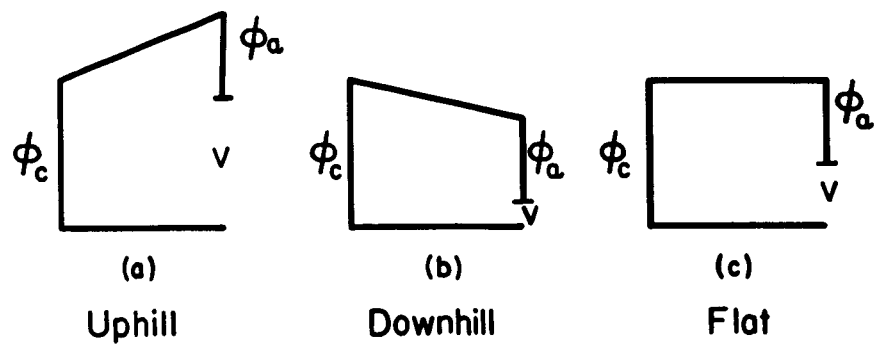


Fig. 7-2

Modes of Operation

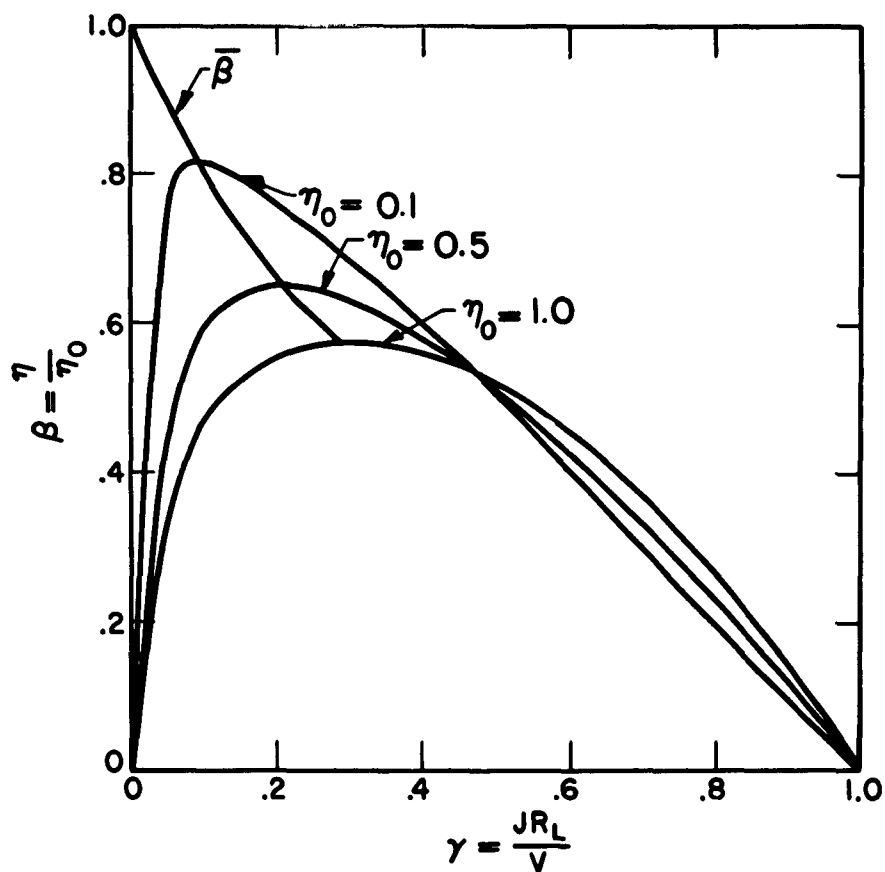


Fig. 7-3. $\bar{\beta}$ as a Function of $\bar{\gamma}$ and the Ideal Efficiency, η_0 .

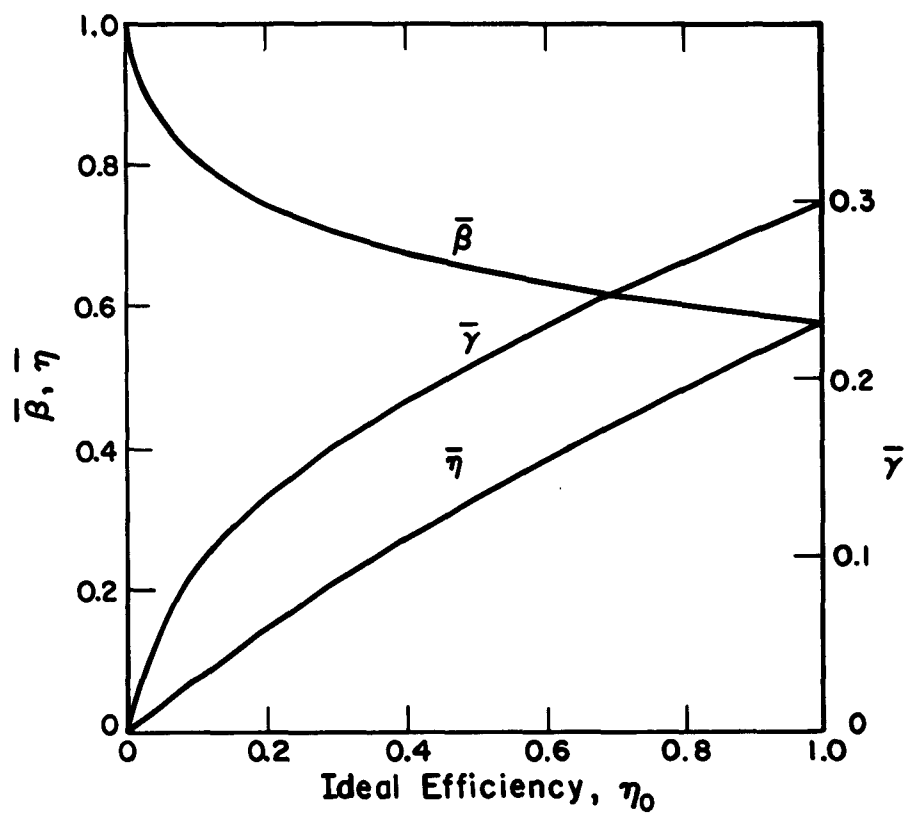


Fig. 7-4. Optimum Values of $\bar{\eta}$, $\bar{\gamma}$ and $\bar{\beta}$ as Functions of the Ideal Efficiency, η_0 .

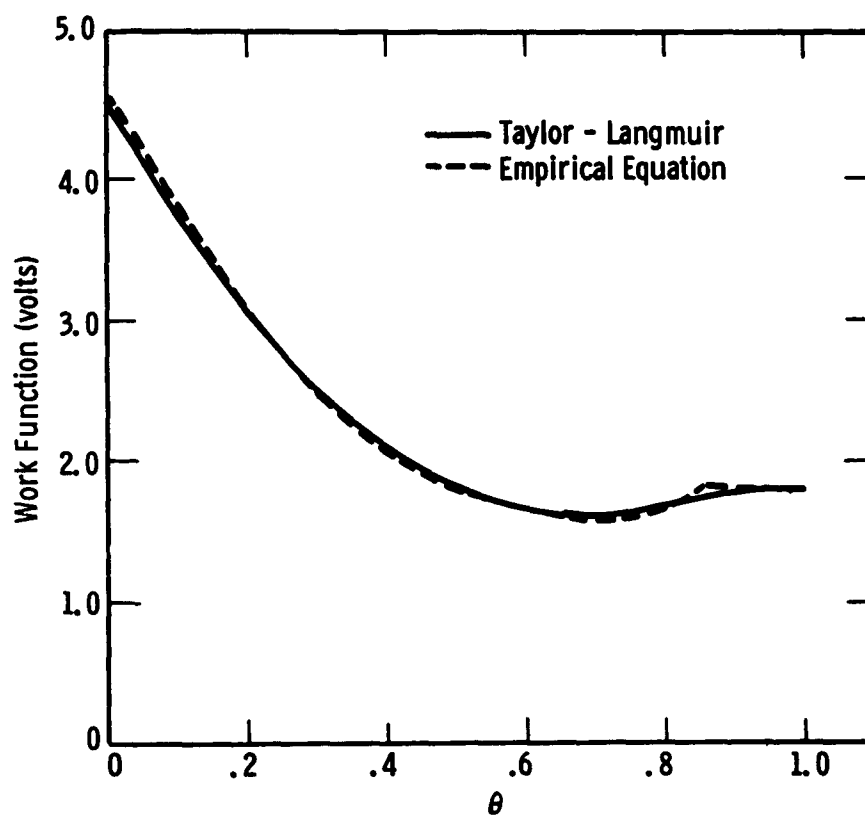


Fig. 7-5. Work Function of Tungsten as a Function of Fractional Coverage by Cesium.

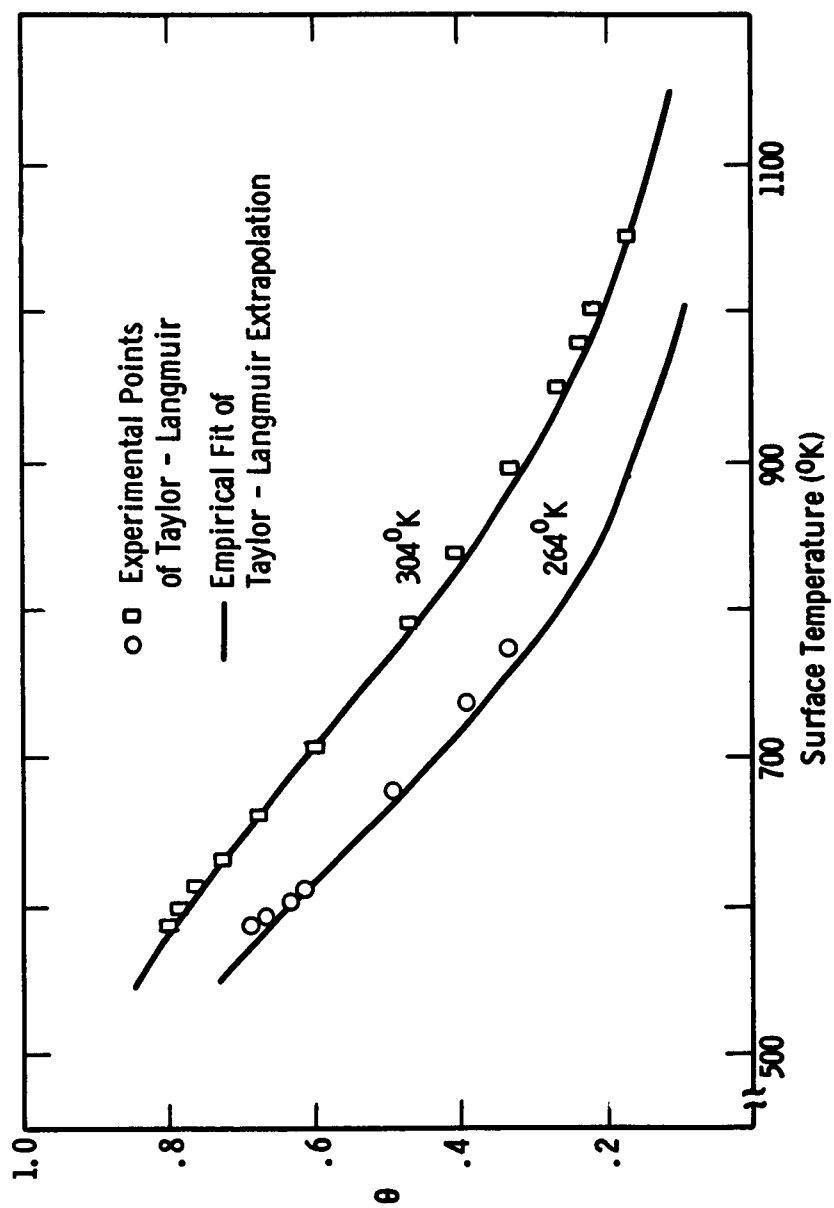


Fig. 7-6. Fractional Coverage of a Function of Cesium Temperature and Surface Temperature.

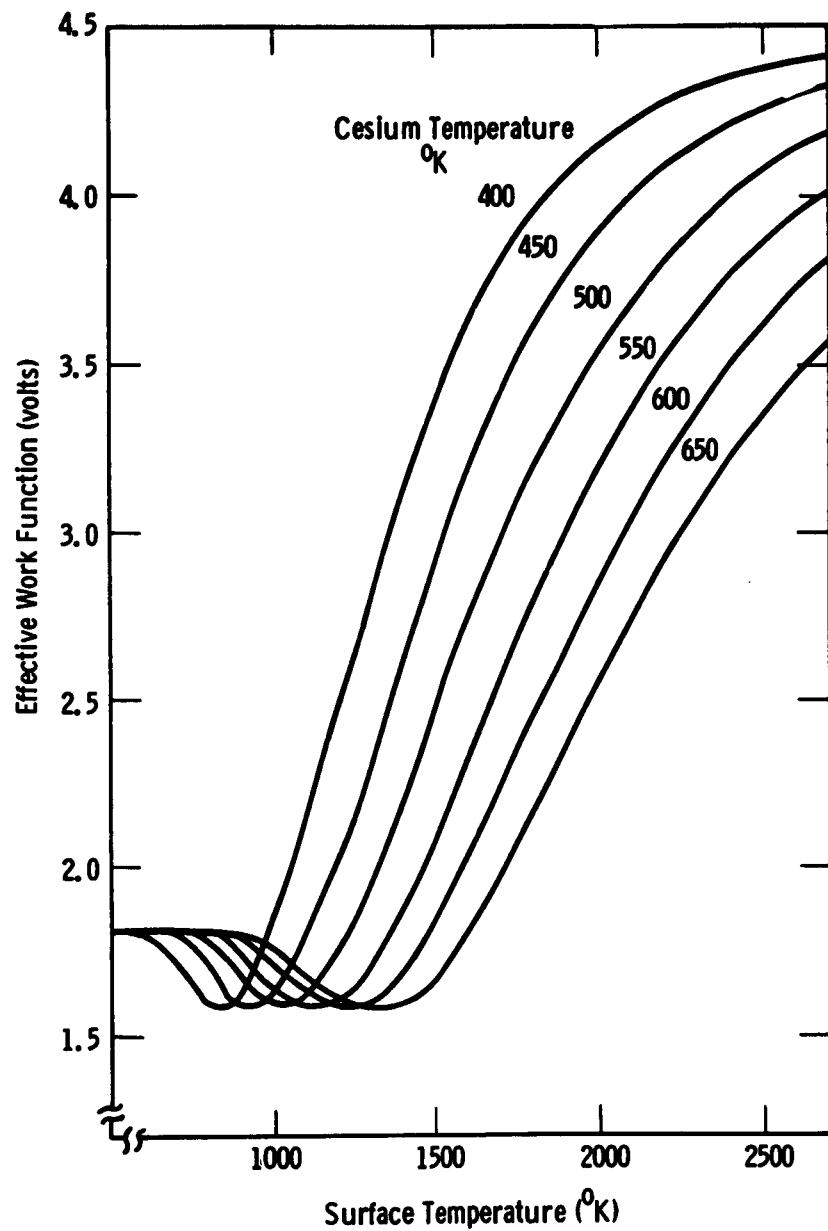


Fig. 7-7. Work Function as a Function of Cesium Bath Temperature and Surface Temperature.

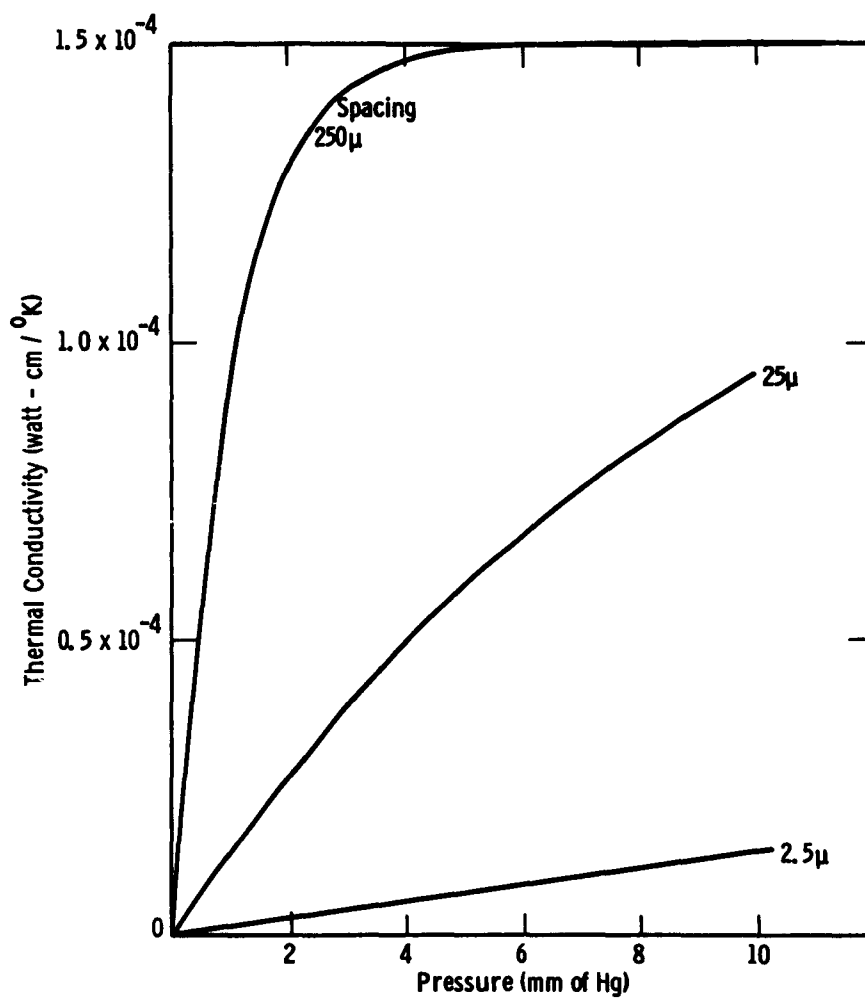


Fig. 7-8. Thermal Conductivity of Cesium Plasma as a Function of Spacing and Pressure.

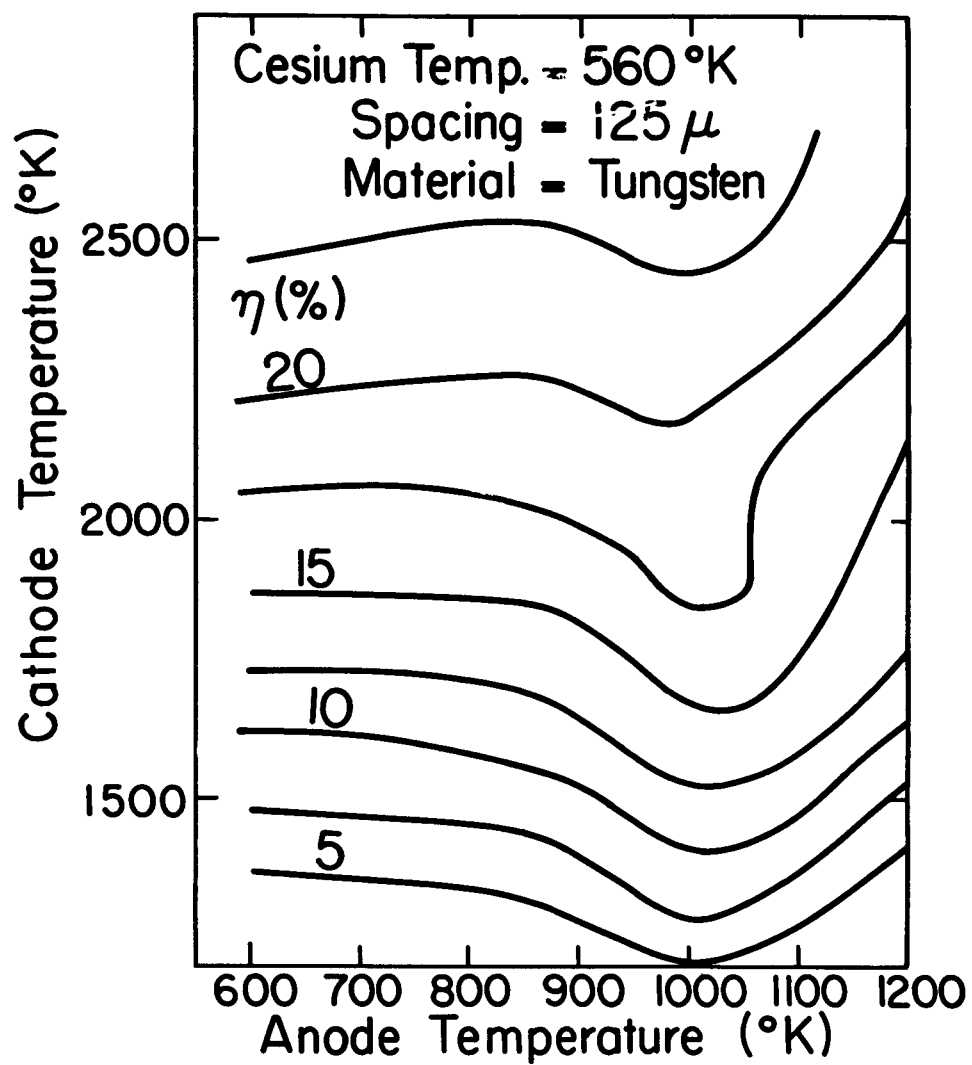


Fig. 7-9. Efficiency as a Function of Cathode and Anode Temperatures

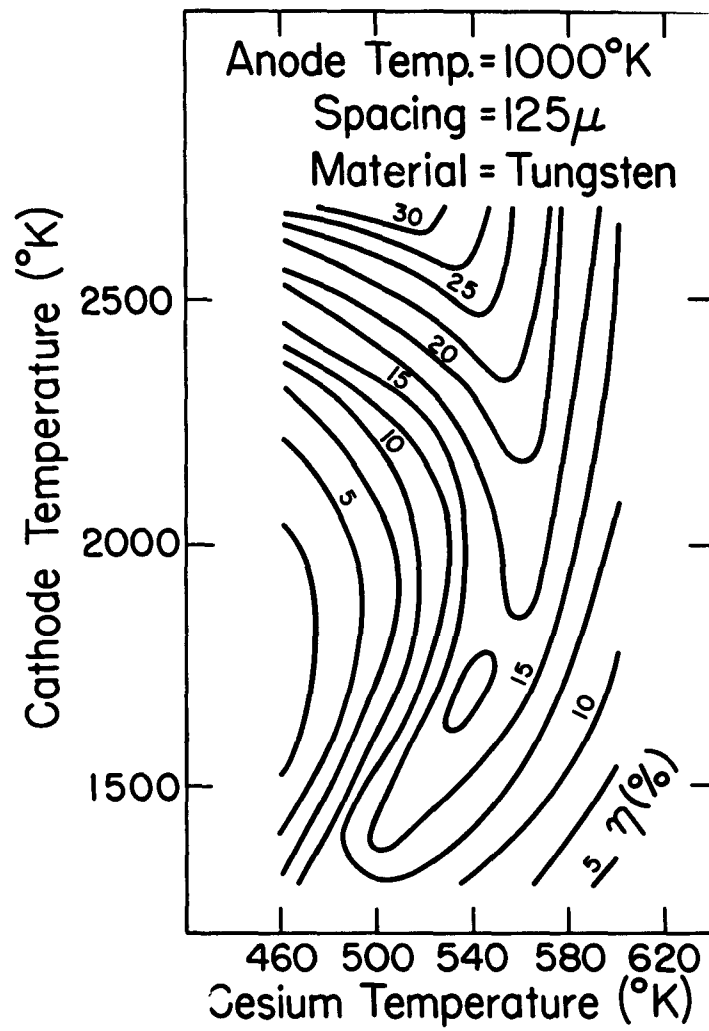


Fig. 7-10. Efficiency as a Function of Cathode and Anode Temperatures

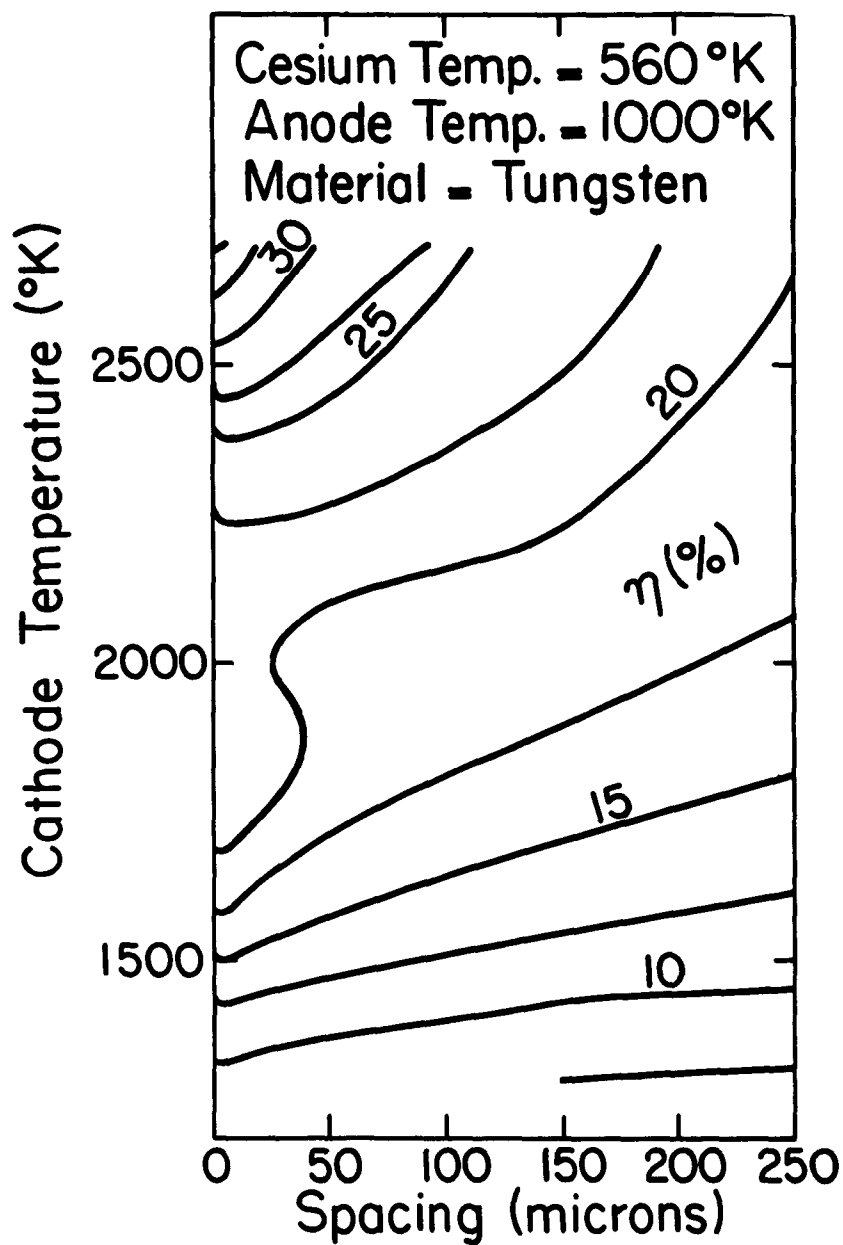


Fig. 7-11. Efficiency as a Function of Spacing and Cathode Temperature.

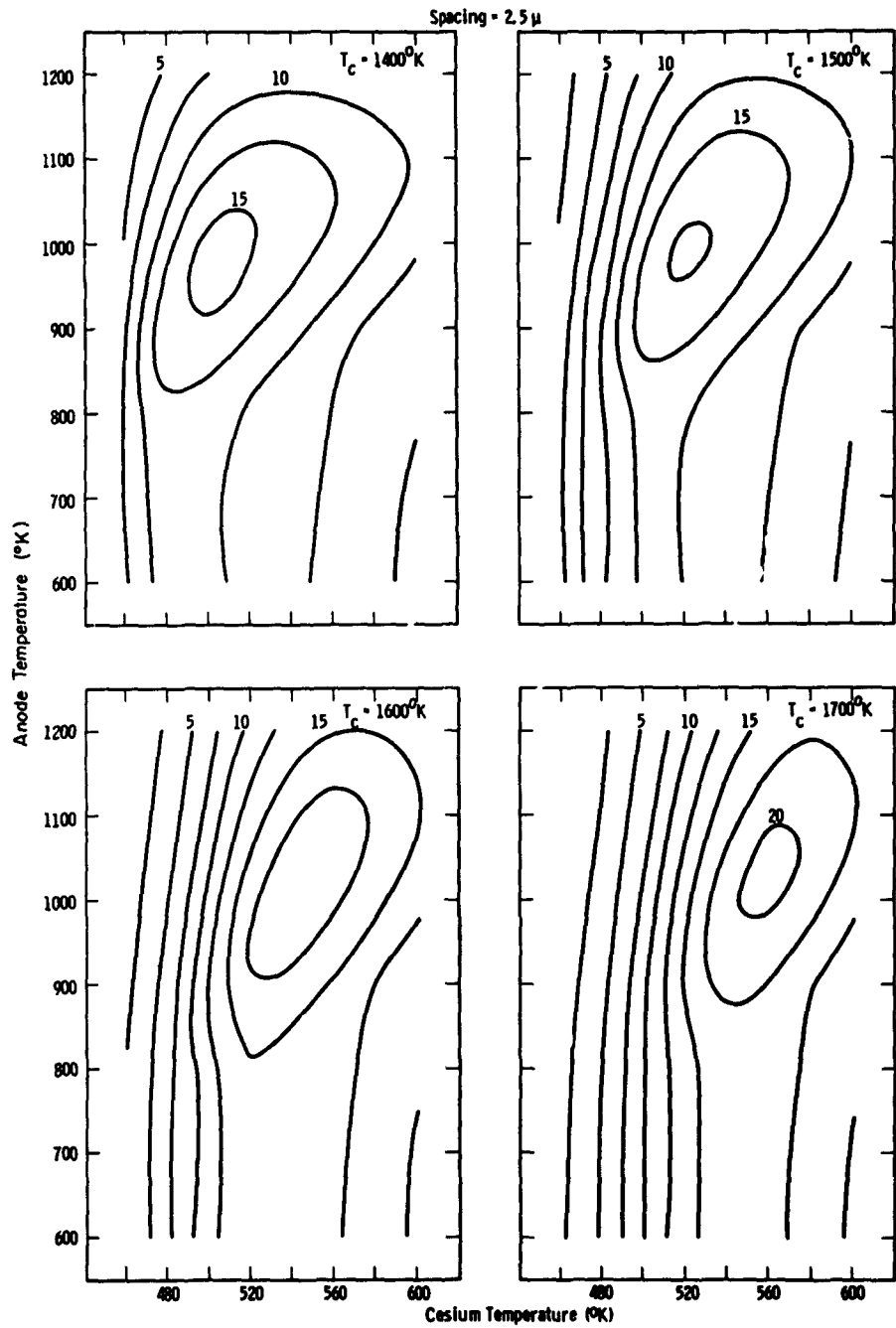


Fig. 7-12. Efficiency as a Function of Spacing and Anode, Cathode and Cesium Temperatures

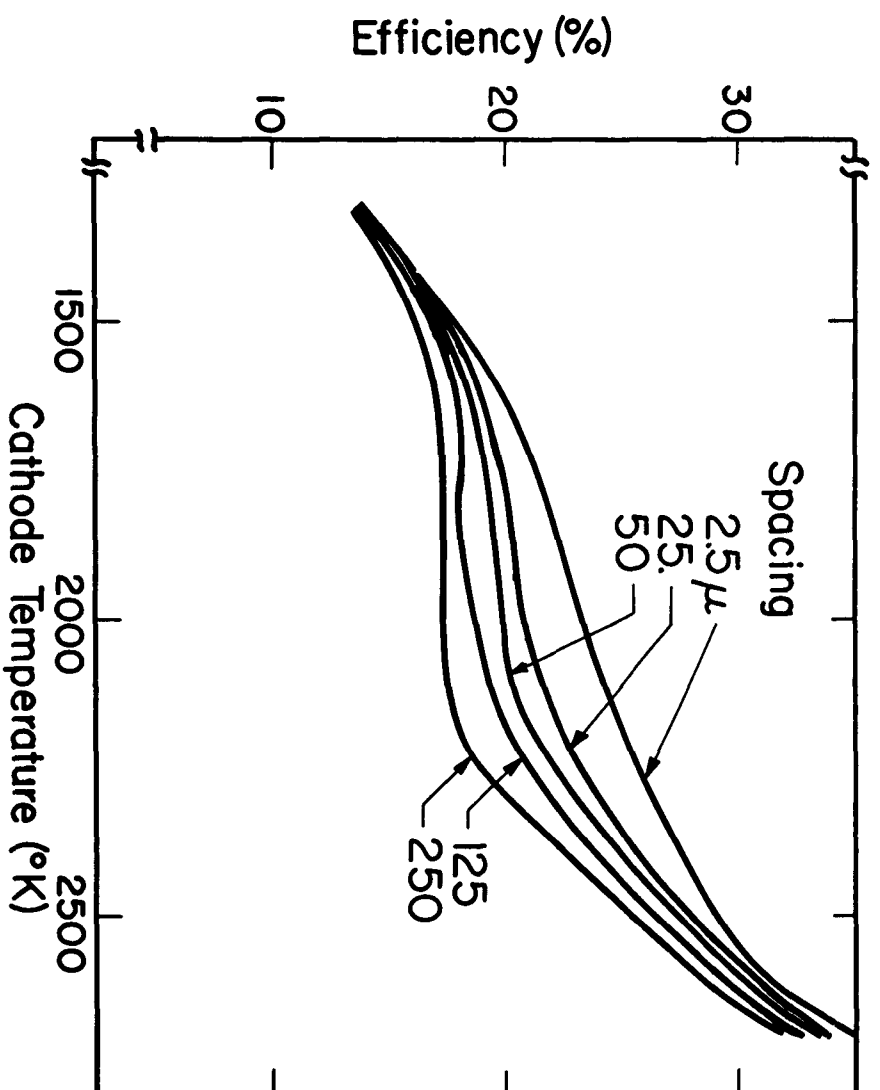


Fig. 7-13. Optimum Anode and Cesium Temperatures as a Function of Cathode Temperature.

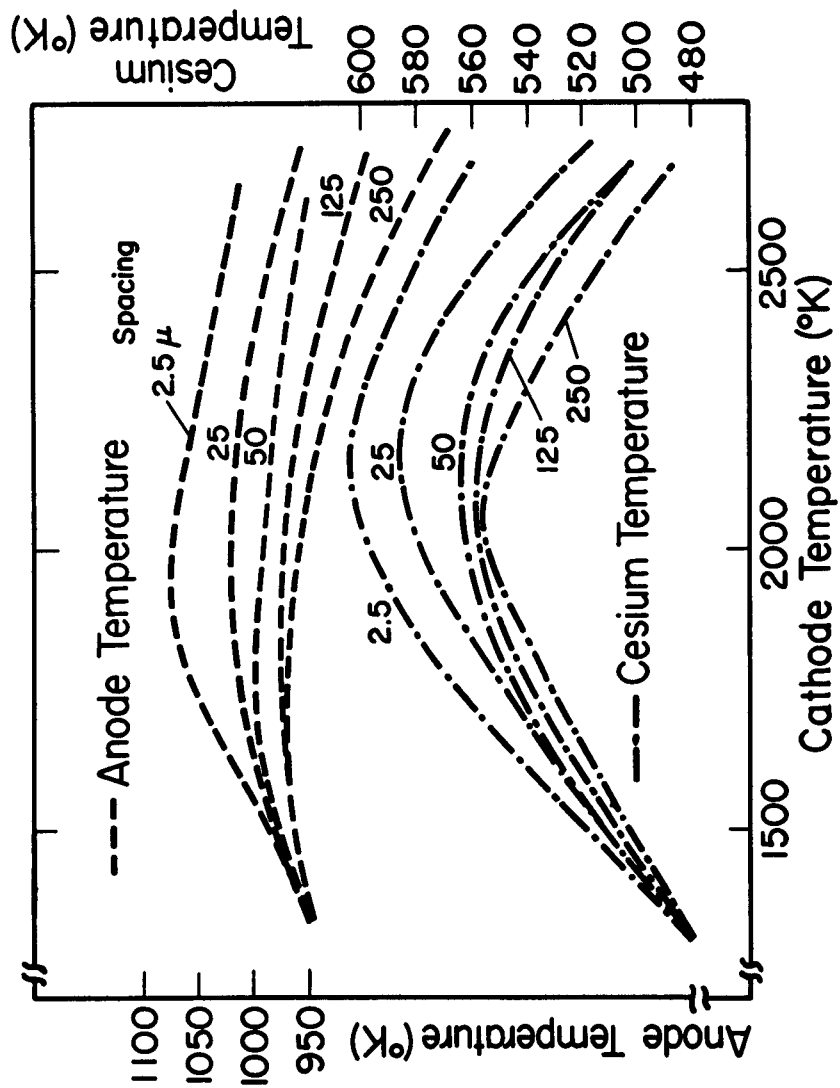


Fig. 7-14. Optimum Anode and Cesium Temperatures as a Function of Cathode Temperature

CHAPTER EIGHT

LIFETIME OF A THERMIONIC ENERGY CONVERTER

The design, construction, and operation of all devices are dictated by their required lifetimes. This requirement varies from minutes for a rocket motor to years for a commercial power plant. The mechanisms of failure must be considered in order to predict this lifetime. In a thermionic energy converter, the basic cause of failure is the evaporative transfer of cathode materials. Other causes such as corrosion, mechanical failure, or radiation damage can in most cases be prevented by ingenious design. Evaporative loss, however, is an inherent limitation because of the high operating temperatures required. To predict the lifetime of a thermionic energy converter, only the allowable loss and the rate of evaporative transfer must be known. The allowable loss is determined by the exact mechanism of failure. Whisker formation, changes in the thermal emissivities, and changes in the work functions are examples of such mechanisms, any of which may be caused by evaporation and/or deposition. The rate of evaporative transfer is dependent upon the geometrical configuration, the operating temperatures, the materials of construction, and the internal pressure of the device.

An energy converter must possess a useful energy output as well as a useful lifetime. In order to compare the operation of different energy converters, some criterion of comparison must be chosen. Some possible criteria are the efficiency, the output power, or the power to weight ratio. Each of these is important in certain applications; for

example, a stationary land-based power station is usually an efficient low cost device while a space power plant is usually a light device. In this paper, the efficiency has been taken as the criterion. This choice was made for several reasons: 1) The efficiency is always of interest to the designer regardless of the application of the device. 2) Calculation of the power-to-weight ratio requires a detailed knowledge of the heat source and sink, and is thus dependent upon considerations beyond the scope of this paper. This point will be discussed further in a later section. 3) The output power and other possible criteria are more specifically related to particular applications than is the efficiency.

A number of authors have calculated efficiencies of thermionic energy converters using a number of different approximations.⁽¹⁾ While the efficiency is a function of a large number of variables, in principle most of these variables are determined by a relatively small number of parameters. If the materials of construction and their properties are known, then the efficiency is a function only of the cathode-to-anode spacing, the cathode and anode temperatures, the means of space charge neutralization, and the lead and load resistances. In most converters presently under investigation, cesium vapor is used for space charge neutralization, and frequently also for modification of the cathode and anode work functions. In this case, the efficiency is also a function of the cesium pressure. In all but the most recent calculations of efficiency referred to above, the interrelationships of work functions, emissivities, temperatures, etc., have been largely ignored. Furthermore, few of the calculations have considered variations in load resistance or the presence of back current. None of

8.3

the calculations have attempted to optimize the values of anode and cesium temperature while simultaneously optimizing lead and load resistance. A recent report⁽³⁾ summarized a method for this simultaneous optimization.

Both lifetime and efficiency can be shown to be functions of the same design parameters: operating temperatures, internal pressure, materials of construction, and geometrical configurations. For a converter built of a given material and operating in the most efficient manner possible, lifetime can be shown to decrease with increasing efficiency. The balancing of the desires for high efficiency and long lifetime requires the knowledge of how these quantities change as the design parameters are changed. In this paper, a proposed method for calculating these quantities is discussed. The relationship of efficiency and lifetime derivable from these calculations is also presented.

A simple approach is to estimate lifetime by dividing the allowable surface recession by the rate of evaporation into vacuum. Since no measurements of the allowable surface recession have appeared in the literature, a value of 2.5 microns was used as a conservative estimate. This value, equivalent to about 10^4 layers of atoms, is small compared to the spacing of most converters presently under consideration. In a later section the exact value used will be shown to be unimportant. Figure 8.1 shows the results of this calculation for molybdenum, columbium, tantalum, and tungsten.⁽⁴⁾

Several important effects occur, particularly in the cesium diode, that are neglected in this calculation. The presence of a partial

cesium coverage may increase or decrease the rate of loss. The presence of contaminant gases (such as water vapor) in the device may also change the rate of loss. Experimental measurements under very carefully controlled conditions are necessary to determine the magnitudes of these effects. Another effect of considerable importance is the reduction of evaporative transfer caused by back-scattering from the cesium atmosphere present in the anode to cathode gap. The magnitude of this effect can be estimated by a relatively simple method.

A first approximation is to assume that all atoms that strike the cold surface (anode) stick and that the partial coverage of cesium has no effect on the evaporation of atoms from the cathode.

For relatively large spacings, the rate of loss is limited by the rate of diffusion through the cathode-to-anode gap. If the diffusion constant D does not change within the gap, then the flux R of metal transported is

$$R = D \frac{\Delta \rho}{d} \quad (1)$$

where $\Delta \rho$ is the difference in density of evaporated atoms at the cathode and anode, and d is the width of the cathode-to anode gap. The evaporative flux R_v at any temperature T is given by

$$R_v = \rho V/4 \quad (2)$$

where ρ is the density and V is the arithmetic average velocity of the evaporating species.⁽⁵⁾ Since the pressure and temperature of evaporated atoms adjacent to the electrodes are nearly equal to those characteristic

of the electrodes, $\Delta\rho$ is equal to the difference of densities characteristic of cathode and anode. Since the cathode temperature is considerably higher than the anode temperature, the density at the cathode ρ_c is much greater than that at the anode ρ_a . Thus $\Delta\rho$ is equal to ρ_c and the transport flux is

$$R = \frac{4D}{V} \frac{R_{vc}}{d} \quad (3)$$

where R_{vc} is the normal evaporative flux at the cathode temperature.

The quantity D/V has the dimensions of length and is proportional to the mean free path, λ . Hard sphere calculations⁽⁶⁾ show that D/V equals $\lambda/3$.

Thus,

$$R = (4/3)(\lambda/d) R_{vc} \quad (4)$$

The evaporative transport problem is analogous to the neutron scattering problem in a non-absorbing medium, where R_{vc} is analogous to the incoming neutron intensity and R to the intensity transmitted. C. W. Maynard has solved this neutron scattering problem numerically for small spacings.⁽⁷⁾ Examination of his results between $1/4$ and 4 mean free paths shows that the equation

$$R = R_{vc}/(1 + 3d/4\lambda) \quad (5)$$

fits the results very accurately. For large spacing this expression approaches that of equation 4.

A more general approach is to consider the space as a succession of reflecting and transmitting slabs. The transmission through each of these slabs must have the same functional relationship to thickness as the transmission through the assembly. If the multiple reflections are summed up, assuming isotropic behavior, the functional relationship is

$$f\left(\sum_1 x_1\right) = 1 + \sum_1 \left(\frac{1 - f(x_1)}{f(x_1)}\right)^{-1} \quad (6)$$

where x_1 is the thickness of the i th slab and $f(x_1)$ is the fraction transmitted through a thickness x_1 .

It can easily be shown that the only function which obeys this relationship is

$$f(x) = (1 + ax)^{-1} \quad (7)$$

This implies that $R = \frac{R_{vc}}{1 + ad}$ is the general form of the solution to the transport equation. For a sufficiently large d , the constant term can be neglected in comparison with ad , thus reducing the equation to the diffusion case where a is $3/4 \lambda$. The scattering approach of Maynard also led to the same value for the constant. Both approaches are based on all collisions being of the hard sphere variety. Thus equation 5 is the general solution for transport where the factor $3/4$ will be different if the collisions do not obey the hard sphere model.

An experimental verification of equation 5 for molybdenum is described in Chapter 3 of this report. No other measurement of mean free path under these non-isothermal conditions was found in the literature.

Theoretical estimates of mean free path assuming isothermal conditions were 0.9 to 20 times the experimental value, depending on the assumptions made.

Since the mean free path is inversely proportional to the pressure and is not a sensitive function of the temperatures, the following relationship was assumed to hold true for the transport flux

$$R = (1 + 0.087 \text{ pd})^{-1} R_{vc} \quad (8)$$

for the pressure p in mm of Hg and the spacing d in microns. The value of 0.087 is based upon only one series of experiments and should be accepted only with considerable reservation.

From equation 8, it is possible to determine lifetime as a function of cathode temperature, spacing, and cesium bath temperature. The relative lifetime, defined as the ratio of the lifetime in a gas filled diode to the lifetime in vacuum, is equal to R_{vc}/R . In Figure 8.2 the relative lifetime is plotted as a function of spacing and cesium bath temperature which determines the pressure. Better determinations of the mean free path as a function of pressure may change the values shown in this figure, but the general validity of the figure should not be affected. The lifetime will obviously increase with increasing cesium pressure and spacing.

With the aid of the efficiency calculations in the previous section of this report, it is possible to determine efficiency and lifetime as functions of only four parameters -- cathode, anode, and cesium bath temperatures and the cathode-anode spacing. If this determination be made,

then for a fixed spacing, a maximum efficiency can be found for a given minimum evaporative lifetime. The measurement of mean free path summarized in a previous section was made using a molybdenum cathode. The relative lifetimes deduced from this value should not be seriously different for tungsten, since both atomic diameter and chemical behavior are very similar. A curve of maximum efficiency as a function of the evaporative lifetime for tungsten is shown in Figure 8.3 for a 125 micron spacing diode. Similar curves can be drawn for other spacings. This efficiency has been simultaneously maximized with respect to anode, cathode, and cesium temperatures for a fixed lifetime. In principle, this procedure could be continued to determine an optimum value of spacing. However, impracticably small values of spacing result.

The extremely large values of lifetime for tungsten shown in Figure 8.3 are clearly of no practical significance. However, for materials of higher vapor pressure than tungsten, an analogous curve would be useful. In particular, if the electron emission properties of molybdenum in the presence of cesium were the same as those of tungsten, then the lifetime scale would be shifted as indicated in Figure 8.3. It is clear that under these conditions, a required lifetime of 1 year or greater will result in an efficiency less than 20% for molybdenum. It must be recalled that this statement is based on the allowable surface recession being 2.5 microns. However, the efficiency in the region of interest for molybdenum is not a sensitive function of lifetime. Allowing 10 times the recession used here does not markedly increase the possible efficiency.

If accurate emission data were available, calculations of the type discussed here could be carried out for other materials. Similarly, lifetime calculations could be carried out if measurements of mean free path for other materials were available. While experimental investigations of these data are presently being made by various laboratories, little information is available in the literature.

As mentioned before, it may often be more desirable to design a system with a maximum value of the ratio of output power to system weight in lieu of maximum efficiency. This is an extremely difficult problem to solve in general since the weight of the diode itself is negligible, and the weight of the system is the dominant factor. Thus, the construction of the system must be known in great detail. For example, in the case of a reactor-powered thermionic converter, a reactor core, shield, assembly, reflector, and radiator would have to be designed for each choice of spacing and cathode, anode, and cesium temperatures in order to determine the weight of the system.

It is possible, however, to say a few things in a semi-quantitative way about the problem. Consider the radiator, which is responsible for a large part of the weight of a space power system. Let P_o be the power output, P_i the input power, η the efficiency of conversion, and T_a the anode temperature. Then by definition of η

$$P_o = \eta P_i \quad (9)$$

The amount of power, P_w , which the radiator must dump as waste heat is given by

$$P_w = P_i - P_o = (1 - \eta) P_i \quad (10)$$

If the waste heat is radiated

$$P_w = C_1 A T_a^4 \quad (11)$$

where A is the surface area of the radiator and C_1 is some numerical constant. Further, if the weight W_r of the radiator is proportional to its area,

$$W_r = C_2 A \quad (12)$$

When combined, the above equations yield for the ratio of output power to radiator weight

$$P_o/W_r = (C_1/C_2) \left(\frac{\eta}{1 - \eta} \right) T_a^4 \quad (13)$$

The quantity $\eta(1 - \eta)^{-1}$ is a monotonically increasing function of η so that for fixed anode temperature, maximizing the efficiency will maximize P_o/W_r as well. However, in many cases, the anode temperatures cannot be considered fixed. A procedure similar to that used in the preceding sections can be followed using the maximum power-to-weight ratio, instead of efficiency as the criterion. The results are very similar to those of the previous section in that higher cathode temperatures result in higher power-to-weight ratios. Figure 8.4 shows the results of optimizing P_o/W_r for a 5 mil spacing tungsten diode.

A comparison of the results using the two different criteria, efficiency and power-to-weight ratio, shows that a significant decrease in efficiency is the price that must be paid for the maximum power-to-weight ratio. This is particularly true in the region between 1600 and 2200°K cathode temperatures where the optimum efficiency does not vary rapidly with temperature.

In Figure 8.4 the relative values of the power-to-weight ratio and the optimum anode temperatures are also plotted. The peak in anode temperatures near a cathode temperature of 2500°K is almost certainly a local maximum, since the power-to-weight ratio can obviously be increased by going to infinite anode temperatures, using a "slightly larger" value of cathode temperature.

When for a fixed spacing and cathode temperature all other parameters are optimized using efficiency as the criterion, the resulting optimum efficiency is a relatively insensitive function of the cathode temperature in the temperature range 1600 to 2200°K. Clearly, a small improvement in temperature capability will not result in a significant improvement in efficiency. Only a large increase in operating temperature provides a marked improvement. In order to operate a thermionic converter of the type discussed here at 25% efficiency, a cathode temperature above 2200°K is necessary. Only tungsten is capable of a reasonable lifetime at this temperature.

A thermionic converter using tungsten electrodes operating with a cathode temperature of 1600 to 2200°K would have an efficiency between 15 and 20% and an indefinite lifetime. If the emission characteristics of

molybdenum are similar to those of tungsten a molybdenum diode could be constructed with a lifetime greater than one year at an efficiency less than 20%.

The introduction of cesium into a thermionic energy converter has two opposing effects upon the efficiency. Thermal and electrical losses occur in the cesium, while the reduction of cathode and anode work functions allows more efficient operation. As the pressure of cesium is increased from zero, the efficiency is increased reaching a maximum. Above this critical value of cesium pressure, the efficiency decreases because of the increasing electrical and thermal losses in the plasma. The attainment of maximum efficiency depends critically upon establishing the optimum cesium pressure. The use of a cathode material possessing a larger affinity for cesium would make possible lower cesium pressure to obtain a given work function. The plasma losses would then be lower. The net result would be a higher efficiency of operation. In short, the use of a cathode material of higher affinity for cesium will result in increased efficiency. It can be shown that the converse is also true. Thus, consideration of the cesium affinity is of considerable importance in the selection of a cathode material.

From examination of the operating characteristics of thermionic converters it is seen that efficiency is a relatively insensitive function of anode and cathode temperature and of spacing. The cesium pressure, on the other hand, is quite a critical parameter and should be controlled very closely. The lead and load resistances are also critical parameters.⁽³⁾ Operation away from these critical values can decrease the efficiency by a sizeable fraction. These relationships should be carefully considered in the design of thermionic converters.

The evaporative lifetime of a thermionic converter can be increased by increasing the spacing and the cesium pressure. While the data presented here are only preliminary, the lifetime of a cesium filled diode will probably be at least 10 times that estimated by the use of evaporation rates into vacuum.

The data necessary for calculations of the type described are extremely scarce and relatively unreliable. The obtaining of more extensive and more accurate information would allow the design of thermionic converters to be made in a relatively routine fashion. For tungsten such a design has been made and the device is presently being built.

The calculations of efficiency have been checked against the results of the few experimental devices available in the literature. Where sufficient information is given to allow comparison, the agreement has been quite reasonable. While the calculations are not to be considered as the exact theoretical results, the values are probably quite close to reality. While the model of plasma is not entirely realistic and the effect of space charge has been largely ignored, the errors introduced are small in the regions of interest. Devices of 35% efficiency are clearly impractical, while a 20% efficient device can probably be built with present techniques and materials.

REFERENCES

1. N. S. Rasor, J. Appl. Phys., 31, p. 163 (1960);
J. M. Houston, J. Appl. Phys. 30, p. 481 (1959);
J. H. Ingold, J. Appl. Phys. 32, p. 769 (1961);
A. Schock, J. Appl. Phys. 32, p. 1564 (1961);
G. N. Hatsopolous and J. Kaye, Proc. I.R.E. 46, p. 1574 (1958).
2. U. S. Patent No. 2,980,819 issued to G. R. Feaster, April 18, 1961.
3. L. S. Richardson and A. E. Fein, Interim Scientific Report No. 2,
on AF33(616)-8292.
4. J. W. Edwards, H. L. Johnston, and P. E. Blackburn, J. Am. Chem. Soc.
74, p. 1539 (1952).
R. Speiser, P. E. Blackburn, and H. L. Johnston, J. Electrochem. Soc.
106, p. 52 (1959).
J. W. Edwards, H. L. Johnston, and P. E. Blackburn, J. Am. Chem. Soc.
73, p. 172 (1951).
O. Kubaschewski and E. L. Evans, "Metallurgical Thermochemistry",
Pergamon Press, 1958, p. 335.
5. S. Dushman, "Vacuum Technique", Wiley, 1949, p. 17.
6. Ibid, p. 74.
7. C. W. Maynard, Nuclear Sci. and Eng. 6, p. 174 (1959).
8. W. E. Forsythe and E. M. Watson, J. Opt. Soc. of Amer., 24, p. 114 (1934).
9. J. B. Taylor and I. Langmuir, Phys. Rev. 44, p. 423 (1933).
10. Unpublished Research, M. Gottlieb and R. Zollweg.

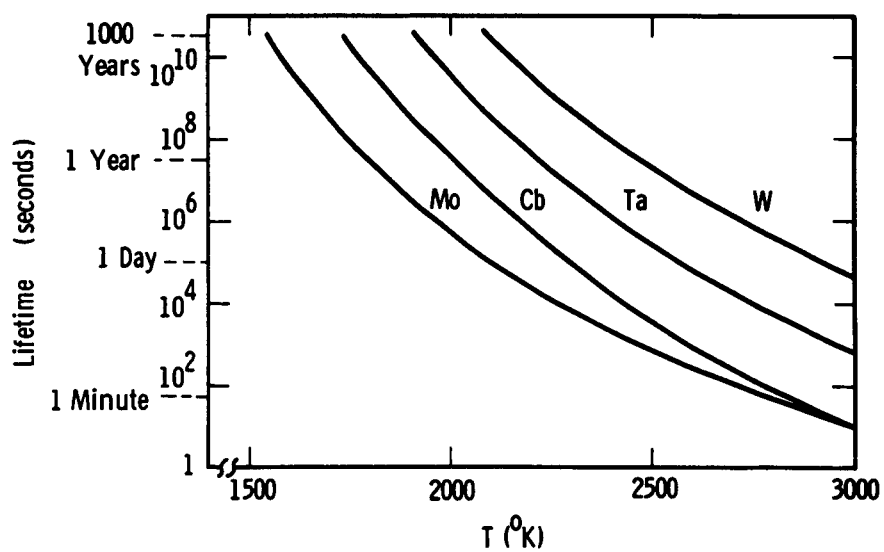


Fig. 8-1. Time to Lose 2.5 Microns by Evaporation from Mo, Cb, Ta and W as a Function of Temperature.

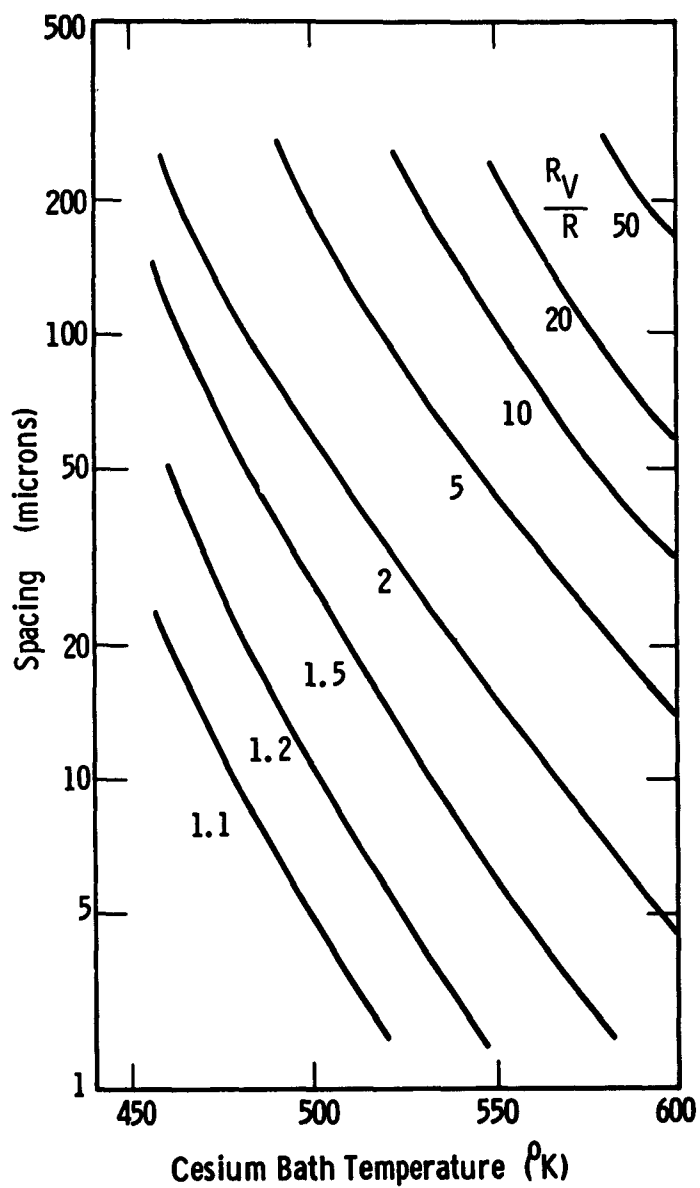


Fig. 8-2. Relative Lifetime of a Cathode as a Function of Cesium Bath Temperature and Spacing.

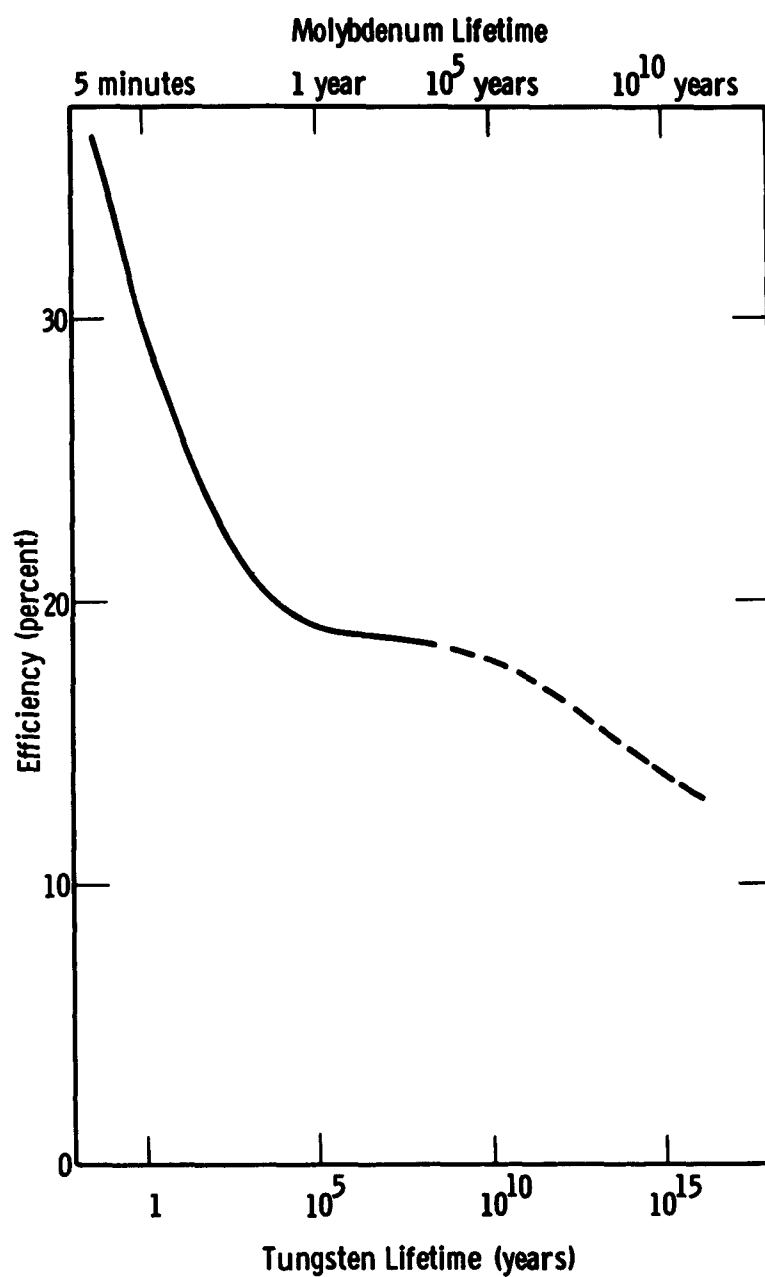


Fig. 8-3. The Relationship between Evaporative Lifetime and Efficiency for Tungsten and Molybdenum.

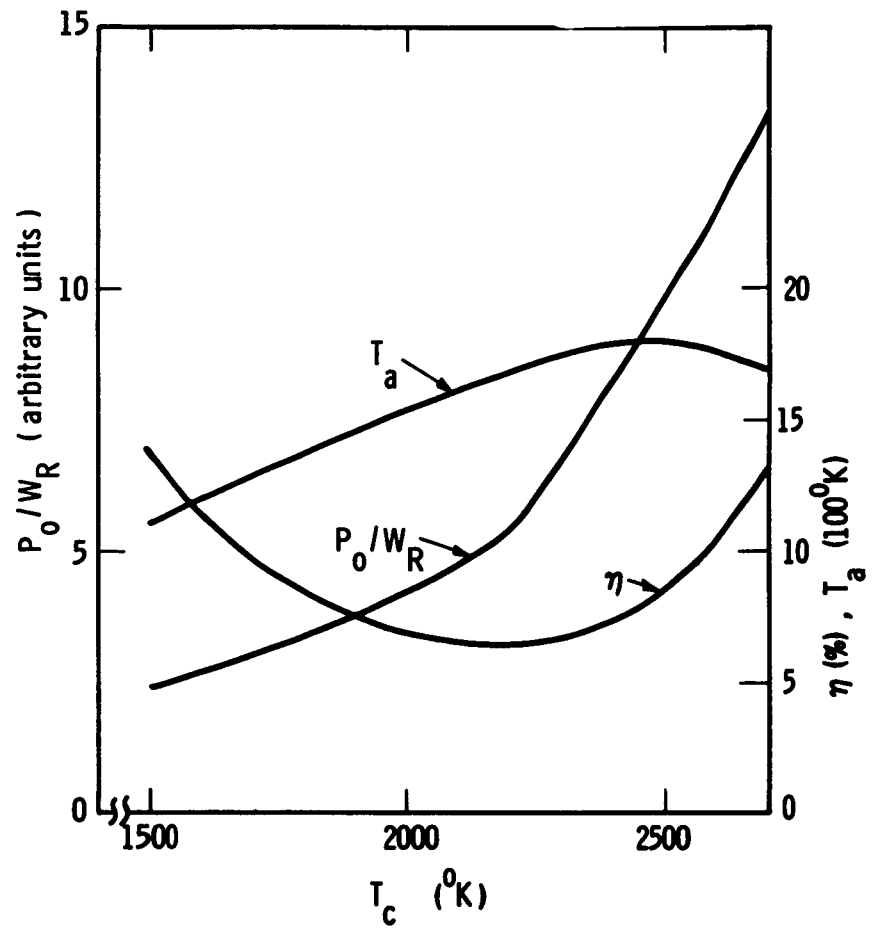


Fig. 8-4. Power to Weight Ratio, Optimum Anode Temperature, and Efficiency at Minimum Weight as a Function of Cathode Temperature.

CHAPTER NINE

ANOMALOUS RICHARDSON EMISSION CONSTANTS

The anomalous behavior of the thermionic electron emission of some materials has sometimes been ascribed to a value of Richardson's constant not equal to the standard value of $120 \text{ amp-cm}^{-2} \text{ } ^\circ\text{K}^{-2}$. It is shown here that such cannot be the case and that such a deviation from Richardson's law must be attributed to either a temperature dependent reflection coefficient or, more likely, a temperature dependent chemical potential of the emitting surface. In particular, those materials which would otherwise require a value of Richardson's constant larger than $120 \text{ amp-cm}^{-2} \text{ } ^\circ\text{K}^{-2}$ must have a temperature dependent chemical potential, for a varying reflection coefficient cannot look like an increase in A.

Richardson's equation for the saturation electron emission current, I, from metals is given as

$$I = (1-r)A T^2 e^{-\mu/KT} \quad (1)$$

where r is the reflection coefficient, μ the chemical potential in ev, T the absolute temperature, K is the Boltzmann constant, and A a constant theoretically equal to $120 \text{ amp-cm}^{-2} \text{ } ^\circ\text{K}^{-2}$. For semiconductors, it has been claimed⁽¹⁾ that a similar equation can be used with the electron mass, m, replaced by the effective mass, m^* . This results solely in multiplying the current above by a factor (m^*/m) . In such a case, it is said that the material has an "anomalous" Richardson constant.

Based upon such a relation, it has been proposed⁽²⁾ that higher currents and consequently higher efficiencies in a thermionic converter can be achieved through the use of a cathode material with a large effective mass.

It will be shown from fundamental concepts that such cannot be the case even if Richardson's equation is not truly valid. In particular, it will be shown that if there were a material with an anomalous Richardson constant, it would be possible to attain efficiencies in excess of Carnot efficiency and therefore violate the second law of thermodynamics.

Stripped of the numerous parts necessary in its construction, the thermionic diode can be basically represented by the schematic of Figure 9-1. A cathode surface of chemical potential μ_1 in contact with a heat reservoir at an absolute temperature T_1 thermally emits electrons across a gap to an anode of chemical potential μ_2 in contact with a heat reservoir at a temperature T_2 . ($T_1 > T_2$) The electrons are returned from the anode to the cathode through an external load.

In Figure 9-2, V is the internal voltage developed by the diode. In practice, for a close-spaced vacuum diode, V is the sum of the voltage delivered to the load plus the voltage drops across the leads. Quantitatively, the three modes are described: downhill if $\mu_1 > \mu_2 + V$, flat if $\mu_1 = \mu_2 + V$, and uphill if $\mu_1 < \mu_2 + V$.

Let the maximum potential barrier between the two electrode surfaces be denoted by μ . For the sake of convenience, assume plane parallel geometry with both surfaces of unit area. Note that here μ may include not only the effect of the chemical potentials of the surface, but

also space charge and Schottky effects. Denote the net current emitted by each of the surfaces by J_1 and J_2 and define

$$J_1 = (1-r_1)f_1(T_1, \mu) \quad (1a)$$

$$J_2 = (1-r_2)f_2(T_2, \mu) \quad (1b)$$

Note that the functions f_1 and f_2 can only be dependent upon the temperature of the surface and the potential μ . The net current leaving surface 1 and absorbed by surface 2 is J_{12} where

$$J_{12} = r_{12}f_1(T_1, \mu) \quad (2)$$

and the net reflective coefficient, r_{12} is given by

$$r_{12} = \frac{(1-r_1)(1-r_2)}{1-r_1r_2} \quad (3)$$

Similarly the current leaving surface 2 and absorbed by surface 1 is

$$J_{21} = r_{21}f_2(T_2, \mu) \quad (4)$$

where r_{21} is the appropriate net reflective coefficient, and by the symmetry of (3.3)

$$r_{21} = r_{12} \quad (5)$$

Now assume that both surfaces are kept at the same temperature, T and that the two surfaces are shorted electrically. Then by the second law of thermodynamics, no current can flow. Thus, from (2), (4), and (5)

$$f_1(T, \mu) = f_2(T, \mu) \quad (6)$$

Since in (6) both T and μ are arbitrary, the functional form for the emission from any surface must be independent of the surface. Thus if (1) is true for any one material (and it is known to be true for many materials), it must be true for all materials.

Thus we have proven that emission currents must be of the form (1). Therefore, the behavior of those materials which exhibit an anomalous Richardson constant on the assumption of a constant chemical potential should really be ascribed to a temperature dependent chemical potential.

There is a further relation which can be derived from such a general consideration. Let us take as the reference level of potential energy the Fermi level of surface 1. Let the total of kinetic and potential energy transported by the electrons leaving surface 1 and absorbed at surface 2 be denoted by $Q_{12}(T_1, \mu)$. Similarly, let $Q_{21}(T_2, \mu)$ be the total energy transported by the electrons leaving surface 2 and absorbed at surface 1. Define $h_1(T_1, \mu)$ and $h_2(T_2, \mu)$ by

$$h_1(T_1, \mu) = Q_{12}(T_1, \mu)/J_{12}(T_1, \mu) \quad (7)$$

$$h_2(T_2, \mu) = Q_{21}(T_2, \mu)/J_{21}(T_2, \mu) \quad (8)$$

It has already been shown that, by setting to zero the net current flow for $T_1 = T_2$ under short circuit conditions, the functions f_1 and f_2 are

identical. Similar reasoning based on the net energy transfer under the same conditions requires that Q_1 and Q_2 be identical. Then from (7) and (8) the functions h_1 and h_2 must be identical. Now for materials obeying Richardson's equation for which the electron velocity directly outside the emitting surface has a Maxwellian distribution, it can be easily shown* that

$$h(T, \mu) = \mu + 2KT \quad (9)$$

However, as has been shown above, this relation is not dependent upon the electron distribution. Thus one has for the net transfer of energy from surface 1 to surface 2, from (2), (3), and (4)

$$Q_{12} = J_{12} (\mu + 2KT_1) \quad (10)$$

and similarly

$$Q_{21} = J_{21} (\mu + 2KT_2) \quad (11)$$

* A. J. Dekker, loc. cit, p. 224.

REFERENCES

1. See for example: A. J. Dekker, Solid State Physics, Prentice Hall, Inc., Englewood Cliffs, N. J. (1957).
2. Los Alamos Quarterly Report for period ending January 20, 1959 - Report No. LAMS 2330, p. 12.

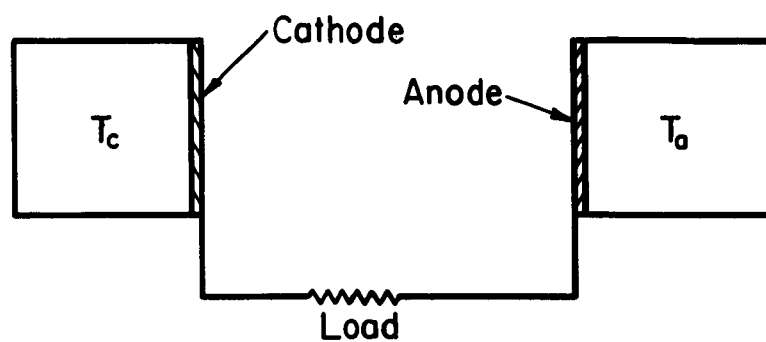


Fig. 9-1 Basic Thermionic Diode

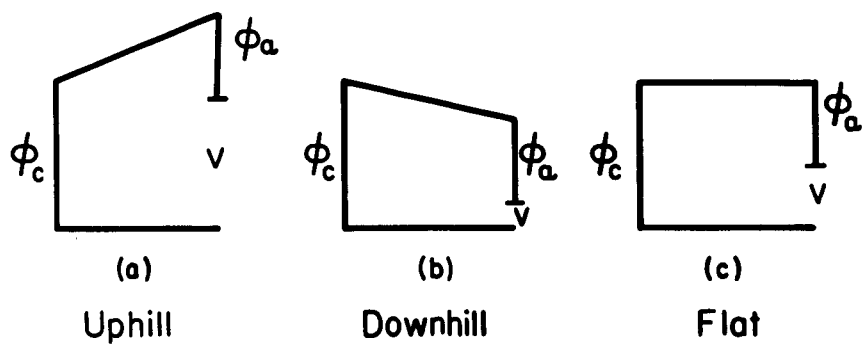


Fig. 9-2. Modes of Operation

CHAPTER TEN

ELECTRON AND ION EMISSION FROM CESIUM COATED REFRACTORY
METALS IN ELECTRIC FIELDS

Attention is called to the dependence of cesium coverage of refractory metal emitters on electric field as well as upon cesium arrival rate (pressure) and emitter temperature. At low cesium coverage a surface phenomena with a discontinuous change of coverage and of electron and ion emission may take place even for uniform work function emitters as a consequence of the Saha-Langmuir equation. This phenomenon may account for the double-mode behavior of electron emission from the Cs-coated probes reported in Chapter Two, as well as certain of the double-mode behavior observed with thermionic converter diodes at lower Cs pressures. It also has a bearing on the relative emission rates of electrons and positive ions.

When one is concerned with electron emission from cesium coated refractory metals such as tungsten, molybdenum, etc., it has become fairly common practice to refer to the extrapolated "S" curves first obtained by Taylor and Langmuir¹ for tungsten and recently verified and extended to other materials by Houston², Aamodt³, and DeSteele⁴. These curves give values for the saturated electron emission at a given temperature and cesium pressure in the absence of an electric field. When a field is applied to remove electrons, it is important to note that increased electron emission may occur not only because of Schottky effect but also because of a change in surface coverage.

The Saha-Langmuir equation^{1,5} gives a relation between Cs atom and ion evaporation rates

$$\ln (2 \mathcal{J}_p) = \ln \mathcal{J}_a + \frac{e}{kT} (\phi - I) \quad (1)$$

where \mathcal{J}_p , \mathcal{J}_a are evaporation rates of ions and atoms, respectively

ϕ is the work function of the emitter with equilibrium Cs coverage

I is the ionization potential of the vapor.

This equation has been experimentally verified for alkali metals on tungsten and oxygenated tungsten but must be generalized to include reflection for alkali metals incident on platinum.⁵ It is reasonable to expect behavior similar to tungsten for other refractory metals such as rhenium, molybdenum, tantalum, etc. Thus Cs on tungsten at low Cs coverage where $\phi > I$ the cesium ion evaporation rate is greater than the cesium atom evaporation rate. Taylor and Langmuir found the atom evaporation rate to depend strongly on coverage as shown in Figure 10-1 which also shows the ion evaporation rate (based on the Saha-Langmuir equation) and the sum of the atom plus ion evaporation rates vs. coverage - all at a constant tungsten emitter temperature of 840°K. At equilibrium coverage the atom arrival rate must equal the sum of the atom and ion evaporation rates. If one assumes a constant Cs pressure such that the arrival rate is indicated by the dotted line in Figure 10-1, there will be three degrees of coverage at which the arrival rate equals the sum of the evaporation rates, points A, B, and C in the figure. Only points A and C are stable, however, since a small fluctuation in coverage at B will lead to a larger change until point A or C is reached. At higher emitter temperatures both evaporation rates will be higher but the curves will be qualitatively similar in shape to Figure 1 except that at very high temperatures the relative minimum near $\theta = 0.07$ will disappear. A family of evaporation curves corresponding to

different emitter temperatures can be drawn to show how coverage will vary with emitter temperature at constant Cs pressure. For a small temperature interval two stable coverages are possible and which occurs will depend upon previous history such as the direction of temperature change and electric field.

When an electric field opposing ion emission is applied, the ion evaporation rate j will be drastically reduced while the atom evaporation rate is relatively unchanged. At equilibrium this necessitates a change in coverage until the total evaporation rate once again equals the arrival rate. It would be possible by means of electric field to force a system initial stable at coverage A with work function $\phi \sim 4.5$ eV, high ion emission and low electron emission over into coverage C with $\phi \sim 3.5$ eV and relatively low ion emission and high electron emission.

With a relatively weak electric field opposing ion emission, ions would continue to evaporate but would be confined to a certain region near the emitter by a sort of semipermeable membrane, permeable to atoms but not ions. The arrival rate of atoms plus ions to the emitter surface is thus increased over that for the field-free case necessitating an increase in surface coverage. With electric fields of the order of 10^4 to 10^5 volts/cm at the emitter surface (which might be achieved by sheaths) the ions would be confined to a region inside the image potential barrier and, although the work function would be altered, it would not be appropriate to speak of ion "evaporation". The surface electric fields referred to above will usually be caused largely by sheaths but these in turn will depend upon external electrode potentials since the latter play a significant role in the removal rate of charge carriers.

A different aspect of the surface phenomena discussed above has been mentioned by Reynolds⁶ to explain the discontinuity in ion production rate with $1/T$ observed with electric fields favoring ion emission. The results shown in Chapter 2 of this report are in the range of cesium coverage where this phenomenon is expected and are in qualitative agreement with the above model. Current-voltage curves obtained in this laboratory for thermionic diodes with tantalum and molybdenum emitters and a cesium pressure of 0.085 mm Hg have also exhibited a double-mode behavior in a narrow emitter temperature region which could be "switched" by changing the electrode voltages in qualitative agreement with the above ideas. For the tantalum emitter with an external voltage of 1.5 V, current in the lower mode was about 0.1 amps/cm² and in the upper mode about 10 amps/cm², whereas, an extrapolation of Houston's data for Ta-Cs gives a field-free saturation emission of about 0.01 amp/cm². An estimate of the Schottky emission enhancement because of a positive ion sheath at this pressure gives a factor of 6 in contrast to the observed 1000-fold increase. These results which appear at temperatures where low Cs coverage is expected are most reasonably explained by the change in coverage discussed above with a relatively minor contribution from Schottky effect.

REFERENCES

1. J. B. Taylor and I. Langmuir, Phys. Rev. 44, 423 (1933).
2. J. M. Houston, Proc. Conf. on Thermionic Proc. and Materials, Bedford, Mass., June 1961.
3. R. L. Aamodt, Proc. Conf. on Thermionic Processes and Materials, Philadelphia, January 1961. R. L. Aamodt, L. J. Brown, and B. D. Nichols, J. Appl. Phys. 33, 2080 (1962).
4. Chapter Two of this report.
5. S. Datz and E. H. Taylor, J. Chem. Phys. 25, 389 (1956).
6. T. W. Reynolds, NASA Technical Note, D-1307, May 1962, "Estimation of Critical Temperatures for Surface Ion Currents from Electron Emission Data".

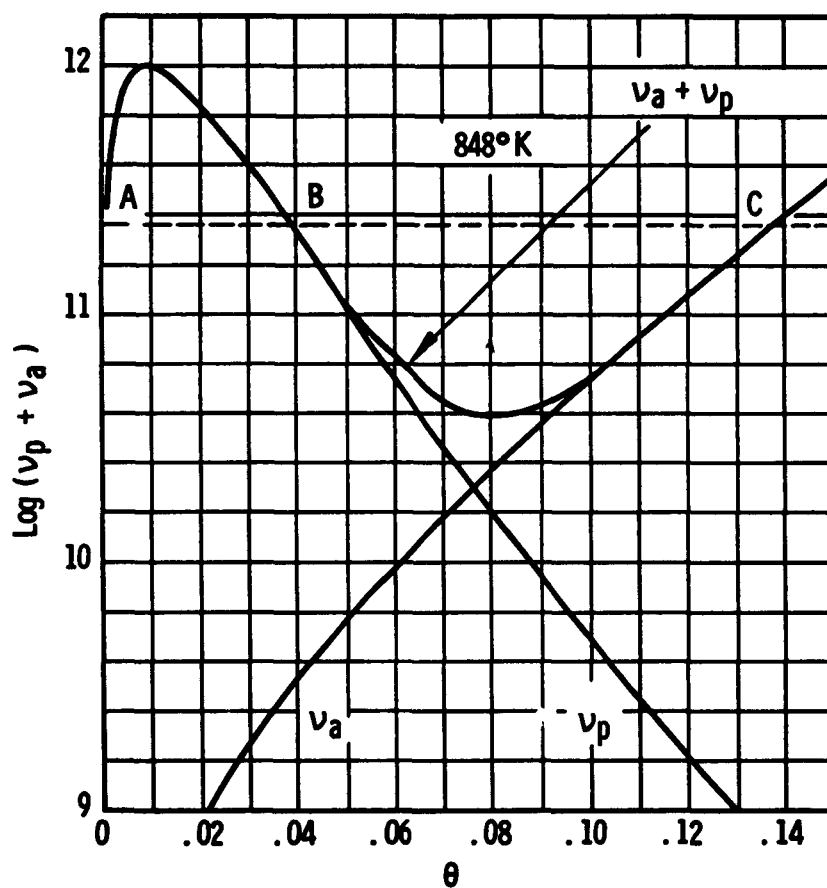
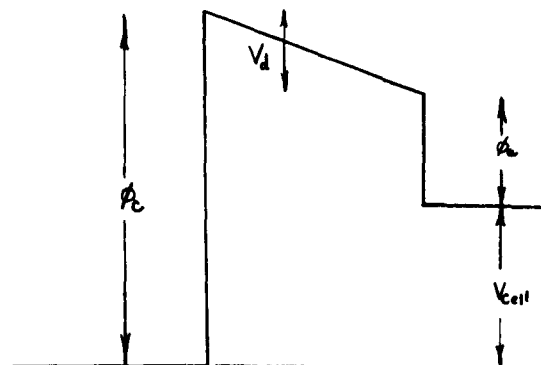


Fig. 10-1. Atom and Ion Evaporation Rates vs. Fractional Monolayer Coverage of Cs on Tungsten after Taylor and Langmuir.

CHAPTER ELEVEN

POTENTIAL DISTRIBUTIONS IN HIGH PRESSURE CESIUM
THERMIONIC DIODES

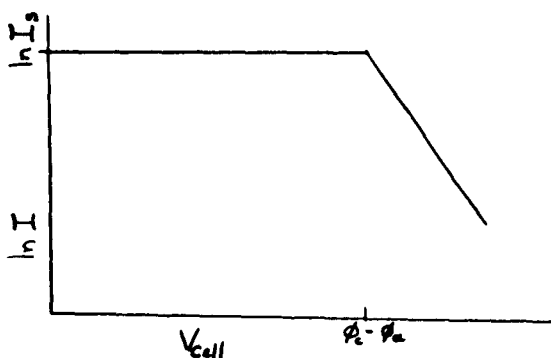
The operation of a thermionic diode can be completely understood only if the details of the potential distribution within the diode are known. The distribution in a vacuum diode or a low pressure gas diode is simple, and a typical case is shown in the figure below.



Potential Diagram in Low Pressure or Vacuum Diode
for No Space Charge

The cathode and anode work functions are ϕ_c and ϕ_a , respectively, and the cell terminal voltage is V_{cell} . If the space charge is very small, or compensated, the interelectrode field is uniform, and the voltage difference is represented by V_d , which in general

may be positive, negative, or zero. An idealized current-voltage curve for such a diode is shown in the figure below.



V-I Plot of Vacuum Diode

The cell current will be equal to the saturation emission current of the cathode, I_s , for the cell voltages up to $(\phi_c - \phi_a)$. For cell voltages higher than this, the internal potential, V_d , becomes positive, and the electrons encounter a retarding potential so that the current is given by

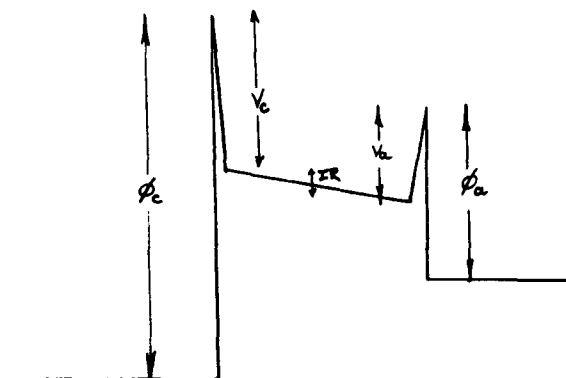
$$I = I_s \exp \left[\ell \frac{(\phi_c - \phi_a) - V_{\text{cell}}}{kT} \right]$$

The slope of this curve is e/kT , from which the electron temperature may be obtained.

In a high pressure thermionic diode the situation is much more complicated, due mainly to two causes. First, the electrons may be highly scattered by gas atoms, giving rise to resistive losses in the plasma. Second, potential sheaths may develop at the electrodes. When a plasma is in contact with a wall, it will build up a region of positive ion space charge over distances the order of a Debye shielding length, given by

$$d_D = \left(\frac{kT}{4\pi N_e e^2} \right)^{1/2}$$

A typical potential diagram for such a cell will be as shown in the figure below.



Potential Diagram in High Pressure Diode

The cathode sheath voltage and the anode sheath voltage are given by V_c and V_a , respectively. The resistive voltage drop in the plasma is IR . If the width of the cathode-anode gap is many electron mean free paths, then the plasma may be characterized by a resistivity ρ , and the cell current density given by

$$J = N_e e \mu E ,$$

in which N_e is the electron density, μ is the electron mobility, and E is the internal field.

The current-voltage curve for the high pressure diode does not have two distinct regions of saturation current and retardation as does the low pressure or vacuum diode, but rather a gradual curve **asymptoting** to saturation current at positive cell voltages. It is further complicated by the possible presence of arc currents associated with volume ionization of the gas for sufficiently positive cell voltages. The electron temperature cannot be taken directly from a current-voltage curve, but a method has been described by Carabateus, Pezaris and Hatsopoulos^{*} by which the electron temperature can be obtained from an experimental V-I curve. This method assumes that the electron density, temperature, and random plasma current density are uniform except at the sheaths.

* Journal of Applied Physics, 32, 352 (March, 1961).

The current at the cathode and anode, respectively, may be written

$$I = I_s - I_e \exp\left(-\frac{V_c}{kT_e}\right) \quad \text{and} \quad I = I_e \exp\left(-\frac{V_a}{kT_e}\right), \quad (1)$$

where the ion currents have been neglected, which is a good approximation for large cell currents. The saturation emission current is I_s , I_e is the random electron plasma current and T_e is the electron temperature. The random current is eliminated, yielding

$$\frac{I_s - I}{I} = \exp\left(e \frac{V_a - V_c}{kT_e}\right) \quad (2)$$

It is seen from the previous figure that

$$V_a - V_c = V_{\text{cell}} + IR - (\phi_c - \phi_a) \quad (3)$$

Taking logarithms, and making the above substitution,

$$\ln \frac{I_s - I}{I} = \frac{e}{kT_e} \left[V_{\text{cell}} + IR - (\phi_c - \phi_a) \right] \quad (4)$$

The electron temperature is obtained from the slope of the curve of $\ln \frac{I_s - I}{I}$ vs. $V_{\text{cell}} + IR - (\phi_c - \phi_a)$.

In the analysis of experimental data carried out in the previously mentioned paper, the authors have neglected the IR term, while in the analysis presented here, this term is evaluated, and is large under the conditions of the measurements. Their analysis also does not obtain the sheath voltages, while in the present work, these

will be computed. Experimental data has been taken in the demountable cell described in Chapter One of this report using a tantalum emitter. The current-voltage data selected for analysis was taken at a temperature of 2000°C and a cesium reservoir temperature of 293°C . These curves are shown in Figures 11-1 for gap settings of 7.6 mils and 14.8 mils.

The resistive voltage drop in the plasma can be obtained using these two curves, under a set of assumptions. These assumptions are: (a) that the sheath voltages are constant for constant cell current, cesium pressure and cathode temperature; (b) that the width of the sheaths are negligible compared to the cathode-anode gap. This is discussed in Appendix I; (c) that the electric field is uniform between the cathode and anode sheaths. Under these assumptions the difference in cell voltage at constant current between the two curves is attributed to the change in IR drop in changing the spacing. Using these values for the resistance, it is possible to calculate the resistance and the IR drop for either of the two spacings. The curve corresponding to 7.6 mil spacing was chosen for analysis. The IR contribution is not negligible, except perhaps for very low currents, as seen from the following table.

<u>V_{cell}</u>	<u>I</u>	<u>IR</u>
0.6	3.05	0.570
0.8	2.99	0.565
1.0	2.74	0.506
1.2	2.53	0.440
1.4	2.27	0.343
1.6	2.02	0.263
1.8	1.65	0.178

The saturation emission current was estimated in two ways.

First, by extrapolating to positive cell voltages the region of the current-voltage curve before arcing, a value of 8 amps/cm² was obtained. Second, by assuming that the same fractional decrease in work function occurs with tantalum as with tungsten for this temperature and cesium pressure, a work function of 3.6 volts is obtained. Using Richardson's equation, a saturation emission current in very good agreement with the extrapolated value is reached. A plot of $\ln \frac{I_s - I}{I}$ vs. $V_{\text{cell}} + IR - (\phi_c - \phi_a)$ is shown in Figure 11-2. The anode work function was taken as 1.7 volts so that $\phi_c - \phi_a = 1.9$ volts was used, although the plot can be made without this information and then $\phi_c - \phi_a$ determined from the plot.

The plot consists of two straight lines which intersect at a point corresponding to a current of about 5 amps/cm². For currents lower than this an electron temperature of 4740°K is arrived at from the slope, and for currents higher than 5 amps/cm² a temperature of

12,240°K is obtained. The interpretation here is that at this value of cell current, the cell suddenly goes over into a mode of operation associated with volume ionization and the formation of very large cathode and anode sheaths.

Knowing the electron temperature, it is then possible to compute the cathode and anode sheath voltage, which will, of course, depend on cell current. By inverting equations (1), the sheath voltages can be expressed as

$$V_a = \frac{kT_e}{e} \ln \frac{I_e}{I}$$

and

$$V_c = \frac{kT_e}{e} \ln \frac{I_e}{I_s - I},$$

where the appropriate value of T_e must be used for each current. The random electron plasma current, I_e , can be calculated from the relation

$$I_e = \frac{1}{4} N_e e V_t$$

where V_t is the random electron velocity,

$$V_t = \sqrt{\frac{2kT_e}{m}}$$

and N_e is the electron density. The cell current can be expressed as

$$I = N_e e V_d = N_e e \mu E$$

where V_d is the electron drift velocity, μ is the electron mobility, and E the uniform electric field between the electrode sheaths. Thus,

$$I_e = \frac{1}{4} I \frac{v_t}{V_d} = \frac{1}{4} I \sqrt{\frac{2kT_e}{m}} \frac{1}{\mu E}$$

Since $E = \frac{IR}{d}$, where d is the spacing,

$$I_e = \frac{1}{4} \sqrt{\frac{2kT_e}{m}} \frac{d}{\mu R}$$

The mobility is given by

$$\mu = \frac{e\tau}{m} ,$$

where τ is the collision period, given by

$$\tau = \frac{1}{N_{Cs} \sigma_c v_t} ,$$

in which N_{Cs} is the cesium atom density, and σ_c the electron-atom collision cross section. Substituting this in the expression for I_e ,

$$I_e = \frac{1}{2} (d N_{Cs} \sigma_c) \frac{kT_e}{e} \cdot \frac{1}{R}$$

The collision cross section has been measured* and is taken here as $\sigma_c = 2 \times 10^{-14} \text{ cm}^2$. The cesium atom density, estimated from the ideal gas law, is $N_{Cs} = 9.6 \times 10^{15}/\text{cm}^3$. Then the random electron plasma current finally reduces to

$$I_e = 1.83 \frac{kT_e}{e} \cdot \frac{1}{R} ,$$

* R. J. Zollweg and M. Gottlieb, Bulletin Am. Phys. Soc., Ser. II, 6, No. 4, 359 (June 1961).

and the sheath voltages to

$$V_a = \frac{kT_e}{e} \ln \left(1.83 \frac{kT_e}{e} \cdot \frac{1}{R} \right)$$

$$V_c = \frac{kT_e}{e} \ln \left(1.83 \frac{kT_e}{e} \frac{1}{(I_s - I)R} \right)$$

The cathode and anode sheath voltages were thus obtained as functions of cell current, and the results are plotted in Figure 11-3. The sheath voltages increase sharply at a cell current density of 5 amps/cm², as does the electron temperature.

The complete potential distribution in the diode is known when the resistance drop in the plasma and the sheath voltages have been determined, and if the work functions are known. The potential distribution in the diode is shown in Figure 11-4 for four current densities. The sharp increase in sheath voltages occurs, of course, at the same current density as does the increase in electron temperature. At the lower currents the cathode sheath voltage corresponds well with the electron temperature, while at the higher currents, the electron temperature is a fraction of the cathode sheath voltage. This suggests that at the higher currents electrons lose energy by inelastic collisions. Volume ionization apparently takes place at these currents. Since the cathode sheath voltage is less than the ionization potential of cesium, this probably by a two step process.

APPENDIX I - SHEATH WIDTHS

An estimate of the width of the potential sheaths can be made by assuming that the plasma is electrically neutral and that the width will correspond to the Debye shielding distance,

$$d_D = \left(\frac{kT}{4\pi N_e e^2} \right)^{1/2} = 6.90 \left(\frac{T_e}{N_e} \right)^{1/2} \text{ cm.}$$

$$N_e = \frac{I}{e \mu E} = \frac{d}{e \mu R}$$

$$\mu = \frac{e}{m} \frac{1}{N \sigma_c V_t} = \frac{1}{N \sigma_c} \left(\frac{e}{m} \right)^{1/2} \sqrt{\frac{e}{2kT_e}}.$$

For the diode described here

$$\mu = 49 \sqrt{\frac{e}{kT_e}}$$

At a cell current density of 5.3 amps/cm², $e/kT_e = 0.987$, $R = 0.185$ ohms, and $\mu = 48.6$,

$$d_D = 6.9 \left(\frac{1.22 \times 10^3}{1.32 \times 10^{16}} \right)^{1/2} = 2.1 \times 10^{-6} \text{ cm.}$$

This value is negligible compared to the cathode-anode spacing.

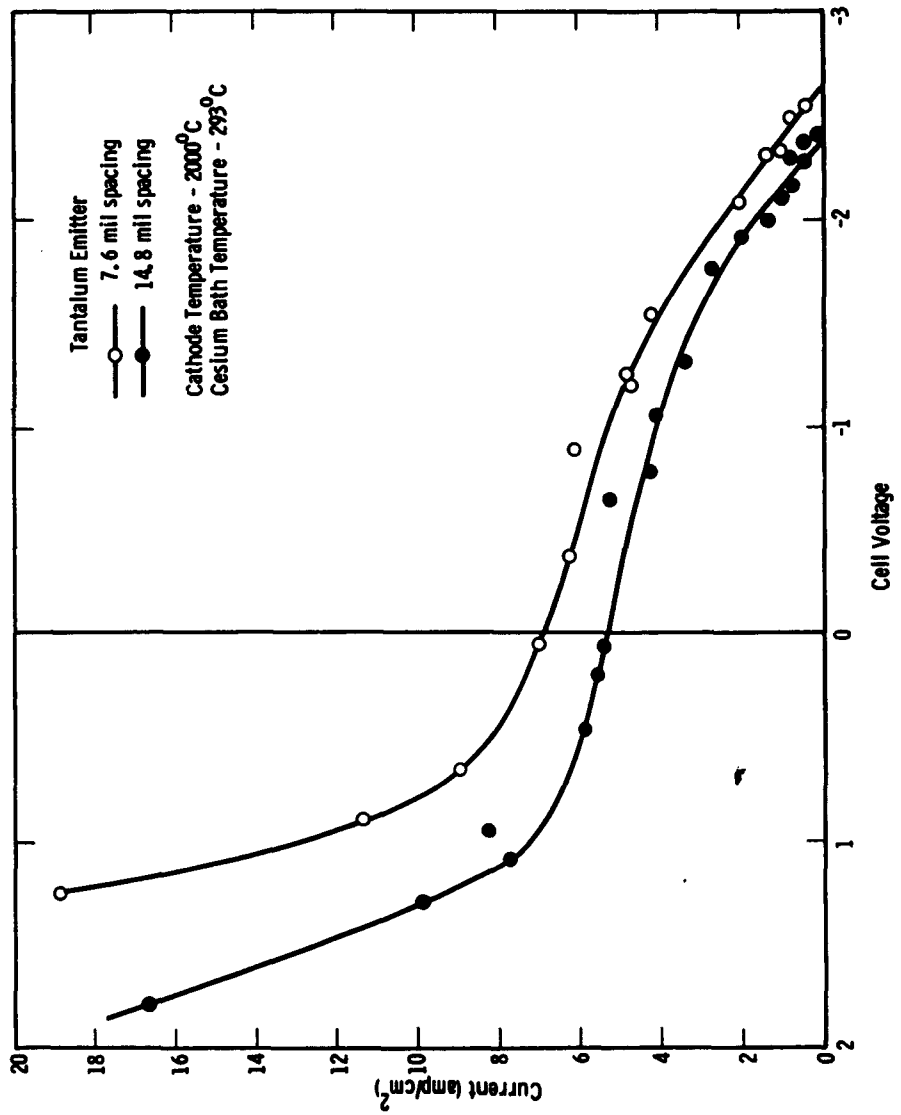


Fig. 11-1. Current Voltage Characteristics at Two Spacings

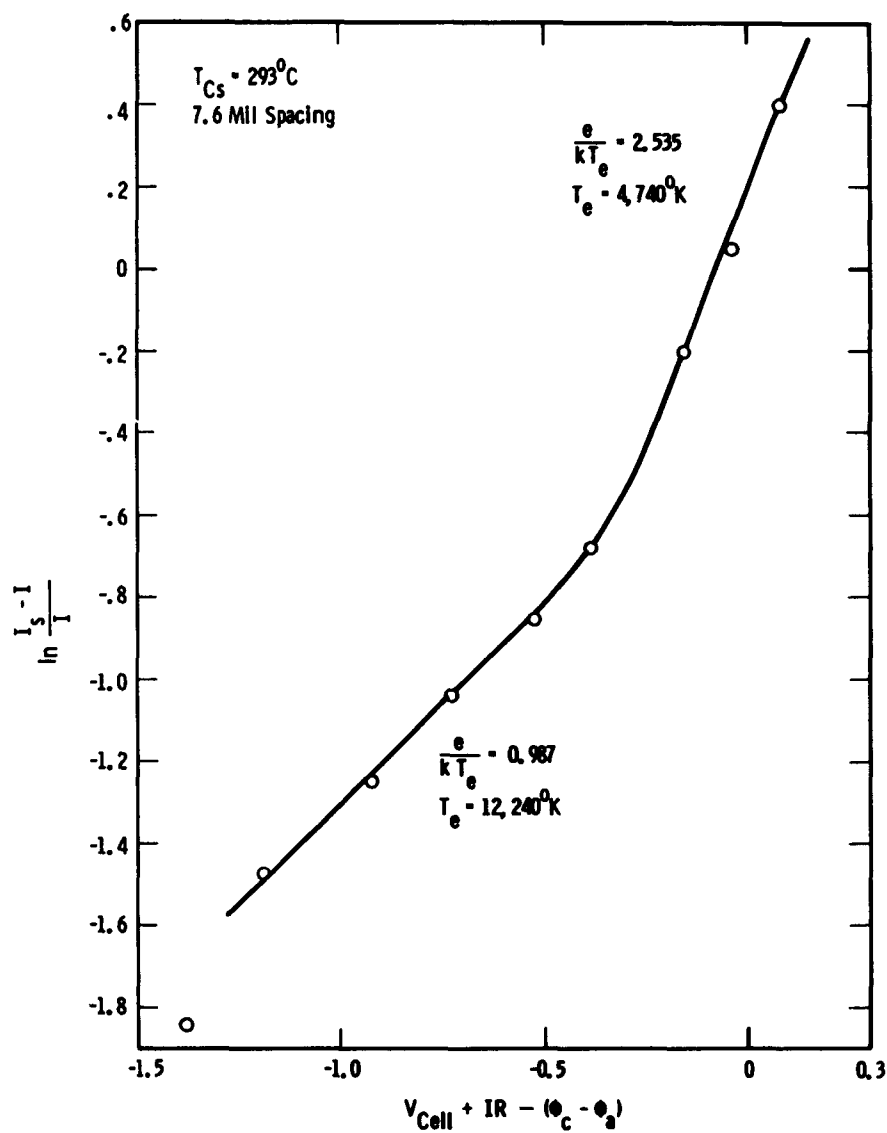


Fig. 11-2. Electron Temperature Plot

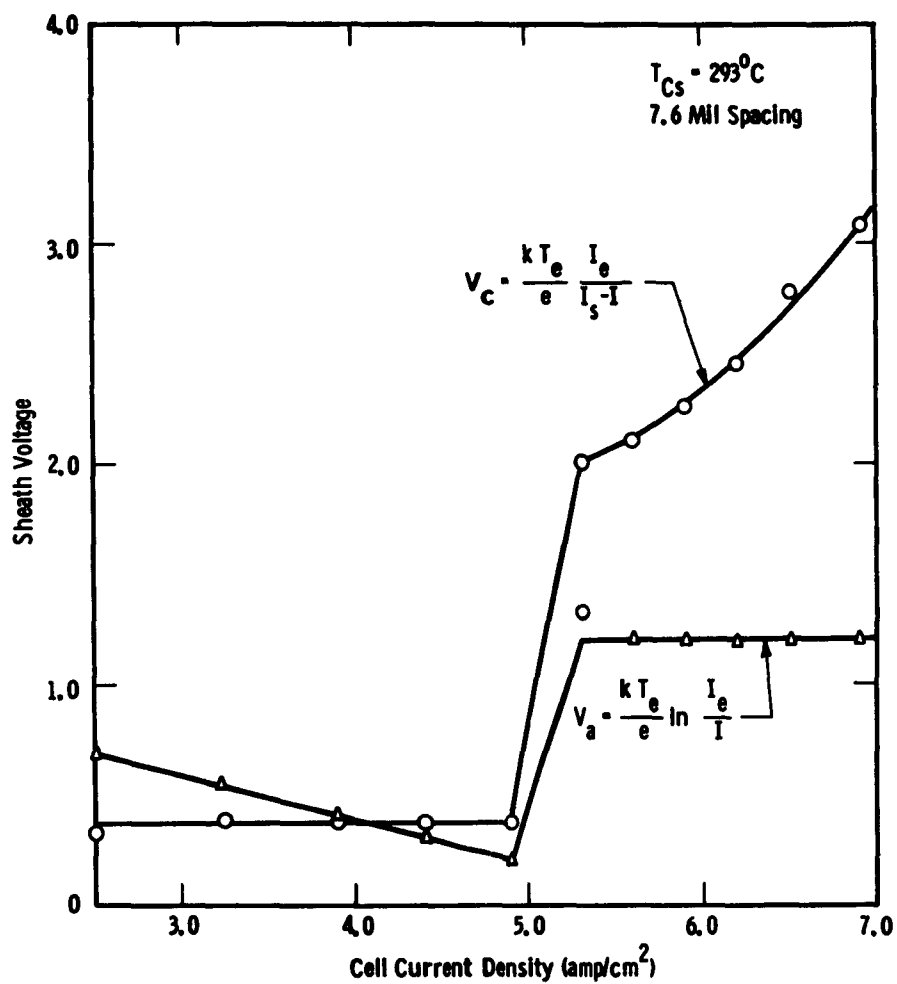


Fig. 11-5. Sheath Voltages vs. Current.

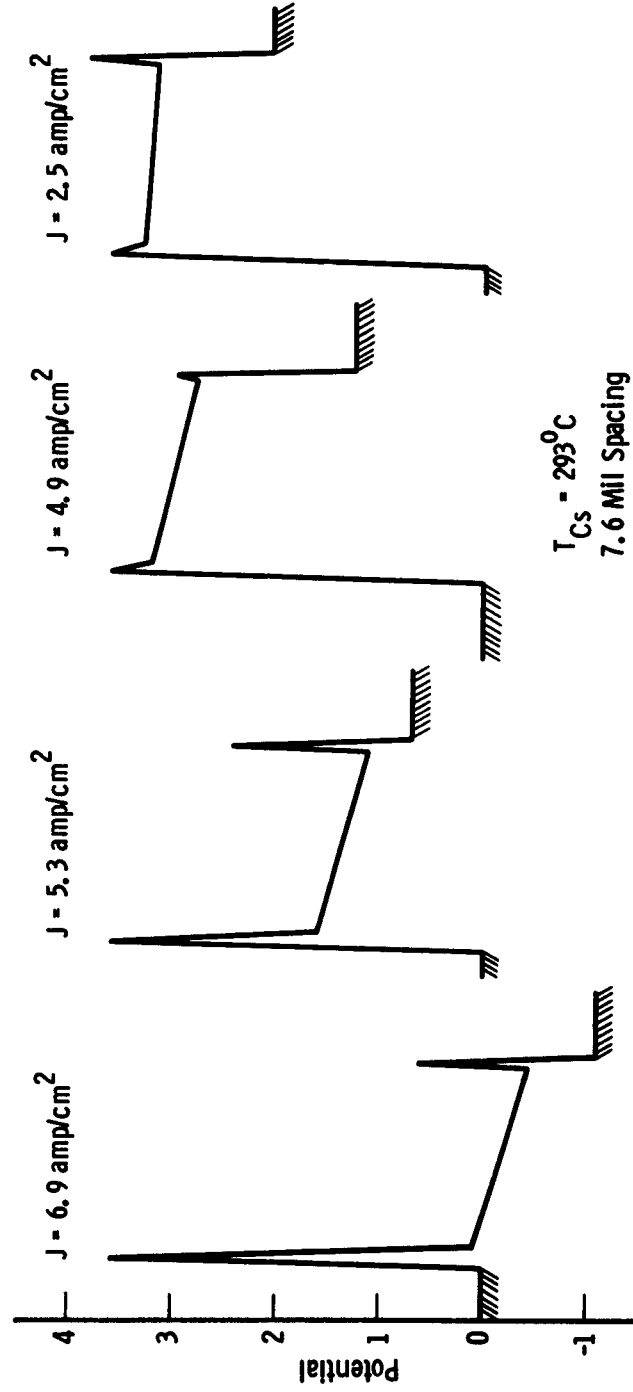


Fig. 11-4. Potential Distributions at Four Different Cell Currents

CHAPTER TWELVE

SPACE CHARGE LIMITED CURRENTS IN HIGH PRESSURE
CESIUM THERMIONIC DIODES

The knowledge of the current-voltage relationships governing the operation of a thermionic diode is necessary in order to understand the results of measurements which are made. For a vacuum thermionic diode, the well-known Childs-Langmuir Law holds in the space charge limited region. According to this relation, the current is proportional to the square of the cell voltage. For the case of the high pressure thermionic diode, the current may be diffusion limited, but will still not necessarily be linear with cell voltage because of the existence of space charge fields in the interelectrode space. In order to estimate electron mobility at high cesium pressure, measurements of current are made in the presence of a magnetic field.

The expression for cell current in the diffusion limited case, at high gas pressures, is given by

$$j = Ne\mu E.$$

The mobility in the presence of a transverse magnetic field is given by

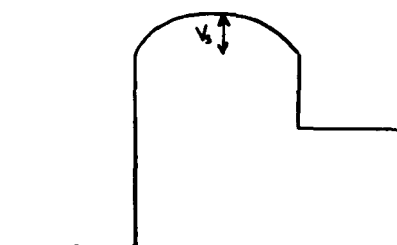
$$\mu_h = \frac{\mu_o}{1 + \omega^2 \tau^2},$$

in which μ_o is the mobility in the absence of the magnetic field, $\omega = \frac{eH}{m}$, and τ is the reciprocal of the collision frequency. The ratio of cell currents without magnetic field to that with magnetic field is given by

$$\frac{j_o}{j_h} = \frac{n_o \mu_o}{n_h \mu_h}$$

The current ratio is then also a measure of the mobility ratio, providing the electron density is known. A crude estimate of the change in electron density, under the conditions at which measurements were done, is made here.

The potential distribution is shown in the figure below for the case of space charge limited current.



A space charge barrier V_s is set up by the cell current. Assume that the net cell current j is given by the current emitted by the cathode, j_e , minus the random plasma current j_r . If the saturation emission current from the cathode is j_s , then that part of this current which surmounts the potential barrier V_s is

$$j_e = j_s \exp\left(-\frac{eV_s}{kT}\right)$$

The random plasma current is

$$j_r = 1/4 Ne\bar{v},$$

so that if we assume that the electron density is uniform in the cell, the net current is

$$j = j_e - j_r = j_s \exp\left(-\frac{eV_s}{kT}\right) - 1/4 Ne\bar{v} = Ne\mu E$$

The ratio of cell current without magnetic field to that with magnetic

field is then given by

$$\frac{j_o}{j_h} = \frac{j_s \exp\left(-\frac{eV_{so}}{kT}\right) - 1/4 N_o e\bar{v}}{j_s \exp\left(-\frac{eV_{sh}}{kT}\right) - 1/4 N_h e\bar{v}} = \frac{N_o \mu_o E_o}{N_h \mu_h E_h}$$

where the subscripts o and h refer to the quantities without and with magnetic field, respectively. If the electron density is uniform, it is easily shown using Poisson's equation that

$$V_s = \frac{1}{2\epsilon_o} N d^2$$

where d is the cathode-anode gap. Using this for V_s

$$\frac{j_o}{j_h} = \frac{j_s \exp\left(-\frac{e^2 d^2 N_o}{2\epsilon_o kT}\right) - 1/4 N_o e\bar{v}}{j_s \exp\left(-\frac{e^2 d^2 N_h}{2\epsilon_o kT}\right) - 1/4 N_h e\bar{v}}$$

The solutions for N_o and N_h can be obtained graphically from

$$\frac{j_o + 1/4 N_o e\bar{v}}{j_s} = \exp\left(-\frac{e^2 d^2}{2\epsilon_o kT} N_o\right)$$

and a similar expression for N_h .

For two typical sets of data,

$$1. \quad T_{cs} = 252^\circ\text{C}$$

$$T_c = 980^\circ\text{K}$$

$$j_s = 3 \times 10^3 \text{ a/m}^2$$

$$j_o = 1.5 \text{ a/m}^2$$

$$j_h = 6 \times 10^{-1} \text{ a/m}^2$$

$$T_e = 1500^\circ\text{K}$$

$$\bar{v} = \sqrt{\frac{2kT}{m}} = 1.5 \times 10^5 \text{ m/sec.}$$

$$d = 5 \times 10^{-4} \text{ m}$$

substituting in the previous equation,

$$5 \times 10^{-4} + 2 \times 10^{-18} N_o = \exp (- 1.75 \times 10^{-14} N_o)$$

$$2 \times 10^{-4} + 2 \times 10^{-18} N_h = \exp (- 1.75 \times 10^{-14} N_h)$$

$$2. \quad T_{cs} = 300^\circ\text{K}$$

$$T_c = 980^\circ\text{K}$$

$$J_s = 3 \times 10^3 \text{ a/m}^2$$

$$J_o = 10 \text{ a/m}^2$$

$$J_h = 6.67 \text{ a/m}^2$$

Substituting these values,

$$3.33 \times 10^{-3} + 2 \times 10^{-18} N_o = \exp (- 1.75 \times 10^{-14} N_o)$$

$$2.22 \times 10^{-3} + 2 \times 10^{-18} N_h = \exp (- 1.75 \times 10^{-14} N_h)$$

The solutions to these equations are shown graphically in the figure.

If it is assumed that $B \propto N$, then

$$\frac{J_o}{J_h} = \left(\frac{N_o}{N_h} \right) \frac{\mu_o}{\mu_h}$$

Using the values obtained graphically for N_o and N_h , for $T_{cs} = 252^\circ\text{C}$

$$\frac{J_o}{J_h} = 0.945 \frac{\mu_o}{\mu_h}$$

and for $T_{cs} = 300^\circ\text{C}$

$$\frac{J_o}{J_h} = .90 \frac{\mu_o}{\mu_h}$$

For these conditions the, the change of electron density with magnetic field is a rather small effect.

The current voltage relationship for the high pressure space charge limited case is given by Cobine, "Gaseous Conductors", McGraw-Hill, 1941, and is summarized here.

$$j = -Ne\bar{v} = -e\mu \frac{dV}{dx}$$

$$= -\frac{j}{\mu} \frac{dx}{dV}$$

By Poisson's equation

$$\frac{d^2V}{dx^2} = \frac{4\pi j}{\mu (dV/dx)}$$

or

$$\frac{dV}{dx} \left(\frac{d^2V}{dx^2} \right) = \frac{4\pi j}{\mu}$$

Integrating,

$$\frac{1}{2} \left(\frac{dV}{dx} \right)^2 = \frac{4\pi j x}{\mu} + C$$

If electrons are emitted with zero velocity, the field at the cathode is zero and $C = 0$.

Integrating again

$$V = \frac{2}{3} \left(\frac{8\pi j}{\mu} \right)^{1/2} x^{3/2} + C_1$$

If the cathode is taken as zero potential, $C_1 = 0$.

$$j = \left(\frac{9}{4} \right) \frac{\mu V^2}{8\pi x^3}$$

If the assumption of zero velocity is not made

$$\frac{1}{2} \left(\frac{dV}{dx} \right)^2 = \frac{4\pi j x}{\mu} + C,$$

where C is a function of the initial velocity.

$$\frac{dv}{dx} = \left(\frac{8\pi n}{\mu} x + 2c \right)^{1/2}$$

$$v = \frac{2}{3} \frac{\mu}{8\pi n} \left(\frac{8\pi n}{\mu} x + 2c \right)^{3/2}$$

$$v^{2/3} = \left(\frac{2}{3} \frac{\mu}{8\pi n} \right)^{2/3} \left(\frac{8\pi n}{\mu} x + 2c \right) = \left(\frac{2}{3} \frac{\mu}{8\pi n} \right)^{2/3} \left(\frac{8\pi n}{\mu} x \right) + \left(\frac{2}{3} \frac{\mu}{8\pi n} \right)^{2/3} 2c$$

$$(jv)^{2/3} = \left(\frac{2}{3} \right)^{1/3} \left(\frac{8\pi n}{\mu} \right)^{1/3} xj + \left(\frac{2}{3} \frac{\mu}{8\pi n} \right)^{2/3} 2c$$

$$\left(\frac{2}{3} \right)^{1/3} \left(\frac{8\pi n}{\mu} \right)^{1/3} xj - v^{2/3} j^{2/3} + \left(\frac{2}{3} \frac{\mu}{8\pi n} \right)^{2/3} 2c = 0$$

This cubic equation in $j^{1/3}$ must be solved in order to obtain explicitly the current-voltage relation.

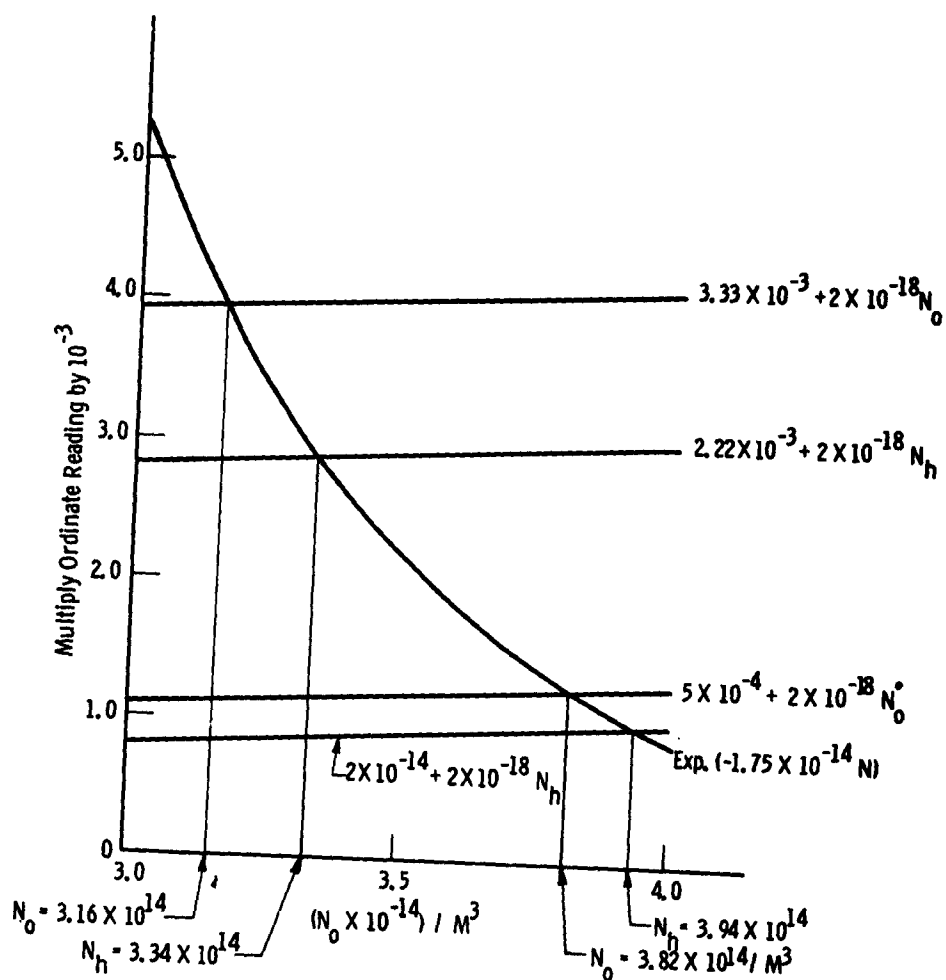


Fig. 12-1. Graphical Solution for Electron Density

DISTRIBUTION LIST FOR ASD-TDR-62-1002

Cys ACTIVITIES AT WPAFB

1 ASAPR (OTS Review)
 1 ASAPRL (Library)
 3 ASAPTS
 1 ASRNG (Tech Director)
 1 ASRNR (Tech Director)
 1 ASRNC (Tech Director)
 1 ARN (Dr. Guderley)
 1 ASEP
 1 AFIT (Library)
 1 ASAPR (Rand)
 1 ASRCPT
 1 ASRCTE
 1 ASRMFP
 3 ASRMFP-2 (A.E. Willis)
 10 ASRNET-3

OTHER DEPT OF DEFENSE ACTIVITIESAIR FORCE

1 AFCL (CRZAP)
 L.G. Hanscom Fld
 Bedford, Mass
 1 AFOSR (SRHPM)
 Attn: Dr. Milton Slawsky
 Building T-D
 Wash 25, DC
 1 SSD (SSTR, Capt Evert)
 AF Unit Post Office
 Los Angeles 45, Calif

NAVY

1 Office of Naval Research
 Code 429
 Attn: Cmdr J. Connelly
 Wash 25, DC
 1 Chief, BuShips
 Attn: Code 681A1D
 Navy Dept
 Wash 25, DC

Cys ARMY

1 USASDL (SIGRA/SL-PRT)
 Ft. Monmouth, NJ
 1 USASDL (SIGFM/SL-PRG)
 Attn: Mr. M.H. Zinn
 Ft. Monmouth, NJ

OTHER U.S. GOVERNMENT AGENCIES

30 ASTIA (TIPDR)
 Arlington Hall Stn
 Arlington 12, Va
 4 Advisory Group on Electron Devices
 Attn: H. N. Serig
 346 Broadway, 8th Floor
 New York 13, NY
 1 US Atomic Energy Commission
 Div of Reactor Development
 Attn: Cmdr. W. Schoenfeld
 Wash 25, DC
 1 US Atomic Energy Commission
 San Francisco Operations Off
 Attn: Reactor Division
 2111 Bancroft Way
 Berkeley 4, Calif
 1 NASA-Lewis Research Center
 SEPO
 Attn: Mr. R. Dennington
 2100 Brookpark Road
 Cleveland 35, Ohio
 100 Office of Technical Services
 1200 South Eads St
 Arlington, Va

DISTRIBUTION LIST FOR ASD-TDR-62-1082

(Continued)

<u>Cys</u>	<u>NON-GOVERNMENT ORGANIZATIONS AND INDIVIDUALS</u>	<u>Cys</u>	<u>NON-GOVERNMENT ORGANIZATIONS AND INDIVIDUALS</u>
1	Defense Research Member Canadian Joint Staff 2450 Massachusetts Ave, NW Wash 8, DC	1	Radio Corp of America Attn: Mr.D.G.Garvin New Holland Pike Lancaster, Pa
1	Advanced Research Projects Agency Attn: Dr. John Huth Wash 25, DC	2	Atomics International Div of North American Aviation Attn: Dr. M.N.Huberman Canoga Park, Calif
1	Jet Propulsion Laboratory Spacecraft Secondary Power Sec Attn: Mr. Paul Goldsmith 4800 Oak Park Drive Pasadena, Calif	1	Ford Instruments Co 3110 Thomas Ave Long Island City, NY
1	Aerospace Corporation Attn: Library Technical Document Group Post Office Box 95085 Los Angeles 45, Calif	1	Marquardt Co 16555 Saticoy St Van Nuys, Calif
1	Los Alamos Scientific Labs Attn: Mr. R. Lee Aamedt Los Alamos, NM	1	RCA Laboratories Attn: Dr. K.G.Hernquist Princeton, NJ
1	General Electric Co Research Laboratories Attn: John M. Houston Schenectady, NY	1	Thermo Electron Engr Corp Attn: Dr.G.M. Hatsopoulos Waltham, Mass
1	The Bendix Corp Research Laboratories Div Attn: Dr. W.M. Kunn, Jr Southfield, Mich	20	Westinghouse Research Labs Attn: Milton Gottlieb Pittsburgh, Pa
1	General Atomics Attn: R. W. Pidd San Diego, Calif		
1	Hughes Research Labs Attn: Dr.R.C. Knechtli Malibu, Calif		
1	Allison Division General Motors Corp Attn: D.L. Dresser Indianapolis, Ind		

Aeronautical Systems Division, Mr/Vionics,
Electronic Technology Lab, Wright-Patterson AFB,
Ohio.
Rpt Nr ASD-TDR-62-1082, HEAT DIODE CONVERTER.
Final report, May 63, 301p., incl illus., tables,
71 refs.

Unclassified Report

The work presented in this report represents an
eighteen month program in which experimental and
theoretical investigations were made on several
aspects of the cesium plasma thermionic converter.
Data were taken on the electron emission properties
of tungsten, tantalum, molybdenum, niobium, rhenium,
iridium and tantalum carbide. Two methods were
used in this study: one was the measurement of the
I-V characteristics of diodes using emitters of
these materials and the other was the direct mea-
surement of the saturation emission current density

(over)

by the plasma-anode technique. It is possible to
make some separation between emission effects and
transport effects by combining results of these
two measurements. Studies were made on several
important loss mechanisms in the thermionic con-
verter. Among these were the thermal conduction
loss in the cesium vapor, losses associated with
electron scattering in the plasma, and losses due
to reflection of electrons by the collector. A
study was also made of the evaporative loss of the
emitter in the presence of cesium. The experi-
mental data collected has been used for an extensive
theoretical analysis of the efficiency and lifetime
of a thermionic converter. Theoretical treatments
are also given for energy and mass transfer in the
cesium plasma and of electron emission in the
presence of a plasma.

1. Thermionic energy
converters
2. Cesium plasma
converters
3. Cesium plasma diodes
- I. AFSC Project 4156,
Task 415604
- II. Contract AC33(616)-
8262
- III. Westinghouse Research
Laboratories,
Pittsburgh 35, Pa.
- IV. Alton Gottlieb et al
- V. 62-918-274-84
- VI. Avail for JTS
- VII. In ASTIA collection

Aeronautical Systems Division, Mr/Vionics,
Electronic Technology Lab, Wright-Patterson AFB,
Ohio.
Rpt Nr ASD-TDR-62-1082, HEAT DIODE CONVERTER.
Final report, May 63, 301p., incl illus., tables,
71 refs.

Unclassified Report

The work presented in this report represents an
eighteen month program in which experimental and
theoretical investigations were made on several
aspects of the cesium plasma thermionic converter.
Data were taken on the electron emission properties
of tungsten, tantalum, molybdenum, niobium, rhenium,
iridium and tantalum carbide. Two methods were
used in this study: one was the measurement of the
I-V characteristics of diodes using emitters of
these materials and the other was the direct mea-
surement of the saturation emission current density

(over)

by the plasma-anode technique. It is possible to
make some separation between emission effects and
transport effects by combining results of these
two measurements. Studies were made on several
important loss mechanisms in the thermionic con-
verter. Among these were the thermal conduction
loss in the cesium vapor, losses associated with
electron scattering in the plasma, and losses due
to reflection of electrons by the collector. A
study was also made of the evaporative loss of the
emitter in the presence of cesium. The experi-
mental data collected has been used for an extensive
theoretical analysis of the efficiency and lifetime
of a thermionic converter. Theoretical treatments
are also given for energy and mass transfer in the
cesium plasma and of electron emission in the
presence of a plasma.

1. Thermionic energy
converters
2. Cesium plasma
converters
3. Cesium plasma diodes
- I. AFSC Project 4156,
Task 415604
- II. Contract AC33(616)-
8262
- III. Westinghouse Research
Laboratories,
Pittsburgh 35, Pa.
- IV. Alton Gottlieb et al
- V. 62-918-274-84
- VI. Avail for JTS
- VII. In ASTIA collection